Synthesis and Characterization of Self-assembled Nanostructures for OLED devices with Thermally Activated Delayed Fluorescence or Circularly Polarized Luminescence

Yu-Yu Hsieh

THESIS UNDER DOUBLE-DEGREE AGREEMENT

To Obtain

DOCTORAL DEGREE IN CHEMISTRY

of

UNIVERSITY OF BORDEAUX

DOCTORAL SCHOOL OF CHEMICAL SCIENCES

and

NATIONAL TAIWAN UNIVERSITY

COLLEGE OF SCIENCE, DEPARTMENT OF CHEMISTRY

by

Yu-Yu HSIEH

Synthesis and Characterization of Self-assembled Nanostructures for OLED devices with Thermally Activated Delayed Fluorescence or Circularly Polarized Luminescence

Synthèse et caractérisation de nanostructure auto-assemblées pour la fabrication de dispositifs OLED fonctionnels

Under Supervision of

Dr. Dario M. BASSANI and **Dr. Ken-Tsung WONG**

Defended on 28 July 2022

Jury Members

Dr. Matteo MAURO	Maître de conferences, University of Strasbourg	Reviewer
Dr. Shih-Sheng SUN	Professor, Academia Sinica	Reviewer
Dr. Clémence ALLAIN	Research Director, ENS Paris-Saclay	President
Dr. Li-Yin CHEN	Professor, National Yang Ming Chiao Tung University	Examiner
Dr. Dario M. BASSANI	Research Director, University of Bordeaux	Thesis Supervisor
Dr. Ken-Tsung WONG	Professor, National Taiwan University	Thesis Supervisor

ABSTRACT

Self-assembly is a promising approach to organize functional organic nanomaterials from the molecular level using molecular design. It plays a critical role in diverse opto-electronic applications where it contributes to structuring the active layer.

In Chapter 1, we introduce the concept of self-assembly and the developments of supramolecular organic functional materials. In Chapter 2, we design systems consisting of D-π-A type TADF chromophores and biuret molecular recognition motifs that combine tunable emission wavelength with the spontaneous formation of well-defined spherical aggregates. Electroluminescent devices using these TADF materials capable of harvesting triplet excitons exhibit 5- to 10-times greater external quantum efficiencies compared to analogous systems without TADF behavior while retaining the formation of sub-micron sized emissive domains. In Chapter 3, we combine biuret motifs with various chiral chromophores, such as axially chiral 1,1'-binaphthalenes, chiral 3,4-alkylenedioxythiophenes and chiral *E*-cyclohexyl derivatives, to self-assemble into ordered aggregates to amplify the chiroptical properties in the ground and excited state. In Chapter 4, we synthesize a series of carbazole-based derivatives with axially chirality in application of circularly polarized exciplex to enhance the intensity of circularly polarized luminescence through charge transfer process and probe several candidate exciplex systems to investigate their photophysical and chiroptical properties in films.

RESUME

L'auto-assemblage est une approche prometteuse pour organiser les nanomatériaux organiques fonctionnels en partant de la structure moléculaire. Il joue un rôle critique dans diverses applications optoélectroniques où il contribue à structurer la couche active.

Dans le chapitre 1, nous introduisons le concept d'auto-assemblage et les développements de matériaux fonctionnels organiques supramoléculaires. Dans le chapitre 2, nous concevons des systèmes constitués de chromophores TADF de type D-π-A combinant des motifs de reconnaissance moléculaire de type bis-urée permettant l'ajustement de la longueur d'onde d'émission et la formation spontanée d'agrégats sphériques bien définis. Les dispositifs électroluminescents utilisant ces matériaux TADF sont capables de récolter des excitons triplets et présentent des efficacités quantiques externes 5 à 10 fois supérieures à celles des systèmes analogues sans comportement TADF, tout en conservant la formation de domaines émissifs de taille inférieure au micron. Dans le chapitre 3, nous combinons des motifs biuret avec divers chromophores chiraux, tels que des 1,1'-binaphtalènes axialement chiraux, des 3,4-alkylènedioxythiophènes chiraux et des dérivés *E*-cyclohexyle chiraux, pour s'auto-assembler en agrégats ordonnés afin d'amplifier les propriétés chiroptiques dans l'état fondamental et excité. Dans le chapitre 4, nous synthétisons une série de dérivés à base de carbazole avec une chiralité axiale capable de former des exciplexes chiraux afin d'améliorer l'intensité de la luminescence polarisée circulairement par un processus de transfert de charge et sondons plusieurs systèmes d'exciplex candidats pour étudier leurs propriétés photophysiques et chiroptiques.

摘要

自組裝是一種有趣的方法，能透過合理設計，將有機分子組成各種機能性奈米材料，並於眾多光電材料的應用中扮演關鍵角色。

在本論文的第一章，我們會簡述自組裝的概念與回顧超分子機能性有機材料的發展。第二章則設計一系列 D-π-A 架構的熱激活化延遲螢光 (TADF) 分子，調控拉電子基團強度，使放光波長從綠到黃橙色，並藉由引入雙縮脲自組裝基團，使之能自發形成大小均勻的螢光奈米囊泡。與傳統螢光分子相比，其電致發光元件最大外部量子效率提升近 5 到 10 倍，並導入噴墨印刷技術，製成微米級解析度的大面積發光元件，兼顧高解析度與優化的元件表現。第三章在不同的不對稱發色團上，如具軸手性的 1,1'-雙萘 (1,1'-binaphthalene)、手性 3,4-伸烷基二氧噻吩 (3,4-alkylenedioxythiophene) 與手性反式環己基衍生物 (*trans*-cyclohexyl derivatives)，橋接上雙縮脲基團，使之自組裝形成規則有序的聚集結構，進而增強其於基態與激發態的旋光性質。第四章則設計一系列具軸手性的咔唑 (carbazole) 分子，作為電洞傳輸材料應用於圓偏振激發錯合物 (circularly polarized exciplex)，來提升圓偏振光 (CPL) 強度，並根據材料能階，找出潛在的激發錯合物系統，進而探討其於薄膜態的光物理與旋光性質。

Table of Content

Molecular Structure Index

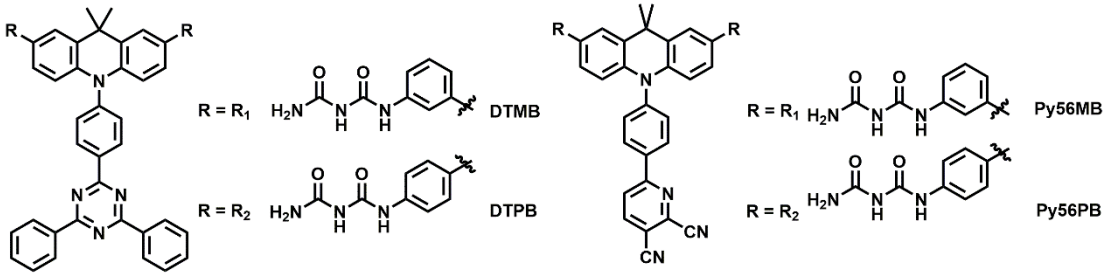

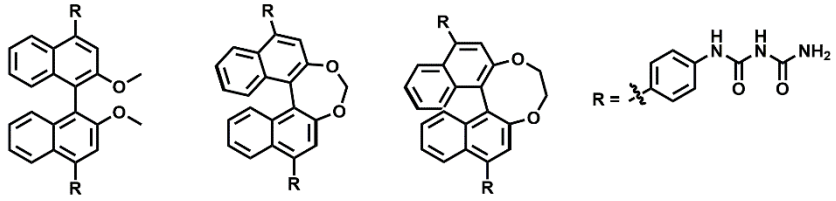

BNPB 7BBNPB 8BBNPB

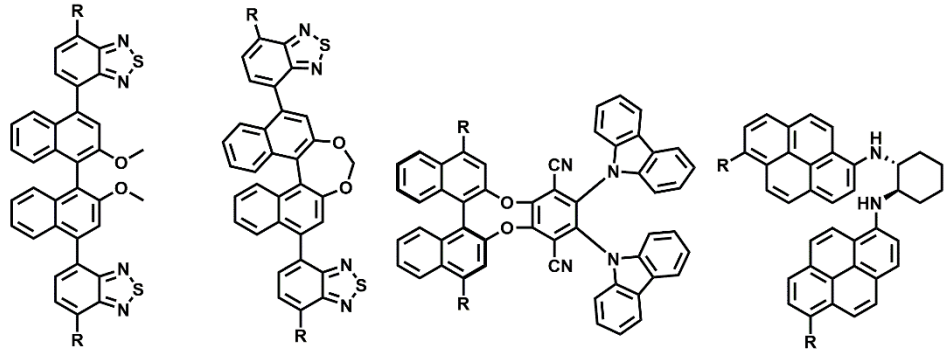

BNBTPB 7BBNBTPB BNCNCzPB DACHPyPB

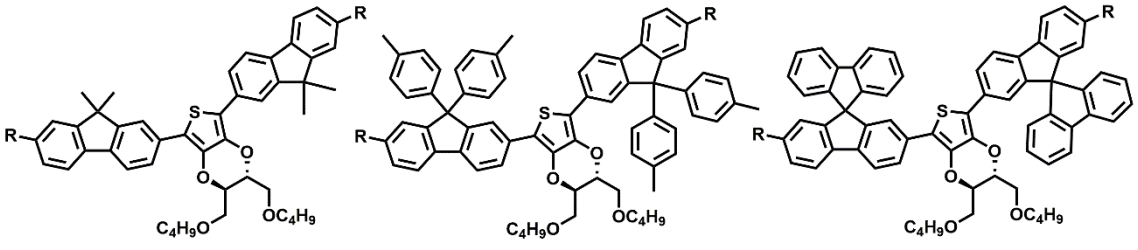

ADOTMFPB ADOTTFPB ADOTSFPB

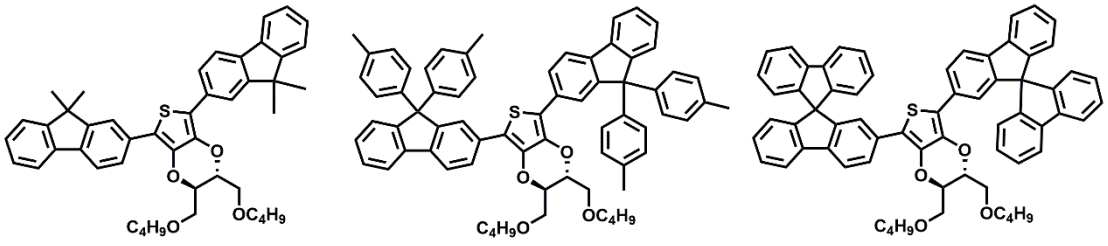

ADOTMF ADOTTF ADOTSF

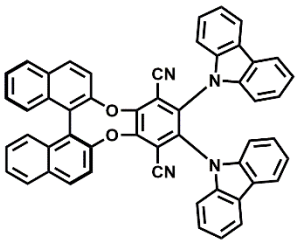

BNCNCz

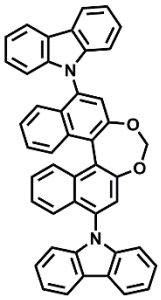

7BBNCz

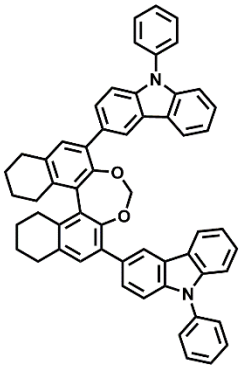

3CzPh

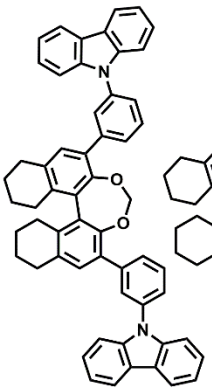

Ph3Cz

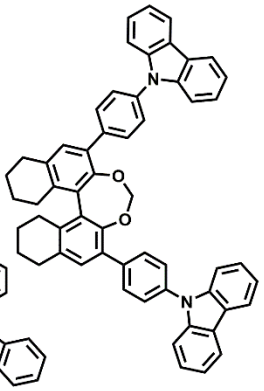

Ph4Cz

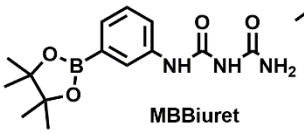

MBBiuret

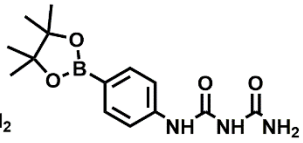

PBBiuret

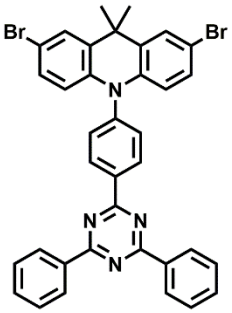

DTBr2

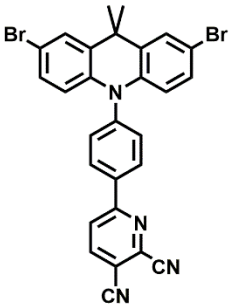

Py56Br2

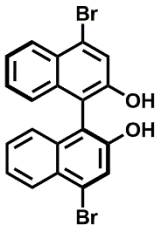

BNOH

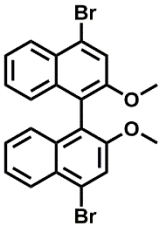

BNOMe

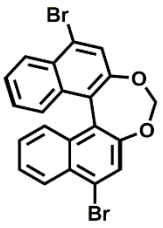

7BBNBr2

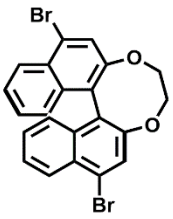

8BBNBr2

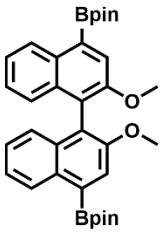

BNBpin2

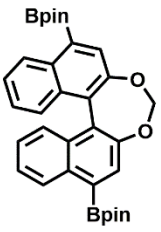

7BBNBpin2

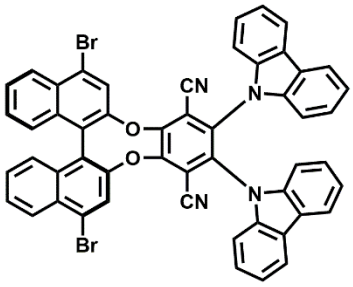

BNCNCzBr2

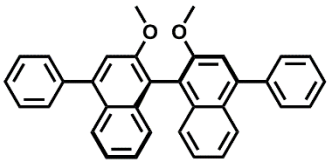

BNPh

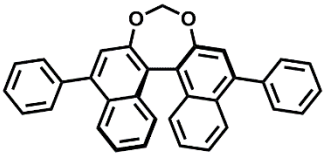

7BBNPh

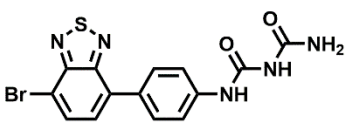

BTBiuret

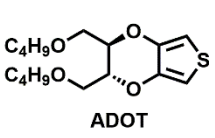

ADOT

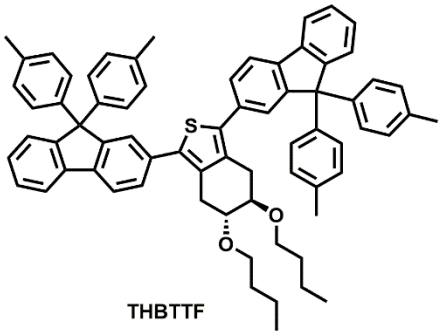

THBTTF

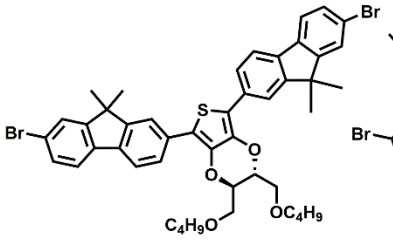

ADOTMFBr2

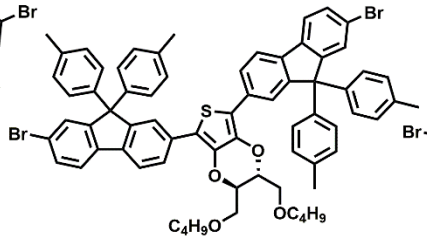

ADOTTFBr2

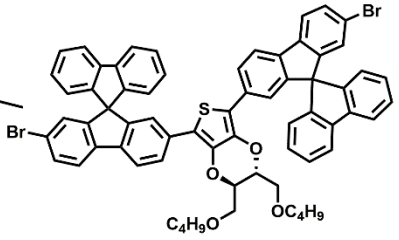

ADOTSFBr2

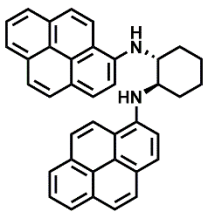

DiPy

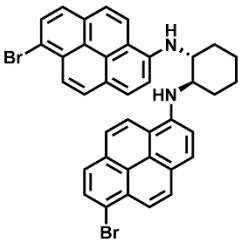

DACHPyBr2

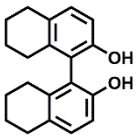

H8-BINOL

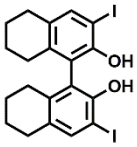

H8-BNI2

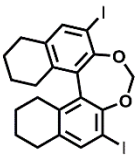

H8-7BBNI2

Chapter 1. Introduction

1-1 Research Motivation

Chemical synthesis involves the breaking or formation of covalent bonds between atoms to obtain the desired organic molecules or materials using a reasonable design strategy. Beyond covalent bonds, non-covalent interactions play a vital role in materials and biological fields as well. The primary building blocks (amino acids, carbohydrates, lipids, nucleotides) can assemble into macromolecules which then form supramolecular structures (proteins, glycogen, DNA) that are organized into complex systems (nuclei, mitochondria, ribosomes),[1] which in turn function cooperatively in metabolic pathways in living systems. Taking inspiration from nature, highly ordered and sophisticated systems constructed by intermolecular non-covalent interactions are studied by supramolecular chemists with the objective of controlling the complex spatial (structural) and temporal (dynamic) features of matter through self-organization.[2] Supramolecular self-assembly describes the evolution toward spatial ordering and confinement through the spontaneous association of various subcomponents, leading to the generation of individual/extended entities at either the molecular (covalent) or supramolecular (non-covalent) level.

1-2 Concept and Types of Self-Assembly

From a thermodynamic viewpoint,[3,4] self-assembly is regarded as the minimization of free energy in a closed system, resulting in an equilibrium state. The latter is sensitive to external stimuli, and self-assembled systems may evolve towards a new equilibrium state when exposed to stress. Thus, the self-assembled structures are thermodynamically more stable than the separate, unassembled units. The self-assembly process can be expressed by the Gibbs free energy equation (**Equation 1-1**):

$$\Delta G_{SA} = \Delta H_{SA} - T\Delta S_{SA} \qquad \textbf{(Equation 1-1)}$$

where self-assembly is a thermodynamically favored process if $\Delta G_{SA} < 0$. ΔH_{SA} is the enthalpy change in the process determined by the potential energy or intermolecular forces between building blocks. ΔS_{SA} is the entropy change related to the formation of the organized or hierarchical assembled structures. In general, ΔS_{SA} decreases upon organization so that ΔH_{SA} should be negative enough to keep ΔG_{SA} less than zero for an energetically-favored process. In **Equation 1-1**, when the $|T\Delta S_{SA}|$ of a system approaches the $|\Delta H_{SA}|$ at or above a critical temperature, self-assembly will not be exothermic. Therefore, controlling the intermolecular interactions in a supramolecular system to keep the free energy negative so as to facilitate spontaneous self-assembly is an interesting issue for scientists.

Prof. Whitesides defined the term “self-assembly” as a process that involves the combination of pre-existing components (separate or distinct parts of disordered structure), that is reversible, and that can be controlled by the proper design of components.[5] Therefore, “self-assembly” is not the synonym of “formation”. Prof. Lehn indicated that “self-organization” is an integrated self-assembly process with an ordered and precise supramolecular structure.[6] In addition, Prof. Whitesides proposed several reasons why scientists would be attracted by self-assembly.[7-9] First, humans are interested in the appearance of order from disorder. Second, living cells are assembled from simple building blocks via hierarchical self-assembly, such as lipid membranes,[10] folded proteins,[11] structured nucleic acids,[12,13] molecular machines.[14,15] To reveal the origin of life, scientists are required to understand the mechanism of self-assembly. Third, self-assembly is one of the few strategies to fabricate nanoassemblies or nanomaterials on a large scale, playing a critical role in the field of nanotechnology.[16-18] Fourth, manufacturing will benefit from the application of self-assembly. Finally, self-assembly is ubiquitous in dynamic, multi-component systems, such as smart materials[19] and self-healing structures.[20]

Historically, the concept of self-assembly came from the investigation of molecular process. The success of self-assembly in a molecular system can be determined by five characteristics in the system as detailed below:[7]

(1) **Components**

A self-assembled system is comprised of groups of molecules or segments that interact with one another via particular binding forces or substrates. These molecules or segments could be the same or different. Their interaction promotes them from less ordered states (solutions, random coils or disordered aggregates) to a final state (a crystal or folded macromolecules) that is more organized.

(2) **Interactions**

Self-assembly takes place when molecules interact with one another through a combination of attractive and repulsive interactions. Compared to thermal energy at RT, the individual noncovalent interactions in self-assembly can be relatively weak, e.g. van der Waal force, π-π stacking, hydrogen bonding and dipole-dipole interactions.[21,22] Complementarity in shape among the self-assembled components increases intermolecular interactions.

(3) **Reversibility or Adjustability**

In the self-assembly process of organized structures, the association should be reversible so as to allow the components to adjust their positions during aggregation. This is an essential aspect since it allows for error correction during the self-assembly process:[23-25] Intermediate architectures in which the components are not correctly organized are at a higher potential energy compared to those structures in which

organization is optimized. Therefore, similarly to crystal growth,[26] they will undergo preferential dissociation to favor formation of the most thermodynamically stable architectures. The strength of the bonds between the components must therefore be comparable to the forces tending to disrupt them. For molecules, these forces originate from thermal motion. Processes in which collisions between molecules result in irreversible binding tend to generate glasses, not ordered materials. Besides, increasing the amount of redundancy,[27] which allows errors to be detected and corrected, is another critical element to reduce the error rate during self-assembly. In gene duplication,[28,29] a well-known self-assembled system in biological organisms, there are multiple genes performing the same function. When an individual gene is mutated or disrupted, the other "back-up" genes could still perform identical roles to ensure the system works normally in living organisms.

(4) **Environment**

The self-assembly of molecules generally occurs in solution or at an interface to allow the motion of the components. The interaction of the components with their environment governs in the direction of the process and numerous elements, such as solvation,[30] temperature[31] or pH value,[32] provide opportunities for externally controlling the self-assembly process. In general, the major component in solution is the solvent. Therefore, the specific and nonspecific interactions between molecules and solvents (i.e.

dispersion, dipole-dipole and hydrogen-bonding) play a decisive role in engineering nanostructures in materials.[33]

(5) **Mass Transport and Agitation**

Self-assembly requires the mass transport of molecules to ensure that adequate concentrations of the components are available throughout the process. Therefore, the molecules or components must be mobile. Thermal energy affords an important part of the motion used to bring molecules into contact in solution.

Based on the five factors above, self-assembly is depicted in **Figure 1-1**.[7] Initially, in step A, aggregation occurs when there is a net attraction and an equilibrium separation between components, representing a balance between attraction and repulsion. These opposite interactions are defined at the molecular level but can be adjusted independently at macroscopic level. In step B, elements that interact with one another irreversibly produce disordered glasses. In step C, if elements can equilibrate or adjust the positions once in contact, they would assemble into ordered materials, a more thermodynamically stable form. In step D, the completed supramolecular organization produces functional units in biological living systems.

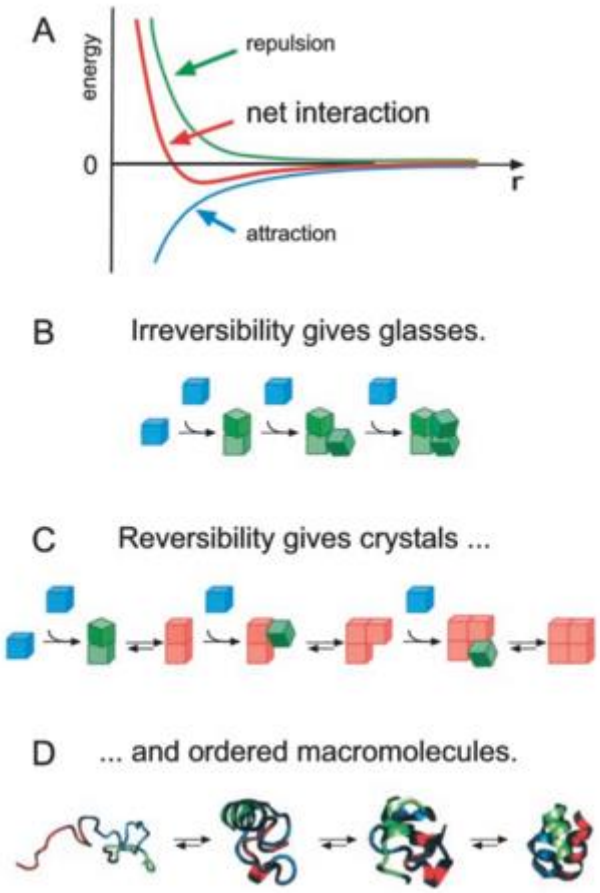

Figure 1-1. Process of self-assembly. Readapted with permission from ref 7. Copyright 2002, The National Academy of Sciences.

Self-assembly could be classified as either static or dynamic (**Table 1-1**).[5] Without external interference, a system tends towards the lowest-energy state and static self-assembly drives the components to form the structures at the equilibrium state. For example, molecular crystals and lipid bilayer in biomembranes are arranged by static self-assembly. It requires energy to form organized structures but ordered assemblies are stable once they are generated. In the presence of a continuous external stimuli, a dynamic

self-assembly system adapts to the surroundings as the components continuously assemble into ordered structures to decrease the overall energy of the system. Once the external interference vanishes, the lowest-energy state of a dynamic self-assembly system disappears and the system collapses to the thermodynamically-favored state. Living organisms represent an example of dynamic self-assembly.

Table 1-1. Examples and types of self-assembly.[a]

Systems	Type	Applications/importance
Atomic, ionic, and molecular crystals	S	Materials, optoelectronics
Phase-separated and ionic layered polymers	S	
Self-assembled monolayers (SAMs)	S, T	Microfabrication, sensors, nanoelectronics
Lipid bilayers and black lipid films	S	Biomembranes, emulsions
Liquid crystals	S	Displays
Colloidal crystals	S	Band gap materials, molecular sieves
Bubble rafts	S	Models of crack propagation
Macro- and mesoscopic structures (MESA)	S or D, T	Electronic circuits
Fluidic self-assembly	S, T	Microfabrication
"Light matter"	D, T	
Oscillating and reaction-diffusion reactions	D	Biological oscillations
Bacterial colonies	D, B	
Swarms (ants) and schools (fish)	D, B	New models for computation/optimization
Weather patterns	D	
Solar systems	D	
Galaxies	D	

[a] S, static; D, dynamic; T, templated; B, biological

The process of static and dynamic self-assembly can be further sub-divided into co-assembly, hierarchical self-assembly and directed self-assembly as depicted in **Figure 1-**

2.[34,35] Co-assembly represents two or multiple building blocks that cooperatively self-assemble into an architecture that could not be constructed by the isolated self-assembly of individual components. As depicted in **Figure 1-3**, Ulijn *et al.* reported the co-assembly of aromatic carbohydrates and dipeptide amphiphiles to generate minimalistic proteoglycan mimics under physiological conditions.[36] With the help of electrostatic interactions, micelles consisting of carbohydrate amphiphiles assemble onto the peptoid nano-tapes to produce micro-sized nanofibers and then form supramolecular hydrogels. By changing the chemical design, the bio-functionality and mechanical properties of these hydrogels are finely tunable and could be utilized in biomedical and tissue engineering applications. Ravoo *et al.* designed a heteromultivalent platform by co-assembling cyclodextrin (**CD**) and calixarene amphiphiles (**CA**) used for selectively binding to tyrosine-rich or lysine-rich peptides, involved in amyloid-β peptides (**Figure 1-4**).[37] As a proof-of-concept, the **CD-CA** coassemblies could be used to inhibit Aβ fibrillation by strong recognition to pathogenic peptide **$A\beta_{42}$** in Alzheimer's disease and the self-assembled heteromultivalent platform with tunable modification has the potential for targeted biomedical applications.

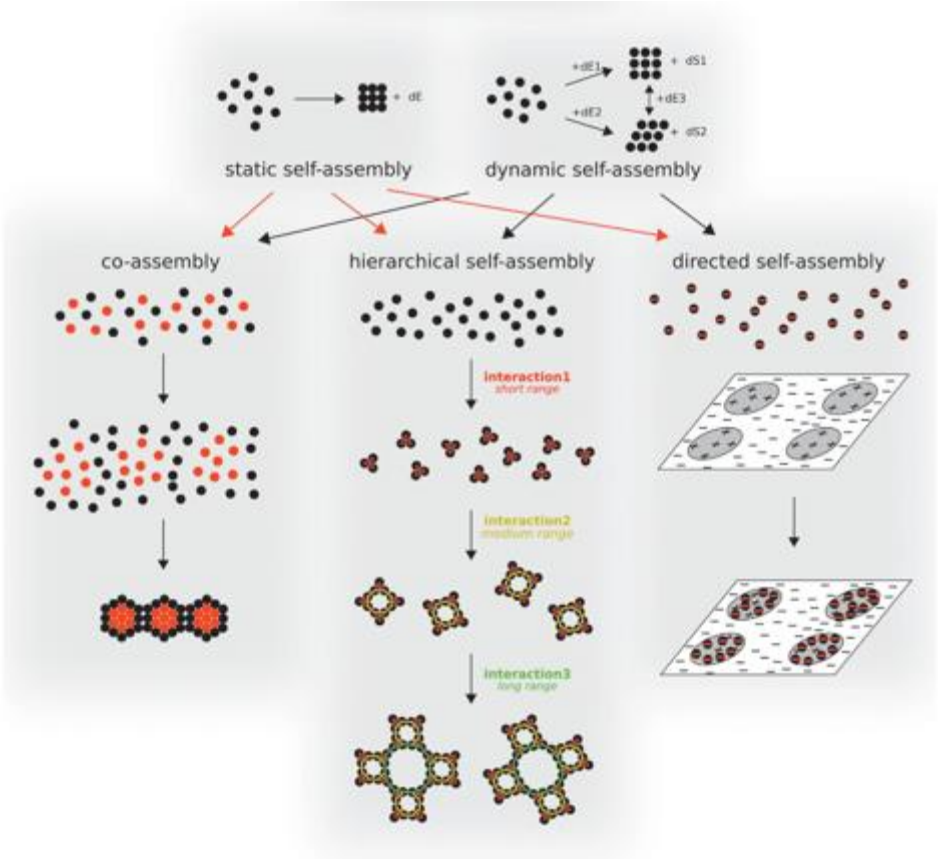

Figure 1-2. Illustrations of static and dynamic self-assembly and the relationship between co-assembly, hierarchical assembly and directed assembly. This illustration is adapted with permission from ref 34 and 35.

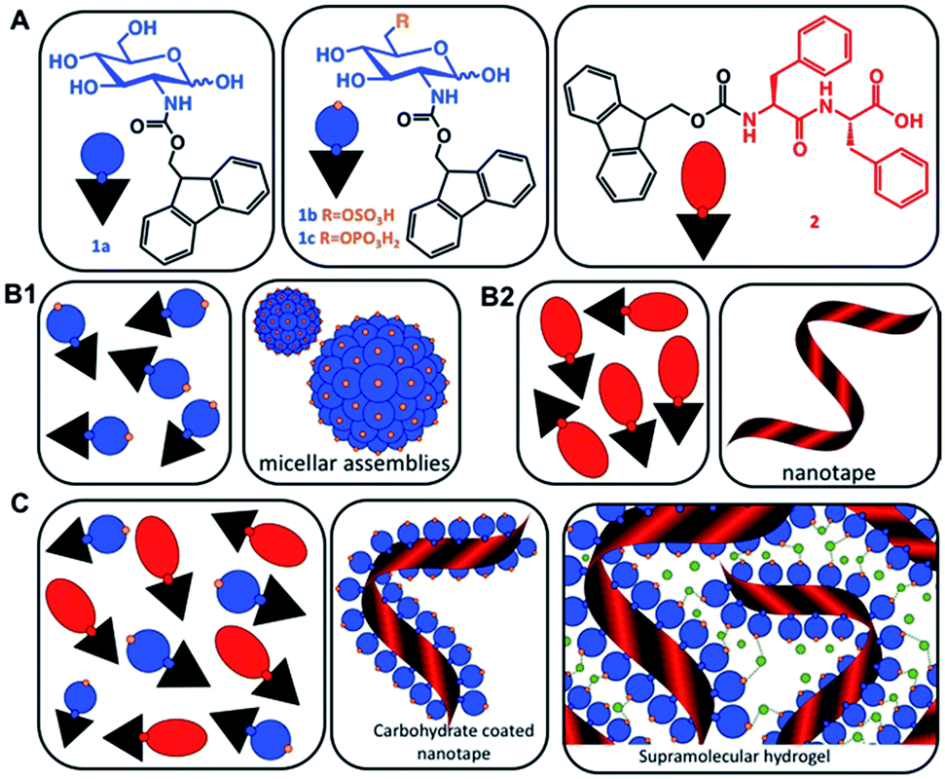

Figure 1-3. (a) Chemical structures of carbohydrate amphiphiles and peptide analogues. Schematic representation of (b) the assembly of the individual components and (c) co-assembly of carbohydrate-functionalized peptide nanotapes and supramolecular hydrogels. Reproduced from ref 36 with permission from the Royal Society of Chemistry.

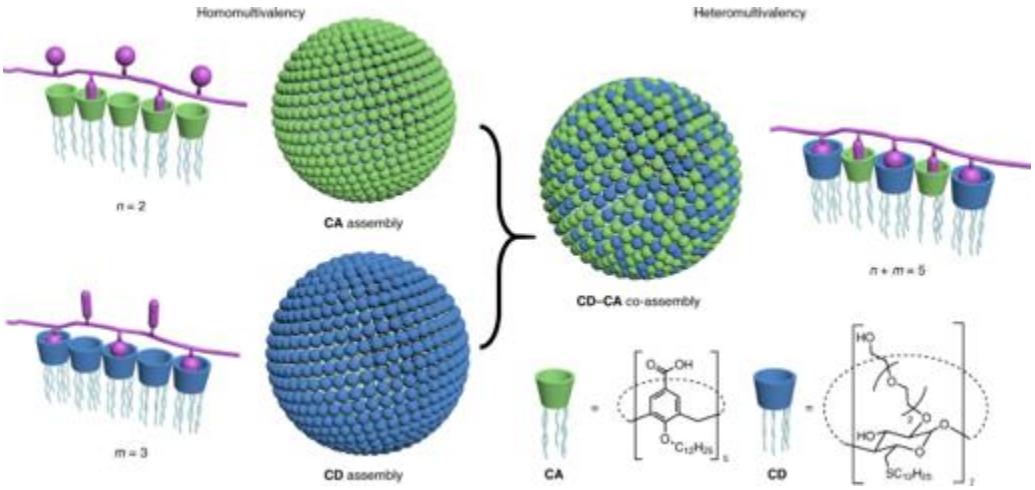

Figure 1-4. Illustration of heteromultivalent peptide recognition by co-assembly of

cyclodextrin and calixarene amphiphiles. Reproduced with permission from ref 37. Copyright 2019 Springer Nature.

Hierarchical self-assembly is a case in which the self-assembly of single building blocks occurs in multiple steps leading to increasing complexity. The primary building blocks assemble into first-order structures, which turn into the building blocks of second-order assemblies. The process may continue and lead to several levels of structural complexity.[38-40] Biological systems offer numerous representative examples in which hierarchical self-assembly is used to construct giant functional structures consisting of smaller molecular building blocks. Voets *et al.* developed a strategy for synthesis of self-assembled nanotubes based on a specific molecular design (**Figure 1-5**).[41] The monomers are composed of complementary guanine and cytosine nucleobases which bind with one another through H-bonding interactions to form cyclic tetramers. Through a nucleation-growth mechanism, the polymerization of the planar tetramers occurs and generates tubular structures with precisely defined inner and outer diameters. Additionally, viruses represent another vivid example of hierarchical self-assembly in biological systems.[42] As depicted in **Figure 1-6**, the bacteriophage *Φ29* spontaneously assembles from a prohead with other subunits, such as appendages and tail knob, and the prohead is composed of several building blocks, e.g. a head–tail connector (gp10), capsid protein (gp8) and

pRNA.[43] The mechanism of viral self-assembly not only helps us understand how viruses replicate and infect hosts, but also provide an exemplar for scientists to design biomimetic materials.

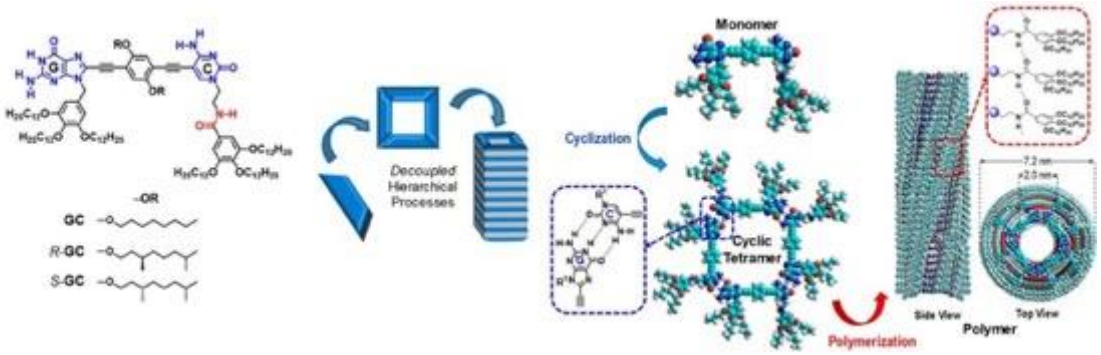

Figure 1-5. Chemical structures of dinucleobase monomers and scheme of the two-step self-assembly from monomers to cyclic tetramers to nanotubes. Reprinted with permission from ref 41. Copyright 2019 American Chemical Society.

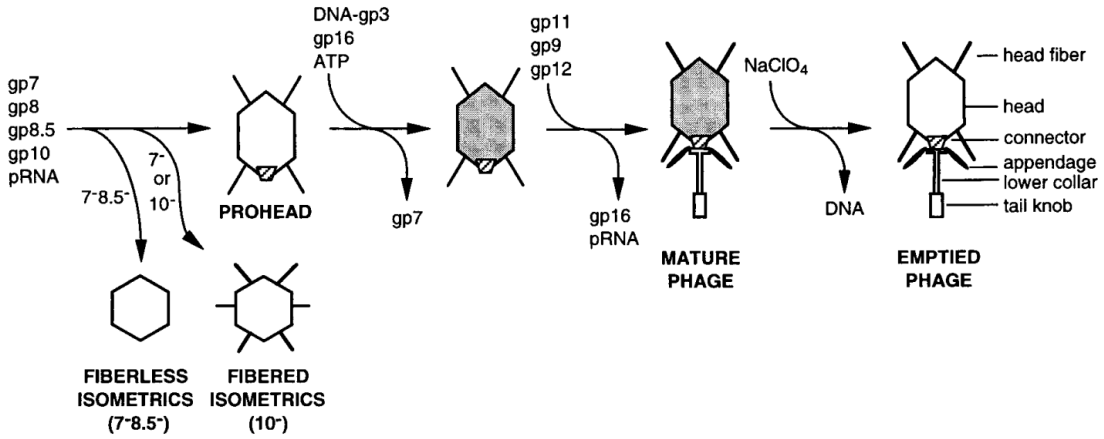

Figure 1-6. Assembly pathways of bacteriophage *Φ*29. Reused with permission from ref 43. Copyright 1998 Cell Press.

Directed self-assembly is characterized by the organization induced in response to

external stimuli, such as temperature, electric fields, or shear forces. By suitable chemical modification of the molecular design, a self-assembly process can be triggered by changes in pH, radiation, the presence of metal ions, or a redox reaction. For example, the distribution of colloidal nanoparticles could be manipulated by modifying the functional groups on the surface of colloids to adapt to various external stimuli (**Figure 1-7**).[44-49] The conformation of a molecule is altered by environmental changes at molecular level and its molecular information is transferred and amplified at microscopic level to produce various morphologies.

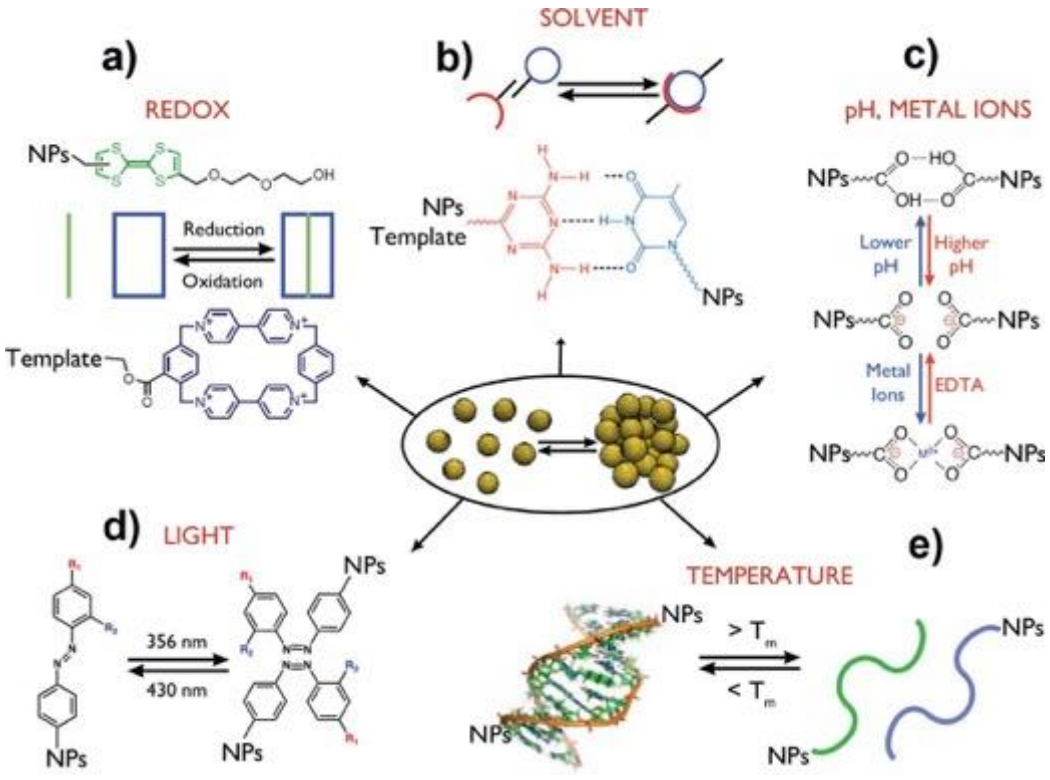

Figure 1-7. Diverse external stimuli for directed self-assembly of colloidal nanoparticles: (a) redox,[44] (b) solvent,[45] (c) pH or metal ions,[46] (d) light,[47] (e) temperature.[48,49] Reused with permission from ref 49. Copyright 2010 American Chemical Society.

1-3 Supramolecular Nanostructures and Their Use in Self-Assembly

Beyond molecules, supramolecular chemistry aims at developing complex chemical systems from smaller components interacting by noncovalent intermolecular forces. Supramolecular chemistry originated from the molecular recognition in host-guest systems such as crown ethers recognizing specific alkali cations in a selective fashion.[50-52] The oxygen atoms of crown ethers form an internal cavity, and their electron lone pairs effectively coordinate with metal ions depending on the correlation between the diameter of the internal cavity of the macrocyclic polyether, the radius of cation, and the denticity of the ligand donor. Crown ether complexes serve as powerful solvation reagents for dissolving inorganic salts in organic solvents and free basic or nucleophilic anions to participate in reactions (**Figure 1-8**).[53] The discovery of crown ether complexes not only promoted the vigorous development of phase-transfer catalysis[54] but also opened the door to supramolecular chemistry.

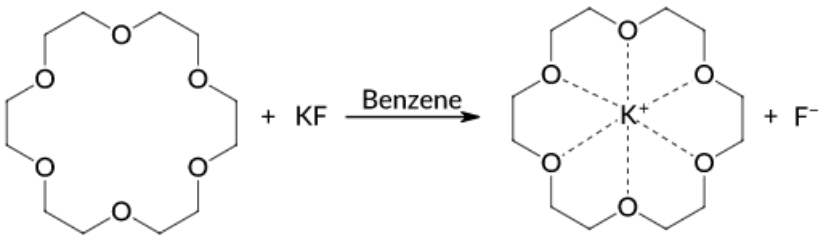

Figure 1-8. Chemical structure of a crown ether complex liberating a nucleophilic

fluoride anion.[54]

In supramolecular chemistry, molecules or building blocks are conceived so as to assemble into supramolecular systems by molecular recognition. The structures at an equilibrium state are characterized by the structure and spatial arrangement of the components and by the nature of the intermolecular bonds. Various type of interactions may be distinguished. These present different degrees of strength and dependence on distance or angle: hydrophobic interactions, π-π interactions, hydrogen bonding and electrostatic interactions.

(1) **π-π Interactions and Hydrophobic Interactions**

In the design of organic nanomaterials, it is common to see that π-π interactions play a critical role in self-assembly processes, especially in optoelectrical materials. π-π interactions not only provide a directional force for the growth of nanostructures, but also allow for long-distance charge transport owing to the intermolecular overlap between the molecular orbitals. However, the strength of π-π interactions is variable and ranges from less than 5 to 50 $kJmol^{-1}$.[22] Okamoto *et al.* proposed a system of enhanced face-to-face π-π stacking between tetracene moieties by introducing aryl (Ar) and perfluoroaryl (FAr) substituents, which have large, permanent quadrupole moments with similar magnitude and opposite signs (**Figure 1-9**).[55] With the aid of Ar-FAr interactions, single crystals of

FPPT with a tight packing structure were obtained. These exhibited excellent photoconductivity comparable to that of rubrene, which has the highest hole mobility in organic single-crystal field-effect transistors, and revealed anisotropic charge transport properties as well. The overlapping π-orbitals of tetracene cores were arranged in the axis *a* and *c,* whose maximum values of photoconductivity were twice higher than that in *b* axis. This approach demonstrated that well-defined molecular arrangements induced by π-π interactions can form architectures in which charge carriers possess exceptional mobility.

Although the importance of hydrophobic interactions is difficult to estimate in Nature, it can greatly influence the metabolic pathways in living systems, such as the organization of cell membrane and the folding in proteins. Hydrophobic interactions result from van der Waals interactions between nonpolar substances due to electron dispersion and favor their association in polar solvents. The decreased interaction surface between polar solvents and non-polar solutes (or vice-versa) results in a decrease in the entropy and free energy of the system. As shown in **Figure 1-10**, Liz-Marzán *et al.* described a novel methodology for preparing 3D clusters of gold nanoparticles.[56] The polystyrene-stabilized gold nanoparticles dispersed in THF evolved into clusters upon the addition of water. By introducing hydrophilic poly(acrylic acid) blocks into copolymer surfactants, the growth of clusters was quenched to control the size of clusters and the

encapsulation of the clusters were driven by hydrophobic interactions to ensure stability in polar solvents.

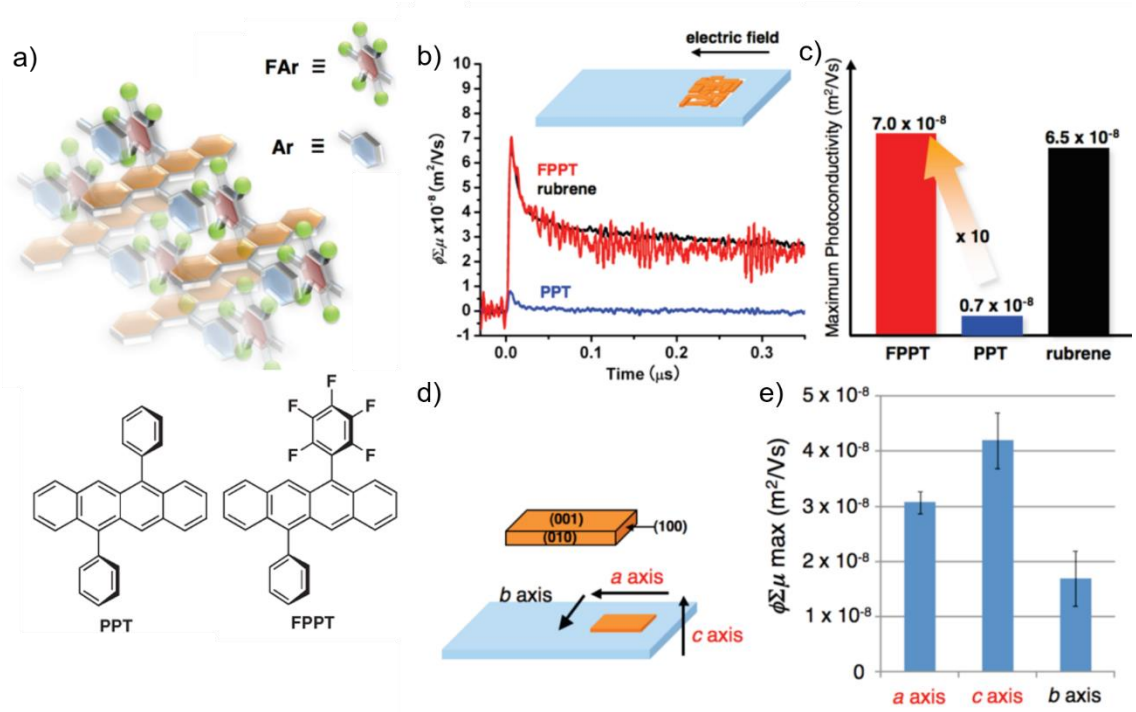

Figure 1-9. (a) Schematic concept of enhancement of π-π stacking by the introduction of aryl (Ar) and perfluoroaryl (FAr) substituents and chemical structures of **PPT** and **FPPT**. (b) Transient photoconductivity and (c) comparison of maximum photoconductivity for **FPPT**, **PPT** and rubrene (red, blue and black lines, respectively) microcrystals. (d) Crystal axes for axis-dependent photoconductive measurement on a **FPPT** single crystal. (e) Results of anisotropic photoconductivity. Reused with permission from ref 55. Copyright 2011, American Chemical Society.

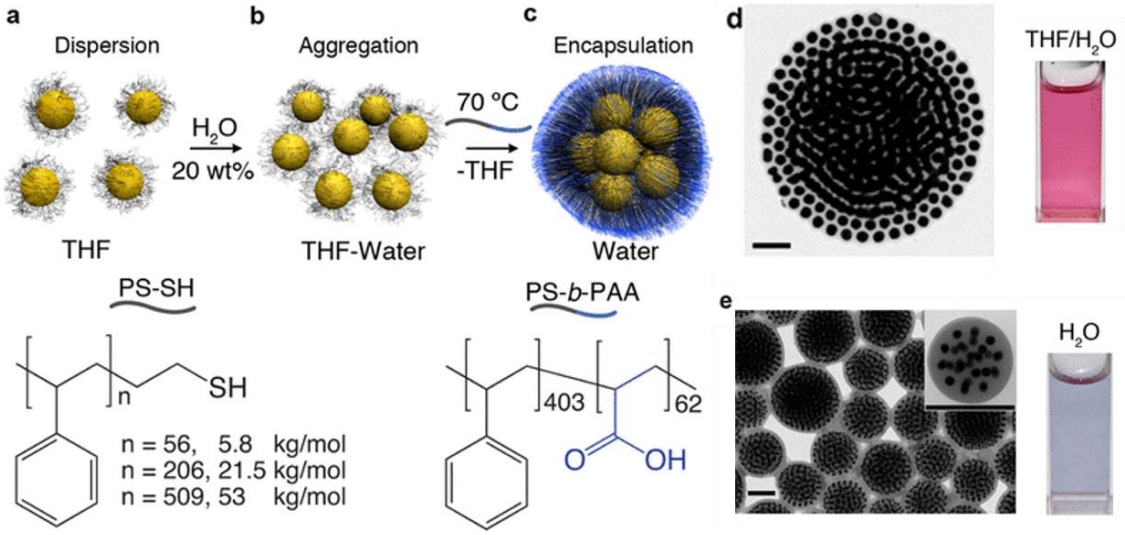

Figure 1-10. Schematic illustration of self-assembly of polystyrene-coated gold nanoparticles. (a) Colloidal dispersion of polystyrene-coated gold nanoparticles in THF solution. (b) Aggregation starts upon the addition of poor solvent (water). (c) The introduction of amphiphilic surfactants quenches the further aggregation of clusters and thermal treatment is applied to eliminate THF to induce rearrangement of particles inside the hydrophobic core and the hydrophilic shell stabilizes the clusters in aqueous solution. TEM images and appearance of gold nanoparticles solutions of (d) before the addition of PS-*b*-PAA and (e) after the introduction of PS-*b*-PAA and thermal treatment. Reused with permission from ref 56. Copyright 2012, American Chemical Society.

(2) **Hydrogen Bonding**

Hydrogen bonds are formed between a hydrogen bond donor (D-H) and an acceptor (A). The electronegativity of D is higher than H, thus, the D-H bond polarization increases

the partial charge on the H atom. When an acceptor A is close to the donor D-H, the acceptor shares electron density (from eg. an electron lone pair or π electrons) with the donor D-H to form a hydrogen bond D-H···A whose strength is around 10-65 kJmol^{-1}.[22] Since hydrogen bonding is specific, one can use hydrogen bonding in precise positions of the molecular components to obtain desired nanostructures. Prof. Würthner's group reported a distinct example of control of supramolecular polymorphs from one perylene bisimide (PBI) derivative monomer (**Figure 1-11**).[57] The three different polymorphs originate from diverse packing arrangements of chromophores owing to the specific intermolecular hydrogen-bonding patterns, π-π stacking modes and orientations of the terminal methyl groups, resulting in analogous but size-dependent thermodynamically stabilities in these polymorphs. As the concentration in monomer increases, the monomers **PBI-4** first assemble into kinetically favored **Aggregate 1** and then overcome energetic barriers by ultrasonication and seeding to form thermodynamically stable **Aggregate 2** and **3**, respectively.

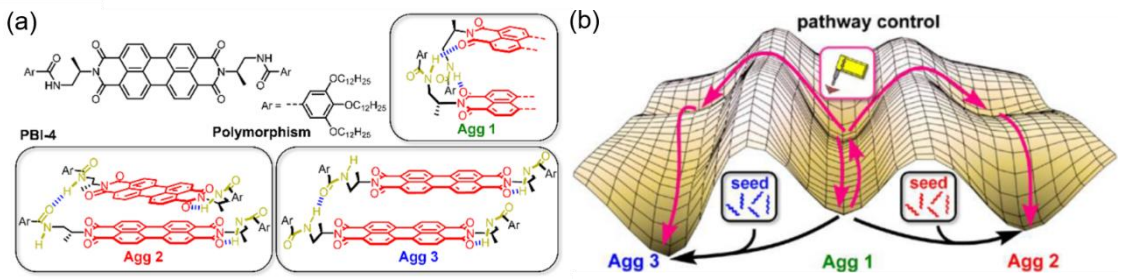

Figure 1-11. (a) Chemical structures of **PBI-4** and their different aggregate structures together with hydrogen bonding patterns. (b) Proposed energy landscape of

supramolecular polymerization of **PBI-4** dimers into various polymorphs **Aggregate 1**-**3**. Reproduced with permission from ref 57. Copyright 2019, American Chemical Society.

(3) **Electrostatic Interactions and Charge-Transfer Interactions**

Electrostatic interactions are attractive or repulsive forces between objects having electric charges. Their strength depends on the dielectric constant of the medium, but is ca. 250 $kJmol^{-1}$ for singly-charged species.[22] If two ionic groups are regarded as point charges, the force between them is proportional to their charge and inversely proportional to the square of the distance between them. For instance, layer-by-layer assembly technique, developed by Decher *et al.*,[58-61] is a feasible and reliable approach to fabricate complicated architectures (**Figure 1-12**). When a positively charged substrate is dipped in a polyanion solution, the polyanion chains are attracted by electrostatic interactions and adsorb onto the substrate.[58] After the substrate is washed by pure water to remove the excess of weakly bound polyelectrolytes and dried, the negatively charged substrate can then be dipped into a polycation solution to construct layer-by-layer complex thin films. To improve the efficiency of deposition process, a spraying variant (**Figure 1-12c**)[59] and grazing-incidence spraying (GIS) approach (**Figure 1-12d**)[60] were established. If a cellulose suspension is sprayed perpendicularly toward the substrate, the arbitrarily arranged cellulose nanofibrils could be observed by orientation analysis from atomic

force microscopic (AFM) images. By adopting the GIS method, and spraying the suspension at a low angle (5-20^{o}) on the substrate, in-plane oriented nanofibrils in thin film are obtained with the help of shear-induced alignment. Large-area highly anisotropic thin films can be produced by this versatile approach and controlled by diverse spraying conditions, such as spraying direction, tilted angle of spray jet, speed and density of suspension droplets.

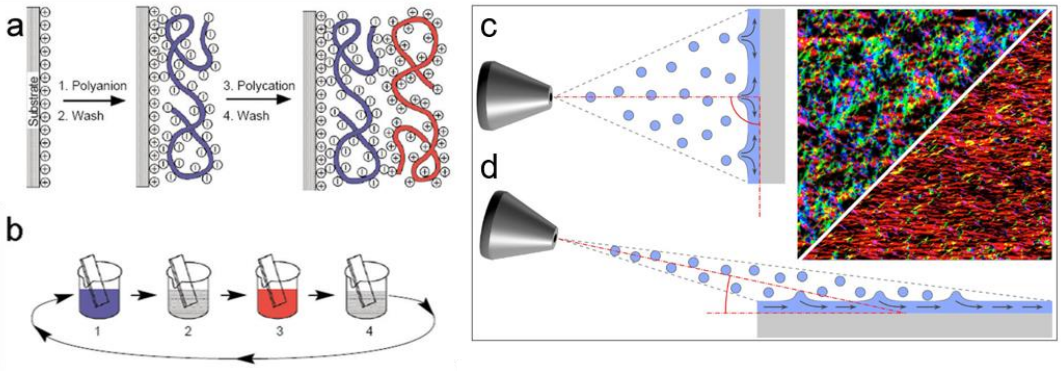

Figure 1-12. (a) Simplified illustration of layer-by-layer assembly technique based on electrostatic interactions. Reproduced with permission from ref 58. Copyright 1997 The American Association for the Advancement of Science (AAAS). Layer-by-layer assembly by (b) dipping, (c) spraying and (d) grazing-incidence spraying (GIS) methods. The insets are the orientation analyzed AFM images of thin film deposited by spraying and GIS method respectively. Reproduced with permission from ref 60. Copyright 2017 American Chemical Society.

Charge-transfer interactions may be regarded as a donor-acceptor (D-A) system. The electron-rich component is an electron donor and the electron-deficient one is an electron acceptor. Charge-transfer interactions promote the formation of staggered D-A systems and co-assembly into diverse supramolecular nanostructures (**Figure 1-13**).[62] The aggregation of chromophores in a parallel orientation can be divided into two major types: sandwich-type H-aggregates[63] and head-to-tail type J-aggregates (**Figure 1-14**).[64] Based on exciton theory,[65] the excitonic state of the dimer splits into two energy levels through the interaction of dipoles.[66,67] H-aggregates, in a face-to-face packing, are characterized by a higher energy allowed transition (hypsochromic shift in absorption) in contrast to the monomeric state, while J-aggregates, in a head-to-tail packing, exhibit a lower energy allowed transition (bathochromic shift in absorption). As for the fluorescence emission, H-aggregate formations is a common self-quenching mechanism owing to the forbidden lowest energy transition, whereas J-aggregates possess a lower-energy allowed transition and emit at longer wavelengths. With these distinct characters in aggregation architecture, H- and J-aggregates have been widely applied to rationalize charge-transfer-mediated photophysical behavior.[68-79]

Stoddart *et al.* reported a charge-transfer driven two-dimensional tessellation of co-crystallization of electron-poor naphthalene diimide (**NDI**)-based molecular triangles and electron-rich tetrathiafulvalene (**TTF**) chromophores (**Figure 1-15**).[80] Diverse

polymorphs of co-crystals can be manipulated by several solvents and concentrations and reveal various charge-transfer mediated spectroscopic results by different packing arrangements. The uncommon studies in synthetic 2D polymorphs and fine-tuning charge-transfer complexes provide opportunities for applications in organic electronics.

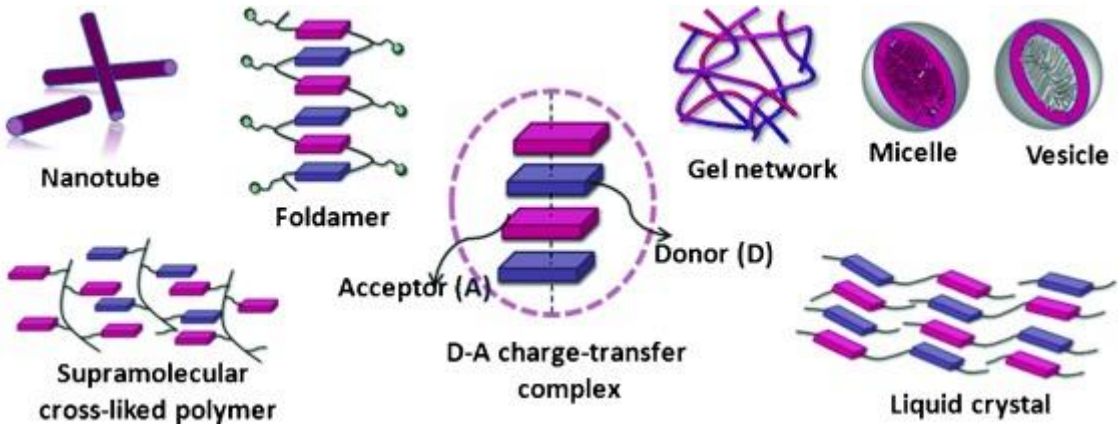

Figure 1-13. The intermediates in donor-acceptor charge-transfer systems in alternative packing and the various co-assembled morphologies.[62] Reproduced with permission from ref 62. Copyright 2009 VCH-Wiley.

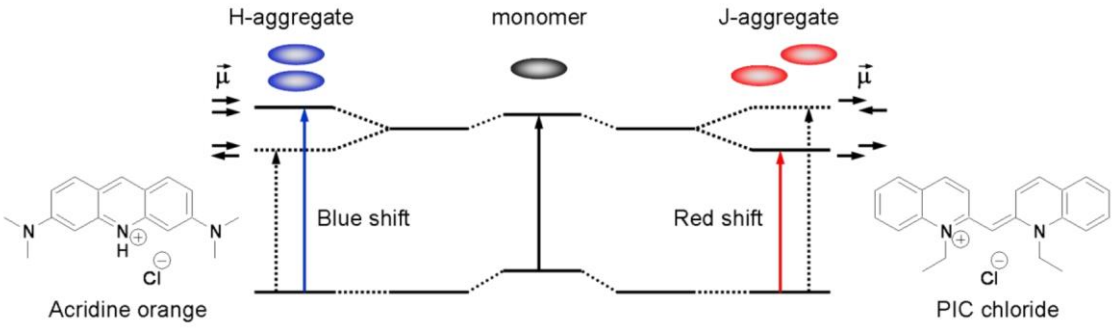

Figure 1-14. Simplified energy diagram for H- and J-aggregate and their typical example of chromophores for these aggregates. H-aggregates in face-to-face packing have higher energy transition (blue shift), while J-aggregates in head-to-tail packing exhibit lower

energy transition (red shift). Reused with permission from ref 68.

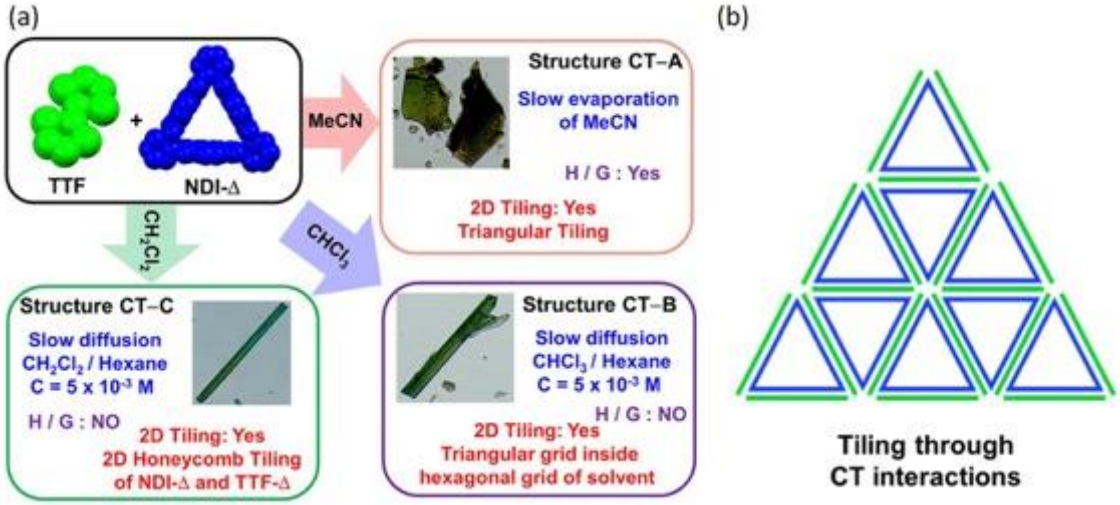

Figure 1-15. (a) Summary of co-crystallization conditions. (b) Expected tiling of the **NDI**-Δ:**TTF** co-crystal through CT interactions.[80] Reproduced with permission from ref 80. Copyright 2017 American Chemical Society.

1-4 Self-Assembly for Opto-Electronic Materials

In the past decades, the development of opto-electronic nanomaterials has attracted enormous attention.[81-84] In inorganic materials, nanowires,[85,86] quantum dots[87,88] and carbon nanotubes[89,90] are famous for their excellent conductivity or interesting optical properties. Compared to inorganic materials, organic materials possess multiple advantages, such as the possibility of tailoring their properties through various chemical modifications at the molecular level, flexibility,[91,92] low cost and suitable for large areas fabrication,[93,94] and have potential for next-generation nanotechnology and electronic

devices.

There are two principal methods to fabricate organic electronic devices: vapor deposition and solution processing. Vapor deposition is characterized by a process in which a material is heated and transformed from the condensed phase to the gas phase under a high vacuum environment, and then back to a thin film condensed phase on a low-temperature substrate. The technique can therefore be used only with materials with low molecular weight and high thermal stability. In contrast, solution processing is more convenient for large area fabrication by making use of industrial printing processes.[95] In solution processing, the growth of organic materials can be manipulated by solvent,[96-101] temperature[102-106] or doping.[107-109]

One classic example of self-assembly utilized to fabricate organic electronics is the bulk heterojunction (BHJ) in organic photovoltaic materials.[110-112] A BHJ results from the mixture of two components (donor and acceptor) with a morphological nano-structure established by phase separation of the components: donor and acceptor elements self-assemble into bicontinuous inter-percolating networks (**Figure 1-16**).[113] Phase separation results from the crystallinity of the conjugated donor molecules and small entropy in mixing of polymers. The morphology of BHJ films could be manipulated by several parameters: solvent for BHJ composites to be casted, ratio of donor/acceptor, thermal or solvent annealing and the intrinsic properties of the components.[114,115] Since the BHJ

structure was proposed by Heeger et al.,[110] the power conversion efficiency of organic photovoltaic was been enhanced from 5.5% to 18%,[116] benefiting from the subtle design of novel materials and finely tuned morphology. In addition, self-assembly has been widely applied in other fields of organic electronics, such as conducting supramolecular materials,[117,118] organic field-effect transistors,[119,120] organic light-emitting diodes[121-123] and so on. Therefore, it is an important issue that allows to efficiently construct organic nanomaterials or devices via self-assembly.

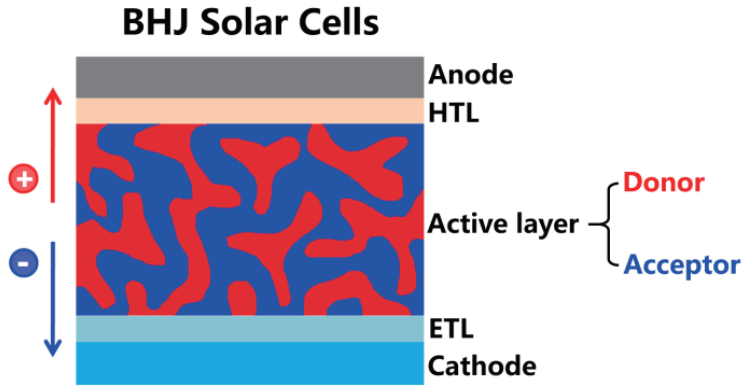

Figure 1-16. The architecture of bulk heterojunction organic solar cells. Reused with permission from ref 113.

1-5 Summary

In pursuit of novel opto-electronic organic materials, the investigation and control of intermolecular interactions between molecules became a major objective in the field of material science. Self-assembly, a spontaneous process of organization of building

blocks to produce well-defined nanostructures by means of noncovalent interactions, provides chemists with a reliable strategy to combine functional moieties to obtain desirable morphologies of nanostructures. The elements of self-assembly involve components, interactions, adjustability, environment and mass agitation. The types of self-assembly could be classified into two major groups: static and dynamic and subdivided into co-assembly, hierarchical self-assembly and directed self-assembly. Self-assembly plays a vital role in nanotechnologies and provides a “bottom-up” approach for fabrication to bypass the difficulty of “top-down” method in process scaling of manufacturing in industries.

Along the guidelines of self-assembly, we synthesized amphiphilic biuret-based molecules, which can self-assemble into distinct nanostructures by hydrogen-bonding, with thermally activated delayed fluorescence (TADF) systems and circularly polarized luminescence (CPL) systems and studied the differences of their intrinsic properties at the molecular level and at the nano-structure level. These led to a series of carbazole-based materials, capable of assembling into intermolecular excited state complexes, and investigated the photophysical and chiroptical properties.

1-6 References

1 (a) Frieden, E. *J. Chem. Educ.* **1975**, *52*, 754. (b) Johnson, E. R.; Keinan, S.; Mori-Sánchez, P.; Contreras-García, J.; Cohen, A. J.; Yang, W. *J. Am. Chem. Soc.* **2010**, *132*, 6498. (c) Černý, J.; Hobza, P. *Phys. Chem. Chem. Phys.* **2007**, *9*, 5291. (d) Strekowski, L.; Wilson, B. *Mutat. Res. - Fundam. Mol. Mech. Mutagen.* **2007**, *623*, 3. (e) McClements, D. J. *Biotechnol. Adv.* **2006**, *24*, 621.

2 (a) Lehn, J.-M. *Supramolecular Chemistry: Concept and Perspectives* (VCH, Weinheim, Germany, **1995**). (b) Atwood, J. L.; Davies, J. E. D.; MacNicol, D. D.; Vögtle, F.; Lehn, J.-M.; *Comprehensive Supramolecular Chemistry* (Pergamon, Oxford, **1996**). (c) Lehn, J.-M. *In Supramolecular Science: Where It Is and Where It Is Going* (Klumer, Dordrecht, Netherlands, **1999**), 287.

3 Bergstrom, L. M. (2011). *Thermodynamics of self-assembly. Application of Thermodynamics to Biological and Material Science.* (IntechOpen, London, **2011**) 11. 289.

4 O'Mahony, C. T.; Farrell, R. A.; Goshal, T.; Holmes, J. D.; Morris, M. A. *The Thermodynamics of Defect Formation in Self-Assembled Systems*. (IntechOpen, London, **2011**)

5 Whitesides, G. M.; Grzybowski, B. *Science* **2002**, *295*, 2418.

6 Lehn, J.-M. *Proc. Natl. Acad. Sci. USA* **2002**, *99*, 4763.

7 Whitesides, G. M.; Boncheva, M. *Proc. Natl. Acad. Sci. USA* **2002**, *99*, 4769.

8 Philip, D.; Stoddart J. F. *Angew. Chem. Int. Ed.* **1996**, *35*, 1155.

9 Ball, P. *The Self-Made Tapestry: Pattern Formation in Nature* (Oxford Univ. Press, Oxford, **1999**).

10 Mouritsen, O. G. *Curr. Opin. Colloid Interface Sci.* **1998**, *3*, 78.

11 Perham, R. N. *Philosophical Transactions of the Royal Society of London. B* **1975**, *272*, 123.

12 Koert, U.; Harding, M.; Lehn, J.-M. *Nature* **1990**, *346*, 339.

13 Yin, P.; Choi, H. M. T.; Calvert, C. R.; Pierce, N. A. *Nature* **2008**, *451*, 318.

14 Balzani, V.; Credi, A.; Raymo, F. M.; Stoddart, J. F. *Angew. Chem. Int. Ed.* **2000**, *39*, 3348.

15 Coskun, A.; Banaszak, M.; Astumian, R. D.; Stoddart, J. F.; Grzybowski, B. A. *Chem. Soc. Rev.* **2012**, *41*, 19.

16 Schwiebert, K. E.; Chin, D. N.; MacDonald, J. C.; Whitesides, G. M. *J. Am. Chem. Soc.* **1996**, *118*, 4018.

17 Schmidt-Mende, L.; Fechtenkotter, A.; Müllen, K.; Moons, E.; Friend, R. H.; MacKenzie, J. D. *Science* **2001**, *293*, 1119.

18 De Rosa, C.; Park, C.; Thomas, E. L.; Lotz, B. *Nature* **2000**, *405*, 433.

19 Rodriguez-Hernandez, J.; Chécot, F.; Gnanou, Y.; Lecommandoux, S. *Prog. Polym.*

Sci. **2005**, *30*, 691.

20 Yu, X.; Chen, L.; Zhang, M.; Yi, T. *Chem. Soc. Rev.* **2014**, *43*, 5346.

21 Whitesides, G. M.; Mathias, J. P.; Seto, C. T. *Science* **1991**, *254*, 1312.

22 Steed, J. W.; Atwood, J. L. *Supramolecular chemistry*. (John Wiley & Sons., **2000**).

23 Winfree, E.; Bekbolatov, R. *Proofreading tile sets: Error correction for algorithmic self-assembly. In International Workshop on DNA-Based Computers.* (Springer, Berlin, Heidelberg, **2003**), 126-144.

24 Ji, Q.; Lirag, R. C.; Miljanić, O. Š. *Chem. Soc. Rev.* **2014**, *43*, 1873.

25 Chen, H. L.; Goel, A. *Error free self-assembly using error prone tiles. In International Workshop on DNA-Based Computers*. (Springer, Berlin, Heidelberg, **2004**), 62.

26 Eigen, M. *Naturwissenschaften* **1971**, *58*, 465.

27 Schulman, R.; Wright, C.; Winfree, E. *ACS Nano* **2015**, *9*, 5760.

28 Bandy, T. J.; Brewer, A.; Burns, J. R.; Marth, G.; Nguyen, T.; Stulz, E. *Chem. Soc. Rev.* **2011**, *40*, 138.

29 Zhang, J. *Genetic Redundancies and Their Evolutionary Maintenance. Advances in Experimental Medicine and Biology*. (Springer, New York, **2012**)

30 Fu, I. W.; Markegard, C. B.; Nguyen, H. D. *Langmuir* **2015**, *31*, 315.

31 Pearson, R. T.; Warren, N. J.; Lewis, A. L.; Armes, S. P.; Battaglia, G.

Macromolecules **2013**, *46*, 1400.

32 Ghosh, A.; Haverick, M.; Stump, K.; Yang, X.; Tweedle, M. F.; Goldberger, J. E. *J. Am. Chem. Soc.* **2012**, *134*, 3647.

33 Würthner, F. *J. Org. Chem.* **2022**, *87*, 1602.

34 Cademartiri, L.; Ozin, G. A. *Concepts of Nanochemistry*. (Wiley-VCH, Weinheim, **2009**)

35 Ozin, G. A.; Hou, K.; Lotsch, B. V.; Cademartiri, L.; Puzzo, D. P.; Scotognella, F.; Ghadimi, A.; Thomson, J. *Mater. Today* **2009**, *12*, 12.

36 Brito, A.; Abul-Haija, Y. M.; Soares da Costa, D.; Novoa-Carballal, R.; Reis, R. L.; Ulijn, R. V.; Pires, R. A.; Pashkuleva, I. *Chem. Sci.* **2019**, *10*, 2385.

37 Xu, Z.; Jia, S.; Wang, W.; Yuan, Z.; Ravoo, B. J.; Guo, D.-S. *Nature Chem.* **2019**, *11*, 86.

38 Keizer, H. M.; Sijbesma, R. P. *Chem. Soc. Rev.* **2005**, *34*, 226.

39 Rest, C.; Kandanelli, R.; Fernández, G. *Chem. Soc. Rev.* **2015**, *44*, 2543.

40 Sang, Y.; Liu, M. *Chem. Sci.* **2022**, *13*, 633.

41 Vázquez-González, V.; Mayoral, M. J.; Chamorro, R.; Hendrix, M. M. R. M.; Voets, I. K.; González-Rodríguez, D. *J. Am. Chem. Soc.* **2019**, *141*, 16432.

42 Chaudhary, A.; Yadav, R. D. *J. Nanoparticle Res.* **2019**, *21*, 1.

43 Tao, Y.; Olson, N. H.; Xu, W.; Anderson, D. L.; Rossmann, M. G.; Baker, T. S. *Cell*

1998, *95*, 431.

44 Olson, M. A.; Coskun, A.; Klajn, R.; Fang, L.; Dey, S. K.; Browne, K. P.; Grzybowski, B. A.; Stoddart, J. F. *Nano Lett.* **2009**, *9*, 3185.

45 Boal, A. K.; Ilhan, F.; DeRouchey, J. E.; Thurn-Albrecht, T.; Russell, T. P.; Rotello, V. M. *Nature* **2000**, *404*, 746.

46 Sun, Z.; Ni, W.; Yang, Z.; Kou, X.; Li, L.; Wang, J. *Small* **2008**, *4*, 1287.

47 Fialkowski, M.; Bishop, K. J. M.; Klajn, R.; Smoukov, S. K.; Campbell, C. J.; Grzybowski, B. A. *J. Phys. Chem. B* **2006**, *110*, 2482.

48 Mirkin, C. A.; Letsinger, R. L.; Mucic, R. C.; Storhoff, J. J. *Nature* **1996**, *382*, 607.

49 Grzelczak, M.; Vermant, J.; Furst, E. M.; Liz-Marzan, L. M. *ACS Nano* **2010**, *4*, 3591.

50 (a) Pedersen, C. J. *J. Am. Chem. Soc.* **1967**, *89*, 7017. (b) Pedersen, C. J. *J. Am. Chem. Soc.* **1970**, *92*, 386. (c) Pedersen, C. J. *Angew. Chem. Int. Ed.* **1988**, *27*, 1021.

51 Steed, J. W. *Coord. Chem. Rev.* **2001**, *215*, 171.

52 Liu, Z.; Nalluri, S. K. M.; Stoddart, J. F. *Chem. Soc. Rev.* **2017**, *46*, 2459.

53 Clark, J. H. *Chem. Rev.* **1980**, *80*, 429.

54 (a) Liotta, C. L.; Harris, H. P. *J. Am. Chem. Soc.* **1974**, *96*, 2250. (a) De Jong, F.; Reinhoudt, D. N. *Adv. Phys. Org. Chem.* **1980**, *17*, 279. (b) Akelah, A.; Sherrington, D. C. *Chem. Rev.* **1981**, 81, 557. (c) Gokel, G. *Monogr. Supramol. Chem.* **1991**, 115.

(d) Lee, J. W.; Yan, H.; Jang, H. B.; Kim, H. K.; Park, S. W.; Lee, S.; Chi, D. Y.; Song, C. E. *Angew Chem.* **2009**, *121*, 7819. (e) Lee, J. W.; Oliveira, M. T.; Jang, H. B.; Lee, S.; Chi, D. Y.; Kim, D. W.; Song, C. E. *Chem. Soc. Rev.* **2016**, *45*, 4638.

55 Okamoto, T.; Nakahara, K.; Saeki, A.; Seki, S.; Oh, J. H.; Akkerman, H. B.; Bao, Z.; Matsuo, Y. *Chem. Mater.* **2011**, *23*, 1646.

56 Sánchez-Iglesias, A.; Grzelczak, M.; Altantzis, T.; Goris, B.; Pérez-Juste, J.; Bals, S.; Tendeloo, G. V.; Donaldson, S. H.; Chmelka, B. F.; Israelachvili, J. N.; Liz-Marzán, L. M. *ACS Nano* **2012**, *6*, 11059.

57 Wehner, M.; Röhr, M. I. S.; Bühler, M.; Stepanenko, V.; Wagner, W.; Würthner, F. *J. Am. Chem. Soc.* **2019**, *141*, 6092.

58 Decher, G. *Science* **1997**, *277*, 1232.

59 Izquierdo, A.; Ono, S. S.; Voegel, J. C.; Schaaf, P.; Decher, G. *Langmuir* **2005**, *21*, 7558.

60 Blell, R.; Lin, X.; Lindström, T.; Ankerfors, M.; Pauly, M.; Felix, O.; Decher, G. *ACS Nano* **2017**, *11*, 84.

61 Hu, H.; Wang, S.; Feng, X.; Pauly, M.; Decher, G.; Long, Y. *Chem. Soc. Rev.* **2020**, *49*, 509.

62 Das, A.; Ghosh, S. *Angew. Chem. Int. Ed.* **2014**, *53*, 2038.

63 Franck, J.; Teller, E. *J. Chem. Phys.***1938**, *6*, 861.

64 Jelley, E. E. *Nature* **1936**, *138*, 1009.

65 Davydov, A. S. *Theory of molecular excitons.* (McGraw-Hill, New York, **1962**)

66 Kasha, M.; Rawls, H. R.; Ashraf El-Bayoumi, M. *Pure Appl. Chem.* **1965**, 2, 371.

67 Kasha, M. *Discuss. Faraday Soc.* **1950**, *9*, 14.

68 Klymchenko, A. S. *J. Nanosci. Lett.* **2013**, *3*, 21.

69 Spano, F. C.; Silva, C. *Annu. Rev. Phys. Chem.* **2014**, *65*, 477.

70 Hestand, N. J.; Spano, F. C. *Chem. Rev.* **2018**, *118*, 7069.

71 Reers, M.; Smith, T. W.; Chen, L. B. *Biochemistry* **1991**, *30*, 4480.

72 Würthner, F., Thalacker, C., Diele, S., & Tschierske, C. *Chem. Eur. J.* **2001**, *7*, 2245.

73 Kaiser, T. E.; Wang, H.; Stepanenko, V.; Würthner, F. *Angew. Chem.* **2007**, *119*, 5637.

74 Würthner, F.; Kaiser, T. E.; Saha-Möller, C. R. *Angew. Chem. Int. Ed.* **2011**, *50*, 3376.

75 Bricks, J. L.; Slominskii, Y. L.; Panas, I. D.; Demchenko, A. P. *Methods Appl. Fluoresc.* **2017**, *6*, 012001.

76 Rösch, U.; Yao, S.; Wortmann, R.; Würthner, F. *Angew. Chem.* **2006**, *118*, 7184.

77 Clark, J.; Silva, C.; Friend, R. H.; Spano, F. C. *Phys. Rev. Lett.* **2007**, *98*, 206406.

78 Spano, F. C. *Acc. Chem. Res.* **2010**, *43*, 429.

79 Kistler, K. A.; Pochas, C. M.; Yamagata, H.; Matsika, S.; Spano, F. C. *J. Phys. Chem. B* **2012**, *116*, 77.

80 Beldjoudi, Y.; Narayanan, A.; Roy, I.; Pearson, T. J.; Cetin, M. M.; Nguyen, M. T.;

Krzyaniak, M. D.; Alsubaie, F. M.; Wasielewski, M. R.; Stupp, S. I.; Stoddart, J. F. *J. Am. Chem. Soc.* **2019**, *141*, 17783.

81 Mitschke, U.; Bäuerle, P. *J. Mater. Chem.* **2000**, *10*, 1471.

82 de Boer, B.; Stalmach, U.; van Hutten, P. F.; Melzer, C.; Krasnikov, V. V.; Hadziioannou, G. *Polymer* **2001**, *42*, 9097.

83 Forrest, S. R.; Thompson, M. E. *Chem. Rev.* **2007**, *107*, 923.

84 Ostroverkhova, O. *Chem. Rev.* **2016**, *116*, 13279.

85 Rao, C. N. R.; Deepak, F. L.; Gundiah, G.; Govindaraj, A. *Prog. Solid State Chem.* **2003**, *31*, 5.

86 Brambilla, G. *J. Opt.* **2010**, *12*, 043001.

87 Nirmal, M.; Brus, L. *Acc. Chem. Res.* **1999**, *32*, 407.

88 Bera, D.; Qian, L.; Tseng, T. K.; Holloway, P. H. *Materials* **2010**, *3*, 2260.

89 Iijima, S.; Ichihashi, T. *Nature* **1993**, *363*, 603.

90 De Volder, M. F.; Tawfick, S. H.; Baughman, R. H.; Hart, A. J. *Science* **2013**, *339*, 535.

91 Forrest, S. R. *Nature* **2004**, *428*, 911.

92 Logothetidis, S. *Mater. Sci. Eng. B* **2008**, *152*, 96.

93 Dimitrakopoulos, C. D.; Malenfant, P. R. *Adv. Mater.* **2002**, *14*, 99.

94 Sekitani, T.; Someya, T. *Adv. Mater.* **2010**, *22*, 2228.

95 Arias, A. C.; MacKenzie, J. D.; McCulloch, I.; Rivnay, J.; Salleo, A. *Chem. Rev.* **2010**, *110,* 3.

96 Al-Ibrahim, M.; Ambacher, O.; Sensfuss, S.; Gobsch, G. *Appl. Phys. Lett.* **2005**, *86*, 201120.

97 Dickey, K. C.; Anthony, J. E.; Loo, Y. L. *Adv. Mater.* **2006**, *18*, 1721.

98 Wei, G.; Wang, S.; Sun, K.; Thompson, M. E.; Forrest, S. R. *Adv. Energy Mater.* **2011**, *1*, 184.

99 Nie, W.; Tsai, H.; Asadpour, R.; Blancon, J. C.; Neukirch, A. J.; Gupta, G.; Crochet, J. J.; Chhowalla, M.; Tretiak, S.; Alam, M. A.; Wang, H. L.; Mohite, A. D. *Science* **2015**, *347*, 522.

100 Min, J.; Jiao, X.; Ata, I.; Osvet, A.; Ameri, T.; Bäuerle, P.; Ade, H.; Brabec, C. J. *Adv. Energy Mater.* **2016**, *6*, 1502579.

101 McDowell, C.; Abdelsamie, M.; Toney, M. F.; Bazan, G. C. *Adv. Mater.* **2018**, *30*, 1707114.

102 Pan, H.; Li, Y.; Wu, Y.; Liu, P.; Ong, B. S.; Zhu, S.; Xu, G. *J. Am. Chem. Soc.* **2007**, *129*, 4112.

103 Sakanoue, T.; Sirringhaus, H. *Nat. Mater.* **2010**, *9*, 736.

104 You, J.; Hong, Z.; Yang, Y.; Chen, Q.; Cai, M.; Song, T. B.; Chen, C. C.; Lu, S.; Liu, Y.; Zhou, H.; Yang, Y. *ACS Nano* **2014**, *8*, 1674.

105 Xing, G.; Mathews, N.; Lim, S. S.; Yantara, N.; Liu, X.; Sabba, D.; Grätzel, M.; Mhaisalkar, S.; Sum, T. C. *Nat. Mater.* **2014**, *13*, 476.

106 Yella, A.; Heiniger, L. P.; Gao, P.; Nazeeruddin, M. K.; Grätzel, M. *Nano Lett.* **2014**, *14*, 2591.

107 Chen, D.; Jordan, E. H.; Gell, M. *Surf. Coat*. **2008**, *202*, 2132.

108 Piliego, C.; Holcombe, T. W.; Douglas, J. D.; Woo, C. H.; Beaujuge, P. M.; Fréchet, J. M. *J. Am. Chem. Soc.* **2010**, *132*, 7595.

109 Liang, P. W.; Liao, C. Y.; Chueh, C. C.; Zuo, F.; Williams, S. T.; Xin, X. K.; Lin, J.; Jen, A. K. Y. *Adv. Mater.* **2014**, *26*, 3748.

110 Yu, G.; Gao, J.; Hummelen, J. C.; Wudl, F.; Heeger, A. J. *Science* **1995**, *270*, 1789.

111 Dennler, G.; Scharber, M. C.; Brabec, C. J. *Adv. Mater.* **2009**, *21*, 1323.

112 Heeger, A. J. *Adv. Mater.* **2014**, *26*, 10.

113 Tong, Y.; Xiao, Z.; Du, X.; Zuo, C.; Li, Y.; Lv, M.; Yuan, Y.; Yi, C.; Hao, F.; Hua, Y.; Lei, T.; Lin, Q.; Sun, K.; Zhao, D.; Duan, C.; Shao, X.; Li, W.; Yip, H.-L.; Xiao, Z.; Zhang, B.; Bian, Q.; Cheng, Y.; Liu, S.; Cheng, M.; Jin, Z.; Yang, S.; Ding, L. *Sci. China Chem.* **2020**, *63*, 758.

114 Huang, Y.; Kramer, E. J.; Heeger, A. J.; Bazan, G. C. *Chem. Rev.* **2014**, *114*, 7006.

115 Hoppe, H.; Sariciftci, N. S. *J. Mater. Chem.* **2006**, *16*, 45.

116 Jin, K.; Xiao, Z.; Ding, L. *J. Semicond.* **2021**, *42*, 060502.

117 Faul, C. F.; Antonietti, M. *Adv. Mater.* **2003**, *15*, 673.

118 Hasegawa, M.; Iyoda, M. *Chem. Soc. Rev.* **2010**, *39*, 2420.

119 Minari, T.; Liu, C.; Kano, M.; Tsukagoshi, K. *Adv. Mater.* **2012**, *24*, 299.

120 Torsi, L.; Magliulo, M.; Manoli, K.; Palazzo, G. *Chem. Soc. Rev.* **2013**, *42*, 8612.

121 Wong, K. T.; Bassani, D. M. *NPG Asia Mater.* **2014**, *6*, *e116*.

122 Busseron, E.; Ruff, Y.; Moulin, E.; Giuseppone, N. *Nanoscale* **2013**, *5*, 7098.

123 Moulin, E.; Busseron, E.; Giuseppone, N. *Supramolecular Materials for Opto-Electronics.* (RSC, Cambridge, **2015**)

Chapter 2. Spontaneous Generation and Applications of Thermally Activated Delayed Fluorescence (TADF) Nanospheres

2-1 Introduction

A series of molecules that spontaneously self-assemble into small electroluminescent (EL) architectures of sub-micrometer size in solution was developed through the use of H-bonding (**Figure 2-1**).[1] By tailoring the emissive properties of the chromophores in solution, spherical aggregates with an average diameter of 300 nm which emit specific colors, including CIE D65 daylight white light, are spontaneously formed upon dissolution of the material. As we shall see below, the spontaneous formation of the spheres results from the presence of H-bonding bis-urea (biuret) groups. The spontaneous generation of sub-micron architectures is particularly interesting for developing ultra-high-resolution displays. However, the previously reported external quantum efficiency (EQE) achieved are only 0.2% to 0.6%, indicating considerable room for improvement. A possible strategy, as outlined below, makes use of thermally activated delayed fluorescence (TADF) chromophores to enhance the EQEs of the OLED devices.

Our goal is to design a system of D-π-A type TADF chromophores endowed with hydrogen-bonding biuret recognition groups, facilitating the spontaneous formation of nanovesicles in solutions, to produce sub-micron scale emitting domains. With TADF-

active cores, triplet excitons could be harvested to enhance exciton utilization efficiency and improve the performance of OLED devices that could be fabricated using ink-jet printing techniques.

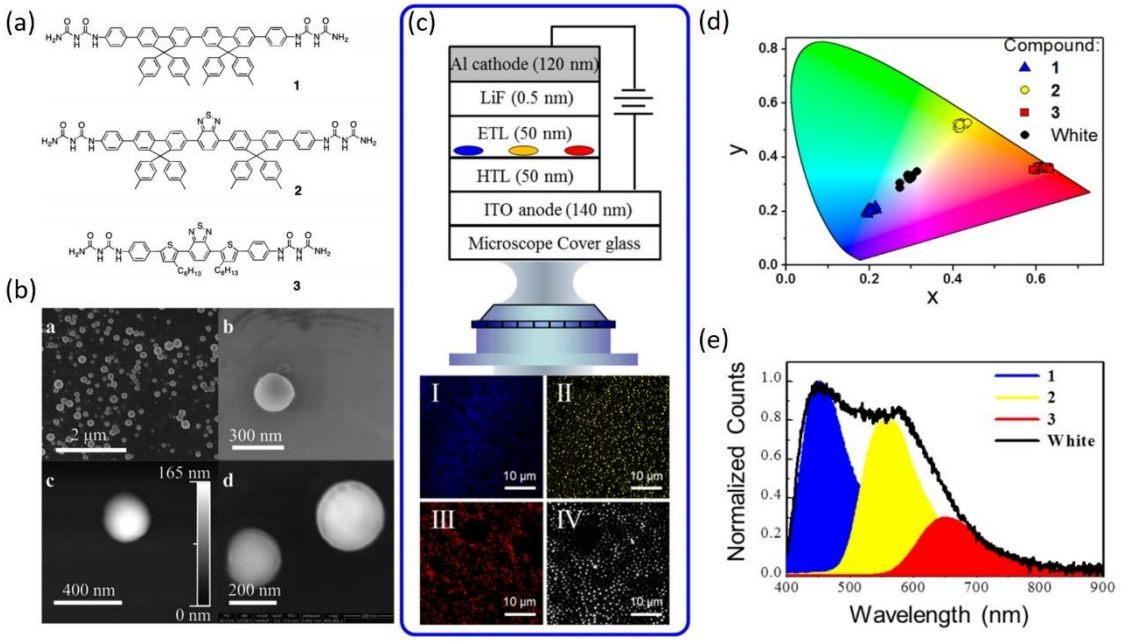

Figure 2-1. (a) The chemical structures of blue-, green- and red-emitting fluorophores. (b) SEM images of spherical aggregates of compound **2** in Fig. 2-1(a). (c) Schematic of EL device with self-assembled nanospheres and the wide-field microscopic images of the EL-compounds from the devices (I: **1**, II: **2**, III: **3**, IV: D65). (d) Chromaticity coordinates of EL-compounds. (e) The spectrum of individual EL-compound in four devices (with black solid line for device IV).[1] Reused with permission from ref 1. Copyright 2016, American Chemical Society.

2-2 Urea and Biuret Units as Functional Self-Assembly Group

Urea is an organic compound with chemical formula $CO(NH_2)_2$, combining two H-donating NH_2 groups and one H-accepting carbonyl (C=O) functional group. Since hydrogen-bonding (H-B) forms between ureido compounds, the orientation of the intramolecular arrangement process must be taken into account during self-assembly. The H-B patterns resulting from intermolecular interactions is illustrated in **Figure 2-2**, including a linear and a zigzag pattern of complementary H-B branches.[2]

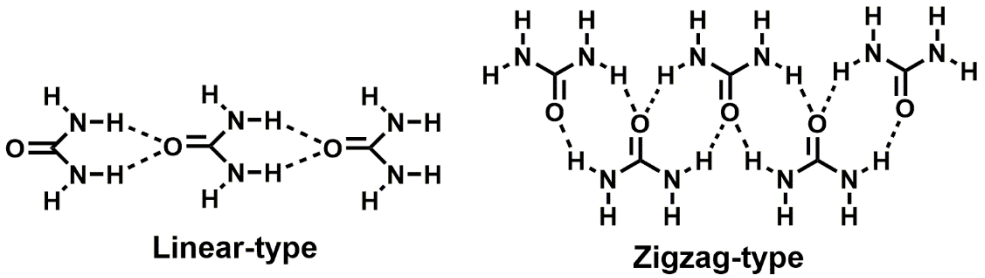

Figure 2-2. Simple hydrogen-bonding patterns of urea derivatives.

Biuret possesses the chemical formula $H_2NC(O)NHC(O)NH_2$ and is a composed of two urea groups is the analogue of urea, but with increased polarity and molecular size. As depicted in **Figure 2-3**, we find that the characteristic intramolecular hydrogen bond between the terminal N-H proton and the distal carbonyl group is the key to controlling its self-assembly process.[3-5] The six-membered ring effectively locks the conformation of biuret into an annular geometry with two distinct H-B sites that are mutually perpendicular. One of them (labeled as **P** in **Figure 2-3**) is analogous to the D-D-A motif

in aminopyrimidines, and the other one (labeled as **A** in **Figure 2-3**) is a typical primary amide H-B motif.[6] The specific geometry and the intramolecular H-B are evidenced in all reported solid-state crystal structures with the biuret sub-motif present. Moreover, as a consequence of the dual binding site, the compounds will crystallize into H-B sheets, which are held together by secondary H-B interactions.

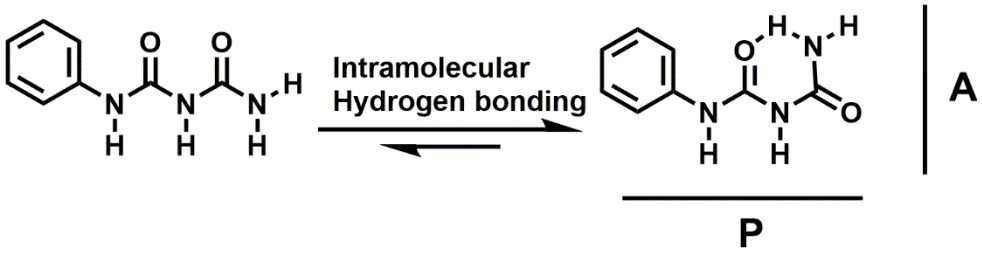

Figure 2-3. Simple hydrogen-bonding arrangement of biuret. The rotation of C-N single bond to form intramolecular hydrogen-bonded six-membered ring leads to two specific hydrogen-bonding sites (P and A) for intermolecular hydrogen-bonding networks. The P site is an analogous to D-D-A motif in aminopyrimidines and A site is a primary amide H-B motif.

2-3 The Principle and Introduction of TADF

The composition of an organic light emitting diode (OLED) device is illustrated in **Figure 2-4**.[7] Electrons and holes are injected into the active layer of the devices by applying an external voltage. Once they recombine, the energy liberated is such that it cannot be easily released as heat, and instead generates excitons in the emitting layer.[7]

According to spin-statistics,[9,10] 25% of excitons will be formed in the singlet state and 75% in the triplet state. Excitons in singlet state are responsible for fluorescence since the transition from the excited singlet state (S_1) to the singlet ground state (S_0) is spin-allowed. On the other hand, for triplet excitons, the spin selection rule dictates that the transition from the excited state (T_1) to S_0 ground state is spin-forbidden. Thus, triplet excited states can principally return to ground state through intersystem crossing, a slower process that frequently results in non-radiative decay. Consequently, the theoretical maximum internal quantum efficiency (IQE) of EL devices consisting of conventional fluorescent materials is limited to 25%.

The external quantum efficiency (EQE, η_{EQE}) is a parameter to evaluate the efficiency of EL devices, i.e. the ratio of numbers of photons emitted outside divided by the numbers of charge carriers injected into the device, and can be described by **Equation 2-1**:[11]

$$\eta_{EQE} = \eta_{out}\eta_{IQE} = \eta_{out}\gamma\phi_f\eta_{s/t} \qquad \textbf{(Equation 2-1)}$$

where η_{out} is the optical outcoupling factor and the internal quantum efficiency (IQE, η_{IQE}). The η_{out} determines the extraction efficiency of emissive photons inside the device to the air outside. The η_{IQE} is the product of the following factors: γ is the carrier balance factor, describing whether equal numbers of electrons and holes are injected and the ratio of them recombining to generate excitons; Φ_f is the photoluminescence quantum yield (PLQY) of

emitting materials, representing how many of the spin-allowed excitons decays in radiative path to emit photons; $\eta_{s/t}$ is the ratio of singlet or triplet excitons based on spin statistics.[11]

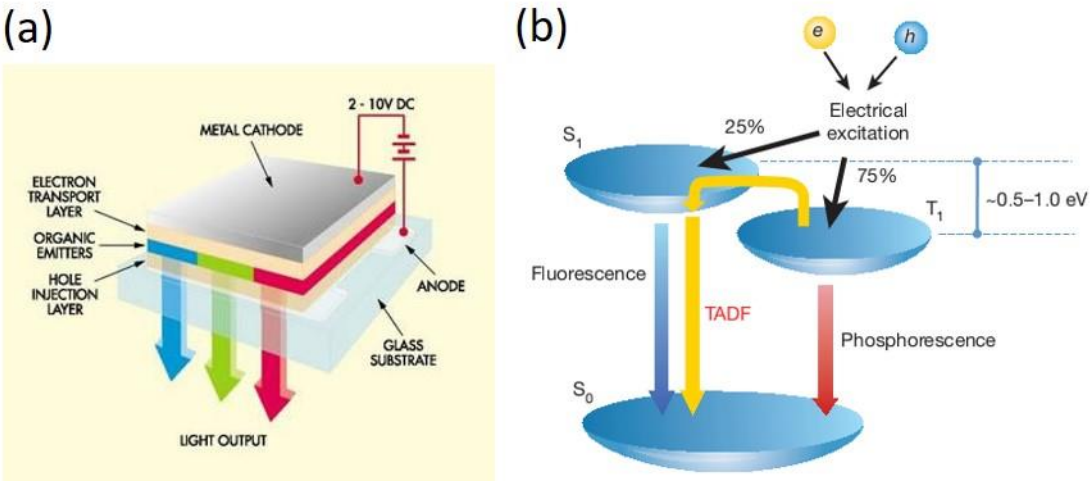

Figure 2-4. (a) Composition of organic an organic light emitting diode (OLED) device. Reused with permission from ref 7. (b) Radiation mechanism of organic emissive molecules possessing TADF properties. Reused with permission from ref 8. Copyright 2012, Springer Nature.

One of the strategies to improve EQE is through thermally activated delayed fluorescence (TADF). By reducing the energy gap between the lowest excited singlet and triplet states (ΔE_{ST}), thermal energy allows reverse intersystem crossing (rISC) of triplet excitons to form singlet excitons to enhance the photoluminescence quantum yield (PLQY). This process is analogous to that observed in eosin, and has been known as E-

type delayed fluorescence since the 1960's.[12] In 2009, Professor Adachi explored the light-emitting mechanism of TADF materials and demonstrated a breakthrough in the spin-related limitation of the efficiency in OLED devices.[13-17] Using rational molecular design, electron-donating and electron-accepting groups were be used to separate the highest occupied molecular orbitals (HOMOs) and lowest unoccupied molecular orbitals (LUMOs), such that the minimized orbital overlap contributes to reducing ΔE_{ST} to the point of being sufficiently small (< 0.1 eV) to allow thermal conversion of triplet to singlet excitons by rISC process. In principle, this can allow OLED devices to achieve 100% IQE.

In recent years, the Wong group identified several TADF materials with excellent performance.[18-20] In 2014, they reported a blue TADF emitter (**DMAC-TRZ)**, which is composed of a 9,10-dihydroacridine donor unit and a triazine acceptor unit possessing a reduced ΔE_{ST} (0.046 eV, **Figure 2-5a**).[21] The quantum yield of the mCBP-doped **DMAC-TRZ** film was 96%, in comparison with 26.5% EQE for a non-doped electroluminescent device. Moreover, experiments on a series of D-π-A type TADF emitters with acridine as donor units and CN-substituted pyridines as acceptor units (**Figure 2-5b**),[22] where the emitting color was tuned from blue to yellow-green by increasing the strength of the acceptor, evidenced that photoluminescence quantum yields for **Py56** can achieve 90.4%. The maximum external quantum efficiency of 29.2% exceeds the theoretical limit for

conventional OLED devices, which is an outstanding performance in the field.

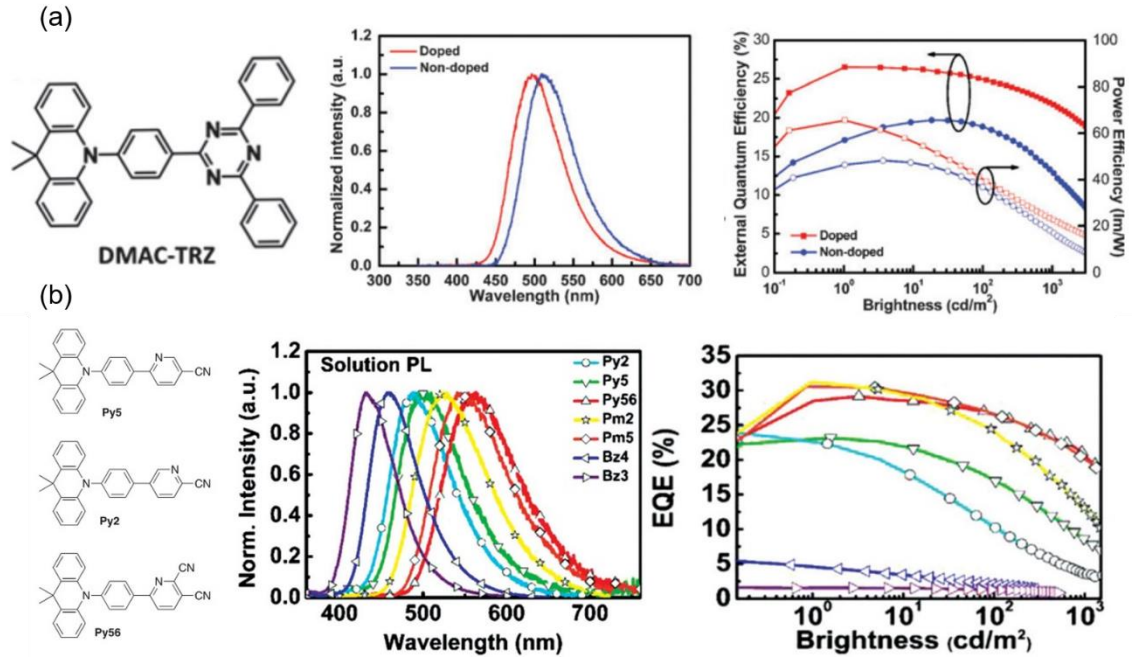

Figure 2-5. (a) The EL-spectrum of **DMAC-TRZ** TADF-emitter and the device performance. Reproduced from ref 21 with permission from the Royal Society of Chemistry. (b) The EL-spectrum and device performance of the series of D-π-A type TADF emitters. Reproduced with permission from ref 22. Copyright 2016 VCH-Wiley.

2-4 Molecular Design and Synthesis

A main objective of this thesis is to engineer TADF materials by using molecular recognition motifs to promote self-organization into sub-micron sized spheres to create high-resolution OLEDs. The concept is shown in **Figure 2-6**, in which D-π-A chromophores are combined with biuret molecular recognition motifs.

The structure of four target molecules is summarized in **Figure 2-7**. A series of acridine-based π-conjugated derivatives including **DTMB**, **DTPB**, **Py56MB** and **Py56PB** uses the same backbone connected by an aromatic linker with different electron-accepting moieties to specifically tailor the emission spectrum by altering the energy gap between ground state (S_0) and excited state (S_1) without altering the conformation of the molecule.

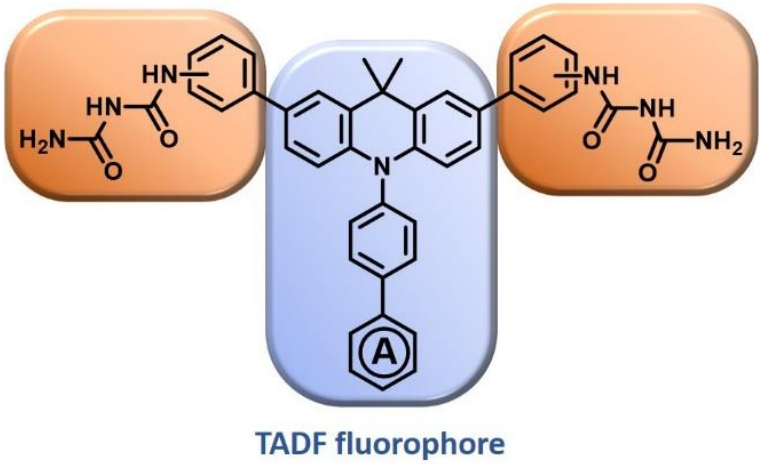

Figure 2-6. Molecular structure of TADF-based chromophores endowed with biuret molecular recognition units.

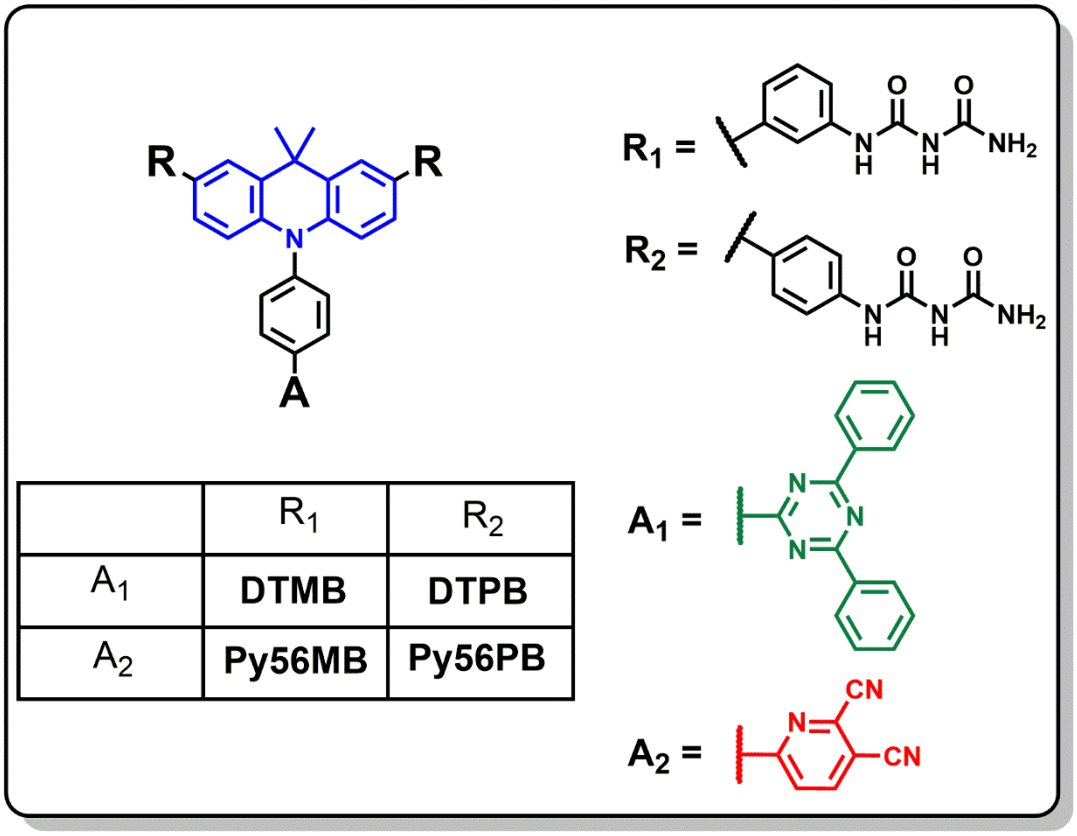

	R_1	R_2
A_1	**DTMB**	**DTPB**
A_2	**Py56MB**	**Py56PB**

Figure 2-7. TADF-based self-assembly molecular design.

In previous work,[23] **MBBiuret** and **PBBiuret** (**Scheme 2-1**) were synthesized by coupling biuret motifs onto electron-rich conjugated structures through Suzuki-Miyaura C–C bond formation. The key intermediates, **MBBiuret** and **PBBiuret**, were prepared in three steps from biuret. First, the process of nitration of biuret produced nitrobiuret in moderate yield and was followed by a condensation reaction between nitrobiuret and 3-bromoaniline (or 4-bromoaniline).[24] Then, aryl bromide was treated with bis-(pinnacolato) diborane via the reaction of Pd(II)-catalyzed borylation to produce an intermediate boronic ester.[25] Lastly, the solution was purified by column chromatography to obtain

MBBiuret and **PBBiuret** in isolated yields of 84% and 72%, respectively.

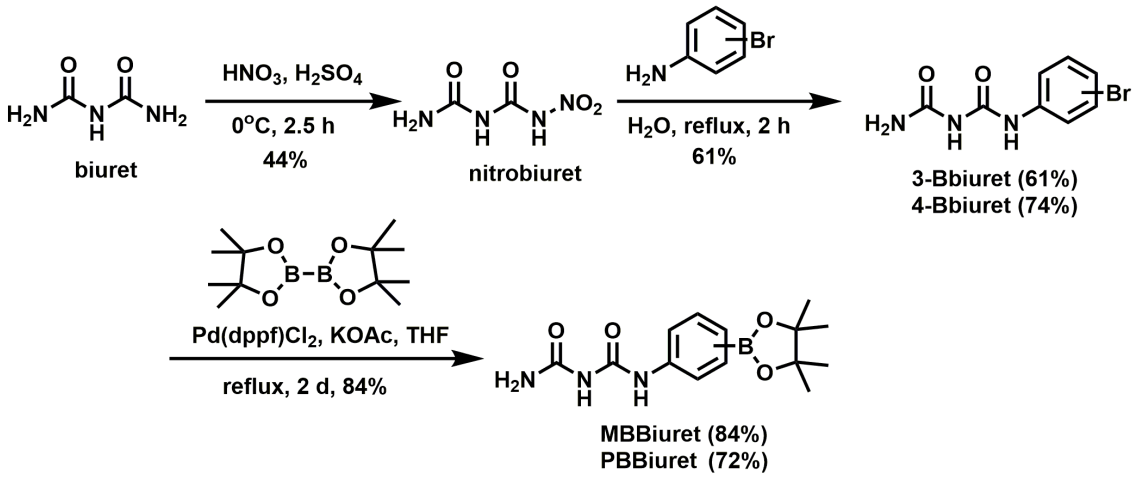

Scheme 2-1. Synthetic pathway and structures of **MBBiuret** and **PBBiuret**.

As shown in **Scheme 2-2**, 4-bromobenzoyl chloride was treated with benzonitrile and ammonia to form the triazine ring of **4-Br-TAZ**, which was reacted with 9,9-dimethyl-9,10-dihydroacridine through Buchwald-Hartwig coupling to produce **DMAC-TRZ**.[21] This was then brominated using *N*-bromosuccinimide (NBS) to obtain **DTBr2**. Next, the brominated TADF-fluorophore was connected to **MBBiuret** or **PBBiuret** via Pd(0)-catalyzed Suzuki-Miyaura coupling reaction to give **DTMB** and **DTPB**.

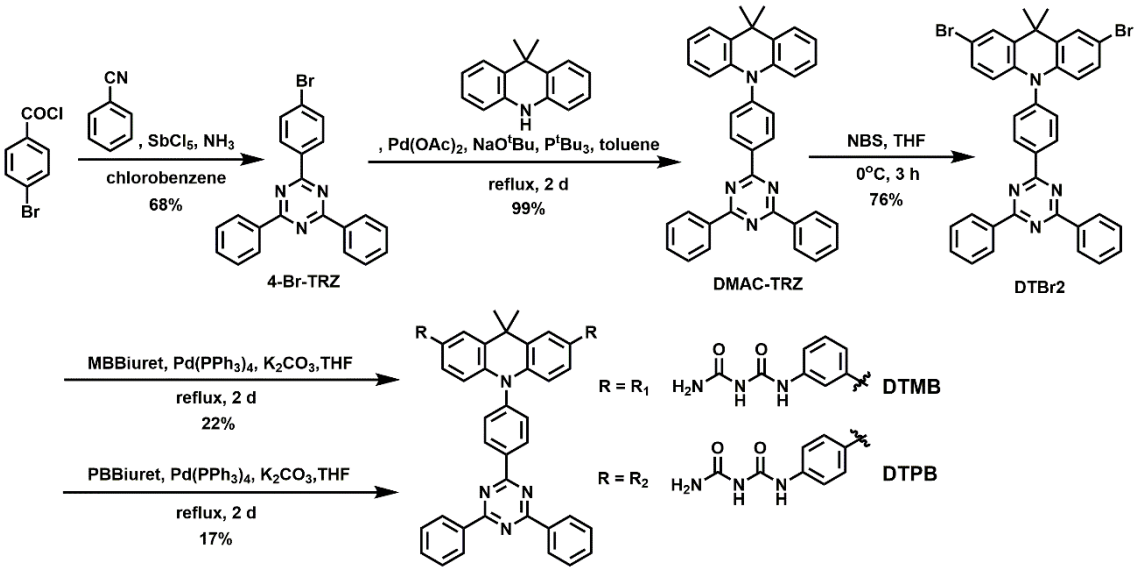

Scheme 2-2. Synthetic pathway and structures of **DTMB** and **DTPB**.

For the pyridine series of chromophores, 9,9-dimethyl-9,10-dihydroacridine was treated with 1-bromo-4-iodobenzene via Buchwald-Hartwig coupling to obtain the corresponding amino aryl bromide. This was treated with ^{n}BuLi at –78°C and quenched with triisopropyl borate, followed by hydrolysis to form the boronic acid derivative. Afterward, the boronic acid derivative was reacted with the CN-substituted pyridine through a Suzuki-Miyaura coupling [22] and then brominated using NBS to obtain **Py56Br2**. Finally, the brominated TADF-fluorophore underwent Pd(0)-mediated Suzuki-Miyaura coupling with **MBBiuret** or **PBBiuret** to give **Py56MB** and **Py56PB** (**Scheme 2-3**). The low reaction yield is related to the poor solubility of biuret derivatives during purification by chromatography.

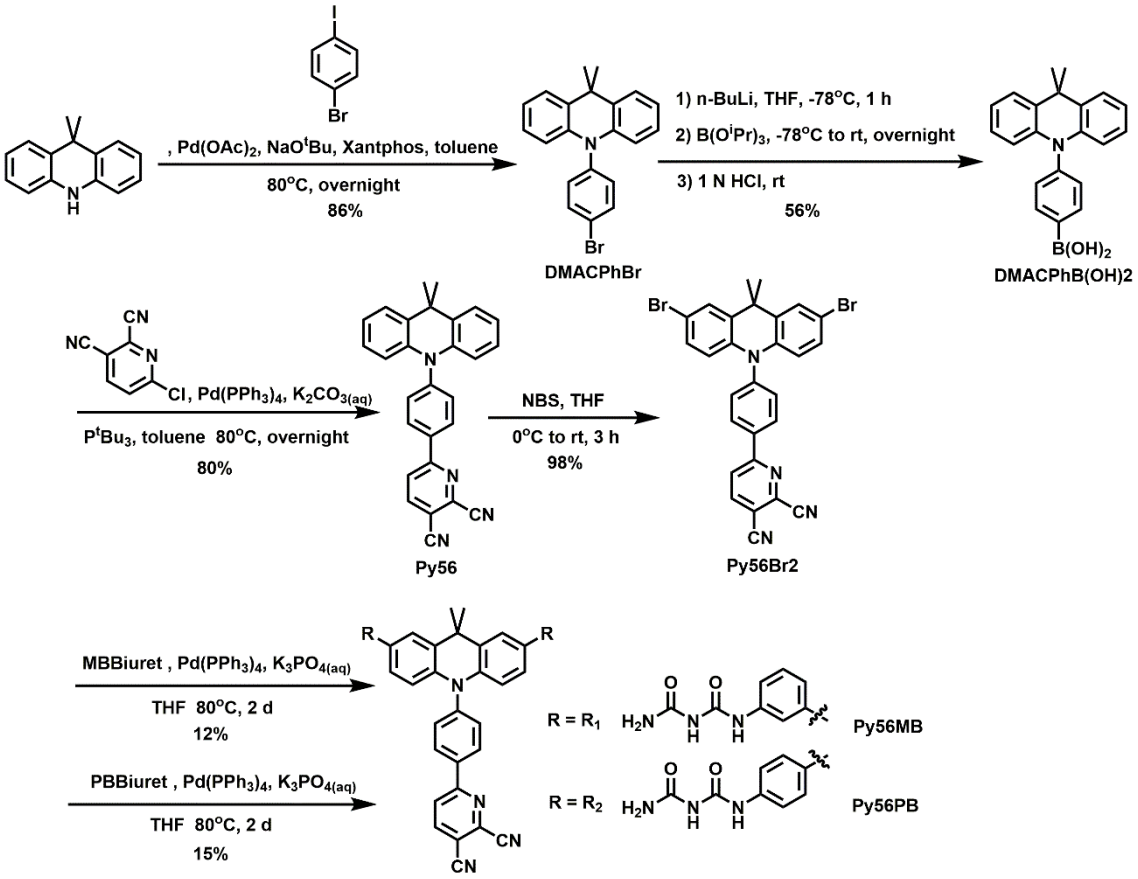

Scheme 2-3. Synthetic pathway and structures of **Py56MB** and **Py56PB**.

2-5 Characterization of Nanostructures

Dynamic light scattering is a well-known method to analyze or determine the size distribution profile of particles in suspension or colloidal systems. As shown in **Figure 2-8**, the DLS analysis of all TADF molecules in 10^{-4} M acetone solution showed multiple patterns of distribution, indicating the presence of at least two families of particles of different size in solution. Although the intensity profile was largely characterized by a large distribution of particles, their average hydrodynamic radius was around 350 nm,

which is close to the diameter of the nanospheres in SEM or TEM images (**Figure 2-13**). From this, we deduce that the larger-sized particles (1-3 μm) is the result of the aggregation or cluster of nanostructures.

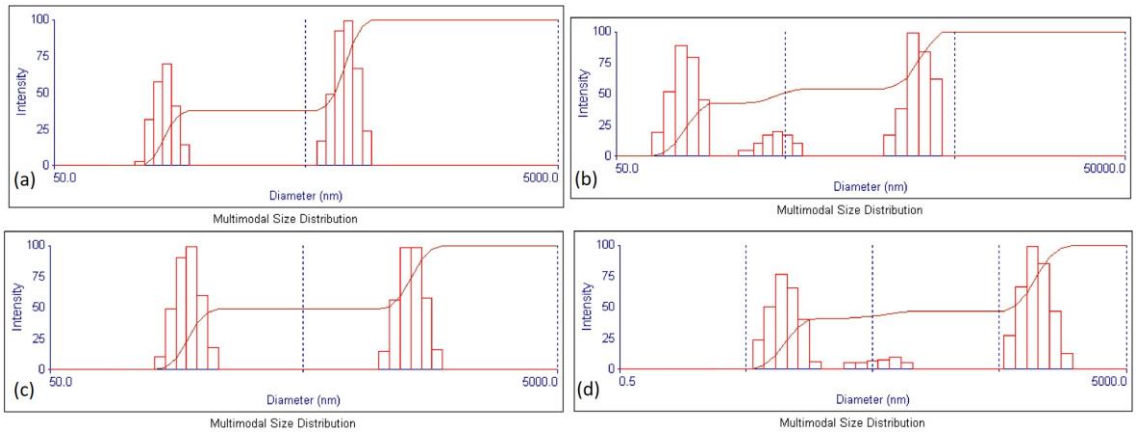

Figure 2-8. Dynamic light scattering (DLS) of (a) **DTMB**, (b) **DTPB**, (c) **Py56MB** and (d) **Py56PB** in 10^{-4} M acetone solution. The samples were examined by Brookhaven's 90Plus/zetaPALS instrument.

While investigating the self-assembly behavior of TADF molecules, we discovered that they spontaneously formed aggregates or spheres when drop casting with diluted (10^{-4} M) THF solution or THF/acetone co-solvent. In pure THF solution, all TADF molecules formed aggregates on the film with a size from 600 nm to 3 μm, as evidenced by scanning electron microscopy (SEM) and transmission electron microscopy (TEM, **Figures 2-9** to **2-13)**. The alteration of environment by adding a hydrophilic solvent allows us to distinguish different nanostructures formed by the TADF molecules. For example, when

the ratio of acetone increased, we observed more homogeneity in structures, ranging from clumps of aggregates in films to well-defined nanospheres, as well as seeing a decrease from over 1 μm to approximately 300 nm in size. When optimizing the condition of self-assembly of the nanoparticles, we could observe the formation of well-defined and uniform nanospheres in size of 200 nm to 400 nm, being deposited by TADF molecules in dilute (10^{-4} M) acetone solution, which is in line with our previous work (**Figure 2-13**).[26]

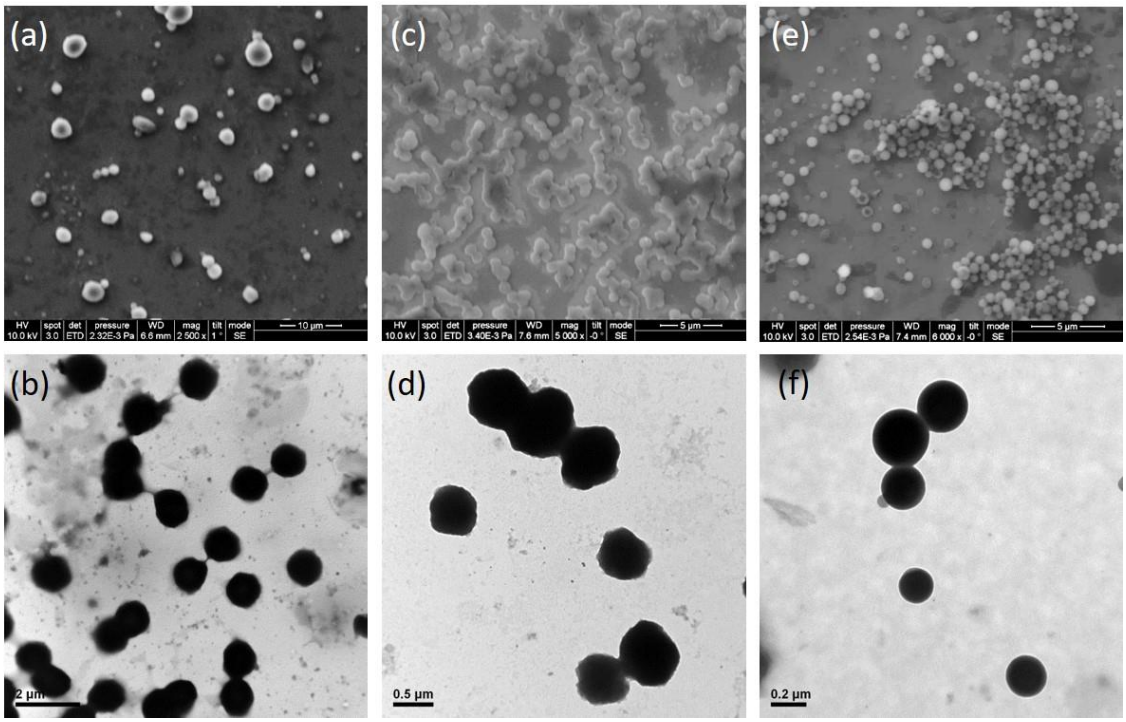

Figure 2-9. SEM and TEM images of **DTMB** in (a,b) THF, (c,d) THF/acetone = 1:1, (e,f) THF/acetone = 3:7 solution. Scale bar = 10 μm for (a), 5 μm for (c)(e), 2 μm for (b), 0.5 μm for (d) and 0.2 μm for (f).

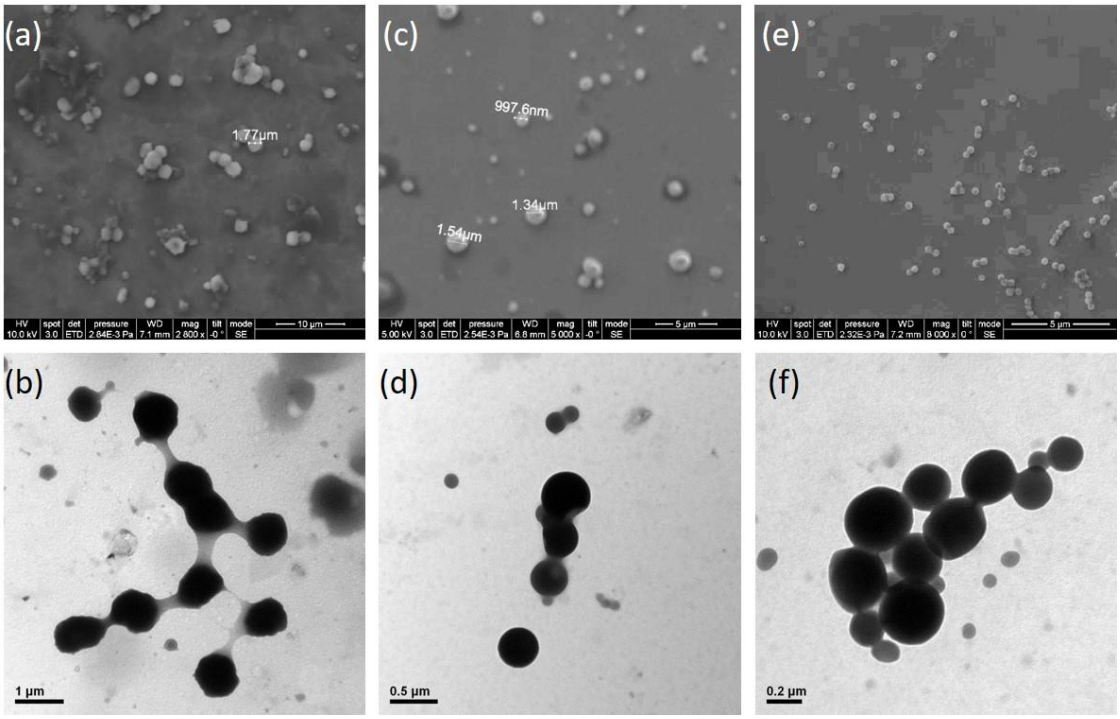

Figure 2-10. SEM and TEM images of **DTPB** in (a,b) THF, (c,d) THF/acetone = 1:1, (e,f) THF/acetone = 1:9 solution. Scale bar = 10 μm for (a), 5 μm for (c)(e), 1 μm for (b), 0.5 μm for (d) and 0.2 μm for (f).

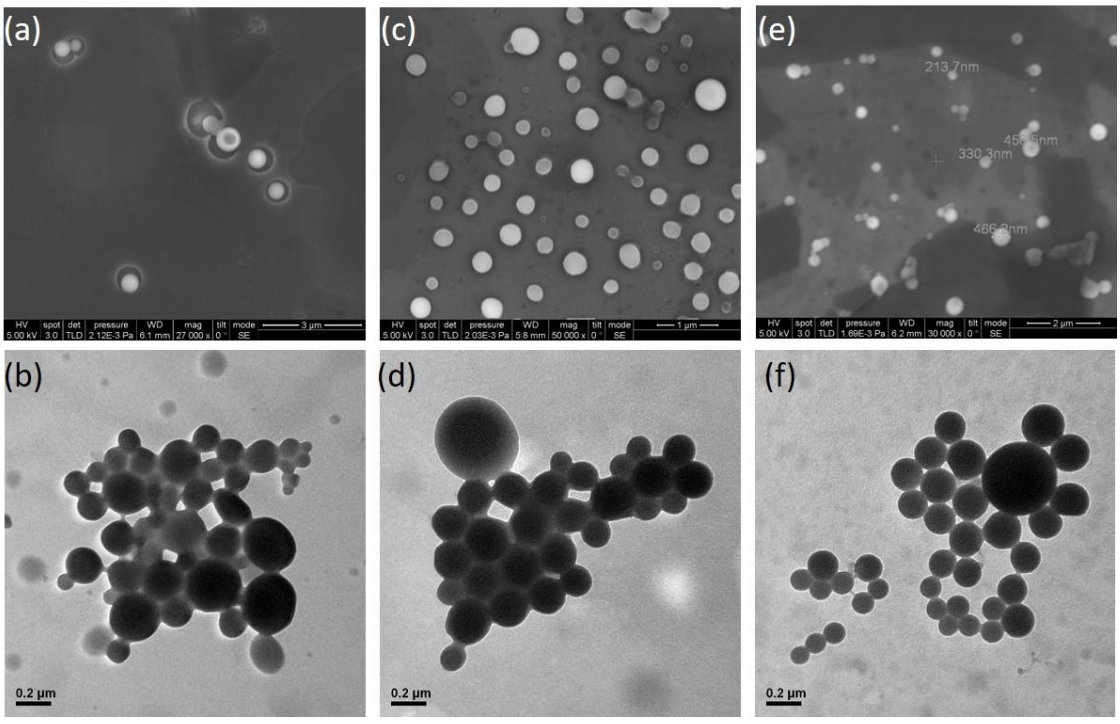

Figure 2-11. SEM and TEM images of **Py56MB** in (a,b) THF, (c,d) THF/acetone = 1:1,

(e,f) THF/acetone = 3:7 solution. Scale bar = 3 μm for (a), 2 μm for (e), 1 μm for (c) and 0.2 μm for (b)(d)(f).

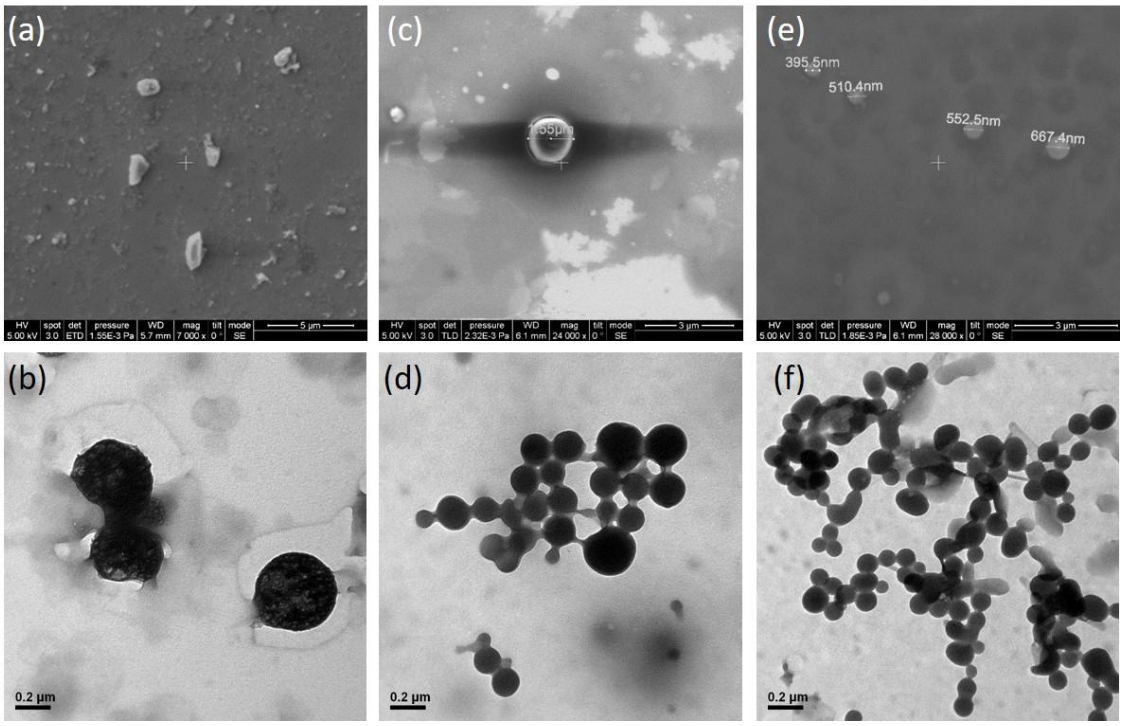

Figure 2-12. SEM and TEM images of **Py56PB** in (a,b) THF, (c,d) THF/acetone = 1:1, (e,f) THF/acetone = 3:7 solution. Scale bar = 5 μm for (a), 3 μm for (c)(e), and 0.2 μm for (b)(d)(f).

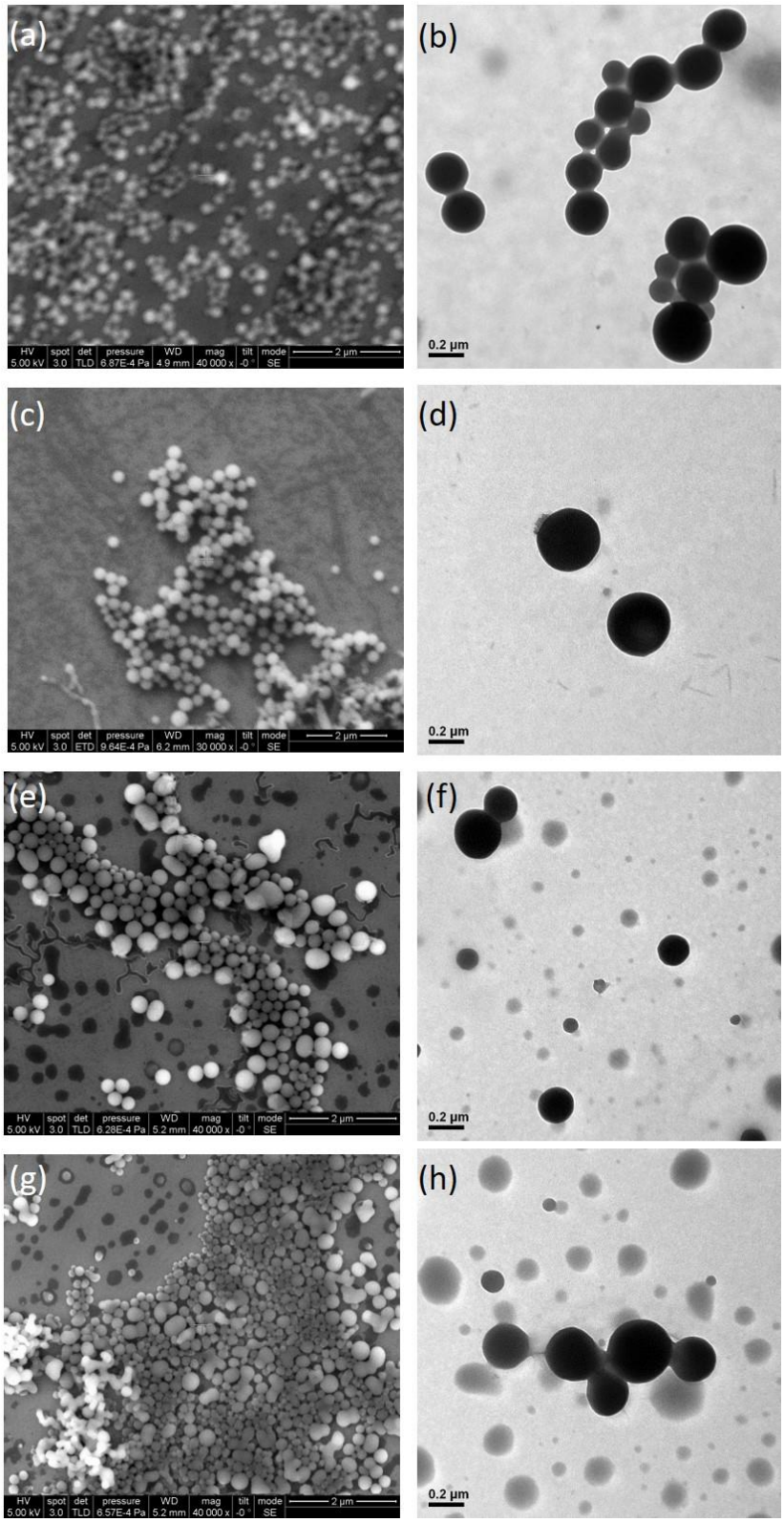

Figure 2-13. SEM and TEM images of (a,b) **DTMB**, (c,d) **DTPB**, (e,f) **Py56MB** and (g,h) **Py56PB** in acetone solution. Scale bar = 2 µm for (a)(c)(e)(g) and 0.2 µm for (b)(d)(f)(h).

2-6 Photophysical Properties

The photophysical properties of **DTMB**, **DTPB**, **Py56MB** and **Py56PB** in solution (10^{-5}M in THF or toluene) and in the solid state are summarized in **Table 2-1**, and the absorption and fluorescence spectra in solution are shown in **Figure 2-14** and **Figure 2-15**. All compounds exhibit intense absorption bands in the ultraviolet region between 300 nm to 400 nm due to π-π* transitions, as well as weak absorption bands around 400 nm assigned to n-π* and intramolecular charge transfer (ICT) transitions. The PL bands of **DTMB** and **DTPB** in THF solution are around 570 nm, with photoluminescence quantum yields (PLQY, Φ) in aerated solutions of less than 0.2. The presence of a strong ICT character in the excited state is evidenced by the solvatochromism of the emission. To eliminate the quenching effect of oxygen, the compounds are dissolved in degassed toluene solution, resulting in an enhancement of Φ = 0.40. For **Py56MB** and **Py56PB**, which have stronger electron-accepting capacity. Tuning the energy gap of photoluminescence results in the PL band emitting near 575 nm, with Φ > 0.10 (degassed toluene solution). However, in a more polar solvent such as THF, the emission band is around 570 nm. The py56 chromophores are thus less sensitive to solvent polarity, probably due to a similar ICT character in both the ground and excited state. This results in a small net (de)stabilization of the excited vs. the ground state, leading to small

solvatochromic effects.[27]

The absorption and emission spectra of the TADF molecules in the solid state are shown in **Figure 2-16**. In comparison with the emission band in toluene solution, the emission in neat films is significantly red-shifted to 540 nm or 600 nm due to molecular aggregation.

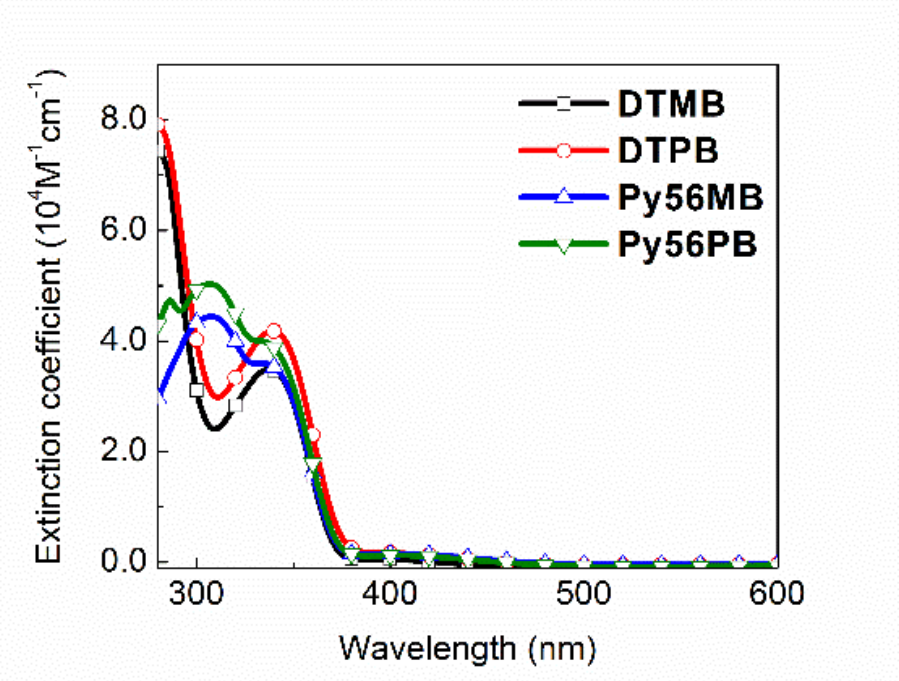

Figure 2-14. UV/Vis absorption spectrum of TADF molecules in 10^{-5}M THF solution.

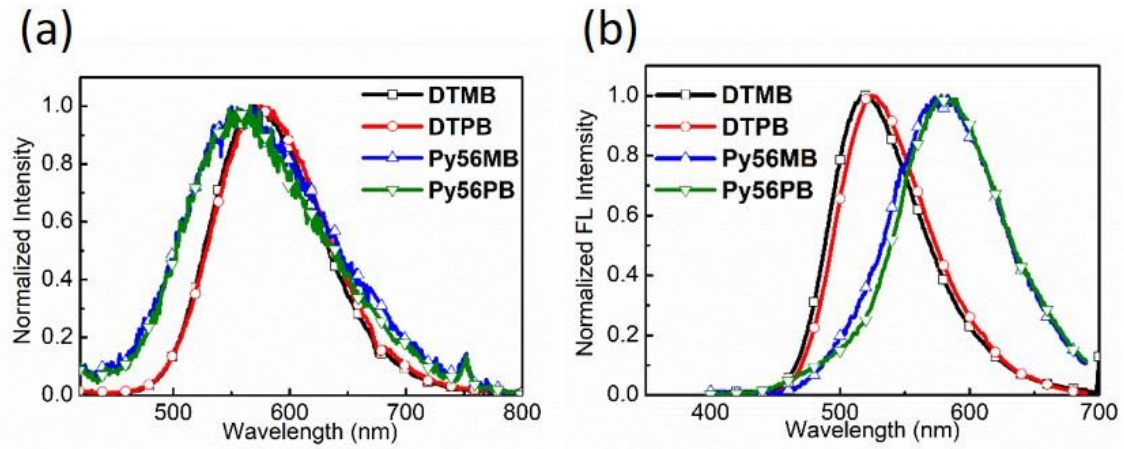

Figure 2-15. PL spectra of TADF molecules in 10^{-5}M (a) THF and (b) toluene solution. Excited at 340 nm.

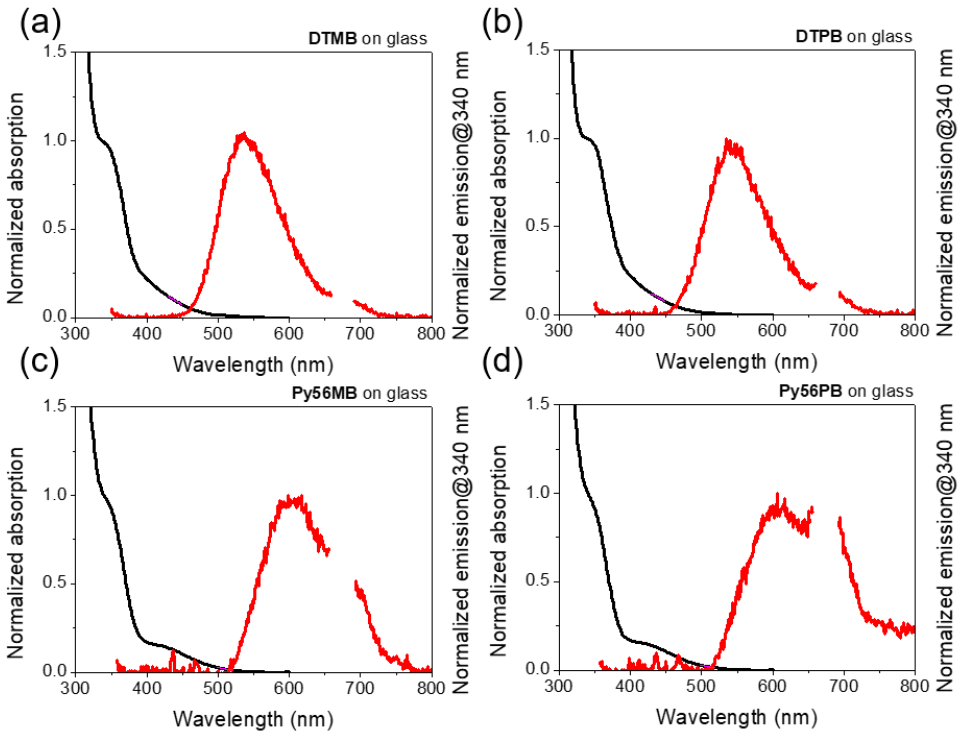

Figure 2-16. Absorption and fluorescence spectra of (a) **DTMB**, (b) **DTPB**, (c) **Py56MB** and (d) **Py56PB** in neat films. Excited at 340 nm.

Table 2-1. Summary of photophysical properties of TADF molecules.

Molecule	$\lambda_{Abs}{}^{a}$ (solution/film, nm)	ε^{a} ($10^4M^{-1}cm^{-1}$)	$\lambda_{PL}{}^{soln}$ (THF/toluene, nm)	$\lambda_{PL}{}^{film}$ (nm)	$\Phi_{THF}{}^{b}$ (%)	$\Phi_{toluene}{}^{b}$ (%)
DTMB	337/337	3.5	569/520	539	16 (7.4)	43 (18)
DTPB	339/340	4.2	570/525	544	11 (5.7)	37 (16)
Py56MB	339/340	3.6	567/573	604	1.9 (1.3)	16 (6.2)
Py56PB	334/341	4.0	566/578	610	1.7 (1.2)	10 (3.7)

[a] Measured in THF solution (10^{-5}M). [b] Fluorescence quantum yields measured in degassed

THF or toluene solution (10^{-5}M) at λ_{Ex} = 350 nm, using 0.1 N H_2SO_4 solution with quinine sulfate as standard. The values in parentheses correspond to aerated solutions.

The photoluminescence spectra of TADF molecules in degassed solution at various temperature are shown in **Figure 2-17** and **Figure 2-18**. In degassed THF solutions, all compounds exhibit similar temperature-dependent behavior with reduced fluorescence intensity and bathochromic shift of the emission maximum wavelength upon lowering the temperature. This behavior is typical of TADF chromophores, whose PL intensity decreases at lower temperature due to less efficient rISC.

In degassed toluene solutions, **DTMB** and **DTPB** behaved similarly as in THF solution. Nevertheless, the photoluminescence intensity of **Py56MB** and **Py56PB** decreased from 300K to 240K and increased once temperature dropped below 240K. We speculated that TADF properties still dominated the process of emission at temperatures above 240K. However, at lower temperatures, a hyproschomic shift can be observed, possibly due to a lowering of the solvent dielectric constant. This can contribute to reducing vibronic coupling, so that the fluorescence intensity increases from 240K to 200K due to lower internal conversion at low temperatures.

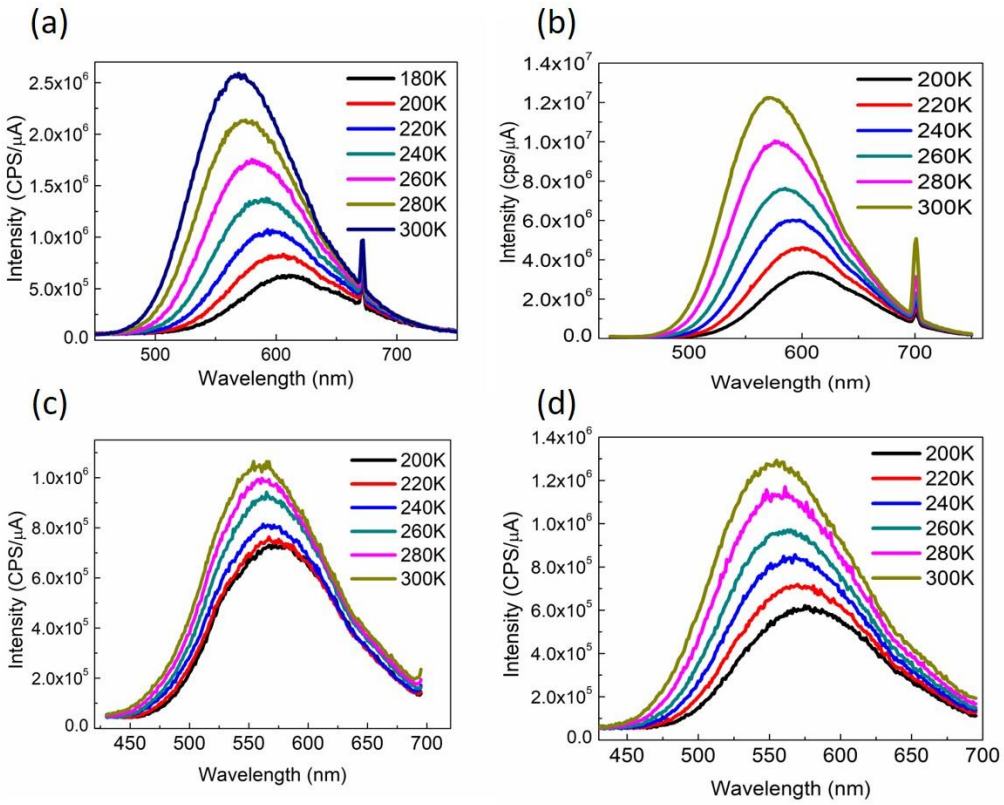

Figure 2-17. The photoluminescence spectra of (a) **DTMB**, (b) **DTPB**, (c) **Py56MB** and (d) **Py56PB** in 10^{-5}M degassed THF solution at different temperatures. Excited at 350 nm.

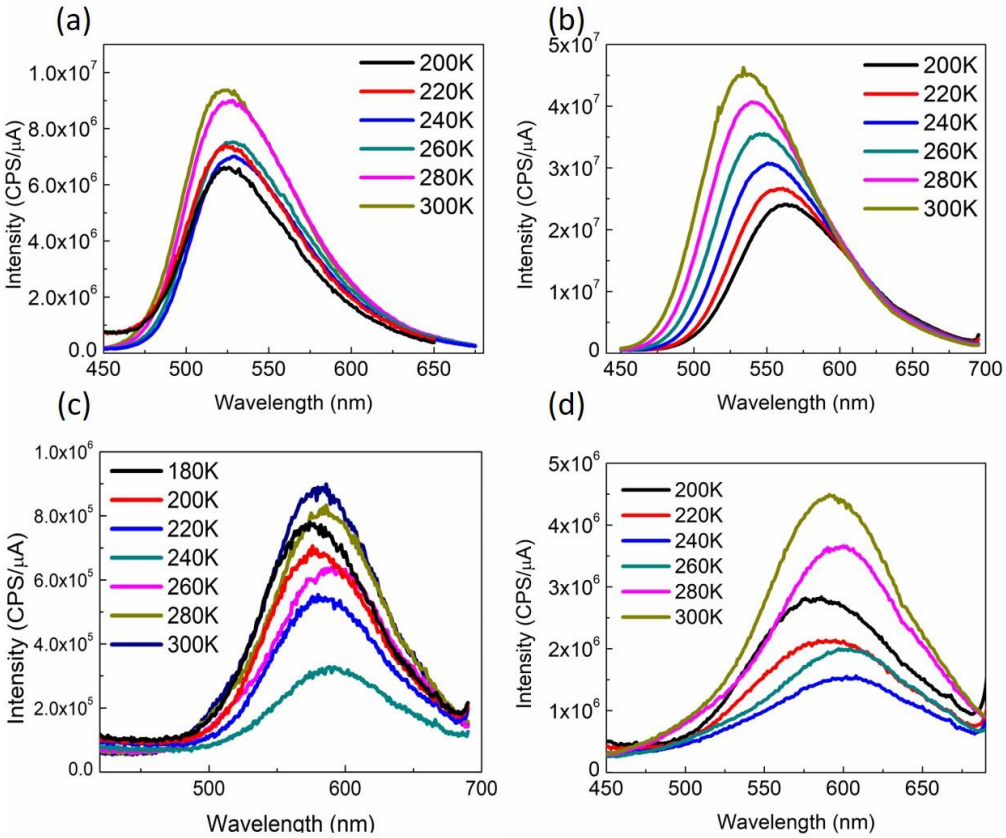

Figure 2-18. The photoluminescence spectra of (a) **DTMB**, (b) **DTPB**, (c) **Py56MB** and (d) **Py56PB** in 10^{-5}M degassed toluene solution at different temperatures. Excited at 350 nm.

The lifetime of an emissive excited state can be measured using time-correlated single photon counting. The latter is a powerful technique in fundamental photophysics to analyze luminescence intensity profile (or its decay) over the time domain. The fluorescence intensity over a course of time can be determined through the best fit of a single- or multi-exponential decay in the $I(t)$ profile. By changing the temperature, changes in the decay profile can allow one to calculate the activation energy (E_a) of the

rISC process from the triplet state (T_1) to singlet state (S_1), from which ΔE_{ST} of the luminophore could be extrapolated to confirm the TADF behavior. The energy level and rate constant of the kinetics of DT- and PY56-based chromophores are shown in **Figure 2-19**,[29] in which the critical parameters of an intersystem crossing (k_{ISC}) and the reverse process (k_{rISC}) between singlet state and triplet state could be used to verify the state of TADF molecules. The rate of the process of reverse intersystem crossing was consistent with a small value of ΔE_{ST}, as derived from **Equation 2-2** where A is a constant, k is Boltzmann's constant and T the temperature.

$$k_{rISC} = A \exp\left(-\frac{\Delta E_{ST}}{kT}\right). \qquad \textbf{(Equation 2-2)}$$

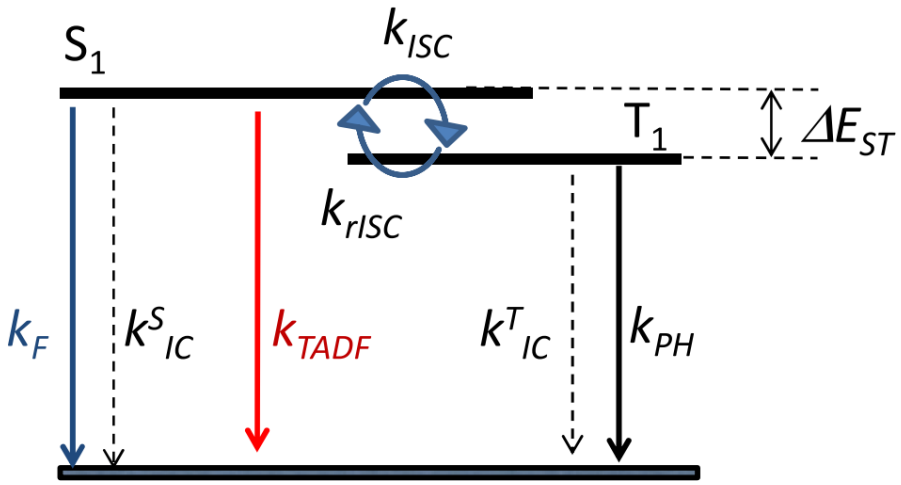

Figure 2-19. Simplified representation of electronic energy levels and rate constants involved in the kinetics of TADF chromophores. Reprinted with permission from ref 29. Copyright 2017 IOP Publishing, Ltd.

From the fitting of the multi-exponential photoluminescence decays in a time-correlated profile, the luminescence intensity in the time domain could be best described by two main decay constants in **Equation 2-3**,[28] and the ratio of quantum yield of delayed fluorescence to prompted fluorescence (Φ_{DF}/Φ_{PF}) was calculated using **Equation 2-4**.

$$I\,(\mathrm{t}) = A_{PF}\exp\left(-\frac{t}{\tau_{PF}}\right) + A_{DF}\exp\left(-\frac{t}{\tau_{DF}}\right). \qquad \textbf{(Equation 2-3)}$$

$$\frac{\Phi_{DF}}{\Phi_{PF}} = \frac{A_{DF}\tau_{DF}}{A_{PF}\tau_{PF}}. \qquad \textbf{(Equation 2-4)}$$

As pointed out by Monkman,[29-31] for the TADF materials with less contribution from delayed fluorescence, such as when $\Phi_{DF}/\Phi_{PF} < 3$, k_{rISC} can be expressed as shown in **Equation 2-5**, from which we are able to derive the value of ΔE_{ST} from **Equation 2-2** and **2-4**.

$$k_{rISC} = \frac{1}{\tau_{DF}\Phi_{ISC}}\left(\frac{\Phi_{DF}}{\Phi_{PF}}\right). \qquad \textbf{(Equation 2-5)}$$

As seen in **Figures 2-20** to **2-27** and summarized in **Table 2-2**, for all TADF compounds, we observed contributions from delayed fluorescence with τ_{DF} around 1 μs and τ_{PF} between 13 ns and 27 ns in degassed THF or toluene solutions. We also identified TADF molecules with smaller value of ΔE_{ST} to facilitate the reverse intersystem crossing and more efficiently harvest triplet excitons to enhance PL quantum yields according to this model.[29] At low temperatures, triplet excitons cannot overcome the activation energy between the singlet and the triplet state contribution to the delayed fluorescence, which corresponds to the decay of the triplet state, is increased to 2 – 3 μs. Interestingly, for all

TADF solutions with chromophores, the addition of 10% DMSO showed significantly reduced time span of molecules in the emission decay process (ex. from 1.40 μs to 380 ns in degassed THF/DMSO (10%) solution for **DTMB**). These results matched with previous work[32] that, even though DMSO does not quench the triplet state, it can disrupt H-bonding of bis-biuret derivatives and cause dissolution of the spherical aggregates. With the addition of DMSO, the destruction of the H-bonding network results in dissolution of the vesicles and subsequent decrease of the delayed component. This suggests that the formation of vesicles enhances the occurrence of TADF process in solution, which is therefore subject to supramolecular gating.[33]

From **Equation 2-6**,[29,30] where τ_{ph}^{0} is the phosphorescence lifetime derived in the temperature range of the deactivation of the rISC process, one can calculate the kinetic rate constants as summarized in **Table 2-3**. The isomers with the same TADF-active chromophore show a consistent trend in kinetic rate constants in the same solvents and their kinetic data (**Table 2-3**) coincide with the photophysical results from the steady-state photoluminescence (**Table 2-1**). For instance, **DTMB** or **DTPB** in toluene solution with reduced ΔE_{ST} shows a ratio of k_{rISC}/k_{ISC} of ca. 0.1 and higher Φ_{DF}/Φ_{PF}, leading to better PLQY. In contrast, for **Py56MB** or **Py56PB** in THF solution, the ratio of k_{rISC}/k_{ISC} is less than 0.01 and suggests inefficient harvesting of triplet excitons, in agreement with a lower PLQY. One explanation is that polar solvent such as THF will stabilize the charge-

transfer process of fluorophores and accelerate the conversion from excited state to ground state due to enhanced vibronic coupling.

$$\tau_{DF} = \tau_{ph}^{o} - \left(\frac{1}{\Phi_{ISC}} - 1\right)\tau_{ph}^{o}\frac{\Phi_{DF}}{\Phi_{PF}}. \qquad \textbf{(Equation 2-6)}$$

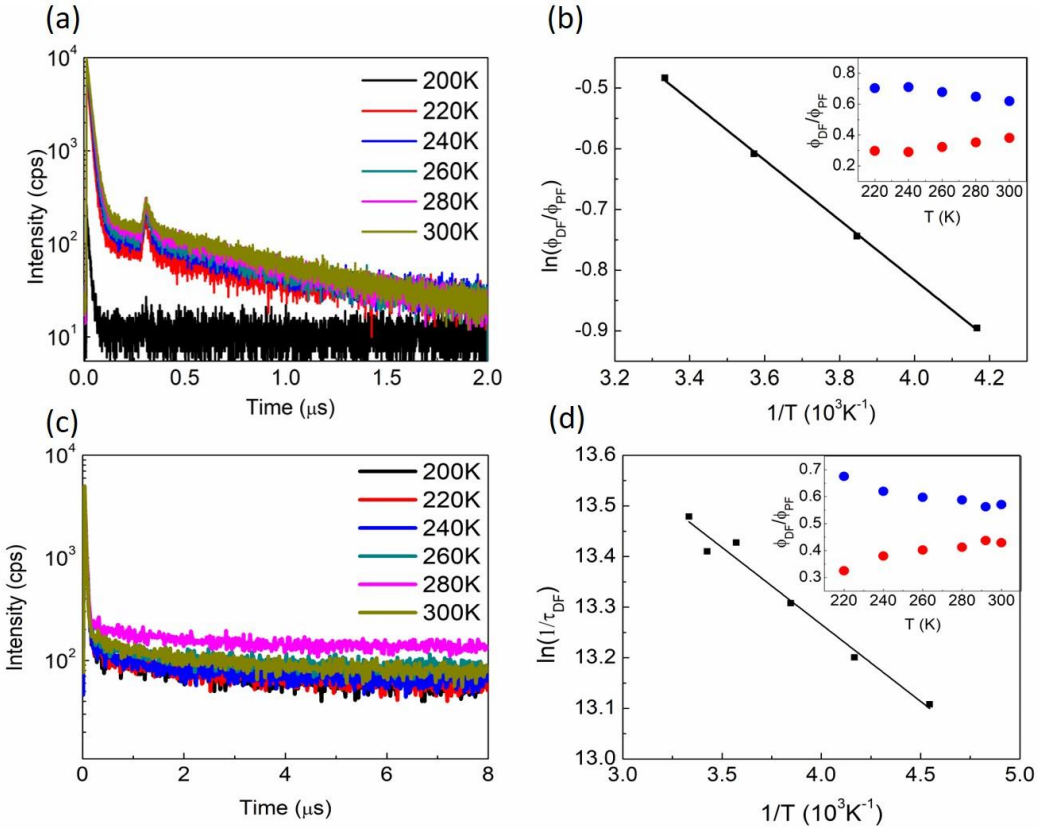

Figure 2-20. Fluorescence decay and Arrhenius plot of the reciprocal of the long-lived component of **DTMB** in 10^{-5}M degassed (a,b) THF and (c,d) toluene solution. λ_{ex} = 370 nm. The insets in (b) and (d) show relative contribution of the prompt (PF, blue) and delayed (DF, red) emission in fluorescence decay profiles.

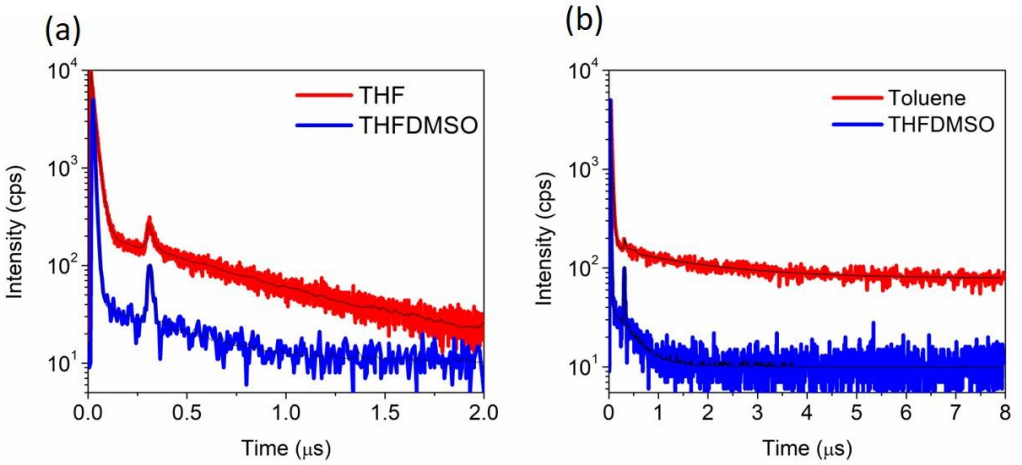

Figure 2-21. Fluorescence decay profile of **DTMB** in (a) THF, (b) toluene solution, in comparison of THF with 10%DMSO solutions at 300K. λ_{ex} = 370 nm.

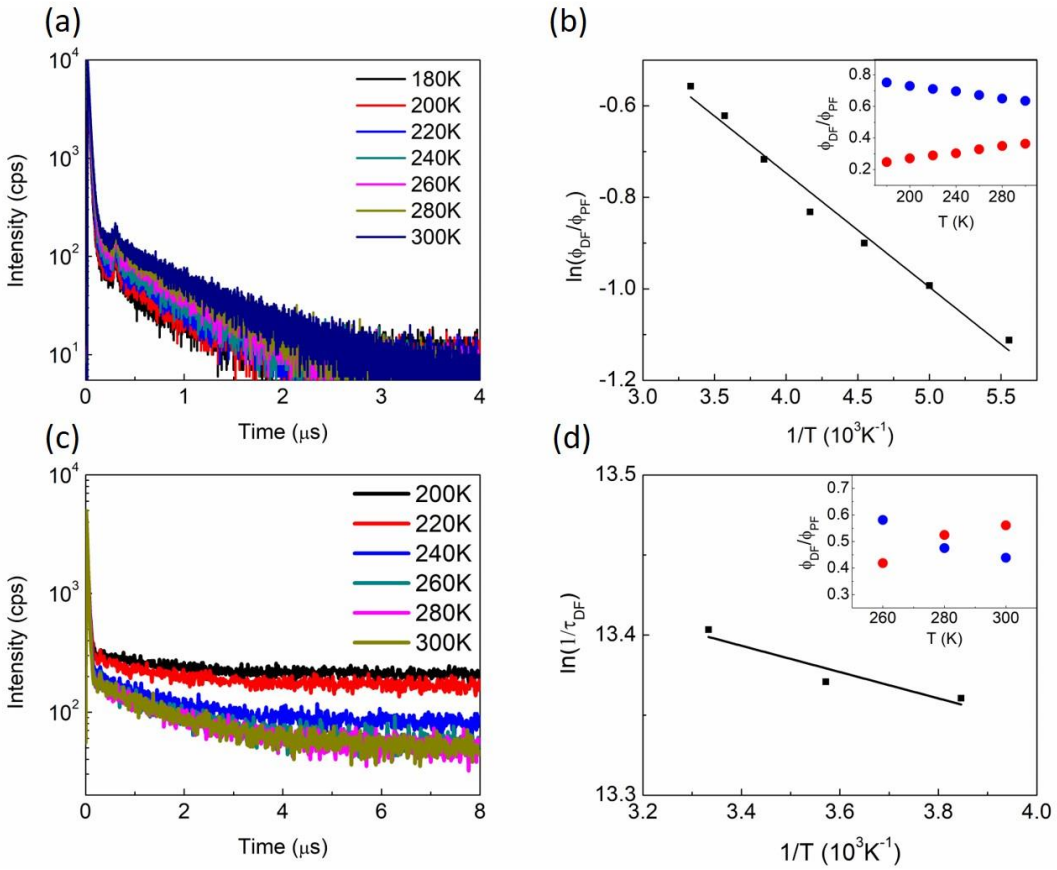

Figure 2-22. Fluorescence decay and Arrhenius plot of the reciprocal of the long-lived component of **DTPB** in 10^{-5}M degassed (a,b) THF and (c,d) toluene solution. λ_{ex} = 370

nm. The insets in (b) and (d) show relative contribution of the prompt (PF, blue) and delayed (DF, red) emission in fluorescence decay profiles.

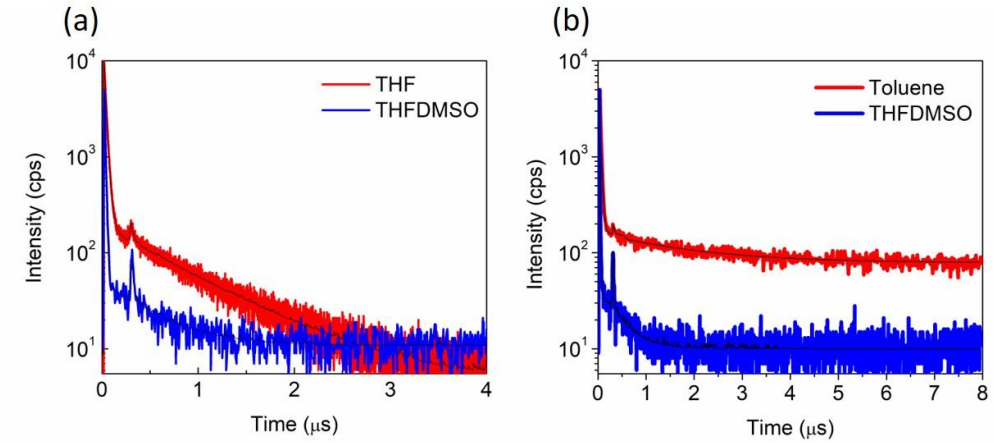

Figure 2-23. Fluorescence decay profile of **DTPB** in (a) THF, (b) toluene solution, in comparison of THF with 10%DMSO solutions at 300K. λ_{ex} = 370 nm.

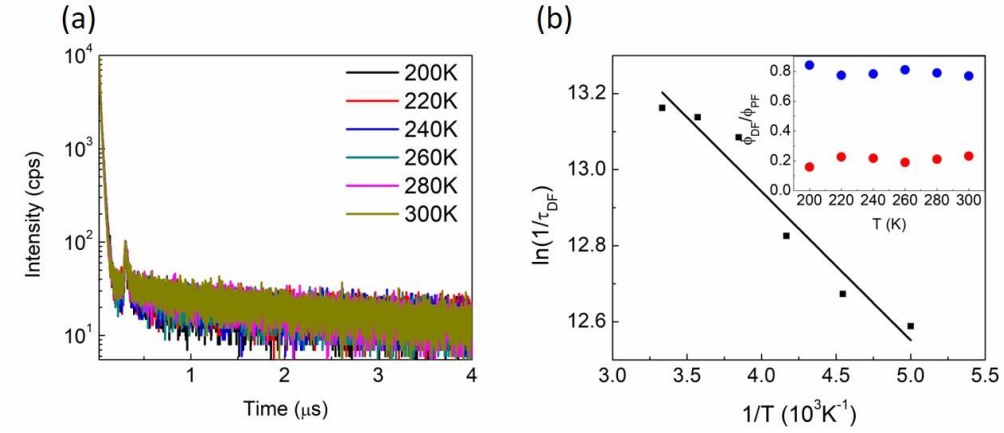

Figure 2-24. (a) Fluorescence decay and (b) Arrhenius plot of the reciprocal of the long-lived component of **Py56MB** in 10^{-5}M degassed THF solution. λ_{ex} = 370 nm. The inset in (b) shows relative contribution of the prompt (PF, blue) and delayed (DF, red) emission in fluorescence decay profiles.

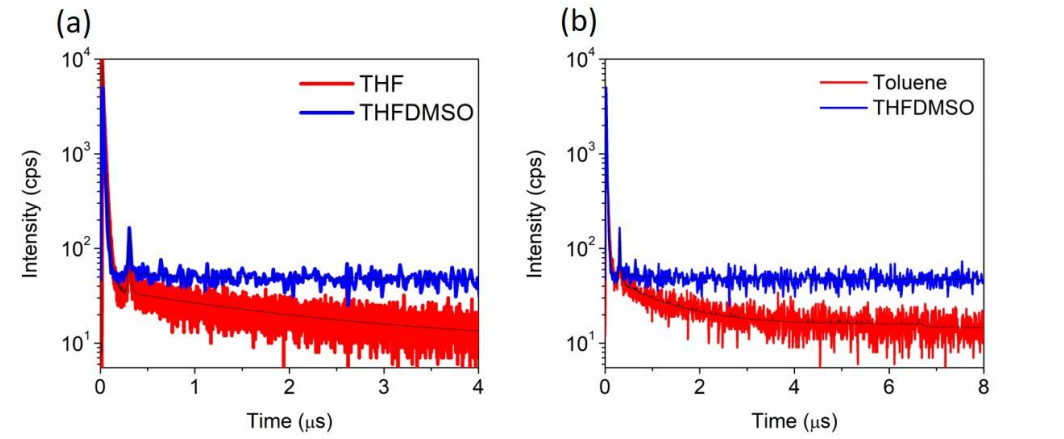

Figure 2-25. Fluorescence decay profile of **Py56MB** in (a) THF, (b) toluene solution, in comparison of THF with 10%DMSO solutions at 300K. λ_{ex} = 370 nm.

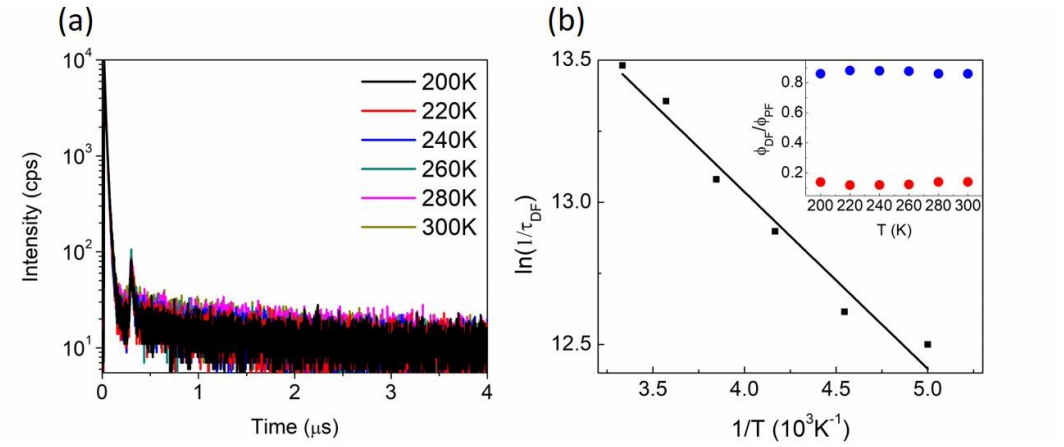

Figure 2-26. (a) Fluorescence decay and (b) Arrhenius plot of the reciprocal of the long-lived component of **Py56PB** in 10^{-5}M degassed THF solution. λ_{ex} = 370 nm. The inset in (b) shows relative contribution of the prompt (PF, blue) and delayed (DF, red) emission in fluorescence decay profiles.

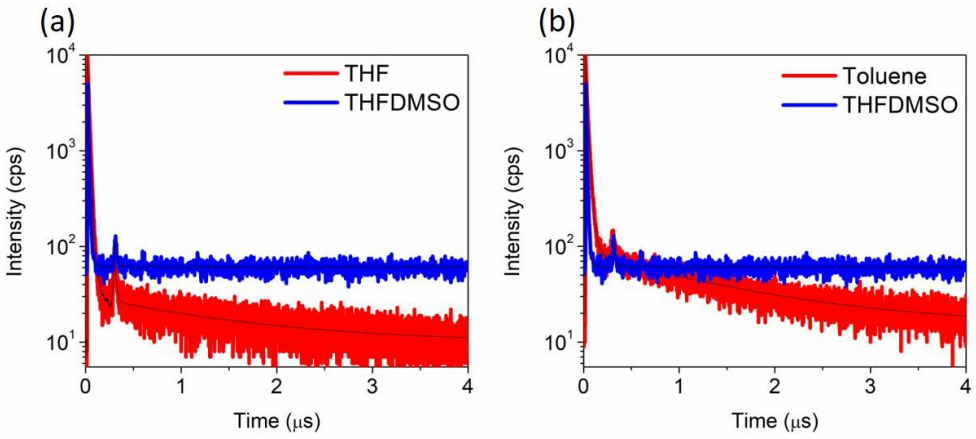

Figure 2-27. Fluorescence decay profile of **Py56PB** in (a) THF, (b) toluene solution, in comparison of THF with 10%DMSO solutions at 300K. λ_{ex} = 370 nm.

Table 2-2. Summary of photophysical parameters of TADF compounds in solution.

Molecule	E_a (ΔE_{ST})[a] (kcal mol^{-1})		τ_{PF}[a] (ns)		τ_{DF}[a] (μs)		Φ_{PF} (%)		Φ_{DF} (%)		Φ_{DF}/Φ_{PF}	
	THF	Tol	THF	Tol	THF	Tol	THF	Tol	THF	Tol	THF	Tol
DTMB	0.98	0.65	20.0	25.9	0.64	1.40	9.90	24.5	6.10	18.5	0.62	0.75
DTPB	1.35	0.42	19.3	27.1	0.68	1.51	7.00	16.2	4.01	20.8	0.57	1.28
Py56MB	0.78	-[b]	20.1	25.0	1.61	1.09	1.46	12.0	0.44	3.92	0.30	0.32
Py56PB	1.45	-[b]	13.8	21.4	1.52	1.38	1.46	6.84	0.24	3.16	0.16	0.46

[a] Measured in degassed solutions (THF or toluene). [b] Measurement not available due to limited solubility in toluene solution at low temperature.

Table 2-3. Summary of rate constant of TADF compounds in solution.

Molecule	$k_{r,S}$		k_{rISC}		k_{ISC}		τ_{ph}^0 (μs)		Φ_{ISC}		Φ_{RISC}	
	THF	Tol	THF	Tol	THF	Tol	THF	Tol	THF	Tol	THF	Tol

DTMB	3.7E6	7.0E6	-[a]	9.1E5	-[a]	2.3E7	-[a]	3.09	-[a]	0.59	-[a]	0.73
DTPB	3.0E5	5.9E6	-[a]	1.5E6	-[a]	2.1E7	-[a]	1.70	-[a]	0.57	-[a]	0.98
Py56MB	6.5E5	2.5E6	3.0E5	-[b]	2.9E7	-[b]	2.60	-[b]	0.53	-[b]	0.44	-[b]
Py56PB	8.7E5	1.7E6	1.8E6	-[b]	4.6E7	-[b]	9.24	-[b]	0.66	-[b]	0.21	-[b]

[a] Not applicable in **Equation 2-6** from Monkman's model.[29] [b] Measurement not available due to low solubility in toluene solution at low temperature.

2-7 Confocal Fluorescence Microscopy (CFM)

Confocal fluorescence microscopy (CFM) is an instrumental technique well suited to investigate the luminescent properties of each single object deposited on transparent substrates. **Figure 2-28** shows the CFM images of the spherical aggregates of the TADF materials. The emission spectrum of the individual aggregates collected by CFM was very similar to the fluorescence spectrum in neat films, which evidenced a bathochromic shift of 20 nm compared to the spectrum in THF solution. As seen in the CFM images of each TADF compound, the formation of uniform and well-defined nanoaggregates whose size is ca. 300 nm to 500 nm is evident. The fluorescence decay profile of individual nanostructures could also be collected using hyperspectral imaging. Taking **DTPB** for example, regardless of its condition in vesicle or on film, it is possible to obtain the prompt decay of τ = 20 ns from the multi-exponential decay curve of best fit (**Figure 2-29**). In contrast, the long-lived decay component assigned to the triplet state was beyond

the time resolution of the instrument which is limited by the repeat rate of the excitation pulses.

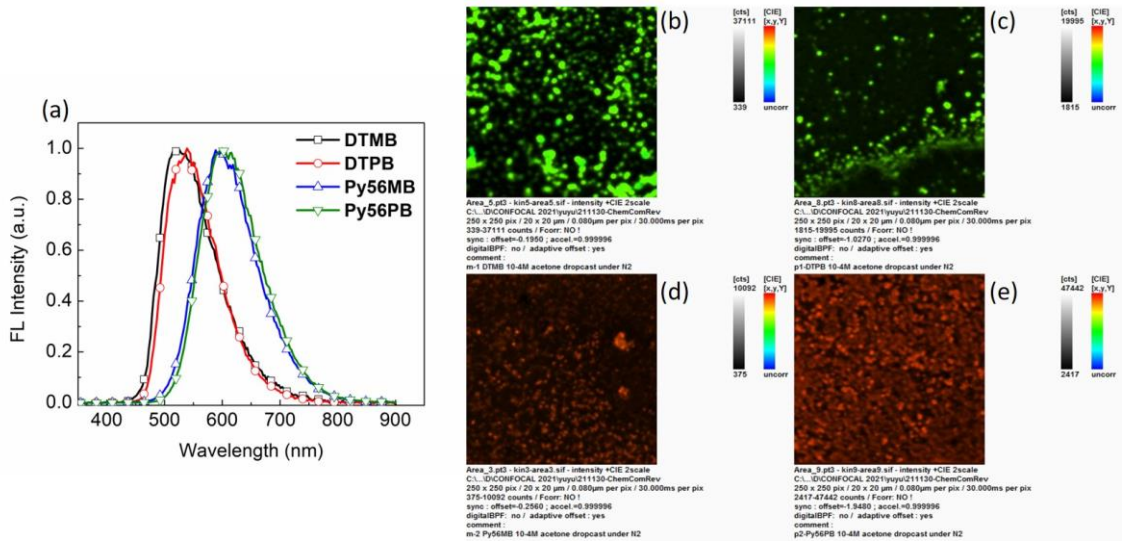

Figure 2-28. (a) Corrected fluorescence spectrum of TADF molecule aggregates on glass substrates. (λ_{ex} = 375 nm, λ_{em} = 405 nm long pass filter). Confocal fluorescence microscope images (37 x 37 µm) of (b) **DTMB**, (c) **DTPB**, (d) **Py56MB** and (e) **Py56PB** deposited on a glass slide (λ_{ex} = 365 nm, λ_{em} = 390 nm long pass filter).

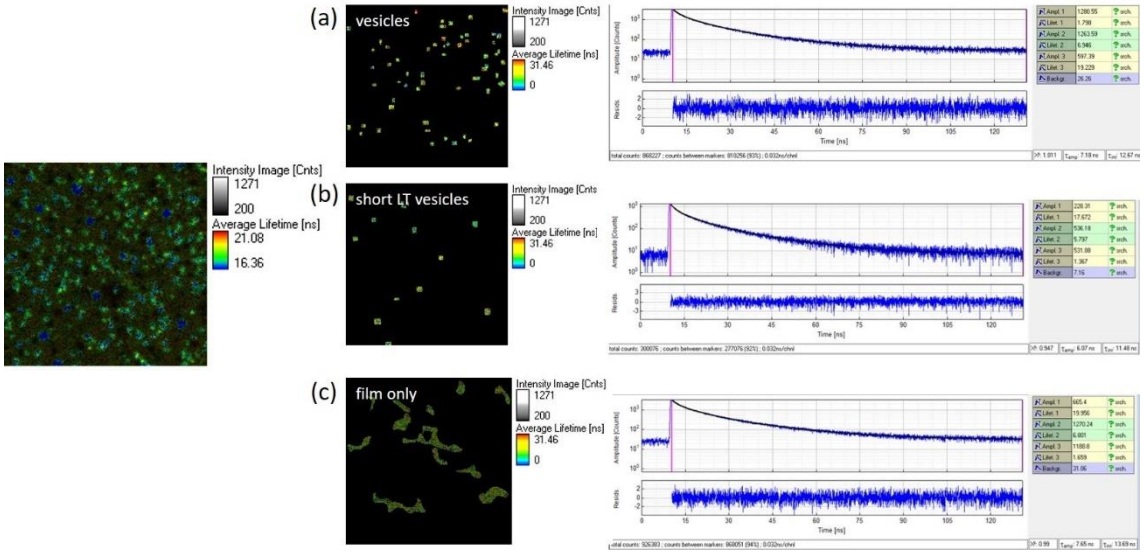

Figure 2-29. Confocal fluorescence microscopic images over time and lifetime spectra

of **DTPB** from individual aggregate (a) vesicle, (b) short life-time vesicle and (c) film. Excited at 375 nm.

2-8 Electrochemical Properties

Cyclic voltammetry (CV) is a method to determine the electrochemical potential at which molecules are oxidized or reduced. When the processes are reversible, this allows one to calculate the energy levels of the HOMO and LUMO orbitals, which is important in identifying ideal materials to use as electron and hole transport layers in OLED devices. These materials should possess an energy gap that is larger than that of the emitter to avoid energy transfer quenching while possessing HOMO and LUMO orbitals near to those of the emitter material to minimize energy loss. All the TADF molecules investigated have almost identical oxidation potentials due to the presence of acridine as an electron donating group. On the other hand, their reduction potential varies due to their different electron accepting moiety. Cyano-substituted pyridine with a stronger electron-withdrawing ability reduces the LUMO level of 0.30 eV to decrease E_g, when compared with triazine. The optical band gap at the onset absorption on film is close to the electrochemical E_g on film (**Figure 2-30** and **Table 2-4**).

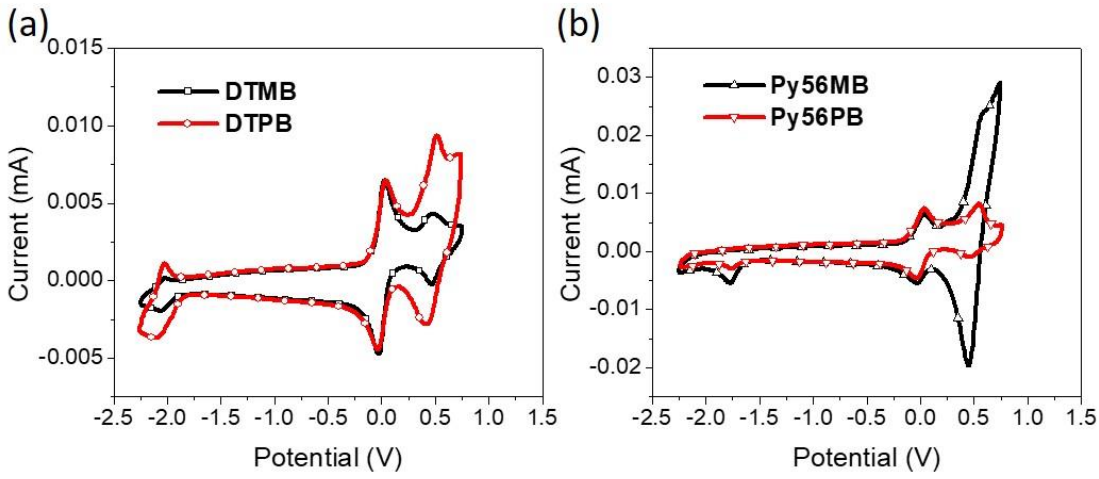

Figure 2-30. Cyclic voltammograms of (a) **DTMB**, **DTPB** and (b) **Py56MB** and **Py56PB** in 1.0 mM acetonitrile (vs. Fc/Fc^+, Fc/Fc^+ = ferrocene/ferrocenium) with 0.1 M of tetrabutylammonium hexafluorophosphate ($TBAF_6$) as a supporting electrolyte. Scanning rate 200 mVs^{-1}.

Table 2-4. Summary of energy level of TADF molecules.

Molecule	HOMO[a] (eV)	LUMO[a] (eV)	Electrochemical E_g on film[b] (eV)	Optical E_g on film[c] (eV)	Optical E_g in solution[c] (eV)
DTMB	–5.60	–3.05	2.55	2.58	2.60
DTPB	–5.58	–3.04	2.55	2.57	2.56
Py56MB	–5.61	–3.32	2.29	2.31	2.51
Py56PB	–5.59	–3.34	2.26	2.30	2.51

[a] $E_{HOMO} = -(5.10 + E_{onset}^{ox})$ eV; $/E_{LUMO} = -(5.10 + E_{onset}^{red})$ eV. [b] Electrochemical band gap calculated according to the equation, $E_g = (E_{LUMO} - E_{HOMO})$ eV. [c] Optical band gap at the onset absorption.

2-9 Application in EL-Devices

This work was performed in collaboration with Dr. Rafael Sánchez at the IMS Laboratory, University of Bordeaux. Because of the issue of quenching of the triplet excitons in a neat TADF film, we may expect lower photoluminescence intensity. Furthermore, the aggregates do not cover the entire surface of the device, which leaves areas in which the electron and hole transport layers are in direct contact. This can lead to charge recombination in the transport layers, which will lower the overall efficiency of the device. To solve this problem, it is necessary to introduce a host material possessing a high energy triplet state, which dilutes the triplet exciton concentration to avoid non-radiative decay. As shown in **Figure 2-31**, a significant enhancement of delayed fluorescence in the time domain in all TADF materials doped in 4,4'-bis(N-carbazolyl)-1,1'-biphenyl (CBP) film (10^{-3}M TADF in 5×10^{-3}M CBP in THF solution), when compared to TADF neat film, can be observed. Besides, the photoluminescence spectra of doped films indicate a blue-shifted emission (**Figure 2-32**). The related photophysical parameters of TADF neat film and doped in CBP film are summarized in **Table 2-5**.

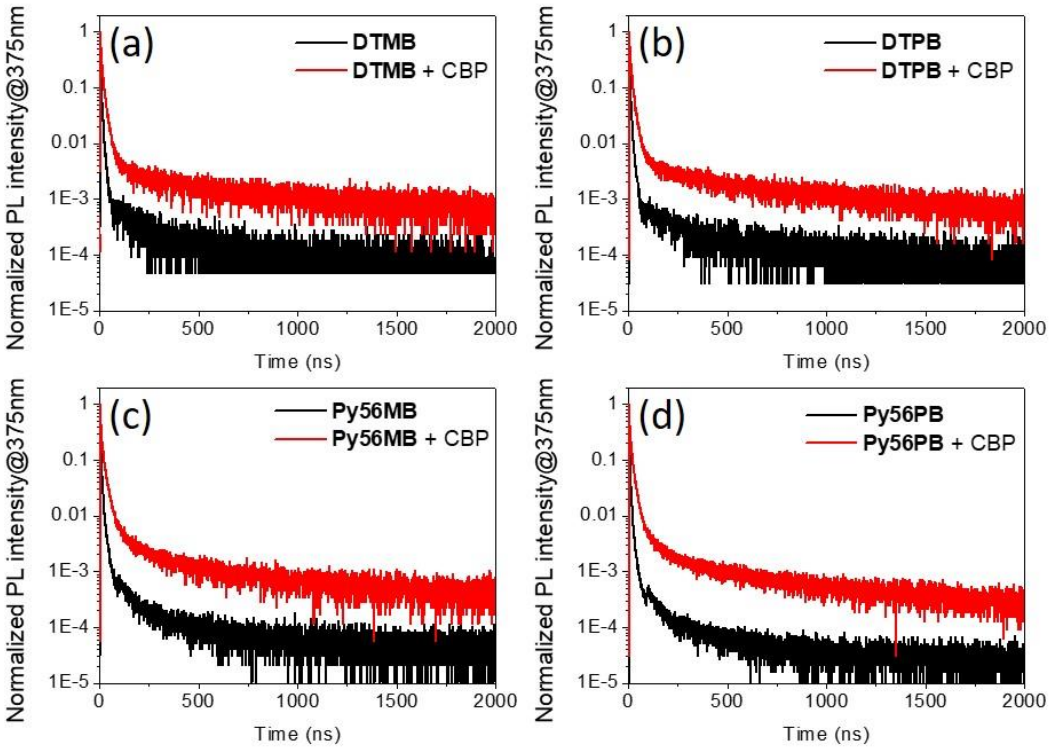

Figure 2-31. Photoluminescence decay spectra of (a) **DTMB**, (b) **DTPB**, (c) **Py56MB** and (d) **Py56PB** in neat film or doped CBP film. Excited at 375 nm.

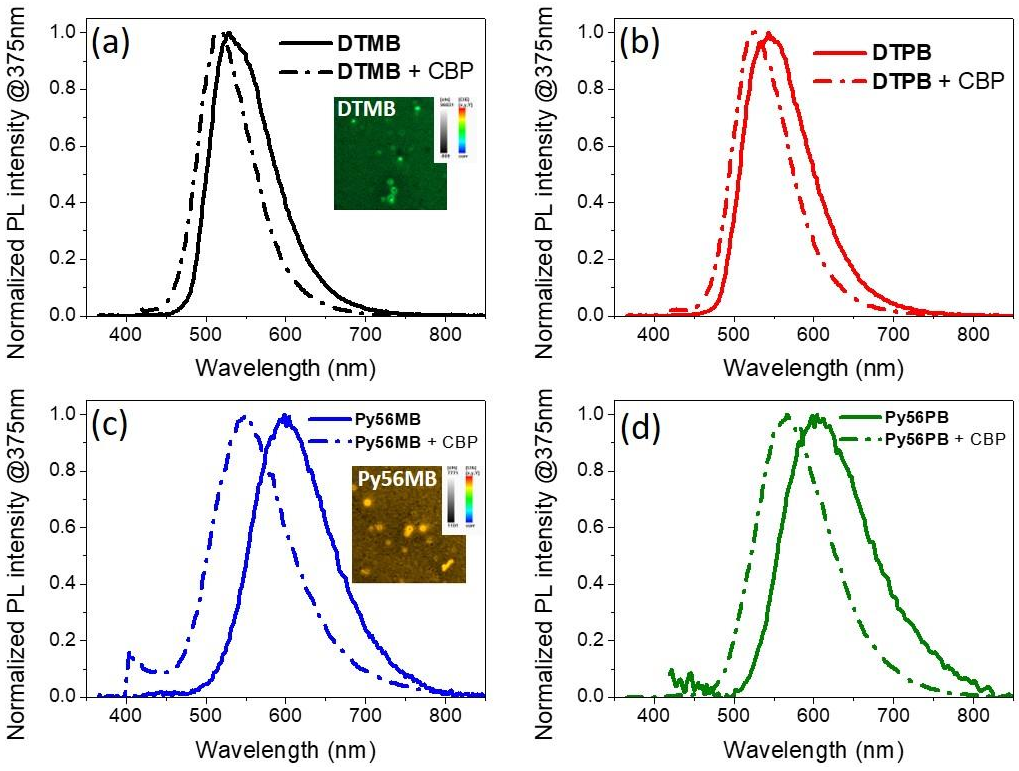

Figure 2-32. Photoluminescence spectra of (a) **DTMB**, (b) **DTPB**, (c) **Py56MB** and (d) **Py56PB** in neat film or doped CBP film. Excited at 375 nm. The images in (a) and (c) are the confocal images of the aggregates of **DTMB** and **Py56MB** respectively.

Table 2-5. Summary of photophysical parameters of TADF neat films or doped in CBP films.

Molecule	λ_{PL}[film c] (nm)	Transient PL[d]					
		A_1	τ_1 (ns)	A_2	τ_2 (ns)	A_3	τ_3 (ns)
DTMB[a]	529	2.44	1.44	0.24	7.10	0.000877	150.78
DTMB:CBP[b]	519	0.90	4.10	0.30	16.66	0.00307	475.67
DTPB[a]	543	2.50	1.46	0.24	7.23	0.000892	191.99
DTPB:CBP[b]	526	0.96	4.02	0.33	16.32	0.00370	485.95
Py56MB[a]	598	2.14	1.69	0.16	8.44	0.00119	127.36
Py56MB:CBP[b]	550	1.01	3.27	0.27	18.91	0.00468	274.97
Py56PB[a]	604	1.92	1.24	0.16	6.72	0.000865	114.94
Py56PB:CBP[b]	567	1.07	3.12	0.28	17.26	0.00364	295.55

[a] Deposited by TADF solutions (10^{-3}M) on glass substrates. [b] Deposited by TADF:CBP in THF solutions (10^{-3}M: 5×10^{-3}M) on glass substrates. [c] Excited at 375 nm. [d] Excited at 375 nm. The decay component was fitted with three exponential decay model as: $I(t) = A_1\times\exp(-t/\tau_1) + A_2\times\exp(-t/\tau_2) + A_3\times\exp(-t/\tau_3)$.

Figure 2-33a illustrates the architecture of electroluminescence (EL) devices, which are composed of ITO/ PEDOT: PSS/ TADF: CBP/ TPBi/ LiF/ Al, where the emitting layer,

which has been deposited in the process including 10^{-3} M THF solution, retains the TADF nano-vesicles. The turn-on voltage and maximum external quantum efficiency (EQE) for the devices were around 2.6 V to 2.8 V and maxed at 1.5% (**Figure 2-33b**). Furthermore, by comparing the CIE coordinates, the color change between PL and EL of **DTMB** and **DTPB** was found to be greater than that of **Py56MB** and **Py56PB** (**Figure 2-34**). The EQE of OLED devices incorporating self-assembled TADF luminophores reached a state that was 5 to 10 times greater than those systems with non-TADF chromophores.[1]

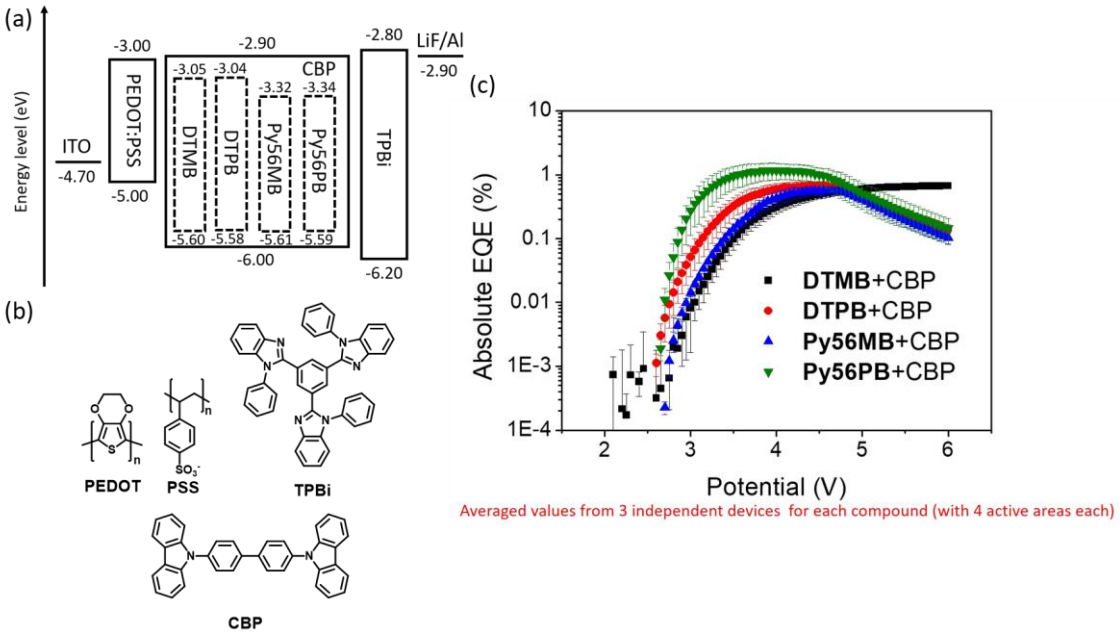

Figure 2-33. (a) Energy level diagram of EL device composed of TADF-based self-assembled materials. (b) Chemical structures of employed materials. (c) Potential vs. external quantum efficiency (EQE) plot for TADF-based EL devices.

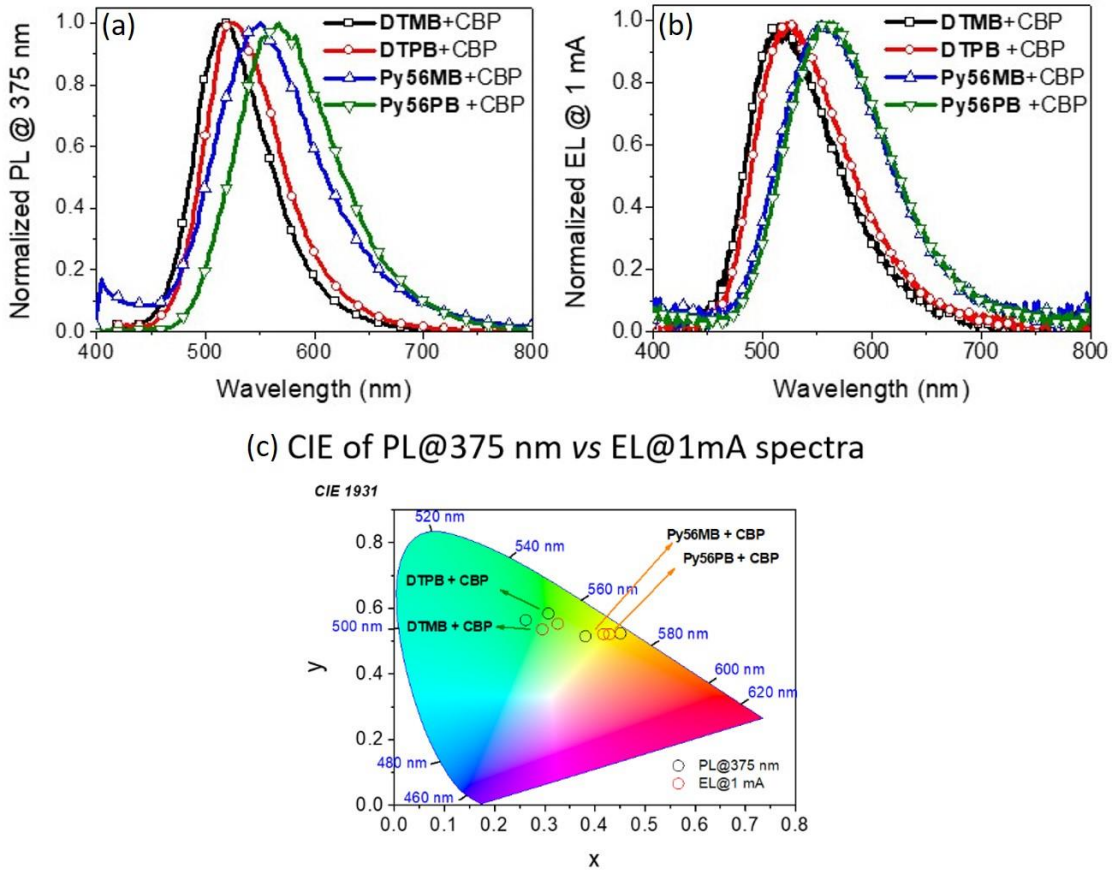

Figure 2-34. (a) PL and (b) EL spectra of TADF compounds doped in CBP film and (c) the chromaticity coordinates of each emission. Excited at 375 nm.

In developing future displays, micro-OLEDs fabricated using inkjet printing process are very attractive. In this manufacturing process, precise deposition at high resolution and minimal material waste can be advantageous for mass production of displays. By adapting the inkjet-printing process to deposit the emitting layer of TADF-materials, it becomes possible to fabricate high-resolution EL-devices with micron/sub-micron domain size while minimizing cross-contamination of nearby colors. Compared with the

TADF neat film, stronger PL and EL intensity of doped films fabricated by using TADF/CBP solution has proven to be a valid approach (**Figure 2-35**). In addition, the nanospheres of TADF materials remained intact in the form of droplets on the substrate, as observed using optical microscopy. The boundary of each droplet is well-defined and the EL-intensity at various positions could be observed by gradually increasing the voltage to 8 V, as well as the arrangement pattern of emitting regions in the active area of the EL devices (**Figure 2-36**).

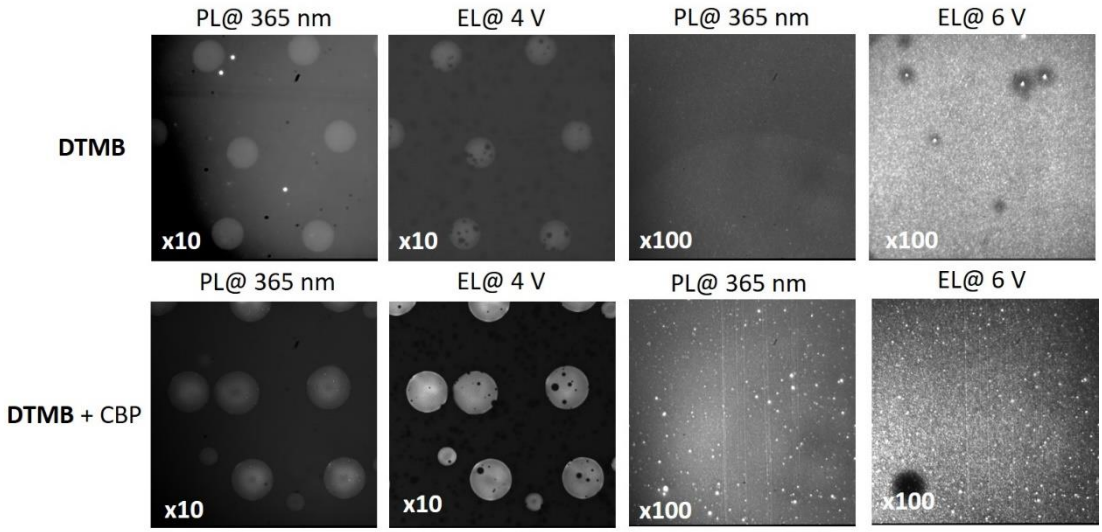

Figure 2-35. Confocal images of PL (λ_{ex} = 365 nm) and EL emission on **DTMB** or **DTMB**/CBP film deposited by ink-jet printing in 10^{-4} M THF/chlorobenzene solution (0.1/0.9, v/v).

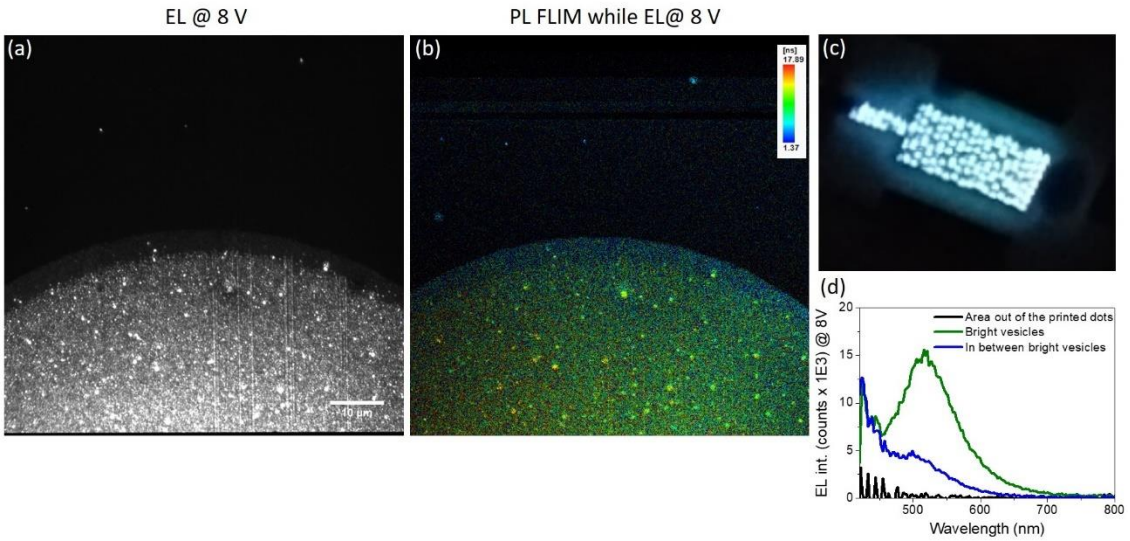

Figure 2-36. Confocal images of EL (a) and PL (b) emission (λ_{ex} = 365 nm) on **DTMB**/CBP film deposited by ink-jet printing process in 10^{-4} M THF/chlorobenzene solution (0.1/0.9 vol.). Scale bar = 10 μm. (c) Microscopic image of active area in EL device with ink-jet printed film. (d) EL spectrum of different emission regions in the microscope image.

2-10 Summary

In summary, the D-π-A type TADF chromophores self-assemble thanks to the presence of biuret motifs. The system has demonstrated the capability of tuning the emission spectrum by altering the energy gap between ground state and excited state using various electron-accepting moieties while retaining the spontaneous formation of the spherical aggregates. The homogeneous morphology of well-defined TADF vesicles in size range of 250 nm to 500 nm was evident from SEM, TEM and DLS analysis. In

addition, the PL spectra of different temperature and fluorescence decay profiles clearly showed that TADF properties contributed significantly to increase the luminescence efficiency. By introducing DMSO to the materials in solution, the TADF behavior disappeared. This is attributed to the dissolution of aggregates, which reduced the efficiency of the TADF process as demonstrated by the absence of quenching of the excited state by DMSO. From this, we may envisage that the supramolecular aggregation enhances TADF, presumably due to exciton hopping. Therefore, supramolecular gating of TADF was evidenced for this material. Furthermore, the photophysical parameters and the kinetic rate constant of TADF materials derived by Monkman's model were consistent with the small ΔE_{ST} determined from variable temperature experiments. The CFM experiments showed the presence of spherical aggregates with longer fluorescence lifetime due to TADF properties. The EL devices, which consisted of an emitting layer of the material doped inside a host CBP matrix, were shown to exhibit improved performance with external quantum efficiency of 1.5%, that was 5 to 10 times greater than the system without TADF materials. Moreover, the CFM images of the active layer deposited by ink-jet printing process show that the spherical aggregates remained intact with a notable increase in PL and EL intensity. The combined results evidence that the formation of spherical aggregates is quite robust and is compatible with the introduction of TADF chromophores as well as inkjet printing. This is an important result in

demonstrating both high-resolution and improved performance in EL devices. The proposed approach strategy provides an interesting strategy to fabricate future generation micro-OLED displays.

2-11 References

1 Tsai, Y. T.; Tseng, K. P.; Chen, Y. F.; Wu, C. C.; Fan, G. L.; Wong, K. T.; Wantz, G.; Hirsch, L.; Raffy, G.; Guerzo, A. D.; Bassani, D. M. *ACS Nano* **2016**, *10*, 998.

2 Skurski, P.; Simons, J. *J. Chem. Phys.* **2001**, *115*, 10731.

3 Hubberstey, P.; Suksangpanya, U. *Hydrogen-bonded supramolecular chain and sheet formation by coordinated guanidine derivatives. Supramolecular Assembly via Hydrogen Bonds II*. (Springer, Berlin, Heidelberg, **2004**) 33-83.

4 Hughes, E. W.; Yakel, H. L.; Freeman, H. C. *Acta Crystallogr.* **1961**, *14*, 345.

5 Craven, B. M. *Acta Crystallogr.* **1973**, *29*, 1525.

6 Corbin, P. S.; Zimmerman, S. C.; Thiessen, P. A.; Hawryluk, N. A.; Murray, T. J. *J. Am. Chem. Soc.* **2001**, *123*, 10475.

7 Patel, B.N.; Prajapati, M.M. *Int. J. Sci. Res. Publ.* **2014**, *4*, 1.

8 Uoyama, H.; Goushi, K.; Shizu, K.; Nomura, H.; Adachi, C. *Nature* **2012**, *492*, 234.

9 Tsutsui, T.; Saito, S. *Organic Multilayer-Dye Electroluminescent Diodes: Is There Any Difference with Polymer LED?* (Kluwer, **1993**), 127.

10 Rothberg, L. J.; Lovinger, A. J. *J. Mater. Res.* **1996**, *11*, 3174.

11 (a) Tsutsui, T.; Aminaka, E.; Lin, C. P.; Kim, D.-U. *Philos. Trans. R. Soc. Lond. A* **1997**, *355*, 801. (b) Nowy, S.; Krummacher, B. C.; Frischeisen, J.; Reinke, N. A.;

Brütting, W. *J. Appl. Phys.* **2008**, *104*, 123109. (c) Brütting, W.; Frischeisen, J.; Schmidt, T. D.; Scholz, B. J.; Mayer, C. *Phys. Status Solidi A* **2013**, *210*, 44.

12 Parker, C. A.; Hatchard, C. G. *Proc. R. Soc. A: Math. Phys. Eng. Sci.* **1962**, *269*, 574.

13 Endo, A.; Ogasawara, M.; Takahashi, A.; Yokoyama, D.; Kato, Y.; Adachi. C. *Adv. Mater.* **2009**, *21*, 4802.

14 Sato, K.; Shizu, K.; Yoshimura, K.; Kawada, A.; Miyazaki, H.; Adachi, C. *Phys. Rev. Lett.* **2013**, *110*, 247401.

15 Wong, M. Y.; Zysman-Colman, E. *Adv. Mater.* **2017**, *29*, 1605444.

16 Im, Y.; Kim, M.; Cho, Y. J.; Seo, J. A.; Yook, K. S.; Lee, J. Y. *Chem. Mater.* **2017**, *29*, 1946.

17 Liu, Y.; Li, C.; Ren, Z.; Yan, S.; Bryce, M. R. *Nat. Rev. Mater.* **2018**, *3*, 1.

18 Lin, T.; Chatterjee, T.; Tsai, W.; Lee, W.; Wu, M.; Jiao, M.; Pan, K.; Yi, C.; Chung, C.; Wong, K. T.; Wu, C. C. *Adv. Mater.* **2016**, *28*, 6976.

19 Li, S. W.; Yu, C. H.; Ko, C. L.; Chatterjee, T.; Hung, W. Y.; Wong, K. T. *ACS Appl. Mater. Interfaces* **2018**, *10*, 12930.

20 Woon, K. L.; Yi, C. L.; Pan, K. C.; Etherington, M. K.; Wu, C. C.; Wong, K. T.; Monkman, A. P. *J. Phys. Chem. C* **2019**, *123*, 12400.

21 Tsai, W. L.; Huang, M. H.; Lee, W. K.; Hsu, Y. J.; Pan, K. C.; Huang, Y. H.; Ting, H. C.; Sarma, M.; Ho, Y. Y.; Hu, H. C.; Chen, C. C.; Lee, M. T.; Wong, K. T.; Wu, C. C.

Chem. Commun. **2015**, *51*, 13662.

22 Pan, K. C.; Li, S. W.; Ho, Y. Y.; Shiu, Y. J.; Tsai, W. L.; Jiao, M.; Lee, W. K.; Wu, C. C.; Chung, C. L.; Chatterjee, T.; Li, Y. S.; Wong, K. T.; Hu, H. C.; Chen, C. C.; Lee, M. T. *Adv. Funct. Mater.* **2016**, *26*, 7560.

23 Fang, F.-C.; Chu, C.-C.; Huang, C.-H.; Raffy, G.; Del Guerzo, A.; Wong, K.-T.; Bassani, D. M. *Chem. Commun.* **2008**, 6369.

24 Plater, M. J.; Sinclair, J. P.; Aiken, S.; Gelbrich, T.; Hursthouse, M. B. *Tetrahedron* **2004**, *60*, 6385.

25 Ishiyama, T.; Miyaura, N. *J. Organomet. Chem.* **2000**, *611*, 392.

26 Tseng, K. P.; Fang, F. C.; Shyue, J. J.; Wong, K. T.; Raffy, G.; Del Guerzo, A.; Bassani, D. M. *Angew. Chem. Int. Ed.* **2011**, *50*, 7032.

27 Reichardt, C.; Welton, T. *Solvents and solvent effects in organic chemistry.* (John Wiley & Sons, Weinheim, **2011**)

28 Baleizão, C.; Berberan-Santos, M. N. *J. Chem. Phys.* **2007**, *126*, 204510.

29 Dias, F. B.; Penfold, T. J.; Monkman, A. P. *Methods Appl. Fluoresc.* **2017**, *5*, 012001.

30 Baleizao, C.; Berberan-Santos, M. N. *ChemPhysChem.* **2011**, *12*, 1247.

31 Berberan-Santos, M. N.; Garcia, J. M. M. *J. Am. Chem. Soc.* **1996**, *118*, 9391.

32 Velu, S. K. P.; Yan, M.; Tseng, K.-P.; Wong, K.-T.; Bassani, D. M.; Terech, P. *Macromolecules*, **2013**, *46*, 1591.

33 Hsieh, Y. Y.; Sánchez, R. S.; Raffy, G.; Shyue, J. J.; Hirsch, L.; Guerzo, A. D.; Wong, K. T.; Bassani, D. M. *Chem. Commun.* **2022**, *58*, 1163.

Chapter 3. Investigation of CPL-Based Self-Assembled Materials

3-1 Introduction of Circularly Polarized Luminescence (CPL)

For a single photon, two circular polarization states, left- and right-circular polarization, are possible.[1] When the wave packet propagates towards the observer, the associated electric and magnetic vectors describe a clockwise helix in the right circular polarization state and vice versa.[2] Therefore, circular polarization confers chiral character to a beam of light owing to the helical chirality associated to the corresponding propagation mode. The growing interest of circularly polarized luminescence is mostly due to the added information provided by the polarization state, which allows the development of smarter photonic materials for advanced technologies, such as 3D displays,[3,4] information storage and processing,[5-7] and communication of spin information (spintronics-based devices).[8-10] At present, flat panel displays fabricated from OLEDs require a polarizer and a quarter-wave plate to produce CPL (**Figure 3-1**).[11] However, this leads to a minimum 50% energy loss compared to the unpolarized light source.[12] In the case of organic light-emitting diodes incorporating materials capable of emitting circularly polarized (CP-OLEDs), one may envision that circularly polarized electroluminescence can be extracted with better energy efficiency.[13,14]

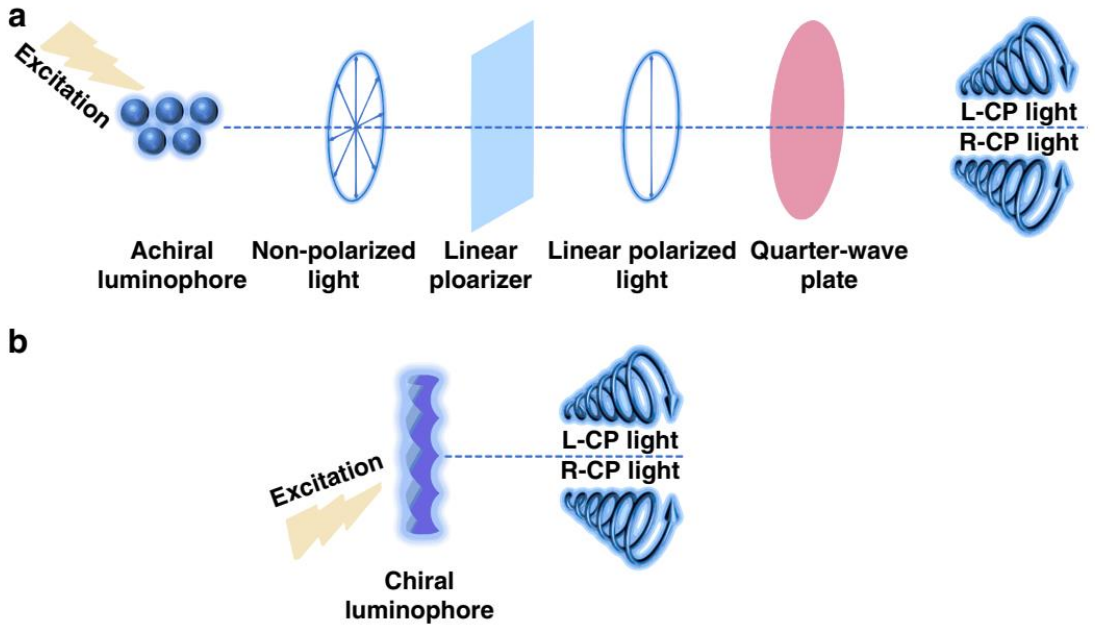

Figure 3-1. Methods for generating circular polarized light. (a) Physical method. (b) Circularly polarized luminescence. Reused with permission from ref 11. Copyright 2021 Springer Nature.

The level of CPL is quantified by the luminescence dissymmetry factor (g_{lum}), as defined in **Equation 3-1**. The values of g_{lum} are found between –2 and +2, representing purely right- and left-polarized luminescence, respectively. So far, the highest level of CPL have been achieved from chiral lanthanide complexes, which typically exhibit $|g_{lum}|$ values within the range of 0.05-0.5.[15] Unfortunately, these complexes often exhibit low quantum yields owing to the forbiddenness of the electronic transition.[16] Hence, the development of chiral organic molecules able to emit CPL with both a large g_{lum} value and a high emission yield is a major objective in the photonics field.

$$g_{lum} = \frac{l_L - l_R}{\frac{1}{2}(l_L + l_R)}$$ (**Equation 3-1**)

The g_{lum} of circularly polarized luminescence from organic small molecules (CPL-OSMs) are typically in the range of 10^{-3} to 10^{-5} owing to the intrinsic chirality of the molecular structures,[17] including point chirality,[18,19] axial chirality,[20,21] helical chirality[22-25] and planar chirality.[26-27] In the past decades, various strategies have been proposed to enhance the g_{lum}, such as self-assembled anisotropic aggregates,[28] aggregation-induced emission (AIE),[29] triplet-triplet annihilation (TTA),[30] Förster resonance energy transfer (FRET)[31] and doping in liquid crystals.[32] In 2019, Campbell *et al.* reported a CP-OLEDs in which the combination of an achiral polymers and chiral helicene derivatives additives showed interesting chiroptical properties with g_{EL} of 1.10 from CPEL and switchable CPL signals by tuning the thickness of active layer. This record-breaking dissymmetry factor is still the best performance in CP-OLEDs until now.[33] In their exploration of the mechanism behind the impressive optical performance, the large chiroptical effects were found to result from the magneto-electric coupling (natural optical activity) rather than the intrinsic structural chirality resulting from the chiral dopants, along with the organization of the blue cylinder phase locally.[34]

Apart from the g_{lum}, the luminescence efficiency of CPL emitters is also important. Therefore, the incorporation of TADF processes, as illustrated in Chapter 2, is an attractive approach to enhance the luminescence efficiency of emitting materials by

harvesting triplet excitons. Circularly polarized TADF (CPTADF) emitters not only possess more intense luminescence thanks to their TADF properties but also emit right- or left-handed CP light, contributing to the interest in the fabrication of CP-OLEDs.[35-37] Recently, there have been two major strategies recommended for constructing CPTADF materials: chiral perturbation,[38] and chiral emitting skeleton (**Figure 3-2**).[39] The former one is based on the introduction of chiral moieties, for instance, axially chiral 1,1'-bi-2-naphthol (BINOL)[38] or chiral *trans*-1,2-diaminocyclohexane (DACH),[36] into a donor-acceptor structure. Although the synthesis of such CPTADF molecule is straightforward, the chiral unit is isolated and not involved in the charge transfer process of the TADF luminophore, which can lead to an inferior CPL chiroptical activity. The chiral emitting skeleton approach instead combines a chiral donor or acceptor in an emissive D-A structure. However, achieving TADF behavior in the chiral backbone along with high dissymmetry factors requires careful tuning.[39]

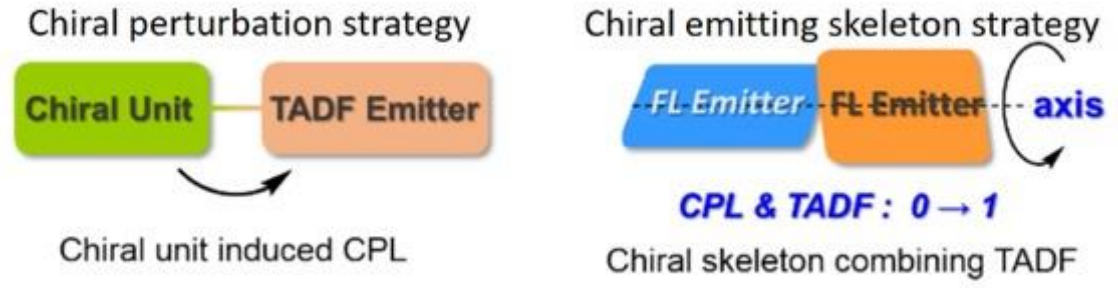

Figure 3-2. Design strategies of CP-TADF molecules. Reprinted with permission from ref 39. Copyright 2019 Wiley-VCH.

In 2013, Professor Kawai's group reported several methodologies for inducing the self-assembly of chiral CPL emitters composed of perylene bisimides and chiral binaphthalenes. These compounds were found to form aggregates possessing higher g_{lum} values than those of the individual components in solution (**Figure 3-3**).[28] This supramolecular enhancement of the dissymmetry factor, from 0.003 to 0.01, is associated with the ordered and regular arrangement of the individual chromophores. It is therefore possible to take advantage of the self-assembly behavior of chiral organic molecules with specific functional groups to improve the their chiroptical properties.

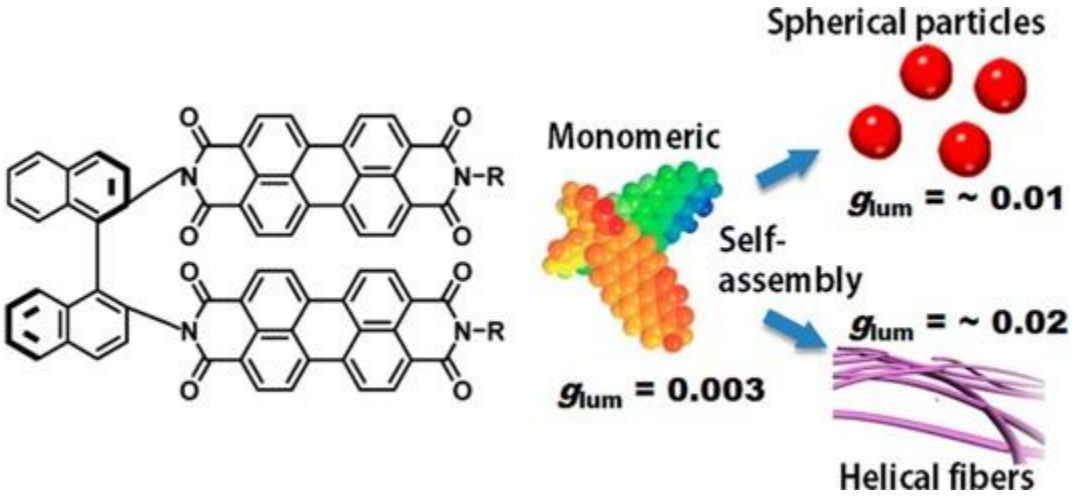

Figure 3-3. Self-assembly methodologies of enhancing dissymmetry factor of CPL. Reused with permission from ref 28. Copyright 2014 American Chemical Society.

3-2 Axially Chiral Binaphthalene-Based CPL Materials

3-2-1 Review of Binaphthalene-Based CPL Structures

The correlation between g_{abs} in CD and g_{lum} in CPL was analyzed by Mori and co-workers from reported CPL-OSM values for various categories of chiral organic molecules (**Figure 3-4**).[40,41] From the global analysis of the linear regression of all published g_{abs} and g_{lum}, they obtained a quantitative relationship that $|g_{lum}| = 0.81 \times |g_{abs}|$ ($r = 0.60$), showing the proportional connection between the dissymmetry factors in CD and CPL spectra. Taking a closer look, the proportionality constant relating g_{abs} and g_{lum} depends on the class of chiral structures, and can vary from 0.93 for binaphthyls, to 0.99 for cyclophanes, and 0.61 for helicenes. In other words, for binaphthyls and cyclophanes with high g_{abs}, we could expect CPL with a high g_{lum}. In addition, the same authors summarized the correlation between g_{lum} and photoluminescence quantum yield (Φ_{lum}) as well. Although there is no significant correlation between g_{lum} and Φ_{lum}, one can still identify specific relationships based on the categories of chiral molecules. For example, the helicene derivatives with helical chirality reveal moderate to large dissymmetry factors (10^{-3} to 10^{-2}) in CPL spectra but with lower luminescence (< 30%). On the other hand, binaphthyl derivatives with axial chirality show high Φ_{lum} (> 60%) and low to moderate g_{lum} (10^{-4} to 10^{-3}), resulting in promising potential application for CP-OLEDs. Consequently, to balance between g_{lum} and Φ_{lum}, we would like to take advantage of the

axial chirality in binaphthalene derivatives to design the eligible CPL emitters for circularly polarized displays.

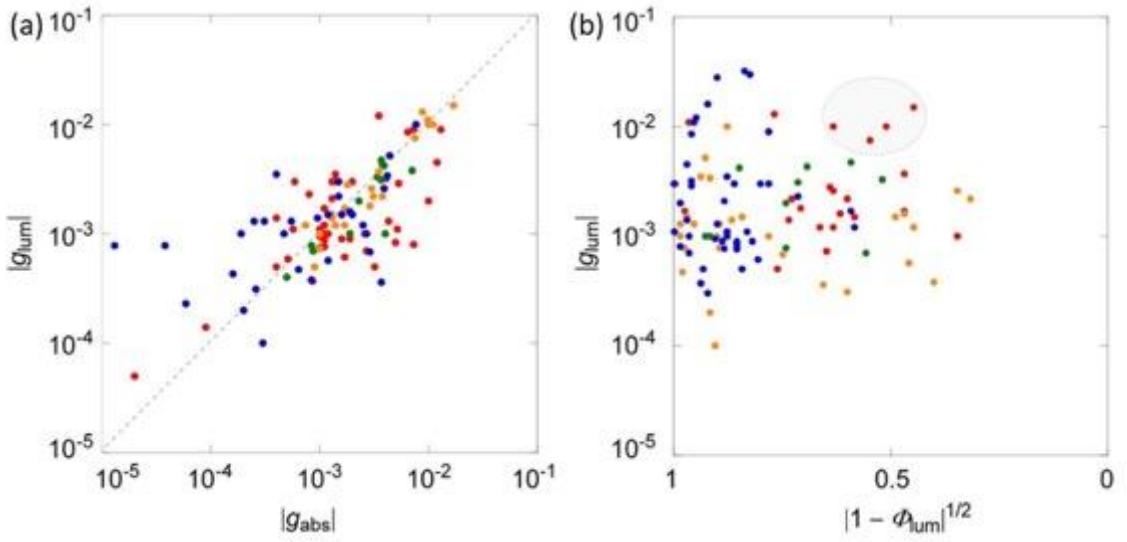

Figure 3-4. (a) Log-log plot between luminescence (g_{lum}) and absorption (g_{abs}) dissymmetry factors. (b) Semi-log plot between g_{lum} and $(1 - \Phi_{lum})^{1/2}$. Blue, helicene derivatives; red, cyclophane derivatives; orange, binaphthyl derivatives; green, BODIPY derivatives. Reused with permission from ref 41.

3-2-2 Molecular Design and Synthesis

Starting from asymmetric binaphthalene fluorophores with axial chirality, we may instill biuret motifs to induce the formation of self-assembled microstructures and expect that the ordered morphology could help enhance the g_{lum} in the CPL spectra (**Figure 3-5**). The chemical structures of six target molecules are shown in **Figure 3-6**. To investigate systematically the effect of the open and bridged forms of the central BINAP

chromophore on the chiroptical properties, we designed **BNPB**, **7BBNPB** and **8BBNPB** for comparison. In addition, for **BNBTPB** and **7BBNBTPB**, we extended the π-conjugation length by introducing benzothiadiazole moieties with the aim to tune the emission color from deep-blue to green-yellow. Previously, Pieters *et al.* investigated binaphthalene-based green CPTADF emitters using the chiral perturbation strategy and showed that they possess high PLQY of 74% in toluene solution and moderate g_{lum} of 1.3×10^{-3} in CPL.[38] Therefore, we modified the chemical structure to link biuret motif to fluorophore to obtain **BNCNCzPB** with the aim to demonstrate CPL and TADF characteristic in the self-assembled vesicles.

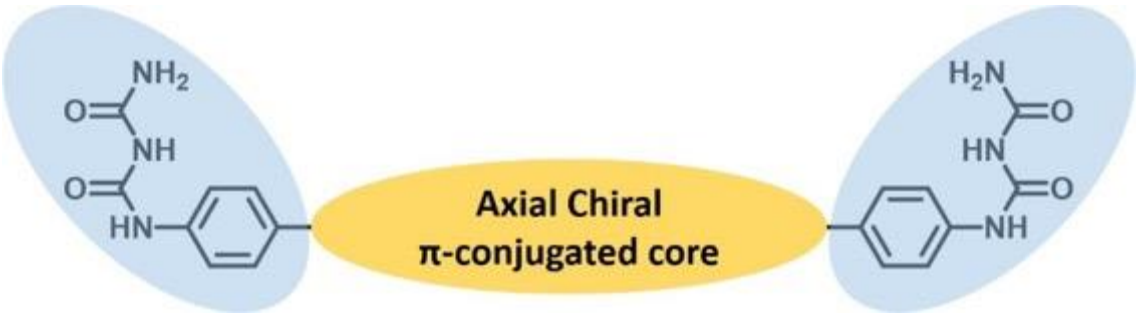

Figure 3-5. Schematic representation of binaphthalene-based self-assembled molecules.

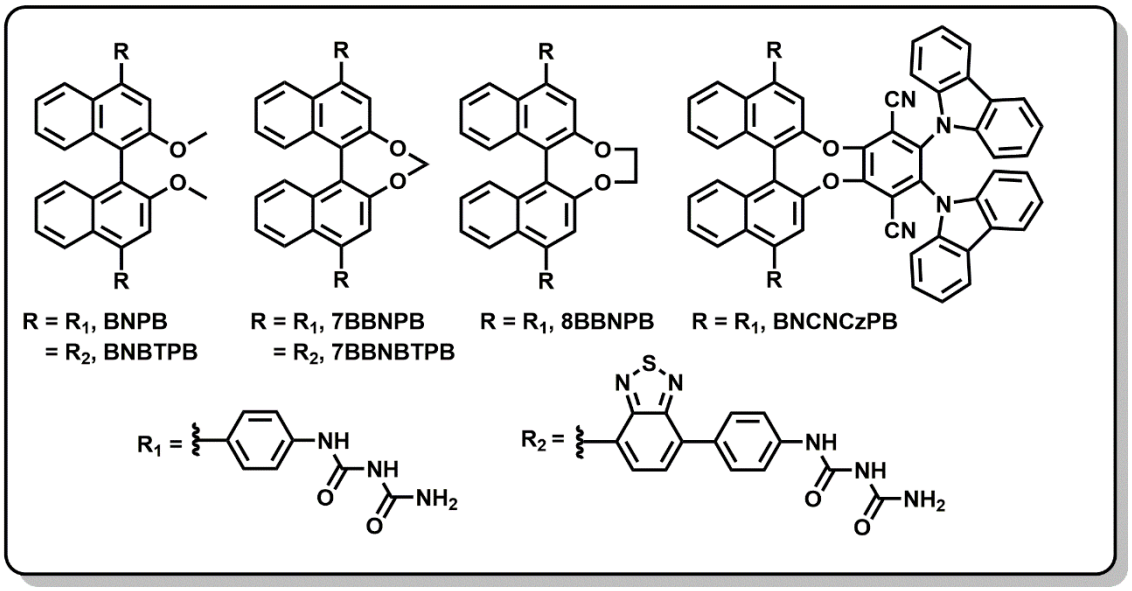

Figure 3-6. Molecular design with binaphthalene-based self-assembled systems.

As shown in **Scheme 3-1**, bromination of 1-naphthylamine gave intermediate **2** in high yield. Next, the aryl amine **2** was converted to the diazonium salt **3** through a Sandmeyer reaction. Reduction of compound **3** by sodium hydride to remove nitrogen afforded monomer **4**. The latter led to the preparation of racemic mixtures of dimers **BNOH** by copper-catalyzed oxidative coupling.[42] To obtain enantiopure compounds, (1S)-(+)-10-camphorsulfonyl chloride was used as a chiral resolving agent and the diastereomeric pairs were separated using silica chromatography. After hydrolysis using sodium hydroxide, the chiral intermediates (R)-**BNOH** and (S)-**BNOH** were obtained.[43]

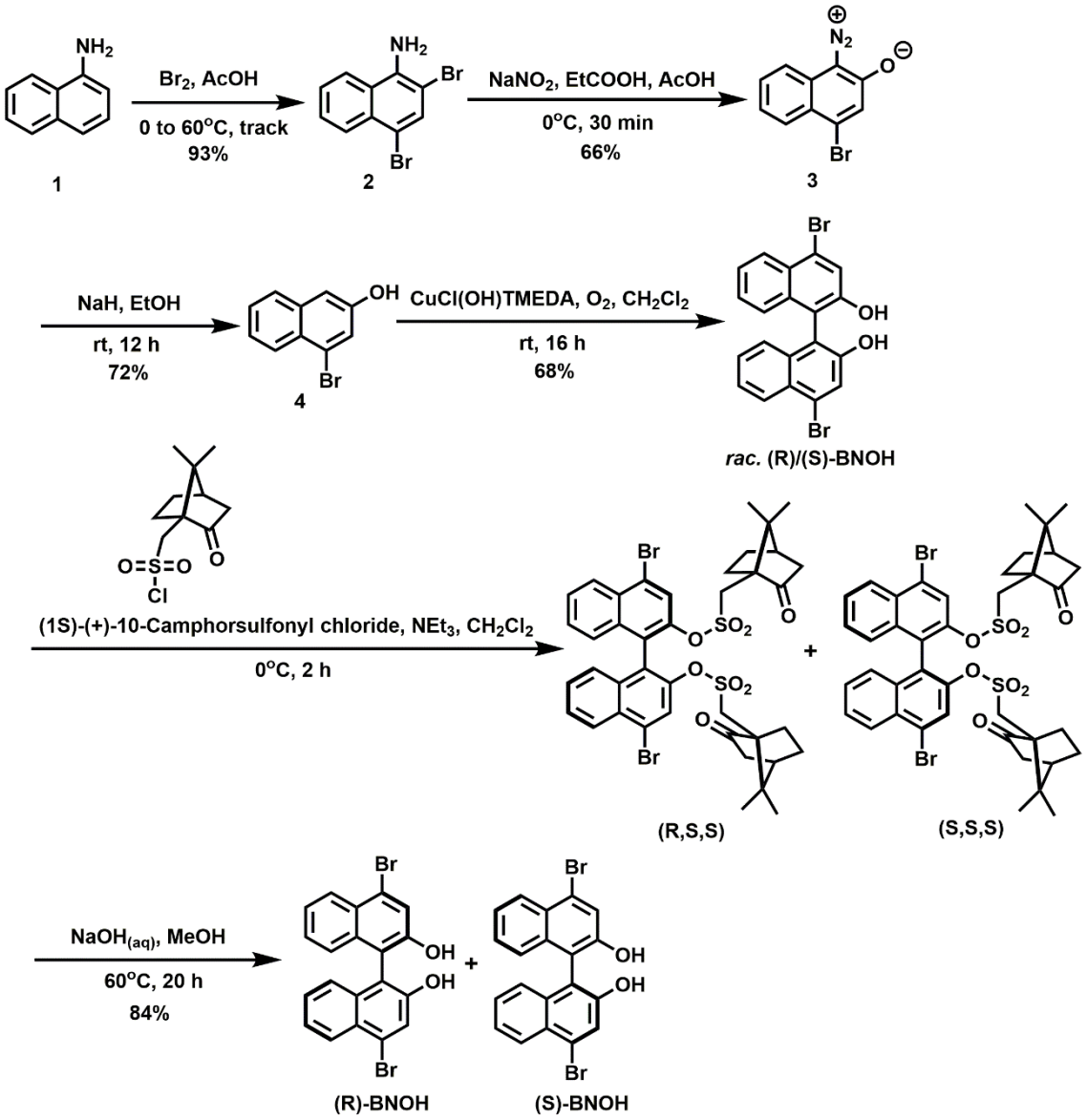

Scheme 3-1. Synthetic pathways of chiral resolution of optically active **BNOH**.

As shown in **Scheme 3-2**, compound **BNOH** was converted to **BNOMe** using methyl iodide, followed by palladium-catalyzed Suzuki-Miyaura coupling with **PBBiuret** to collect target molecule **BNPB**. For the bridged forms,[44,45] the bisdiol was linked by methylene or ethylene groups to lock the axial chiral conformation via an S_N2

reaction, followed by palladium-mediated Suzuki-Miyaura coupling with **PBBiuret** to produce **7BBNPB** and **8BBNPB**. For the two yellow emitters, **BNOMe** or **7BBNBr2** were treated with bis(pinacolato)diboron by palladium-catalyzed reaction overnight to collect the corresponding boronic acid derivatives. These were then reacted with **BTBiuret** through Suzuki-Miyaura coupling to obtain **BNBTPB** and **7BBNBTPB**.

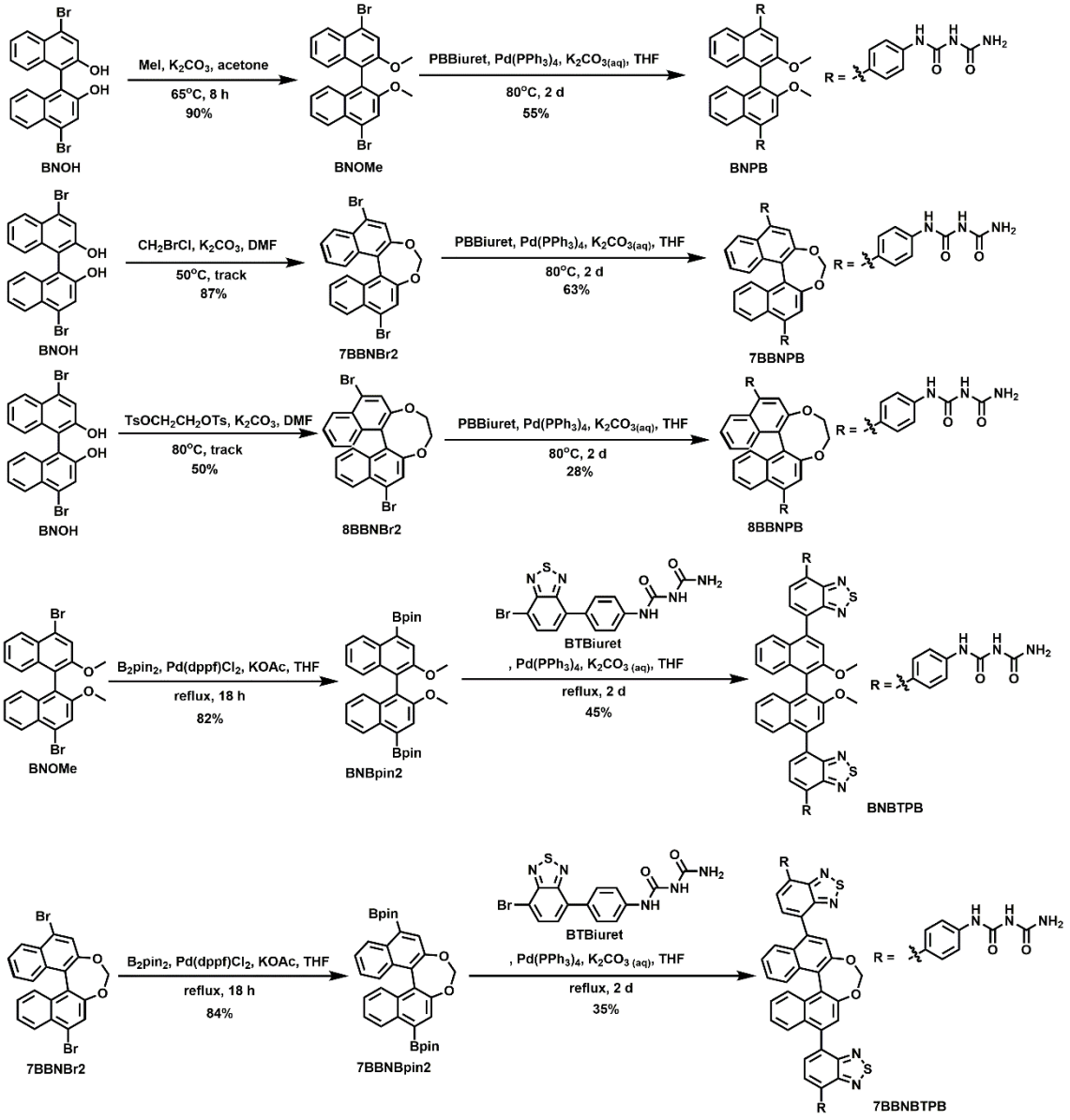

Scheme 3-2. Synthetic pathways and structures of binaphthalene-based molecules.

For **BNCNCzPB**, the key intermediate **BNOH** underwent two S_NAr reactions with tetrafluoroterephthalonitrile and carbazole in a one-pot procedure to afford **BNCNCzBr2**.[38] Then, the target compound **BNCNCzPB** was be obtained by Pd(0)-mediated Suzuki-Miyaura coupling with **BNCNCzBr2** and **PBBiuret** (**Scheme 3-3**).

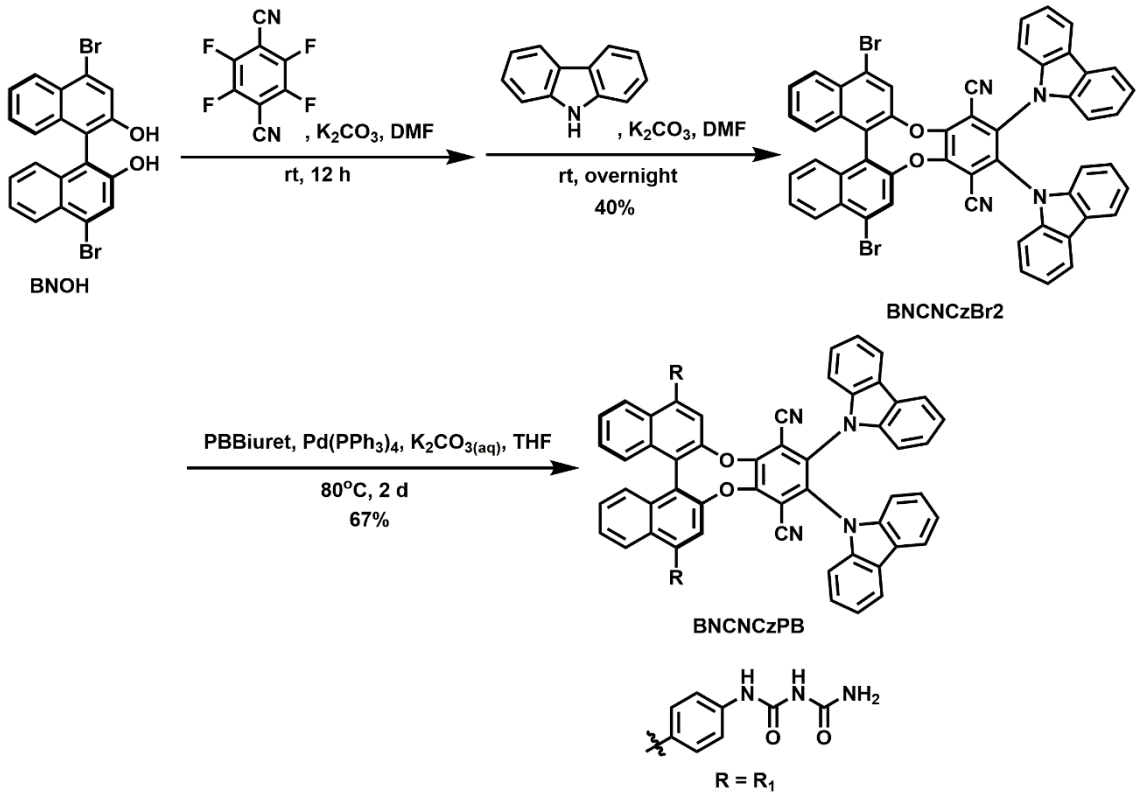

Scheme 3-3. Synthetic pathways and structure of **BNCNCzPB**.

3-2-3 Characterization of Nanostructures

To characterize the nanostructures formed by the BN series of molecules, the morphologies of the self- assembled aggregates were observed by SEM upon deposition

on SiO_2 substrates and shown in **Figures 3-7** to **3-12**. For all six molecules, uniform and well-defined nanospheres in the size of 200-500 nm in acetone or methanol solutions were observed. However, when drop-cast from a THF environment, the compounds exhibit greater morphological variety and would organize into various nanostructures, such as vesicles (**BNPB**, **7BBNPB**, **BNBTPB** and **BNCNCzPB**), films (**7BBNBTPB**) or clusters (**8BBNPB**).

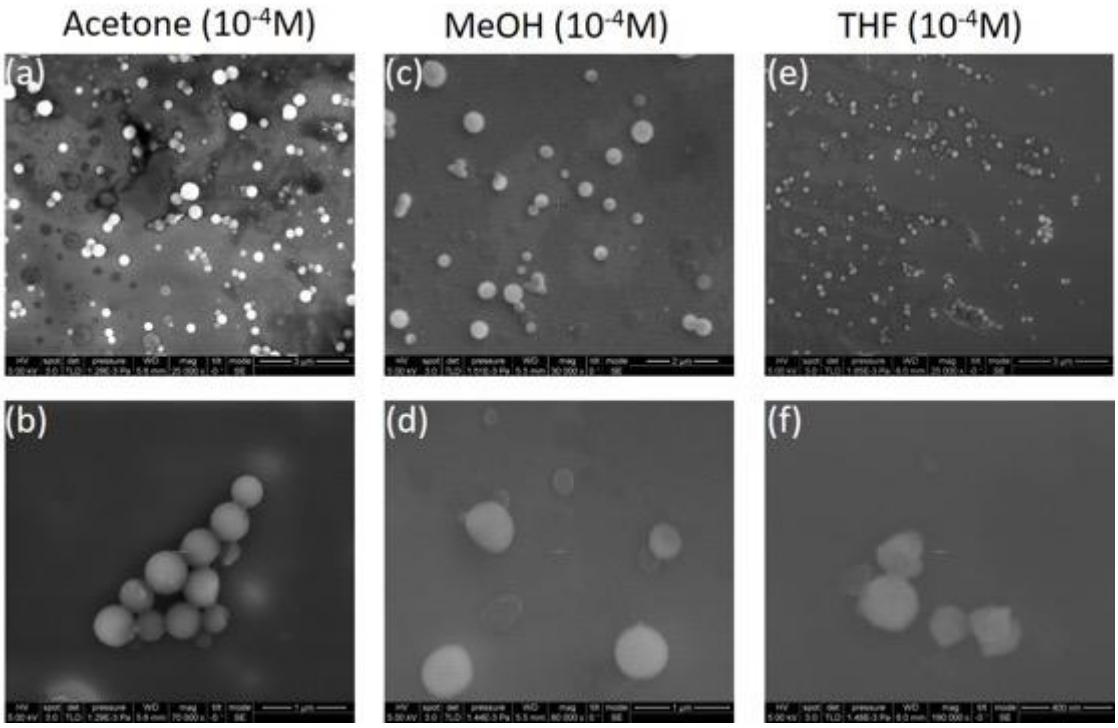

Figure 3-7. SEM images of **BNPB** in (a,b) acetone, (c,d) methanol and (e,f) THF solutions (10^{-4}M). Scale bar = 5 μm for (e), 2 μm for (a)(c), 1 μm for (b)(d) and 0.5 μm for (f).

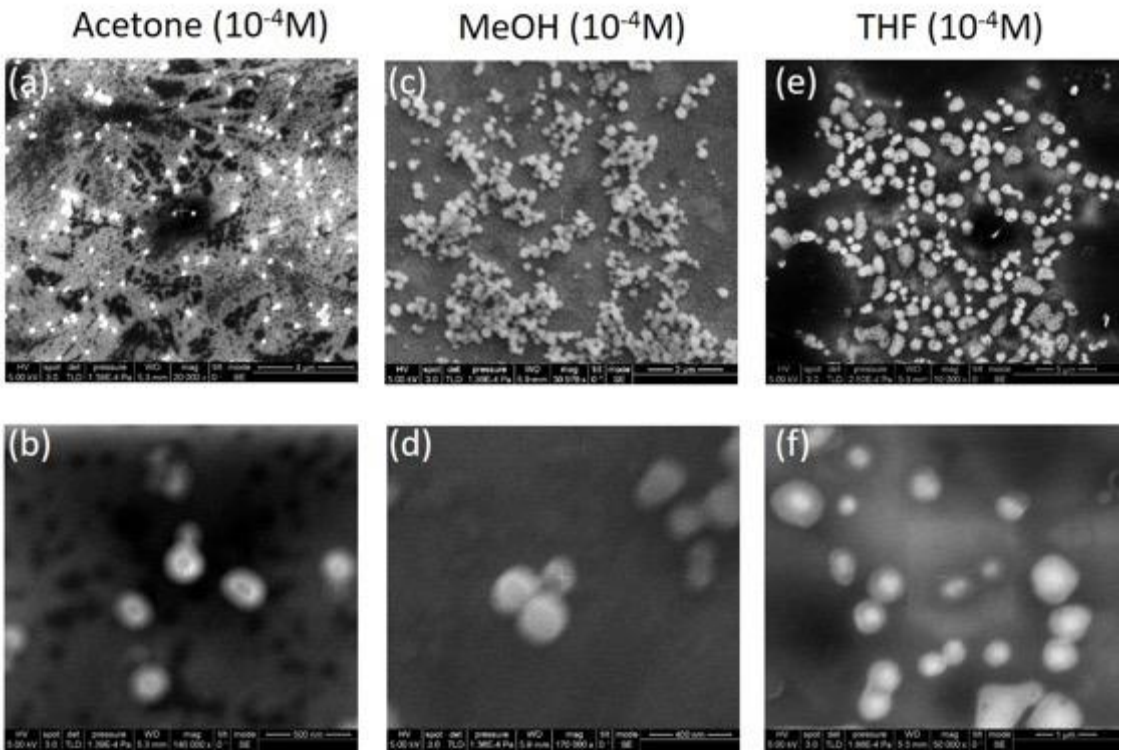

Figure 3-8. SEM images of **7BBNPB** in (a,b) acetone, (c,d) methanol and (e,f) THF solutions (10^{-4}M). Scale bar = 4 μm for (a), 2 μm for (c)(e), 1 μm for (f) and 0.5 μm for (b)(d).

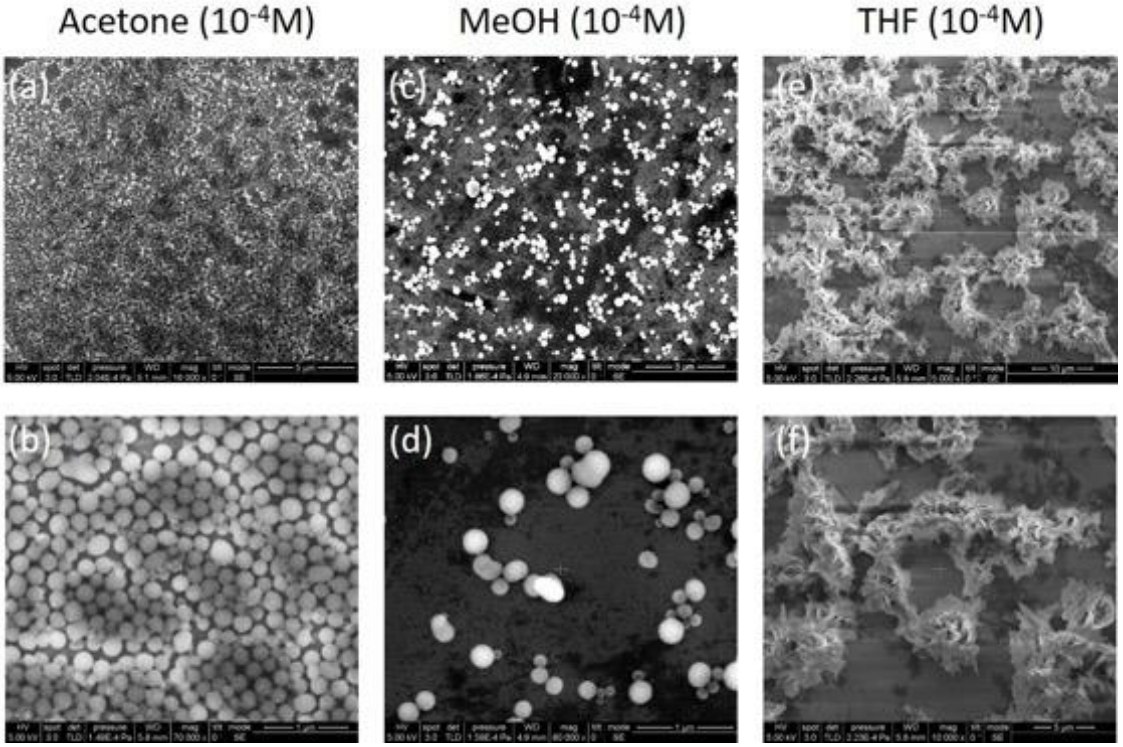

Figure 3-9. SEM images of **8BBNPB** in (a,b) acetone, (c,d) methanol and (e,f) THF solutions (10^{-4}M). Scale bar = 10 μm for (e), 5 μm for (a)(c)(f), 1 μm for (b)(d).

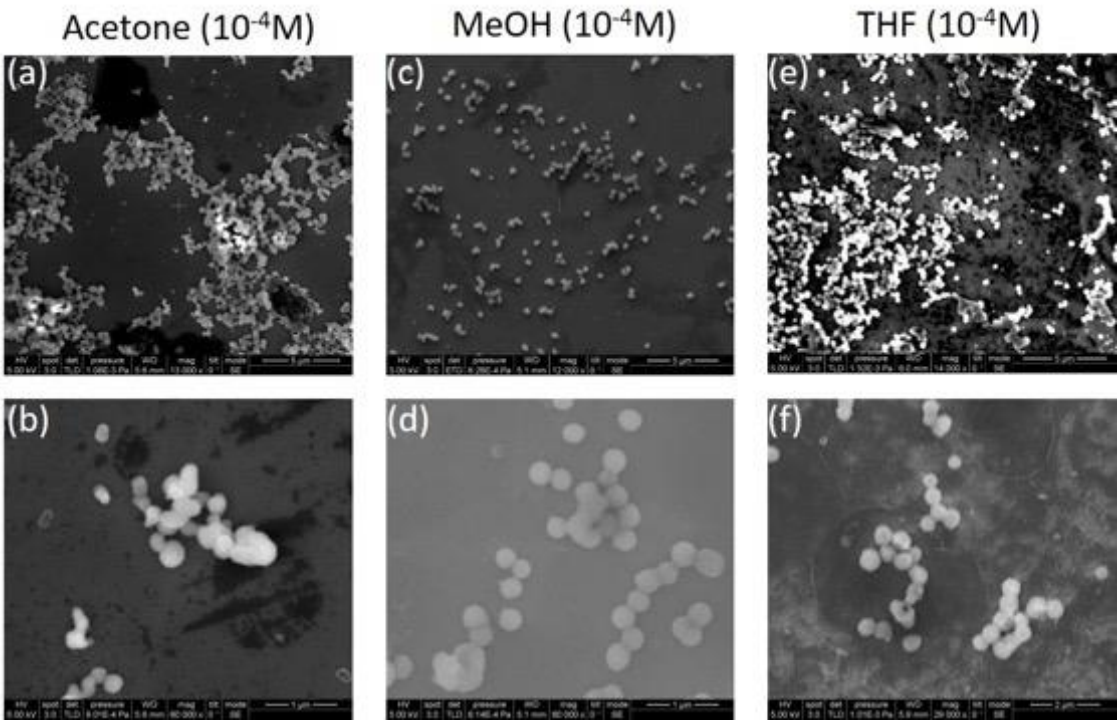

Figure 3-10. SEM images of **BNBTPB** in (a,b) acetone, (c,d) methanol and (e,f) THF solutions (10^{-4}M). Scale bar = 5 μm for (a)(c)(e), 2 μm for (f) and 1 μm for (b)(d).

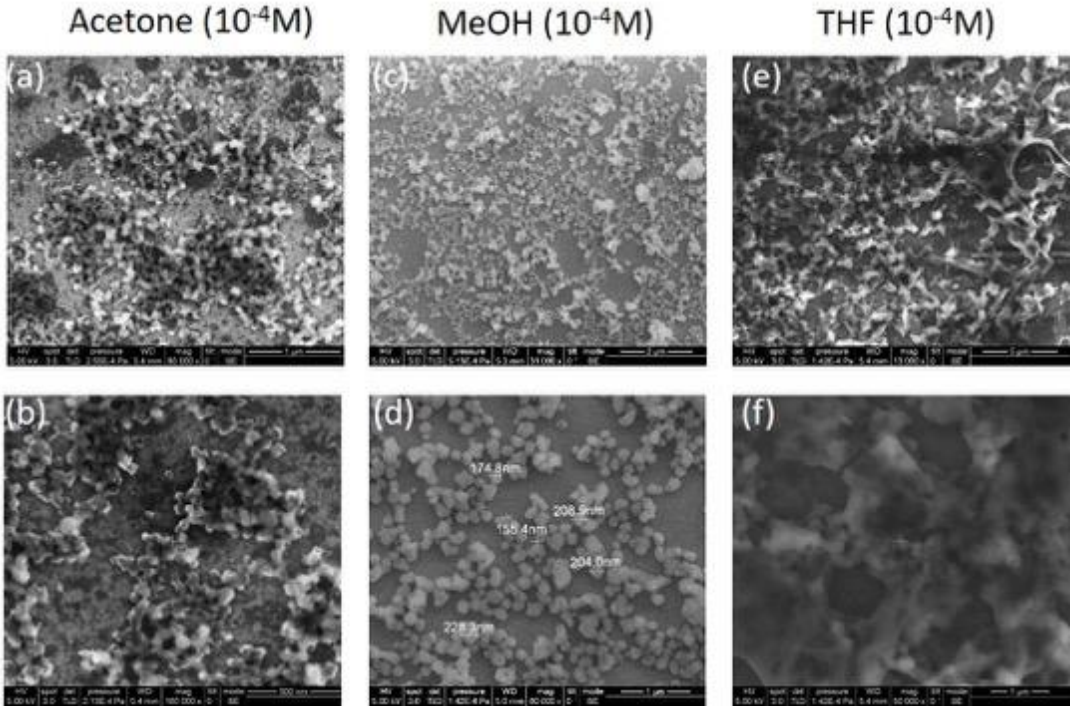

Figure 3-11. SEM images of **7BBNBTPB** in (a,b) acetone, (c,d) methanol and (e,f) THF solutions (10^{-4}M). Scale bar = 5 μm for (e), 2 μm for (c), 1 μm for (a)(d)(f) and 0.5 μm for (b).

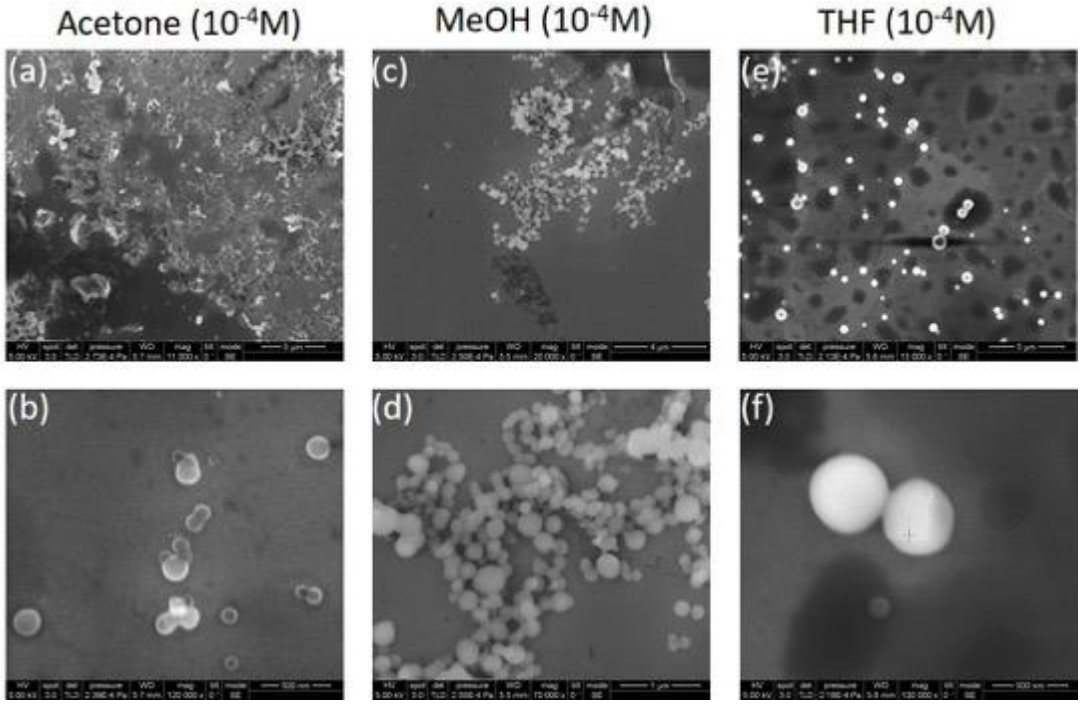

Figure 3-12. SEM images of **BNCNCzPB** in (a,b) acetone, (c,d) methanol and (e,f) THF

solutions (10^{-4}M). Scale bar = 4 μm for (a)(c)(e), 1 μm for (d) and 0.5 μm for (b)(f).

3-2-4 Photophysical Properties

As shown in **Figure 3-13** and summarized in **Table 3-1**, all the binaphthalene-based compounds possess a strong π-π* absorption band around 340 nm. Compared to unlocked chromophore **BNPB**, the locked **7BBNPB** shows a bathochromic shift in the emission wavelength attributed to the greater planarity enforced by the methylene bridge along with through-bond conjugation.[46-49] Indeed, compound **8BBNPB** with a longer and more flexible eight-member ring has similar excited state behavior as **BNPB**. The presence of an electron-accepting moiety (benzothiadiazole) extends the conjugation length of fluorophore. Thus, **BNBTPB** and **7BBNBTPB** have an absorption band near 400 nm and emission wavelengths near 530-550 nm vs. **BNPB** and **7BBNPB** which instead emit in the deep-blue. In contrast to the open-form **BNPB** (0.81), the closed forms **7BBNPB** (0.72) and **8BBNPB** (0.66) with less rigid structures lead to a decrease in in the photoluminescence quantum yield. Similarly, the introduction of benzothiadiazole results (0.28 of **BNBTPB** and 0.42 of **7BBNBTPB**) in a diminished photoluminescence efficiency.[50-52]

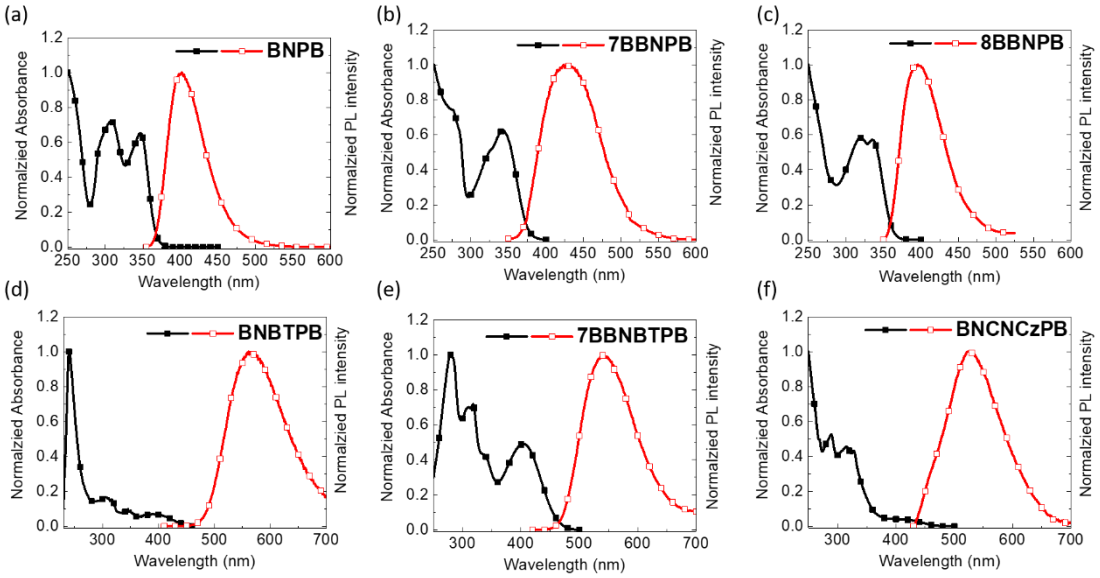

Figure 3-13. UV/Vis absorption and PL spectra of (a) **BNPB**, (b) **7BBNPB**, (c) **8BBNPB**, (d) **BNBTPB**, (e) **7BBNBTPB** and (f) **BNCNCzPB** in THF solutions (10^{-5}M). λ_{ex} =350 nm.

Table 3-1. Summary of photophysical properties of binaphthalene-based molecules.

Molecule	λ_{Abs} [a] (soln, nm)	ε^{a} (10^4 $M^{-1}cm^{-1}$)	λ_{PL} [soln] (THF, nm)	Φ_{THF} [b](%)
BNPB	307, 346	5.2, 4.1	402	81
7BBNPB	346	3.7	432	72
8BBNPB	335	5.3	396	66
BNBTPB	303, 344, 403	7.1, 3.3, 3.6	549	28
7BBNBTPB	318, 404	6.3, 4.1	538	42
BNCNCzPB	314, 328, 403	5.8, 5.1, 0.56	525	21 (28)[c]

[a] Measured in THF solution (10^{-5}M). [b] Fluorescence quantum yields were measured in aerated THF solutions (10^{-5}M), using an integration sphere coupled to a photonic

multichannel analyzer (Hamamatsu C9920). [c] Measured in aerated THF solutions (10^{-5}M), λ_{Ex} = 350 nm, using quinine sulfate in 0.105 M $HClO_4$ solution as standard.[53] Values in parentheses correspond to degassed solutions.

As depicted in **Figure 3-14**, **BNCNCzPB** exhibits an intense π-π* absorption band in the ultraviolet region and a weaker intramolecular charge-transfer band around 400 nm. The photoluminescence efficiency of this green-yellow emitter is increased from 21% to 28% in THF solutions after degassing, suggesting no or modest contribution from the triplet manifold. To verify the TADF character in **BNCNCzPB**, we take advantage of variable-temperature photoluminescence spectra to observe the thermal rISC of the triplet excitons. However, the PL intensity in degassed THF solution is enhanced upon decreasing temperature. Therefore, the TADF character is absent in the **BNCNCzPB** in THF solution. In agreement with this, the transient photoluminescence spectra of **BNCNCzPB** in THF or toluene solution at room temperature only evidences a short-lived contribution at around 20 ns. Furthermore, we dissolved **BNCNCzPB** in degassed 2-methyltetrahydrofuran solution (5 μM) to compare the fluorescence spectra in 77 K and 300 K. In contrast to the broad and structureless emission band in 300 K, the spectra in 77 K shows hypsochromic shift from 525 to 475 nm and vibronic fine structure, which suggest that the intramolecular charge transfer state collapses to a localized emitting state. Unfortunately, it was not possible to acquire the phosphorescence spectrum in view of

determining the energy of the triplet state. The situation is different for **BNPB**: Upon lowering the temperature to 77K, the broad PL emission centered at 387 nm is replaced by a structured emission at 540 nm. The latter is assigned to phosphorescence emission from the triplet state. Thus, the introduction of phenyl-biuret motifs at 4- and 4'- of the binaphthalene chromophore results in a significant decrease of the energy of the triplet state. It is therefore likely that **BNCNCzPB**, with the same skeleton to **BNPB**, possesses a lower triplet energy which will inefficiently undergo thermal rISC for emitting delayed fluorescence.

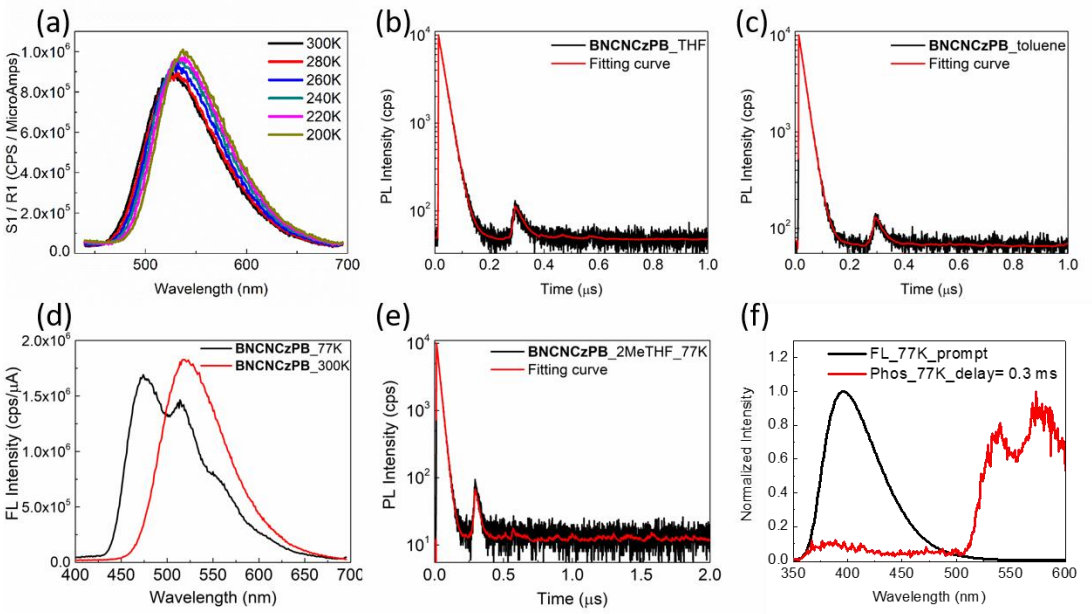

Figure 3-14. (a) Variable temperature PL spectra of **BNCNCzPB** in THF solution (10^{-5}M). λ_{ex} =350 nm. Transient PL spectra of **BNCNCzPB** in degassed (b) THF or (c) toluene solution at 300 K. λ_{ex} =370 nm (d) PL spectra and (e) transient PL spectra of **BNCNCzPB** in degassed 2-methyltetrahydrofuran solution (5 μM) at 77 K and 300K. λ_{ex}

=350 nm for (d) and 370 nm for (e). (f) PL and phosphorescence spectra of **BNPB** in toluene solution (10^{-5}M) at 77 K. The phosphorescence spectrum is acquired after a 0.3 ms delay. λ_{ex} =320 nm.

3-2-5 Chiroptical Properties

To investigate the chiroptical properties of the BN series of compounds, we used CD and CPL spectra to analyze the relationship between photophysical behavior and chirality in the ground and excited states (**Figure 3-15**). For most of the emitters, near-perfect mirror-image relationship for the enantiomers was observed.[54-56] The R**BNPB** exhibits negative Cotton effect in the long-wavelength region, while other blue emitters (R**7BBNPB** and R**8BBNPB**) and green-yellow emitters R**BNBTPB**, R**7BBNBTPB** and R**BNCNCzPB** reveal positive Cotton effects in the long-wavelength region. As the number of methylene units bridging the two naphthyl groups increases, the CD intensity first increases, and then decreases. This can be rationalized by considering the restricted torsional motion of the C–C bond joining the two naphthyl groups which is expected to be smallest for the single methylene spacer and larger in the absence or presence of the longer tethers.[47, 57-60] In comparison with open form, R**BNPB** and bridged R**7BBNPB**, the cisoid conformation leads to 3-fold enhancement of the $|g_{abs}|$ value from 6.0×10^{-4} to 1.7×10^{-3}; however, when the number of carbon atoms is increased to two, $|g_{abs}|$ is reduced

to 8.8×10^{-4} owing to its more flexible structure. As for the green-yellow emitters (R**BNBTPB**, R**7BBNBTPB** and R**BNCNCzPB**), they all have similar CD intensities and their $|g_{abs}|$ values are around 10^{-4}.

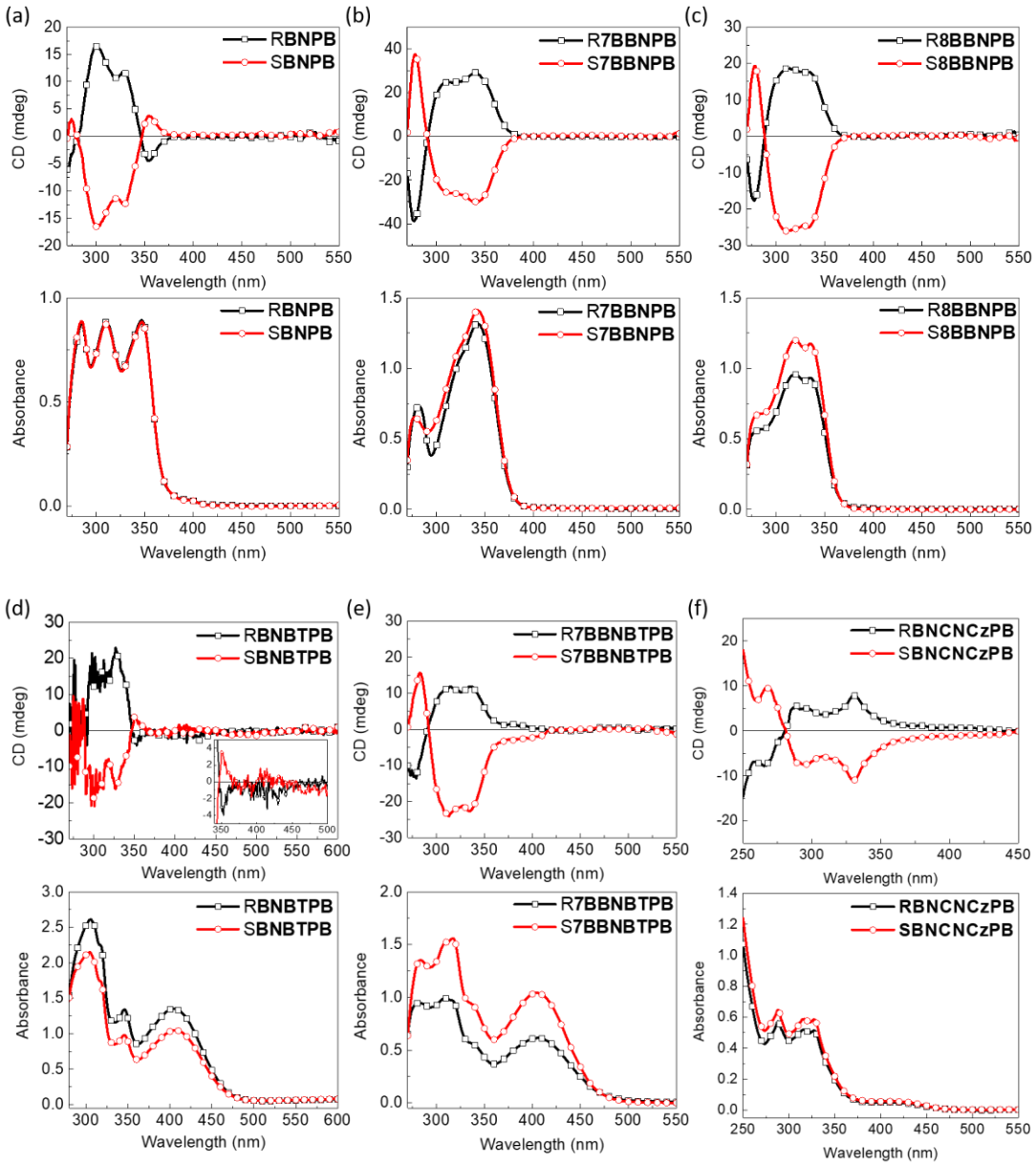

Figure 3-15. CD spectra of (a) R/S-**BNPB**, (b) R/S-**7BBNPB**, (c) R/S-**8BBNPB**, (d) R/S-**BNBTPB**, (e) R/S-**7BBNBTPB** and (f) R/S-**BNCNCzPB** (THF, 10^{-5}M). The inset in (d) is the magnified CD spectra of R/S-**BNBTPB** between 350-500 nm.

The observation of circular dichroism signals for all the chiral chromophores suggests that the luminescence may also present chiroptical effects. The CPL spectra were measured in different solvents and concentrations to find the optimal conditions for g_{lum} in solution, possibly enhanced by the self-assembly of H-bonded nanostructures. As shown in **Figure 3-16**, S**BNPB** shows distinct CPL in THF solutions with a mirror image relationship for the two enantiomers. Upon diluting the concentration from 10^{-4} to 10^{-5}M, a stronger ellipticity and fluorescence intensity resulted in higher g_{lum} in 3.8×10^{-4} at 398 nm. A similar result was obtained in diluted THF/toluene solutions (1/9, v/v), albeit with a lower emission intensity.

In the case of the R/S-**BNBTPB** and R/S-**7BBNBTPB**, no significant CPL was detected regardless of the solvent (THF or toluene solution) or concentration (**Figure 3-17**). As for the R/S-**BNCNCzPB** compounds, their CPL spectra are weak or absent (**Figure 3-18**). From the **Equation 3-2** of g_{lum}, the magnitude and angle between the electric transition dipole moment (μ) and the magnetic transition dipole moment (m) significantly influence the g_{lum} value and we may surmise that the magnitude of μ is larger due to the higher PLQY of the compounds.

$$g_{lum} = 4 \times \frac{|m|}{|\mu|} cos\theta_{\mu,m} \qquad \textbf{(Equation 3-2)}$$

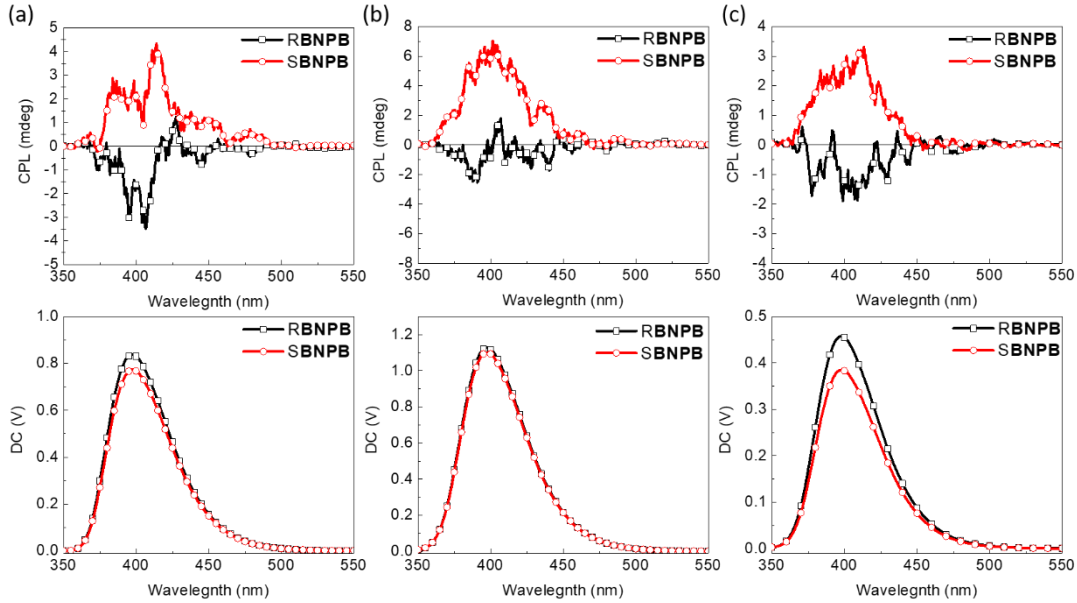

Figure 3-16. CPL spectra of R/S-**BNPB** in THF (a) 10^{-4}M (b) 10^{-5}M solutions and (c) toluene solutions (10^{-5}M). λ_{ex} =300 nm.

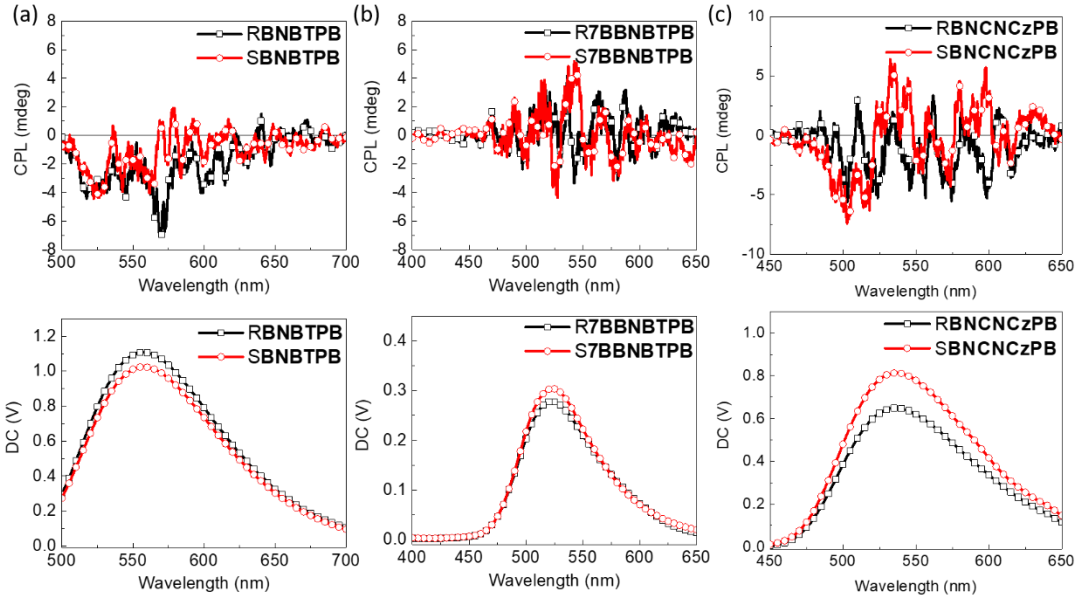

Figure 3-17. CPL spectra of (a) R/S-**BNBTPB**, (b) R/S-**7BBNBTPB** and (c) R/S-**BNCNCzPB** in THF solutions (10^{-5}M). λ_{ex} =300 nm.

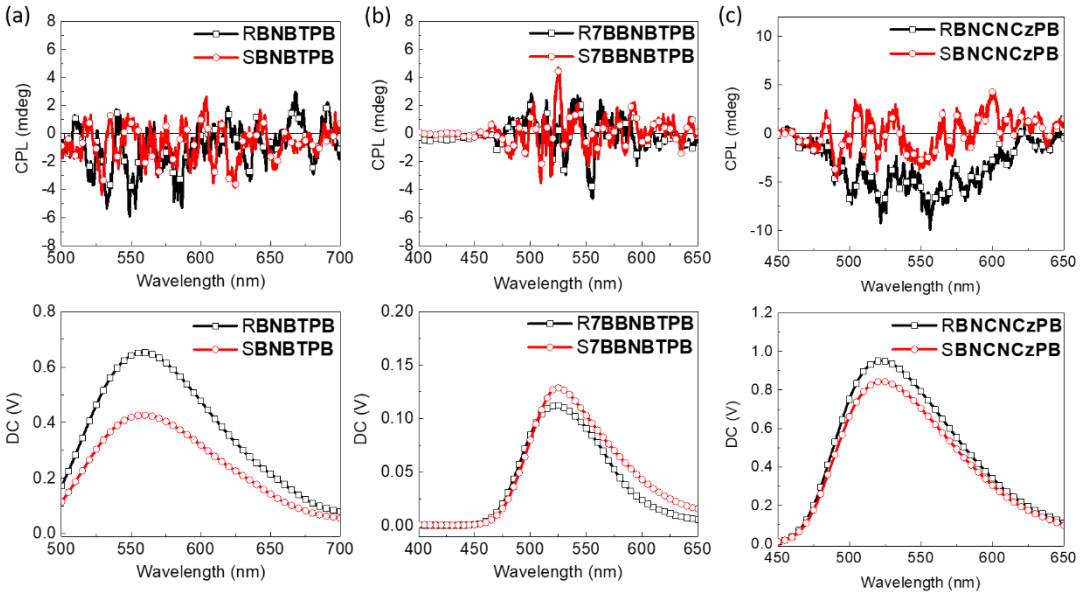

Figure 3-18. CPL spectra of (a) R/S-**BNBTPB**, (b) R/S-**7BBNBTPB** and (c) R/S-**BNCNCzPB** in toluene solutions (10^{-5}M). λ_{ex} =300 nm.

From the preliminary results collected for R**BNPB**, R**7BBNPB** and R**8BBNPB**, it is possible to see moderate CPL intensity and inversion of signal in toluene solutions (5×10^{-5} M) compared to THF (**Figure 3-19**). Remarkably, for R**BNPB** in the open form, the g_{lum} value is increased from 10^{-4} in THF to 10^{-2} in toluene solution. This should be confirmed by the spectrum of the S-form enantiomer, especially since the dissymmetry factor is highly dependent on the aggregation conditions and could not be obtained reproducibly. As for R**7BBNPB** and R**8BBNPB** in the closed structure, the cisoid conformation significantly increases the g_{lum} value of R**7BBNPB** to 0.12 but it is only slightly enhanced in R**8BBNPB** (10^{-3} in g_{lum}). To verify whether self-assembly of the vesicles contributes

to the observed increase of the g_{lum} value, DMSO was added to break up the intermolecular hydrogen-bonding network and induce the dissolution of the vesicles. This was found to lead to the disappearance of the CPL signal, in agreement with the enhancement of the asymmetry due to aggregation. Examination of the linear dichroism signal did not reveal strong linear contributions which may induce artefacts in the determination of the g_{lum} value. Further investigation of the photophysical and chiroptical properties of **BNPB** and **7BBNPB** in solution and in the solid state is needed to exclude artefacts (eg LP) for the enhancement of the CPL signal in these systems.

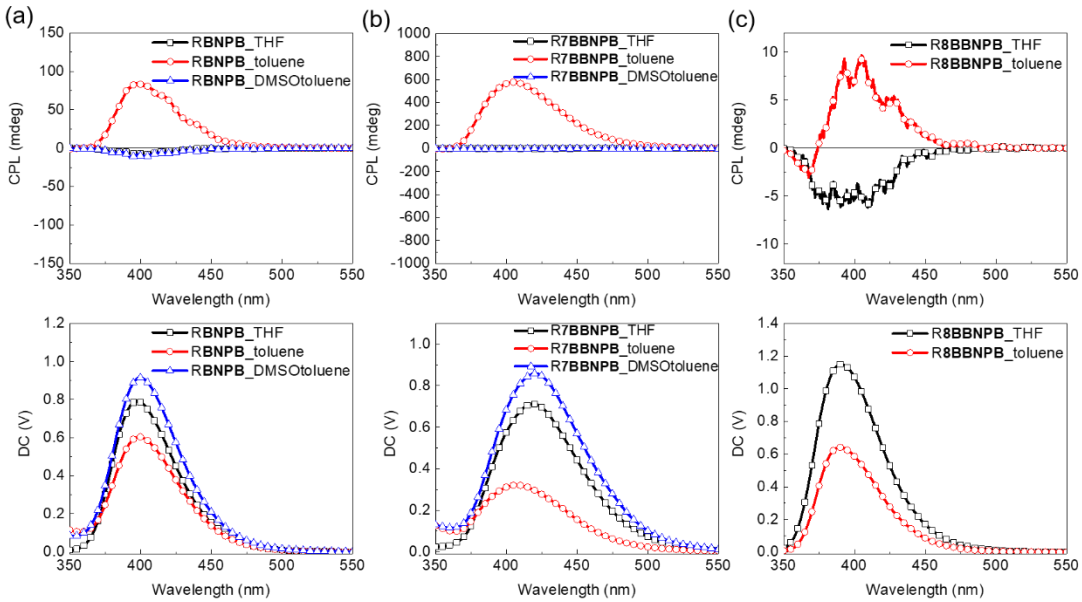

Figure 3-19. CPL spectra of (a) R**BNPB**, (b) R**7BBNPB** and (c) R**8BBNPB** in THF, toluene or toluene/DMSO solutions. λ_{ex} =300 nm.

3-2-6 Summary

Fluorescent systems composed of axially chiral binaphthalenes combined with self-

assembled biuret motifs were found to spontaneously form nanospheres whose size ranged ca. 250 to 500 nm diameter in specific environments (concentration, solvent composition). The aggregates show tunable emission from deep-blue to yellow through the introduction of benzothiadiazole groups into the π-conjugated backbone. As expected, all the chromophores exhibit intense Cotton effect with mirror-image relationship for their enantiomers in the CD spectra, indicating optical activity in the ground state. For the group of deep-blue emitters, the g_{abs} value of the bridged R**7BBNPB** (1.7×10^{-3}) in cisoid conformation is 3-fold higher than the one of the open form R**BNPB** (6.0×10^{-4}). From the preliminary results of CPL spectra, the cisoid conformation brings about a positive effect on the amplifying of g_{lum} and a remarkable CPL signal with g_{lum} that may reach 0.12 for one of the enantiomers. This will need to be confirmed for the other enantiomer. Upon addition of DMSO to solution of vesicles, the CPL signals were found to disappear, strongly suggesting that the aggregation exerts a positive influence in enhancing the g_{lum} through self-organization. For **BNCNCzPB**, a possible CPTADF emitter, the steady-state and time-resolved PL spectra at variable temperature show that the TADF character is absent. From the phosphorescence spectra of **BNPB** at low temperature, the energy level of the triplet state was found to be around 2.30 eV, which is too far below the energy of the singlet state (3.24 eV) to expect efficient rISC at or near room temperature. Thus, the π-conjugated fluorophore in **BNCNCzPB** leads to an increase of ΔE_{ST} and turns off the

rISC channel needed to harvest triplet excitons.

3-3 3,4-Alkylenedioxythiophene (ADOT) Derivative CPL Materials

3-3-1 Introduction

Poly(3,4-ethylenedioxythiophene) (PEDOT), a polymerized form of EDOT, is one of the most commercially successful π-conjugated polymers owing to its high conductivity and remarkable stability.[61] The C-3 and C-4 positions of the thiophene unit can be connected to a chiral auxiliary to produce functional chiral π-conjugated polymers, such as poly(3,4-propylenedioxythiophene) (PProDOT) derivatives.[62] Upon introduction of chiral alkyl chains, the resulting chiral polymers exhibited higher solubility and strong CD signals as helical π-stacked aggregates (**Figure 3-20**).[63] Furthermore, chiral co-polymer PEDOT derivatives could be synthesized by electrochemical polymerization,[64] a simple and reproducible method for the fabrication of polymers films. On the other hand, chirality could be induced in ADOT chromophores by the condensation of thiophene moieties and chiral diols to produce chiral π-conjugated polymers, highlighting the interesting and sometimes complex relationship between optoelectronic properties and stereochemistry.[65,66]

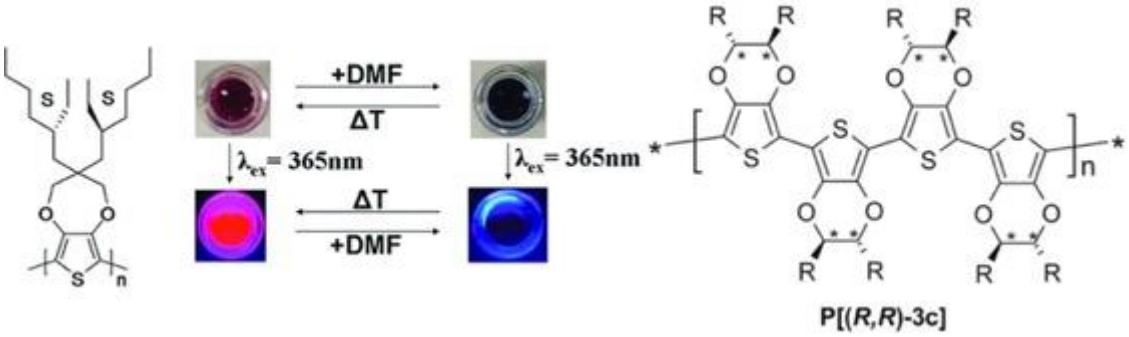

Figure 3-20. Examples of chiral EDOT derivatives materials. Readapted with permission from ref 63. Copyright 2007, American Chemical Society. Reused with permission from ref 64. Copyright 2011 Elsevier Ltd.

3-3-2 Molecular Design and Synthesis

Previous work from the Wong group showed that tetrahydrobenzothiophene (THBT)-based chromophores with C_2-chirality from D(-)- or L(+)-tartaric acid exhibit moderately intense CD spectra and can be used as chiral dopants in liquid crystal displays (**Figure 3-21**).[67] However, the laborious synthetic routes for tetrahydrobenzothiophene limits their potential application. Therefore, to shorten the tedious synthesis, we envisaged to replace the two carbon atoms in the THBT fluorophore with two oxygen atoms to construct chiral EDOT-like ADOT chromophores which could be expected to preserve chiroptical CD and CPL properties (**Figure 3-22** and **3-23**). In addition, the introduction of fluorene derivatives could increase the chromophore rigidity to suppress the nonradiative decay of the excited state (**ADOTMF**, **AFOTTF** and **ADOTSF**). Finally, we can also envisage that the addition of biuret motifs will lead to the formation of spherical aggregates which may in turn result in the enhancement of the chiroptical properties through aggregation (**ADOTMFPB**, **AFOTTFPB** and **ADOTSFPB**).

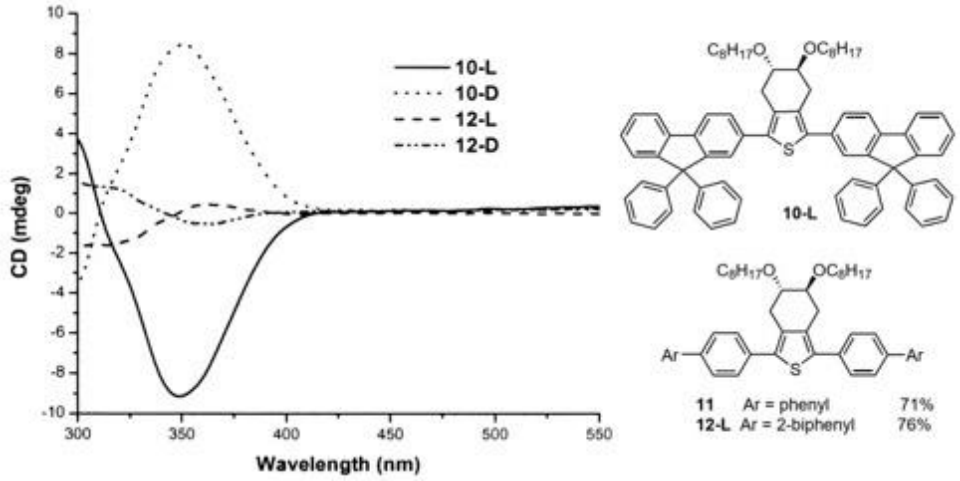

Figure 3-21. CD spectra and chemical structure of the THBT series of compounds. Adapted with permission from ref 67. Copyright 2002 Elsevier Science Ltd.

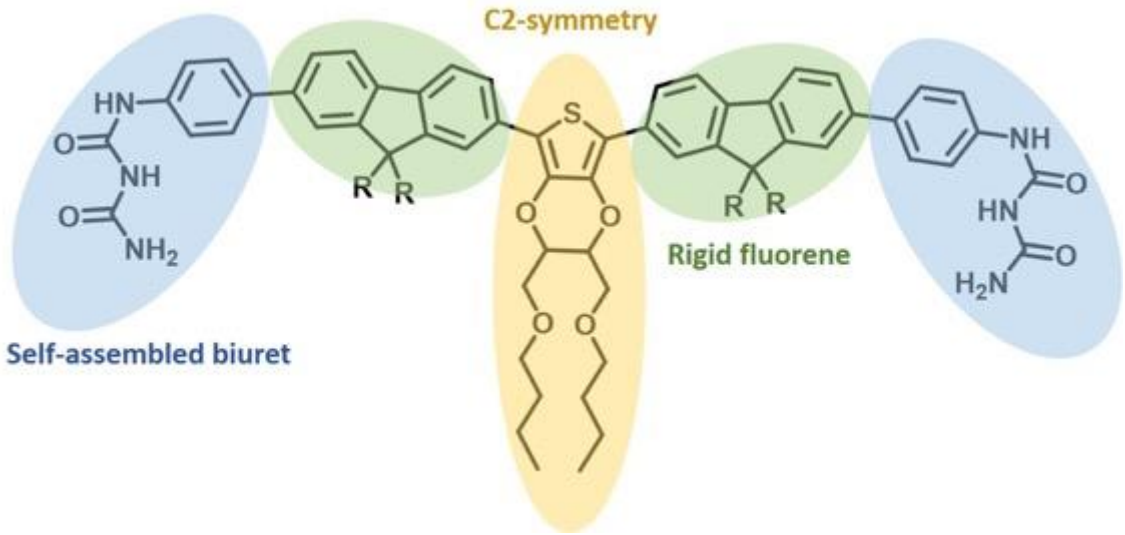

Figure 3-22. Schematic representation of ADOT and ADOTPB series of compounds.

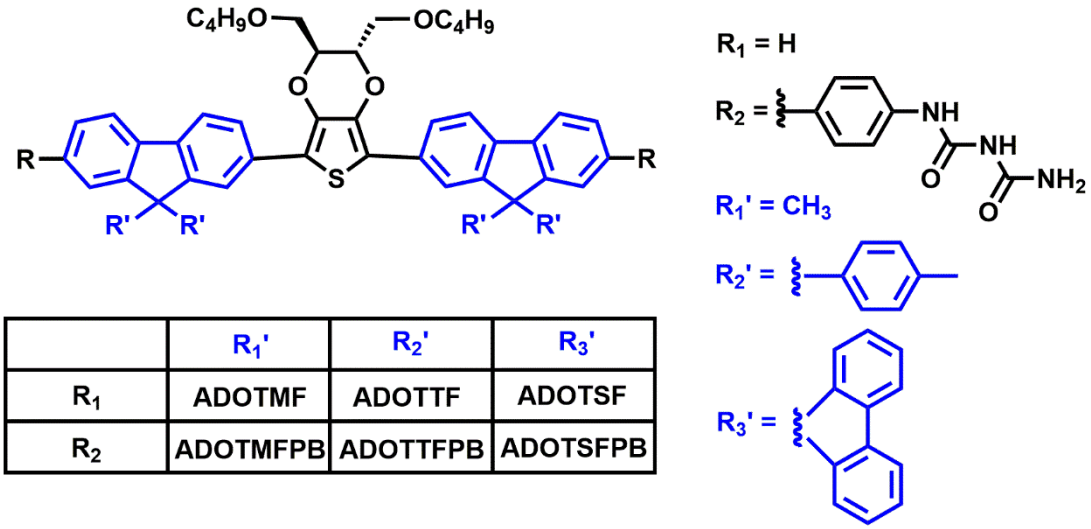

	R1'	R2'	R3'
R1	ADOTMF	ADOTTF	ADOTSF
R2	ADOTMFPB	ADOTTFPB	ADOTSFPB

Figure 3-23. Molecular design of the ADOT and ADOTPB series of molecules.

As depicted in **Scheme 3-4**, starting from optical active (D)- or (L)-tartaric acid, diol **5** was collected following acid-catalyzed esterification. With the protected diol **5**, the diester **6** was reduced to the diol **7** by LAH. Next, the alcohol group in **7** was converted to a methanesulfonyl group in **8** which, after deprotecting of **8,** lead to the diol **9**. In the lithium acetylide-ethylenediamine complex, the methanesulfonyl group was replaced to a terminal alkynyl group in diyne **10**, and the alcohol group was changed to an *n*-butyl group with the help of base. After TMS-protection of terminal alkyne **11**, intermediate **12** underwent Zr-promoted Takahashi cyclization followed by quenching with sulfur monochloride to afford chromophore **13**. Bromination of compound **13** gave intermediate **14** which could be linked to a ditolylfluorene boronic acid derivative via palladium-catalyzed Suzuki-Miyaura coupling to obtain model molecule **THBTTF**.[67]

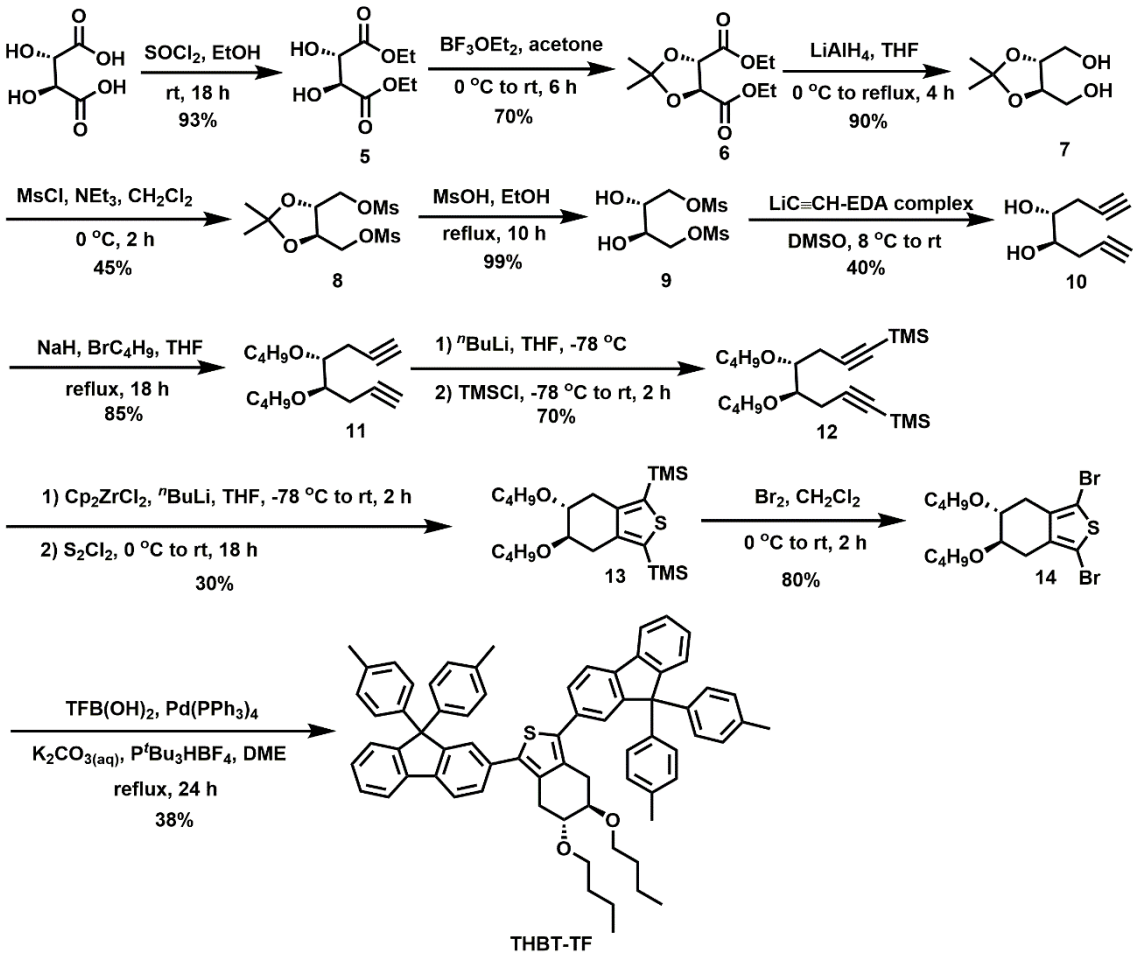

Scheme 3-4. Synthetic pathway and structure of model compound **THBTTF**.

For the ADOT series (**Scheme 3-5**), diol **7** underwent alkylation to intermediate **15** possessing *n*-butyl groups which then was deprotected in acidic media to afford compound **16**.[68] Following methoxylation of 3,4-dibromothiophene to obtain compound **17**, Bäuerle's procedure was used to conduct acid-catalyzed transetherification to produce chromophore **ADOT** from **16** and **17**.[69] Using Yu's protocol for the arylation of dioxythiophene,[70] **ADOTMF**, **ADOTTF** and **ADOTSF** were synthesized by palladium-catalyzed direct C–H arylations.

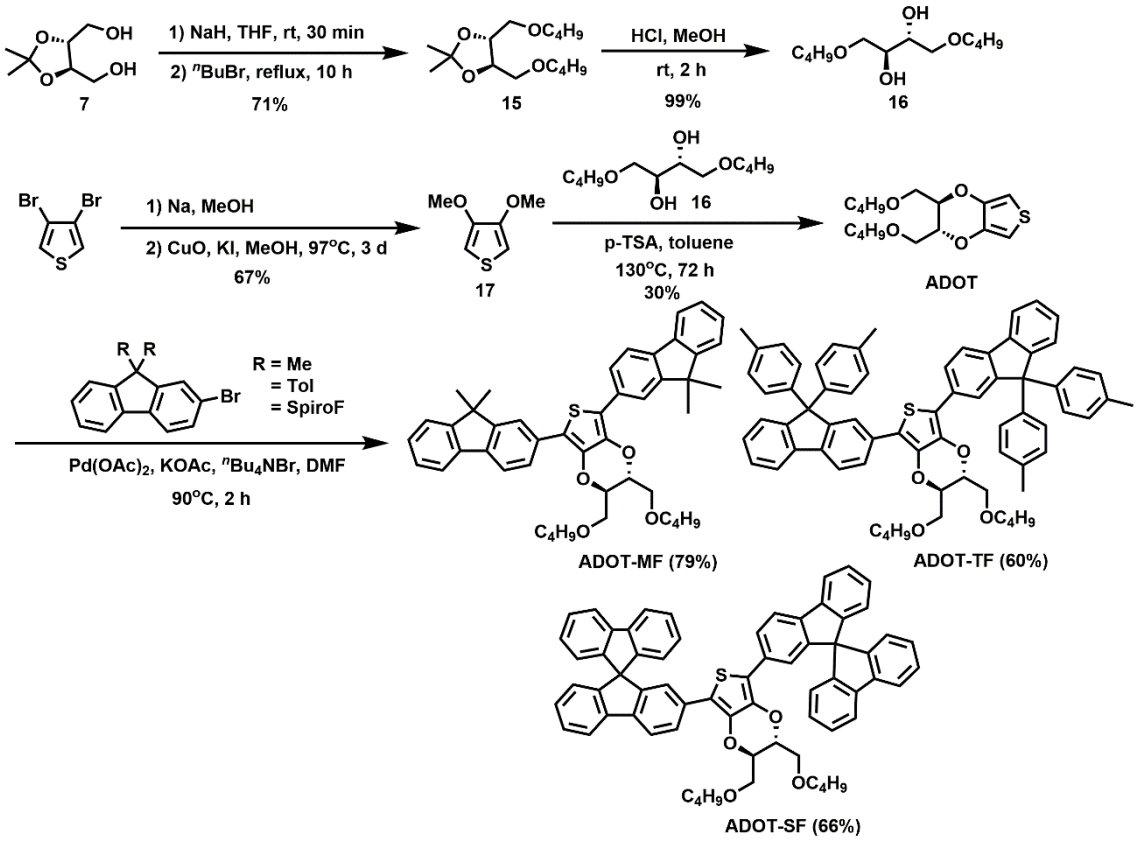

Scheme 3-5. Synthetic pathway and structure of ADOT series.[68-70]

As shown in **Scheme 3-6**, after reacting with bromine, **ADOTMF**, **ADOTTF** and **ADOTSF** were converted to the corresponding bis-brominated intermediates which could be linked to the phenylbiuret motifs using palladium-catalyzed Suzuki-Miyaura coupling, thus affording **ADOTMFPB**, **ADOTTFPB** and **ADOTSFPB**.

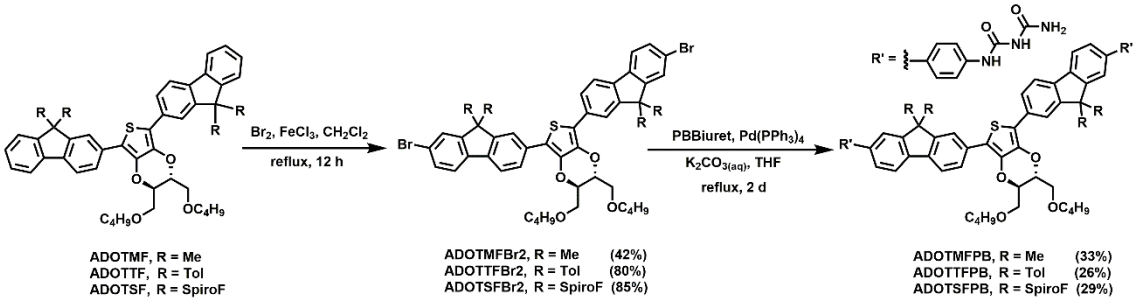

Scheme 3-6. Synthetic pathway and structure of ADOTPB series.

3-3-3 Characterization of Nanostructures

To confirm the self-organization behavior of ADOTPB series of compounds, SEM was used to characterize the morphologies in various environments (**Figure 3-24** to **3-26**). Surprisingly, no solvent effect could be found when comparing acetone, methanol or THF solutions, with all three molecules forming well-defined nanospheres whose size was ca. 200-500 nm in diameter. The morphologies of nanovesicles are relatively uniform and homogeneous, especially in THF solutions.

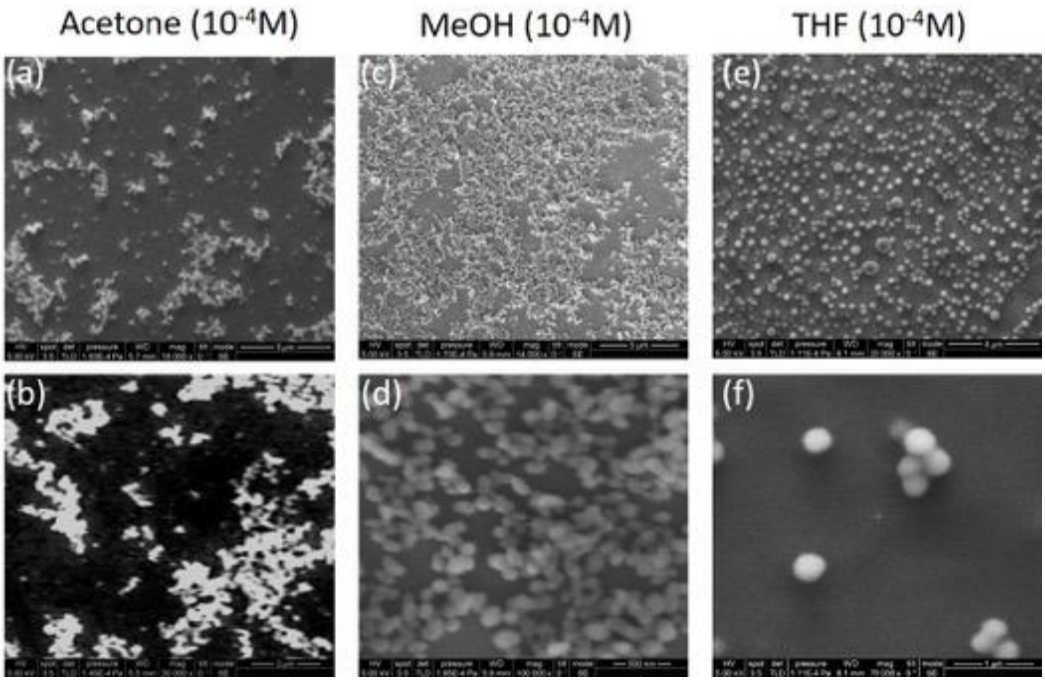

Figure 3-24. SEM images of **ADOTMFPB** in (a,b) acetone, (c,d) methanol and (e,f) THF solutions. Scale bar = 4 μm for (a)(c)(e), 2 μm for (b), 1 μm for (f) and 0.5 μm for (d).

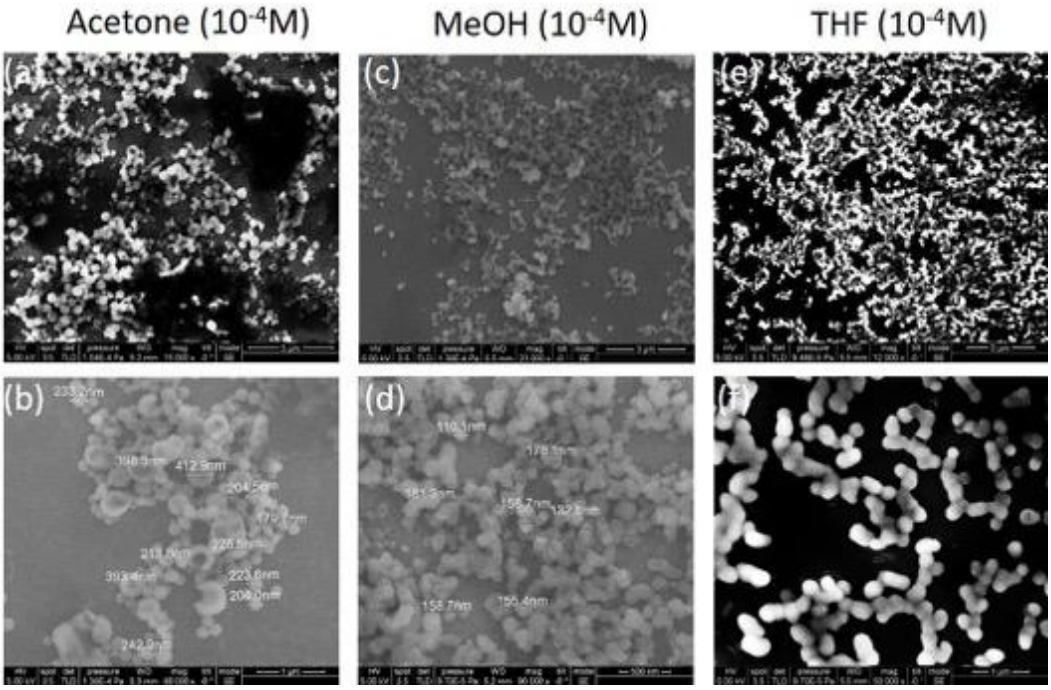

Figure 3-25. SEM images of **ADOTTFPB** in (a,b) acetone, (c,d) methanol and (e,f) THF solutions. Scale bar = 3 μm for (a)(c)(e), 1 μm for (b)(f) and 0.5 μm for (d).

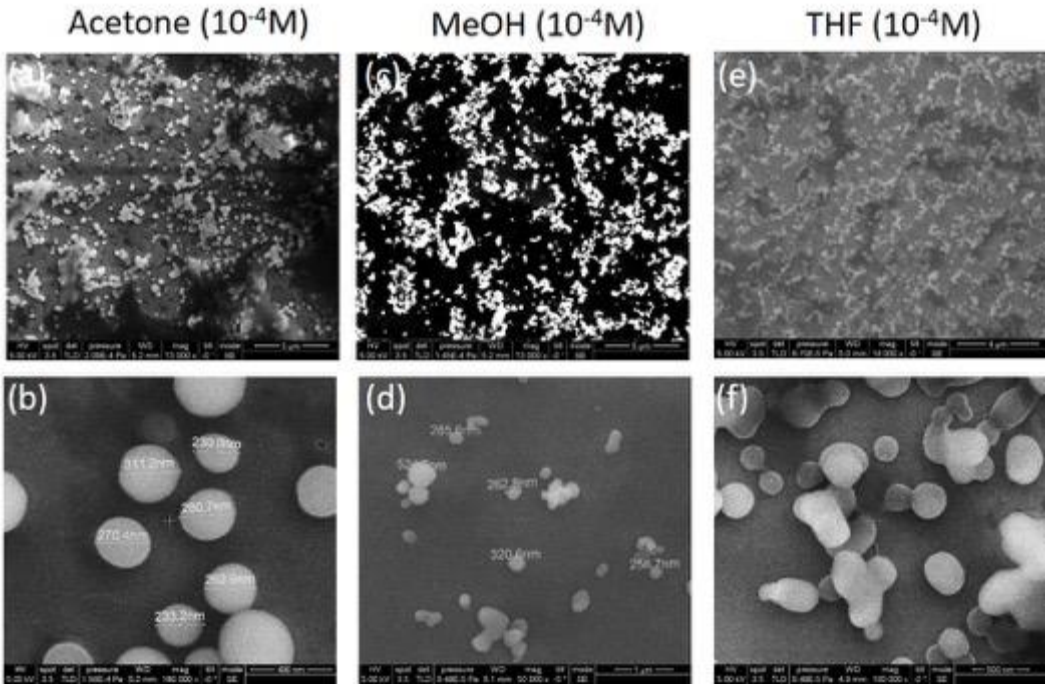

Figure 3-26. SEM images of **ADOTSFPB** in (a,b) acetone, (c,d) methanol and (e,f) THF solutions. Scale bar = 5 μm for (a)(c)(e), 1 μm for (d) and 0.5 μm for (b)(f).

3-3-4 Photophysical Properties

The absorption and fluorescence spectra of the ADOT-based compounds in solution (toluene, 10^{-5}M) are shown in **Figure 3-27** and their photophysical properties are summarized in **Table 3-2**. All the three molecules exhibit intense π-π* absorption bands below 400 nm, which are significantly red-shifted by 40 nm compared to **THBTTF**. The bathochromic shift likely results from the replacement of two carbon atoms in **THBT** chromophore with two oxygen atoms which increases the stability of the CT character of the electronic transition. The emission bands of the three molecules are located at 430-460 nm and exhibit some vibrational fine structure which, along with the small Stokes shift, suggests localized emission behavior. Compared to **THBTTF**, ADOT-based molecules have smaller Stokes shifts, which means little conformational change occurs between the ground state and excited state and, possibly, less non-radiative decay than for **THBTTF**.

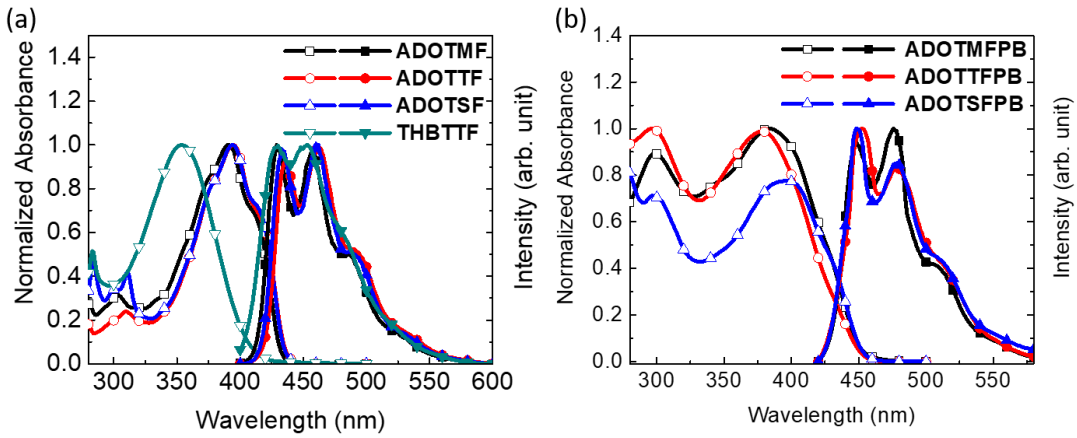

Figure 3-27. UV/Vis absorption and PL spectra of (a) ADOT series in toluene solutions (10^{-5}M) and (b) ADOTPB series in THF solutions (10^{-5}M). Excited at 370 nm.

Table 3-2. Summary of photophysical properties of ADOT-series molecules.

Molecule	$\lambda_{Abs}{}^{a}$ (soln, nm)	ε^{a} (10^4 $M^{-1}cm^{-1}$)	$\lambda_{PL}{}^{soln}$ (toluene, nm)	$\Phi_{Toluene}{}^{ab}$ (%)	Stokes shift^{c} (cm^{-1})
ADOTMF	391	5.3	429, 457	37	2260
ADOTTF	395	5.6	436, 462	33	2380
ADOTSF	394	5.4	433, 462	34	2290
THBTTF	353	-	430, 453	28	5070

[a] Measured in toluene solution (10^{-5}M). [b] Fluorescence quantum yields were measured in aerated toluene solutions (10^{-5}M) and excited at 370 nm, using an integration sphere coupled to a photonic multichannel analyzer (Hamamatsu C9920). [c] Stokes shift = λ_{Abs} - λ_{PL} in wavenumber.

As depicted in **Figure 3-27** and summarized in **Table 3-3**, the absorption and fluorescence spectra of the ADOTPB series of chromophores measured in solution (THF, 10^{-5}M) are similar to the ADOT-series, with strong π-π* absorption bands around 375-400 nm. As for the emission spectra, the maximal fluorescence wavelength of the ADOTPB compounds are all relatively red-shifted to ca. 450-480 nm. This can be assigned to the extension of π-conjugation length of the central chromophore through conjugation to the phenyl-biuret moieties. This also leads to a smaller $S_0 - S_1$ energy gap,

which accelerates internal conversion through vibronic coupling, as reflected in the somewhat lower emission quantum yields for these compounds. In contrast to **ADOTMFPB** and **ADOTTFPB**, the more rigid **ADOTSFPB** retains a similar Φ_{lum} after coupling to the biuret groups.

Table 3-3. Summary of photophysical properties of ADOTPB-series molecules.

Molecule	$\lambda_{Abs}{}^{a}$ (soln, nm)	ε^{a} (10^4 $M^{-1}cm^{-1}$)	$\lambda_{PL}{}^{soln}$ (THF, nm)	$\Phi_{THF}{}^{ab}$(%)
ADOTMFPB	384	3.4	448, 476	22
ADOTTFPB	378	4.4	453, 478	19
ADOTSFPB	396	4.1	448, 479	34

[a] Measured in THF solution (10^{-5}M). [b] Fluorescence quantum yields were measured in aerated THF solutions (10^{-5}M) and excited at 370 nm, using an integration sphere coupled to a photonic multichannel analyzer (Hamamatsu C9920).

3-3-5 Chiroptical Properties

The chiroptical properties of the ADOT series of compounds in the ground state were evaluated from the CD spectra in solution (chloroform, 10^{-5}M) (**Figure 3-28**). The three emitters d-**ADOTMF**, d-**ADOTTF** and d-**ADOTSF** show a negative Cotton effect around 390 nm in the CD spectra and exhibit a mirror-image relationship for the two enantiomers. Based on the relationship between the CD signal and absorbance, there is

no exciton coupling,[54,55] which means that there are no intramolecular interactions between the electronic transition moments of chromophores leading to an enhancement of the Cotton effect. The g_{abs} value in CD spectra of the three pairs of enantiomers are all in the range of 10^{-4}-10^{-5} attributed to the intrinsic chirality of chiral central fluorophore. In addition, the CD intensity of l-**ADOTTF** is close to l-**THBTTF** whose g_{abs} values of 10^{-4}; that is, the substitution of carbon atoms by oxygen atoms in asymmetric chromophore does not reduce the amplitude of the CD spectra.

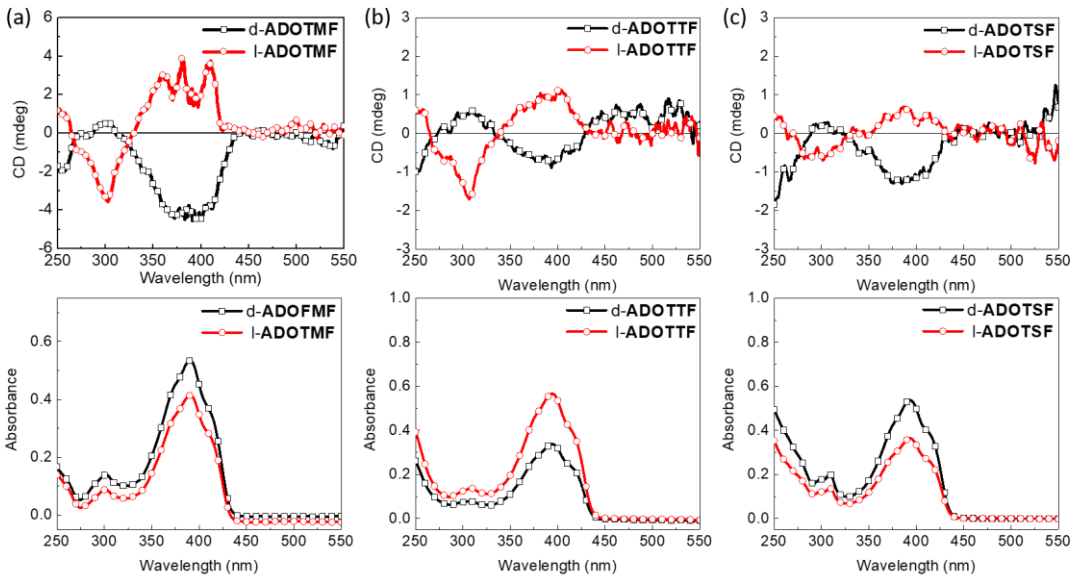

Figure 3-28. CD spectra of (a) d/l-**ADOTMF**, (b) d/l-**ADOTTF** and (c) d/l-**ADOTSF** in chloroform solutions (10^{-5}M).

The ADOTPB series of molecules was investigated in solution (THF, 10^{-5}M) with the aim of elucidating the effect of self-assembly on the chiroptical properties. The CD

spectra of d-**ADOTMFPB**, d-**ADOTTFPB** and d-**ADOTSFPB** all show negative Cotton effects with the opposite signal in the spectra of the enantiomers. For all compounds, the observed magnitude of the CD spectra provided g_{abs} values of ca. 10^{-4}, which implies that the contribution from aggregation is not significant in this case (**Figure 3-29**).

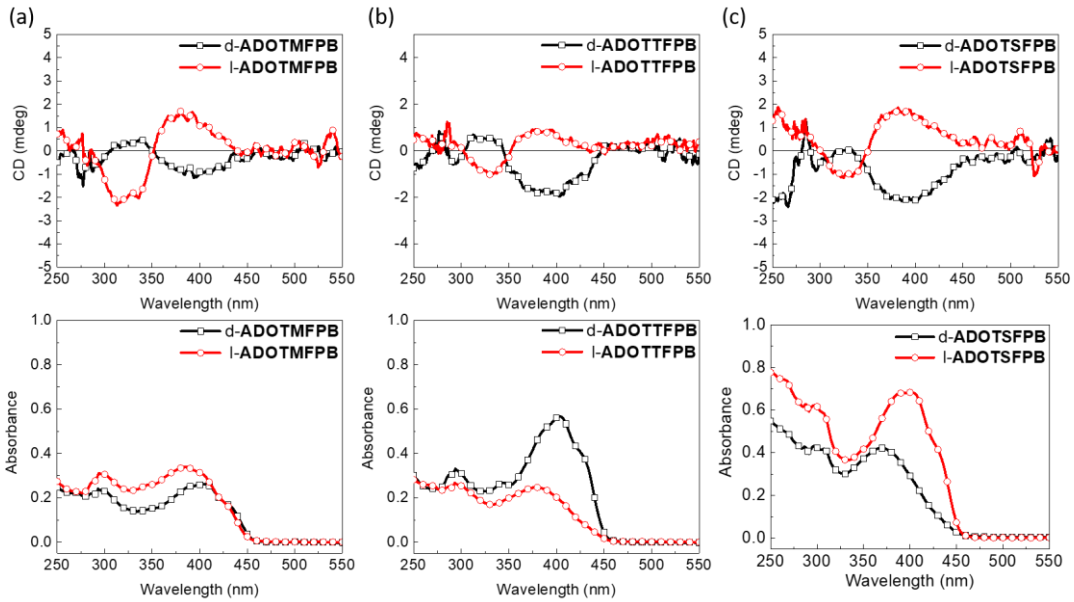

Figure 3-29. CD spectra of (a) d/l-**ADOTMFPB**, (b) d/l-**ADOTTFPB** and (c) d/l-**ADOTSFPB** in THF solutions (10^{-5}M).

The CPL spectra for the d- and l-forms of the ADOT series in solution (acetone, 10^{-4}M) are shown in **Figure 3-30**. It can be seen that the signals are very weak and that the two enantiomers do not give opposite signals. As expected, the resulting values of g_{lum} are around 10^{-4}, which is near the instrumental detection limit and likely limited to the contribution from the intrinsic chirality of ADOT chromophore.

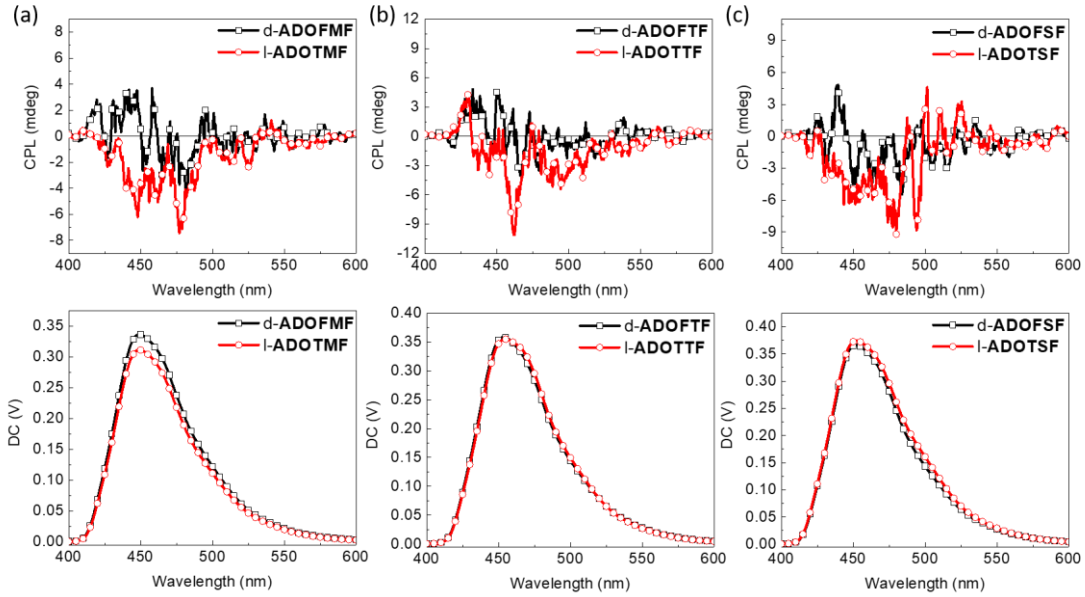

Figure 3-30. CPL spectra of (a) d/l-**ADOTMF**, (b) d/l-**ADOTTF** and (c) d/l-**ADOTSF** in acetone solutions (10^{-4}M). Excited at 350 nm.

In addition, we may use l-**THBTTF** as a model compound to investigate the effect of substitution on the CPL performance (**Figure 3-31**). The g_{lum} value of l-**THBTTF** (10^{-4}) is identical to the value of l-**ADOTTF**, revealing that the substitution on the asymmetric fluorophore does not affect the optical activity as observed from the CPL spectra.

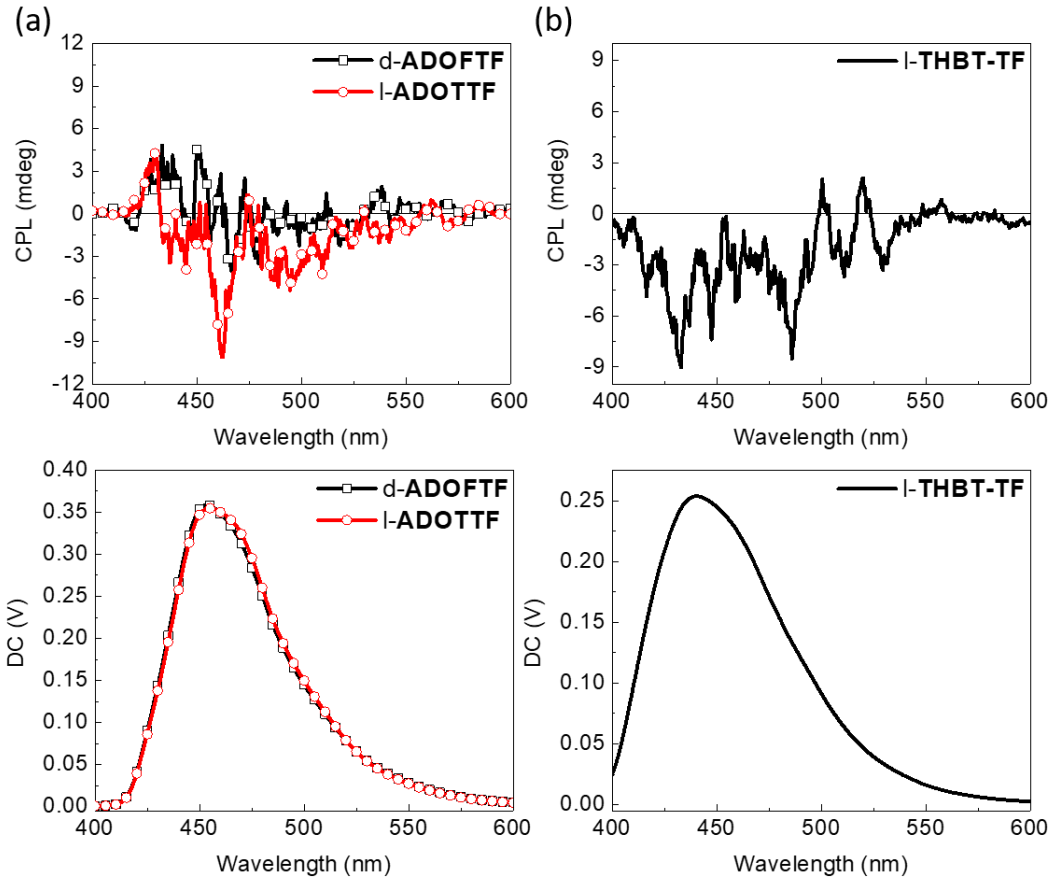

Figure 3-31. CPL spectra of (a) d/l-**ADOTTF** and (b) l-**THBTTF** in acetone solutions (10^{-4}M). Excited at 350 nm.

The presence of the biuret motifs in compounds l-**ADOTMFPB** and l-**ADOTSFPB** results in better mirror-image relationship with the enantiomers in CPL spectra but the magnitude of CPL signals are not significantly improved by the formation of organized nanostructures. With regards to d- and l-**ADOTTFPB**, no CPL signal could be obtained in agreement with the absence of significant CD signals in the ground state (**Figure 3-32**).

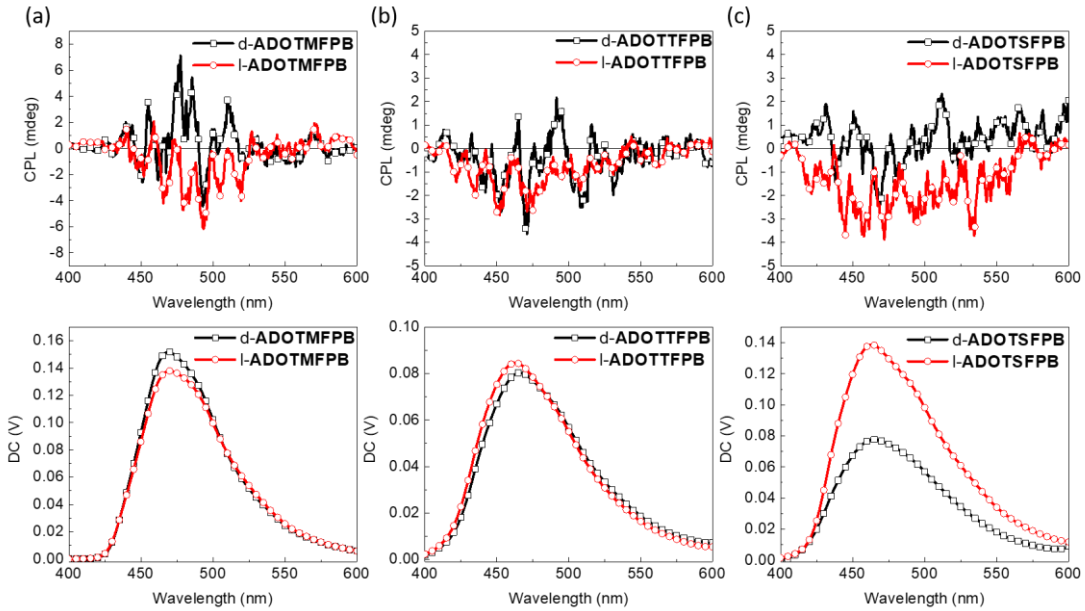

Figure 3-32. CPL spectra of (a) d/l-**ADOTMFPB**, (b) d/l-**ADOTTFPB** and (c) d/l-**ADOTSFPB** in acetone solutions (10^{-5}M). Excited at 350 nm.

3-3-6 Summary

In this section, the previous work on the chiral molecules **THBTTF** for chiral dopants in liquid crystal displays was extended. The tedious synthetic routes were simplified by targeting the oxy-analogue **ADOT**, in which two carbon atoms are replaced by two oxygen atoms. The resulting **ADOT** compounds (**ADOTMF**, **ADOTTF** and **ADOTSF**) retain similar absorption spectra and display deep-blue emission with comparable Φ_{lum}. Concerning the chiroptical properties, the **ADOT** series with simple alkyl chains show clear Cotton effects with g_{abs} of 10^{-4} assigned to the intrinsic chirality of the chromophore. They exhibit weak optical activity in emission with CPL spectra giving g_{lum} of 10^{-4}, similar to **THBTTF**. The addition of the biuret motifs, gives rise to

self-assembly as evidenced by the formation of nanovesicles in solutions for all of the **ADOTPB** series of compounds (**ADOTMFPB**, **ADOTTFPB** and **ADOTSFPB**). However, the self-assembly does not influence the chiroptical properties and the **ADOTPB** series show the identical values of g_{abs} of 10^{-4} in the CD spectra and no or weak CPL. To summarize, the small inductive effect of the alkyl chains in the chiral chromophore gives rise to a similarly small enhancement of the chiroptical properties of the compounds in solution or in the aggregated state.

3-4 Chiral Pyrene-Based Circularly Polarized Excimer Materials

3-4-1 Review of Circularly Polarized Excimer Materials

As we have seen above, the chiroptical properties of supramolecular materials are not solely due to the intrinsic chirality of their molecular structure, but also to the formation of self-assembled architectures.[71-73] In numerous systems, pyrene is well-known to exhibit excimer emission resulting from the formation of an excited-state dimer. Thus, in the past years, circularly polarized excimer emission (CPEE) from pyrene derivatives have aroused great interest.[74-76] Considering that excimer emission is a property related to an excited state with no ground-state counterpart, we can expect that the electronic transition dipole moment is small, which may contribute to a large g_{lum} value according to **Equation 3-2**. With this in mind, pyrene has been connected to different chiral units with point,[77] planar,[78] axial[79] and helical chirality[80] and the corresponding photophysical properties were investigated (**Figure 3-33**).

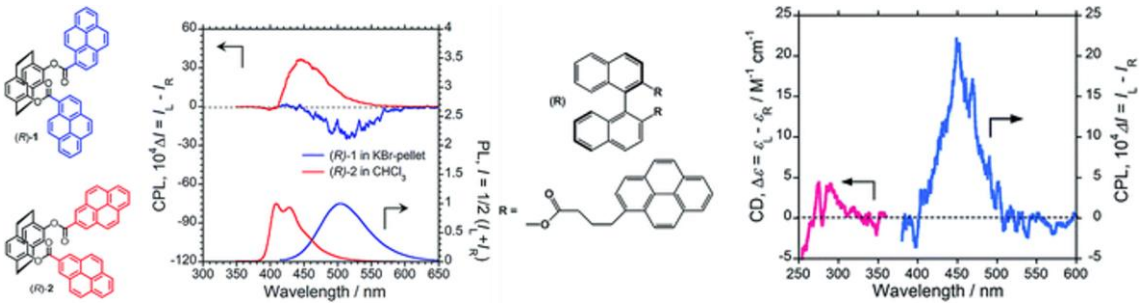

Figure 3-33. Examples of circularly polarized pyrene-based cyclophanes giving rise to the formation of excimers. Reused with permission from ref 78 and 79. Copyright 2016

Royal Society of Chemistry.

In previous work (**Figure 3-34**), bis-pyrene derivatives **DiPy** composed of a chiral *trans*-1,2-diaminocyclohexane unit (DACH) were investigated as symmetric references for future asymmetric systems. From the PL spectra in various solvents, it was observed that a significant shift in the emission wavelength, characterized by a calculated dipole moment of the excited state of 11.8 D (from Lippert-Mataga plots).[81,82] The latter is much too large to be associated with an excimer system and corresponds to the transfer of one unit of charge over a distance of 2.4 Å. From this, we deduce that symmetry breaking occurs in the excited state and leads to the formation of an exciplex at lower energy with respect to the formation of an exciplex. The CPL in cyclohexane solution (5 μM), shows a band centered in 420 nm attributed to the monomer emission of pyrene with g_{lum} of 10^{-3}, followed by a an intense and broad exciplex emission at 470 nm. A g_{lum} of 0.016 is observed for the exciplex emission, which shows that, at least in this case, the intramolecular exciplex is prone to chiroptical activity.

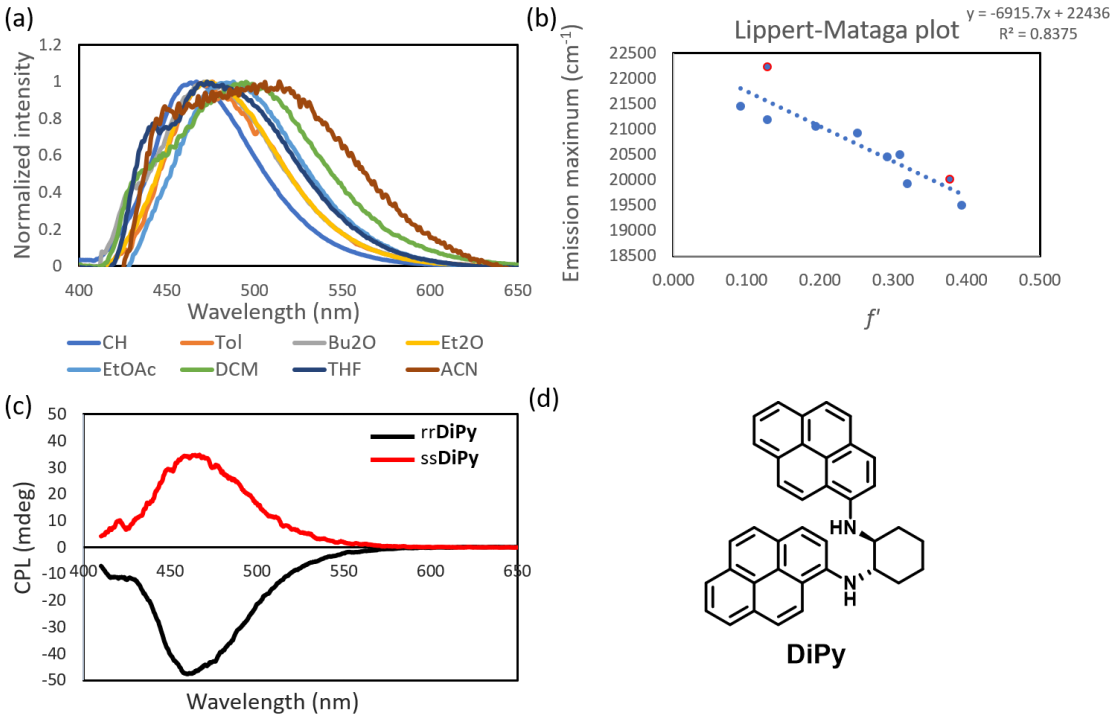

Figure 3-34. (a) PL spectra of **DiPy** in various solutions. (b) Lippert-Mataga plot of **DiPy**. (c) CPL spectra of rr/ss-**DiPy** in cyclohexane solutions (5 μM). (d) Chemical structure of **DiPy**.

3-4-2 Molecular Design and Synthesis

The impressive results obtained for **DiPy** suggest that the introduction of biuret motifs would lead to the formation of self-assembled nanostructures that could result in the enhancement of the chiroptical properties. As shown in **Scheme 3-7**, starting from a *cis-/trans-* mixture of 1,2-diaminocyclohexane, we followed the reported literature procedure using (D)- or (L)-tartaric acid to conduct chiral resolution through the enantiopure tartrate salt complexes.[83] The salts were hydrolyzed in basic condition to

afford ss- or rr-1,2-diaminocyclohexane. Then, the optically active diamine was reacted with 1,6-dibromopyrene through Buchwald-Hartwig coupling reaction to give **DACHPyBr2**.[84] The bis-brominated intermediate was reacted with **PBBiuret** via Pd(0)-catalyzed Suzuki-Miyaura coupling reaction to give ss- or rr-**DACHPyPB**.

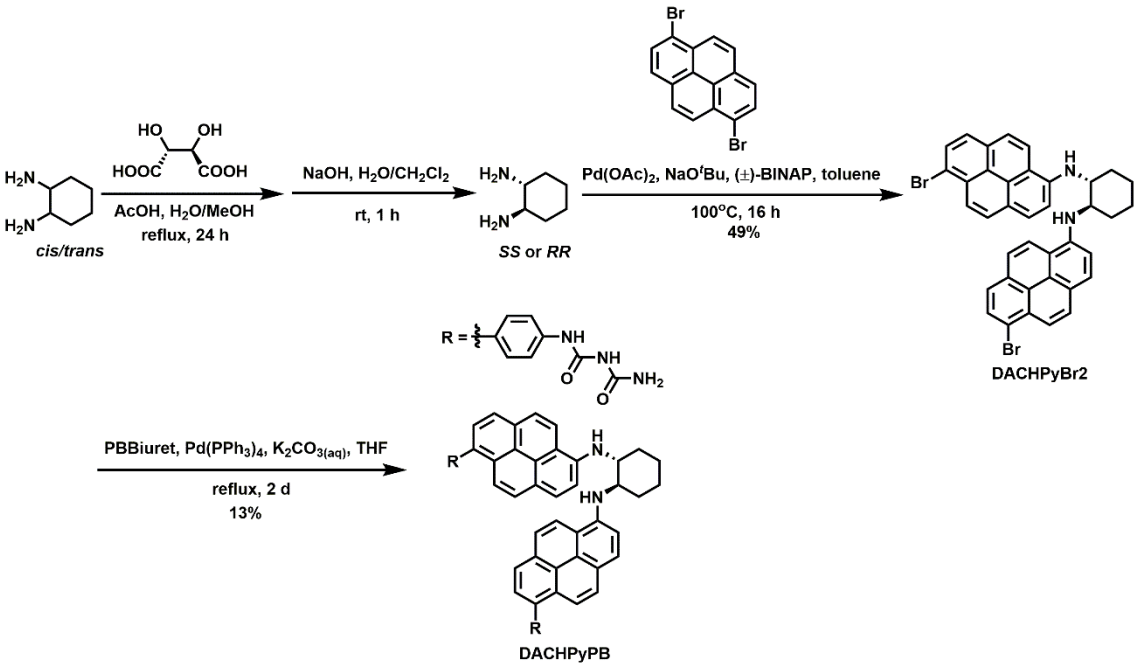

Scheme 3-7. Synthetic route and structure of **DACHPyPB**.

3-4-3 Characterization of Nanostructures

From the SEM images of **DACHPyPB** drop-cast onto glass substrates shown in **Figure 3-35**, the formation of the self-assembled vesicles is found to occur from process **DACHPyPB** in different solvents. In acetone solutions, **DACHPyPB** can form clusters of ruptured vesicles with a size of ca. 100-250 nm. In methanol solutions, well-defined nanospheres with a size of 300-500 nm could be obtained. Based on these results, we will

use the conditions of methanol solution to further study the influence of aggregate formation on the photophysical and chiroptical properties.

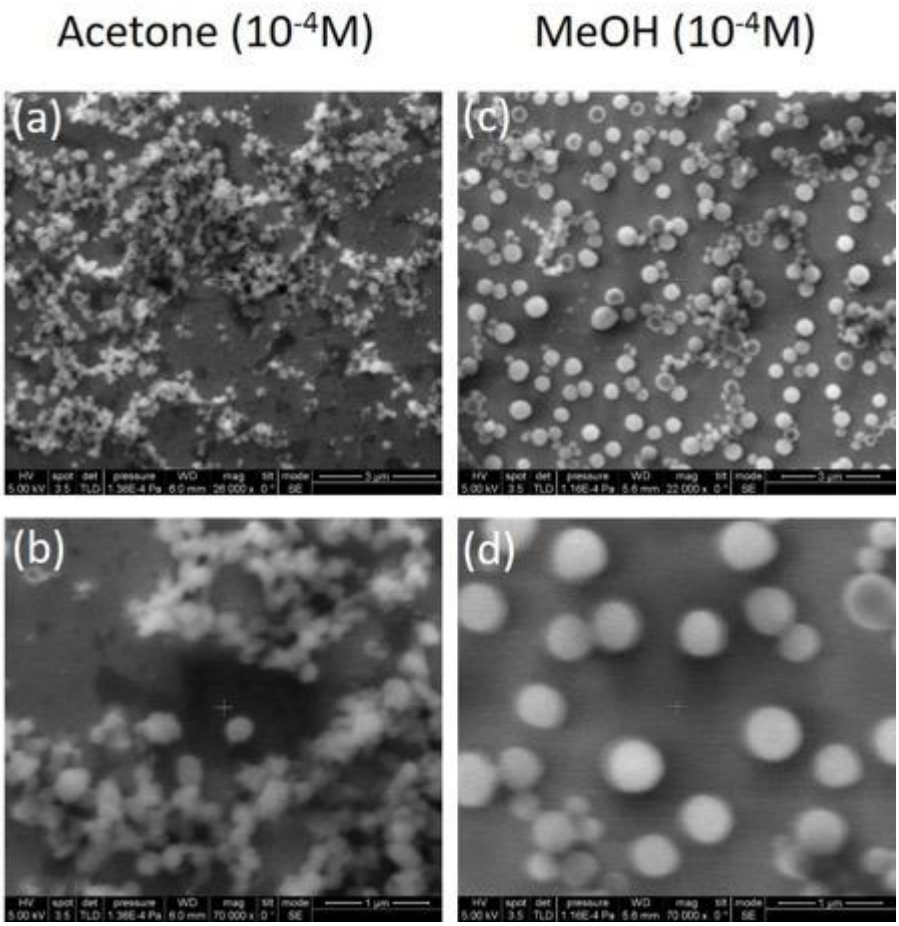

Figure 3-35. SEM images of **DACHPyPB** in (a,b) acetone and (c,d) methanol solutions. Scale bar = 3 μm for (a)(c) and 1 μm for (b)(d).

3-4-4 Photophysical Properties

The photophysical properties of **DACHPyPB** in solution (THF, 10^{-5}M) are shown in **Figure 3-36** and summarized in **Table 3-4**. The molecule exhibits intense absorption bands around 293, 400 and 418 nm, attributed to the extension of the pyrene π-conjugated

system with the amino group and the phenyl-biuret. A strong PL band is located at 466 nm owing to the emission from the pyrene monomer and the tailing of PL in 520-600 nm is assigned to the exciplex emission. To estimate its dipole moment in excited state, we acquired the PL spectra in various solvents and analyzed the energy of the emission wavelength as a function of solvent polarity according to the Lippert-Mataga plots.[81,82] A dipole moment of 11.2 D is found for the excited state, which is large and similar to the value obtained for **DiPy**, thereby indicating exciplex formation due to symmetry breaking. The chiroptical property in ground state were investigated using CD spectroscopy. Both rr- and ss-**DACHPyPB** are CD-active and show a near-perfect mirror image relationship for the two enantiomers in solution, with weak negative Cotton effect between 250 and 370 nm, and strong positive and negative bands at 433 nm and 402 nm, respectively (10^{-5}M THF solution). The bisignate Cotton effect with a g_{abs} of 4.0×10^{-3} in CD spectra can be ascribed to the exciton coupling between the neighboring pyrene moieties.[54,55]

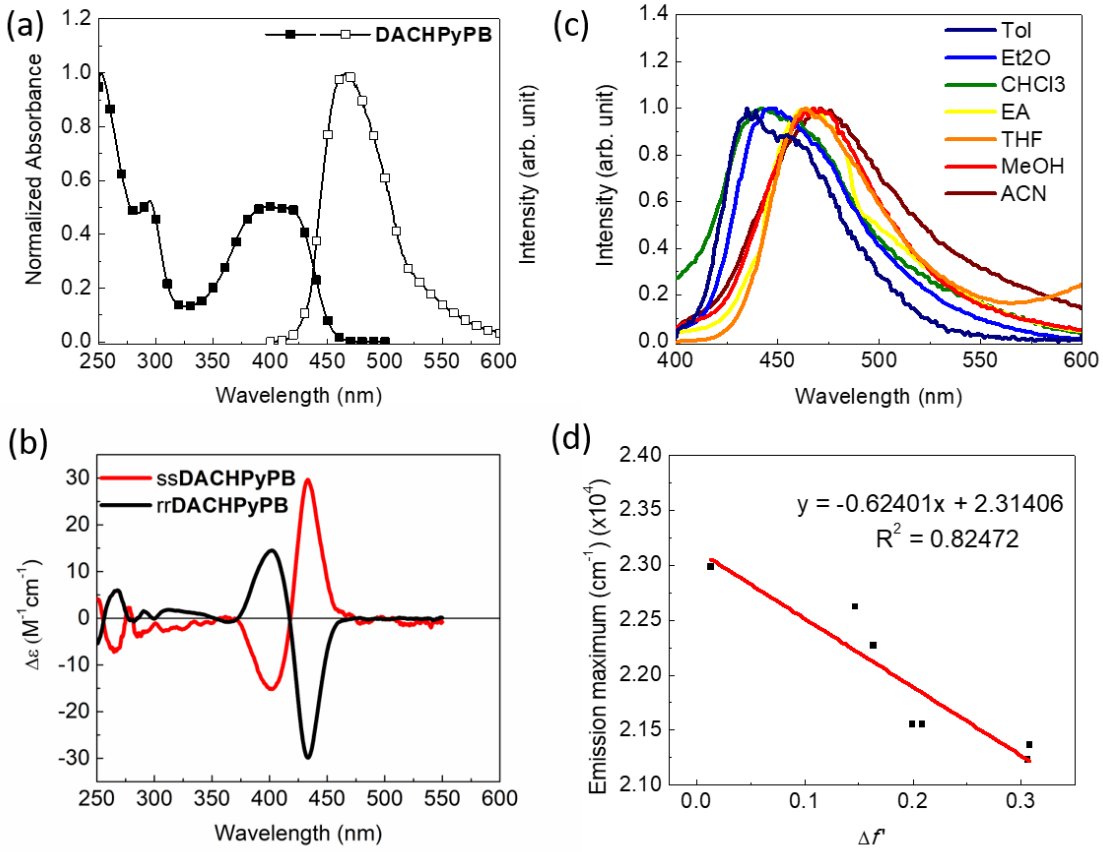

Figure 3-36. (a) Absorption and PL spectra of **DACHPyPB** in solution (THF, 10^{-5}M). Excited at 380 nm. (b) CD spectra of ss/rr-**DACHPyPB** in solution (THF, 10^{-5}M). (c) PL spectra of **DACHPyPB** in various solutions. Excited at 380 nm. (d) Lippert-Mataga plot of **DACHPyPB**.

Table 3-4. Summary of the photophysical properties of **DACHPyPB**.

Molecule	λ_{Abs} [a] (soln, nm)	ε [a] (10^4 $M^{-1}cm^{-1}$)	λ_{PL} soln (THF, nm)	Φ_{THF} [b] (%)
DACHPyPB	293, 400, 418	2.0, 1.7, 1.7	466	50

[a] Measured in THF solution (10^{-5}M). [b] Fluorescence quantum yields were measured in aerated THF solutions (10^{-5}M) and excited at 380 nm, using an integration sphere coupled

to a photonic multichannel analyzer (Hamamatsu C9920).

The optical activity of **DACHPyPB** in excited state was investigated using CPL spectroscopy, and the results are shown in **Figure 3-37**. Strong monomer emission is observed at 480 nm from both enantiomers giving modest left- or right-handed CPL signals that are identical but opposite in sign for ss**DACHPyPB** and rr**DACHPyPB**. In comparison with its CD and CPL spectra, ss**DACHPyPB** displays a positive Cotton effect in both the ground and excited state. In more concentrated THF solutions (10^{-4}M), ss**DACHPyPB** shows an intense CPL centered at 480 nm with a g_{lum} of 8.6×10^{-4} and a PL tail beyond 520 nm that might result from exciplex emission. On the other hand, in diluted solutions (10^{-5}M), the major CPL band show a g_{lum} of 1.0×10^{-3}, which is similar to that of the monomer emission in ss**DiPy**. From this, we conclude that the formation of self-assembled aggregates may interfere with the conformational motion required to reach an emissive exciplex geometry. Therefore, the organized arrangement in ss**DiPy** reduces the CPL contribution from exciplex emission. In diluted toluene solutions, ss**DACHPyPB** shows much stronger exciplex intensity with a low g_{lum} of 7.6×10^{-4}, inferring that the forced aggregation in poor solvent promotes the occurrence of exciplex formation that is less prone to chiral induction.[85] It is also possible that exciplex formation in the aggregates occurs intermolecularly rather than intramolecularly for **DiPy**.

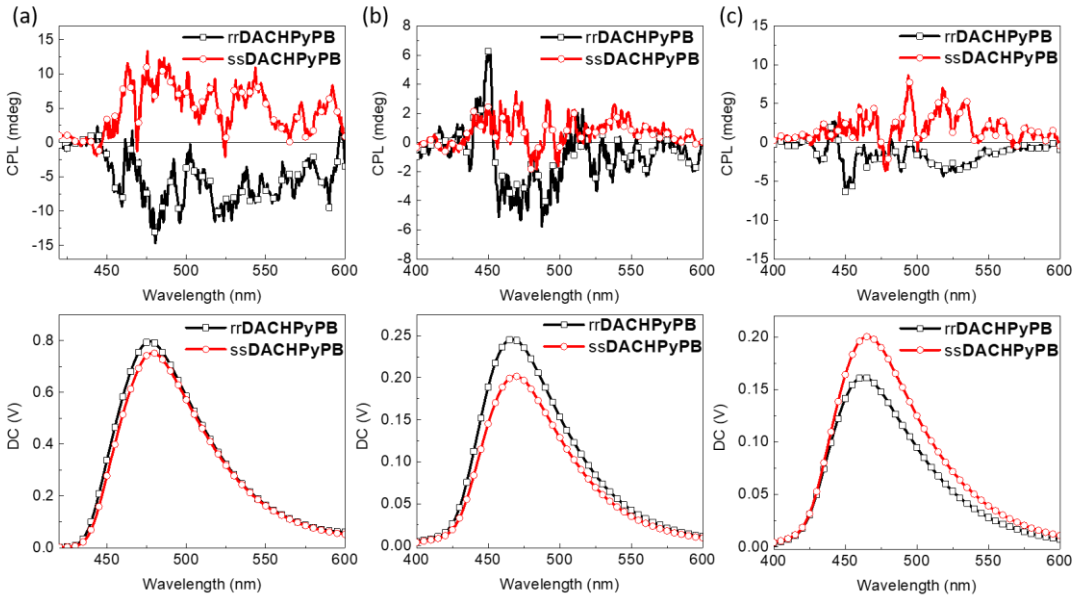

Figure 3-37. CPL spectra of ss/rr-**DACHPyPB** in THF (a) 10^{-4}M (b) 10^{-5}M solutions and (c) toluene solutions (10^{-5}M). Excited at 350 nm.

3-4-5 Summary

In this section, we examined a pair of chiral cyclohexyl derivatives substituted with pyrene chromophores that undergo exciplex formation through excited-state symmetry-breaking. By appending biuret motifs, the compounds now form uniform spherical aggregates in organic solvents. From the Lippert-Mataga plots, the biuret-appended chromophore **DACHPyPB** also possesses a high dipole moment of 11.2 D in the excite state which is attributed to formation of a pyrene exciplex. In the ground state, the compounds exhibit a bisignate Cotton bands at 418 nm is assigned to exciton coupling between the pyrene moieties. Unexpectedly, the formation of self-assembled vesicles

resulted in a loss of CPL activity as shown by the weak g_{lum} obtained compared to that of **DiPy** without biuret. This could be due to structural constraints that disfavor those conformations suitable for the formation of an emissive exciplex or, possibly, a cancelling of the polarization due to contributions from emission from different locations on the aggregates if these are highly ordered. In the future, it would be interesting to investigate the chiroptical emission from individual aggregates of **DACHPyPB** in the solid state through the use of a confocal fluorescence microscope equipped with optics for CPL detection.

3-5 References

1. Riehl, J. P.; Richardson, F. S. *Chem. Rev.* **1986**, *86*, 1.
2. Brittain, H. G. *Chirality* **1996**, *8*, 357.
3. Schadt, M. *Annu. Rev. Mater. Sci.* **1997**, *27*, 305.
4. Zhan, X.; Xu, F. F.; Zhou, Z.; Yan, Y.; Yao, J.; Zhao, Y. S. *Adv. Mater.* **2021**, *33*, 2104418.
5. Sherson, J. F.; Krauter, H.; Olsson, R. K.; Julsgaard, B.; Hammerer, K.; Cirac, I.; Polzik, E. S. *Nature* **2006**, *443*, 557.
6. Wagenknecht, C.; Li, C.-M.; Reingruber, A.; Bao, X.-H.; Goebel, A.; Chen, Y.-A.; Zhang, Q.; Chen, K.; Pan, J.-W. *Nat. Photonics* **2010**, *4*, 549.
7. Shuvaev, S.; Fox, M. A.; Parker, D. *Angew. Chem. Int. Ed.* **2018**, *57*, 7488.
8. Naaman, R.; Waldeck, D. H. *J. Phys. Chem. Lett.* **2012**, *3*, 2178.
9. Naaman, R.; Waldeck, D. H. *Annu. Rev. Phys. Chem.* **2015**, *66*, 263.
10. Naaman, R., Paltiel, Y., & Waldeck, D. H. *Nat. Rev. Chem.* 2019, 3, 250.
11. Deng, Y.; Wang, M.; Zhuang, Y.; Liu, S.; Huang, W.; Zhao, Q. *Light: Sci. Appl.* **2021**, *10*, 1.
12. Farshchi, R.; Ramsteiner, M.; Herfort, J.; Tahraoui, A.; Grahn, H. T. *Appl. Phys. Lett.* **2011**, *98*, 162508.

13. Brandt, J. R.; Wang, X.; Yang, Y.; Campbell, A. J.; Fuchter, M. J. *J. Am. Chem. Soc.* **2016**, *138*, 9743.

14. Nuzzo, D. D.; Kulkarni, C.; Zhao, B.; Smolinsky, E.; Tassinari, F.; Meskers, S. C. J.; Naaman, R.; Meijer, E. W.; Friend, R. H. *ACS Nano* **2017**, *11*, 12713.

15. Lunkley, J. L.; Shirotani, D.; Yamanari, K.; Kaizaki, S.; Muller, G. *J. Am. Chem. Soc.* **2008**, *130*, 13814.

16. Lis, S.; Elbanowski, M.; M˛akowska, B.; Hnatejko, Z. *J. Photochem. Photobiol. A* **2002**, *150*, 233.

17. Sánchez-Carnerero, E. M.; Agarrabeitia, A. R.; Moreno, F., Maroto, B. L.; Muller, G.; Ortiz, M. J.; de la Moya, S. *Chem. Eur. J.* **2015**, *21*, 13488.

18. Harada, T.; Nakano, Y.; Fujiki, M.; Naito, M.; Kawai, T.; Hasegawa, Y. *Inorg. Chem.* **2009**, *48*, 11242.

19. Yeung, CT.; Yim, KH.; Wong, HY.; Pal, R.; Lo, WS.; Yan, SC.; Wong, M. YM.; Yufit, D.; Smiles, D. E.; McCormick, L. J.; Teat, S. J.; Shuh, D. K.; Wong, WT.; Law, GL. *Nat. Commun.* **2017**, *8*, 1128.

20. Sánchez-Carnerero, E. M.; Moreno, F.; Maroto, B. L.; Agarrabeitia, A. R.; Ortiz, M. J.; Vo, B. G.; Muller, G.; Moya, S. D. L. *J. Am. Chem. Soc.* **2014**, *136*, 3346.

21. Zinna, F.; Bruhn, T.; Guido, C. A.; Ahrens, J.; Bröring, M.; Di Bari, L.; Pescitelli, G. *Chem. Eur. J.* **2016**, *22*, 16089.

22. Field, J. E.; Muller, G.; Riehl, J. P.; Venkataraman, D. *J. Am. Chem. Soc.* **2003**, *125*, 11808.

23. Otani, T.; Tsuyuki, A.; Iwachi, T.; Someya, S.; Tateno, K.; Kawai, H.; Saito, T.; Kanyiva, K. S.; Shibata, T. *Angew. Chem. Int. Ed.* **2017**, *56*, 3906.

24. Zhao, W. L.; Li, M.; Lu, H. Y.; Chen, C. F. *Chem. Comm.* **2019**, *55*, 13793.

25. Mori, T. *Chem. Rev.* **2021**, *121*, 2373.

26. Morisaki, Y.; Gon, M.; Sasamori, T.; Tokitoh, N.; Chujo, Y. *J. Am. Chem. Soc.* **2014**, *136*, 3350.

27. Hassan, Z.; Spuling, E.; Knoll, D. M.; Lahann, J.; Bräse, S. *Chem. Soc. Rev.* **2018**, *47*, 6947.

28. Kumar, J.; Nakashima, T.; Tsumatori, H.; Kawai, T. *J. Phys. Chem. Lett.* **2014**, *5*, 316.

29. Liu, J.; Su, H.; Meng, L.; Zhao, Y.; Deng, C.; Ng, J. C. Y.; Lu, P.; Faisal, M.; Lam, J. W. Y.; Huang, X.; Wu, H.; Wong, K. S.; Tang, B. Z. *Chem. Sci.* **2012**, *3*, 2737.

30. Han, D.; Yang, X.; Han, J.; Zhou, J.; Jiao, T.; Duan, P. *Nat. Commun.* **2020**, *11*, 5659.

31. Wade, J.; Brandt, J. R.; Reger, D.; Zinna, F.; Amsharov, K. Y.; Jux, N.; Andrews, D. L.; Fuchter, M. J. *Angew. Chem. Int. Ed.* **2021**, *60*, 222.

32. San Jose, B. A.; Yan, J.; Akagi, K. *Angew. Chem. Int. Ed.* **2014**, *53*, 10641.

33. Wan, L.; Wade, J.; Salerno, F.; Arteaga, O.; Laidlaw, B.; Wang, X.; Penfold, T.;

Fuchter, M. J.; Campbell, A. J. *ACS Nano* **2019**, *13*, *7*, 8099.

34. Wade, J.; Hilfiker, J. N.; Brandt, J. R.; Liirò-Peluso, L.; Wan, L.; Shi, X.; Salerno, F.; Ryan, S. T. J.; Schöche, S.; Arteaga, O.; Jávorfi, T.; Siligardi, G.; Wang, C.; Amabilino, D. B.; Beton, P. H.; Campbell, A. J.; Fuchter, M. J. *Nat. Commun.* **2020**, *11*, 6137.

35. Imagawa, T.; Hirata, S.; Totani, K.; Watanabe, T.; Vacha, M. *Chem. Commun.* **2015**, *51*, 13268.

36. Li, M.; Li, S. H.; Zhang, D.; Cai, M.; Duan, L.; Fung, M. K.; Chen, C. F. *Angew. Chem. Int. Ed.* **2018**, *57*, 2889.

37. Frederic, L.; Desmarchelier, A.; Favereau, L.; Pieters, G. *Adv. Funct. Mater.* **2021**, *31*, 2010281.

38. Feuillastre, S.; Pauton, M.; Gao, L.; Desmarchelier, A.; Riives, A. J.; Prim, D.; Tondelier, D.; Geffroy, B.; Muller, G.; Clavier, G.; Pieters, G. *J. Am. Chem. Soc.* **2016**, *138*, 3990.

39. Li, M.; Wang, Y.-F.; Zhang, D.; Duan, L.; Chen, C.-F. *Angew. Chem. Int. Ed.* **2020**, *59*, 3500.

40. Tanaka, H.; Inoue, Y.; Mori, T. *ChemPhotoChem* **2018**, *2*, 386.

41. Nagata, Y.; Mori, T. *Front. Chem.* **2020**, *8*, 448.

42. Newman, M. S.; Sankaran, V.; Olson, D. R. *J. Am. Chem. Soc.* **1976**, *98*, 3237.

43. Ng, M.-K.; Chow, H.-F.; Chan, T.-L.; Mak, T. C. W. *Tetrahedron Lett.* **1996**, *37*, 2979.

44. Takaishi, K.; Hinoide, S.; Matsumoto, T.; Ema, T. *J. Am. Chem. Soc.* **2019**, *141*, *30*, 11852.

45. Li, Y.; Xue, C.; Wang, M.; Urbas, A.; Li, Q. *Angew. Chem. Int. Ed.* **2013**, *52*, 13703.

46. Suzuki, S.; Fujii, T.; Baba, H. *J. Mol. Spectrosc.* **1973**, *47*, 243.

47. Takaishi, K.; Kawamoto, M.; Tsubaki, K. *Org. Lett.* **2010**, *12*, 1832.

48. Takaishi, K.; Yamamoto, T.; Hinoide, S.; Ema, T. *Chem. Eur. J.* **2017**, *23*, 9249.

49. Takaishi, K.; Hinoide, S.; Matsumoto, T.; Ema, T. *J. Am. Chem. Soc.* **2019**, *141*, 11852.

50. Im, Y.; Kim, M.; Cho, Y. J.; Seo, J. A;, Yook, K. S.; Lee, J. Y. *Chem. Mater.* **2017**, *29*, 1946.

51. Uejima, M.; Sato, T.; Yokoyama, D.; Tanaka, K.; Park, J. W. *Phys. Chem. Chem. Phys.* **2014**, *16*, 14244.

52. Xu, S.; Duan, Y.; Liu, B. *Adv. Mater.* **2020**, *32*, 1903530.

53. Nawara, K.; Waluk, J. *Anal. Chem.* **2019**, *91*, 5389.

54. Harada, N.; Nakanishi, K. *Acc. Chem. Res.* **1972**, *5*, 257.

55. Nakanishi, K.; Berova, N.; Woody, R. W. *Circular dichroism: Principles and Applications.* (Wiley, New York, **2000**), 361.

56. Kimoto, T.; Tajima, N.; Fujiki, M.; Imai, Y. *Chem. Asian. J.* **2012**, *7*, 2836.

57. Deuβen, H. J.; Shibaev, P. V.; Vinokur, R.; Bjørnholm, T.; Schaumburg, K.; Bechgaard, K.; Shibaev, V. P. *Liq. Cryst.* **1996**, *21*, 327.

58. Van Es, J. J. G. S.; Biemans, H. A. M.; Meijer, E. W. *Tetrahedron Asymmetry* **1997**, *8*, 1825.

59. Rosini, C.; Superchi, S.; Peerlings, H. W. I.; Meijer, E. W. *Eur. J. Org. Chem.* **2000**, *2000*, 61.

60. Delden, R. A. V.; Mecca, T.; Rosini, C.; Feringa, B. L. *Chem. Eur. J.* **2004**, *10*, 61.

61. Matsushita, S.; Jeong, Y. S.; Akagi, K. *Chem. Commun.* **2013**, *49*, 1883.

62. Loewe, R. S.; Khersonsky, S. M.; McCullough, R. D. *Adv. Mater.* **1999**, *11*, 250.

63. Grenier, C. R. G.; George, S. J.; Joncheray, T. J.; Meijer, E. W.; Reynolds, J. R. *J. Am. Chem. Soc.* **2007**, *129*, *35*, 10694.

64. Jeong, Y. S.; Akagi, K. *Macromolecules* **2011**, *44*, *8*, 2418.

65. Caras-Quinteroa, D.; Bäuerle, P. *Chem. Commun.* **2002**, 2690.

66. Xu, Z.; Kang, J.-H.; Wang, F.; Paek, S.-M.; Hwang, S.-J.; Kim, Y.; Kim, S.-J.; Choy, J.-H.; Yoon, J. *Tetrahedron Lett.* **2011**, *52*, 2823.

67. Wong, K.-T.; Chen, R.-T. *Tetrahedron Lett.* **2002**, *43*, 3313.

68. Rapi, Z.; Nemcsok, T.; Pálvölgyi, Á.; Keglevich, G.; Grün, A.; Bakó, P. *Chirality* **2017**, *29*, 257.

69. Caras-Quintero, D.; Bäuerle, P. *Chem. Commun.* **2004**, 926.

70. Liu, C.-Y.; Chong, H.; Lin, H.-A.; Yamashita, Y.; Zhang, B.; Huang, K.-W.; Hashizume, D.; Yu, H.-H. *Org. Biomol. Chem.* **2015**, *13*, 8505.

71. Liu, M.; Zhang, L.; Wang, T. *Chem. Rev.* **2015**, *115*, 7304.

72. Albano, G.; Pescitelli, G.; Di Bari, L. *Chem. Rev.* **2020**, *120*, 10145.

73. Sang, Y.; Han, J.; Zhao, T.; Duan, P.; Liu, M. *Adv. Mater.* **2020**, *32*, 1900110.

74. Inai, Y., Sisido, M., & Imanishi, Y. *J. Phys. Chem.* **1990**, *94*, 2734.

75. Kumar, J.; Nakashima, T.; Tsumatori, H.; Mori, M.; Naito, M.; Kawai, T. *Chem. Eur. J.* **2013**, *19*, 14090.

76. Ohishi, Y., & Inouye, M. *Tetrahedron Lett.* **2019**, *60*, 151232.

77. Amako, T.; Nakabayashi, K.; Suzuki, N.; Guo, S.; Rahim, N. A. A.; Harada, T.; Fujiki, M.; Imai, Y. *Chem. Commun.* **2015**, *51*, 8237.

78. Hara, N.; Shizuma, M.; Harada, T.; Imai, Y. *RSC Adv.* **2020**, *10*, 11335.

79. Nakanishi, S.; Nakabayashi, K.; Mizusawa, T.; Suzuki, N.; Guo, S.; Fujiki, M.; Imai, Y. *RSC Adv.* **2016**, *6*, 99172.

80. Yang, W.; Longhi, G.; Abbate, S.; Lucotti, A.; Tommasini, M.; Villani, C.; Catalano, V. J.; Lykhin, A. O.; Varganov, S. A.; Chalifoux, W. A. *J. Am. Chem. Soc.* **2017**, *139*, *37*, 13102.

81. Mataga, N; Kaifu, Y.; Koizumi, M. *Bull. Chem. Soc. Jpn.* **1956**, *29*, 465.

82. E. Von Lippert, Z. *Electrochem.* **1957**, *61*, 962.

83. Bieszczad, B.; Gilheany, D. G. *Angew. Chem. Int. Ed.* **2017**, *56*, 4272.

84. Kwit, M.; Gawronski, J. *Tetrahedron* **2003**, *59*, 9323.

85. Takaishi, K.; Iwachido, K.; Ema, T. *J. Am. Chem. Soc.* **2020**, *142*, 1774.

Chapter 4. Investigation of Hole-Transporting (HT) Type Materials Forming Exciplexes with Circularly Polarized Emission

4-1 Principle and Introduction

As we mentioned in Chapter 2, the spatial separation of HOMO and LUMO orbitals in a fluorophore is a critical element to minimize ΔE_{ST} and promoting efficient TADF. Apart from tailoring the electron donating and accepting moieties to tune the intramolecular charge transfer (CT) properties in a TADF chromophore, the formation of a CT excited-state complex (exciplex) between donor and acceptor molecules is another approach to promote TADF.[1-3] As shown in **Figure 4-1**, an emissive exciplex may possess a triplet state at a similar energy as the exciplex S_1 state and thus undergo rISC.[1] Since during exciton formation the HOMO and LUMO are distributed over the donor and acceptor moieties, respectively, ΔE_{ST} can be substantially reduced and thus facilitate the rISC process between nearly energy-degenerate singlet and triplet states. Practical advantages in exciplex-type OLEDs compared to conventional TADF OLEDs include shortening of cumbersome synthetic routes, tuning emission wavelength by altering diverse donor and acceptor materials, and simplified architecture in device fabrication. To achieve high-performance exciplex-based OLEDs, some additional design guidelines should be considered: (1) efficient electron and hole mobilities in the donor and acceptor

materials, (2) sufficient difference between HOMO of the donor and the LUMO of the acceptor molecules to enhance CT, (3) sufficient accumulation of charge carriers at the D:A interface, (4) high triplet energy of the individual materials compared to the triplet energy of the exciplex.[1]

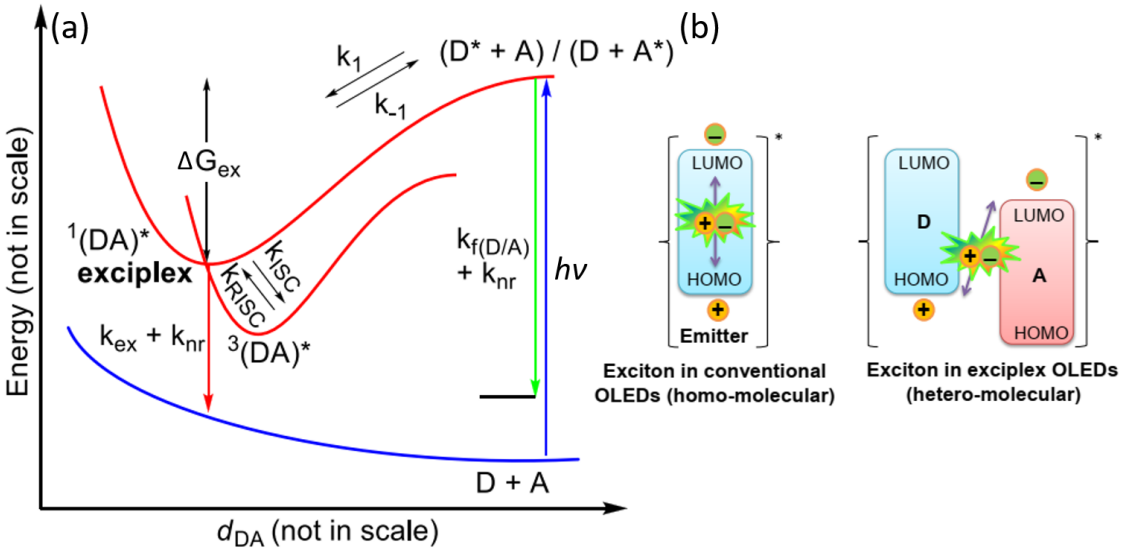

Figure 4-1. (a) Simplified energy diagrams in various processes during exciplex formation in solution under photoexcitation or carrier recombination. (b) Schematic representation of excitons in conventional and exciplex OLEDs. Reused with permission from ref 1. Copyright 2018, American Chemical Society.

In the past decade, an abundant variety of research related to exciplex-based OLEDs has been reported.[4-14] In 2012, Adachi *et al.* demonstrated an ingenious approach to carry out efficient rISC process to surpass traditional fluorescent EQE limit in exciplex-based OLEDs composed of blend of a donor material (4,4',4''-tris[3-methylphenyl(phenyl)

amino]triphenylamine, **m-MTDATA**) and an acceptor material (tris-[3-(3-pyridyl)mesityl]borane, **3TPYMB**). The high contribution of delayed fluorescence component to the PL efficiency of the exciplex emission thanks to harvesting of triplet excitons contributed to the performance of this exciplex-type OLED with an EQE of 5.4%,[14] which is already higher than conventional fluorescent OLEDs. Later, Chou et al. reported that **PO-T2T**, possessing deep LUMO/HOMO (-2.83/-6.83 eV) energy, can be mixed with various hole-transporting materials with different HOMO levels to finely tune the exciplex emission from blue to red (**Figure 4-2**). Combining the tandem architectures of blue (**mCP**:**PO-T2T**) and yellow (**DTAF**:**PO-T2T**) exciplex systems gave rise to the first tandem all-exciplex white OLEDs with excellent device performance with EQE of 11.6%.[15] In 2020, with appropriate D/A (**BCzPh**/**CN-T2T**) combination and intelligent fabrication of the electroluminescence device, Wong *et al.* reported green exciplex OLEDs based on the bulk-heterojunction (BHJ) architecture,[16] improving the inefficient interfacial exciplex OLEDs and increasing the EQE from 7.7% to a record-high 26.4%. This clearly shows the feasibility and strength of this approach and its usefulness for future commercial applications (**Figure 4-3**).

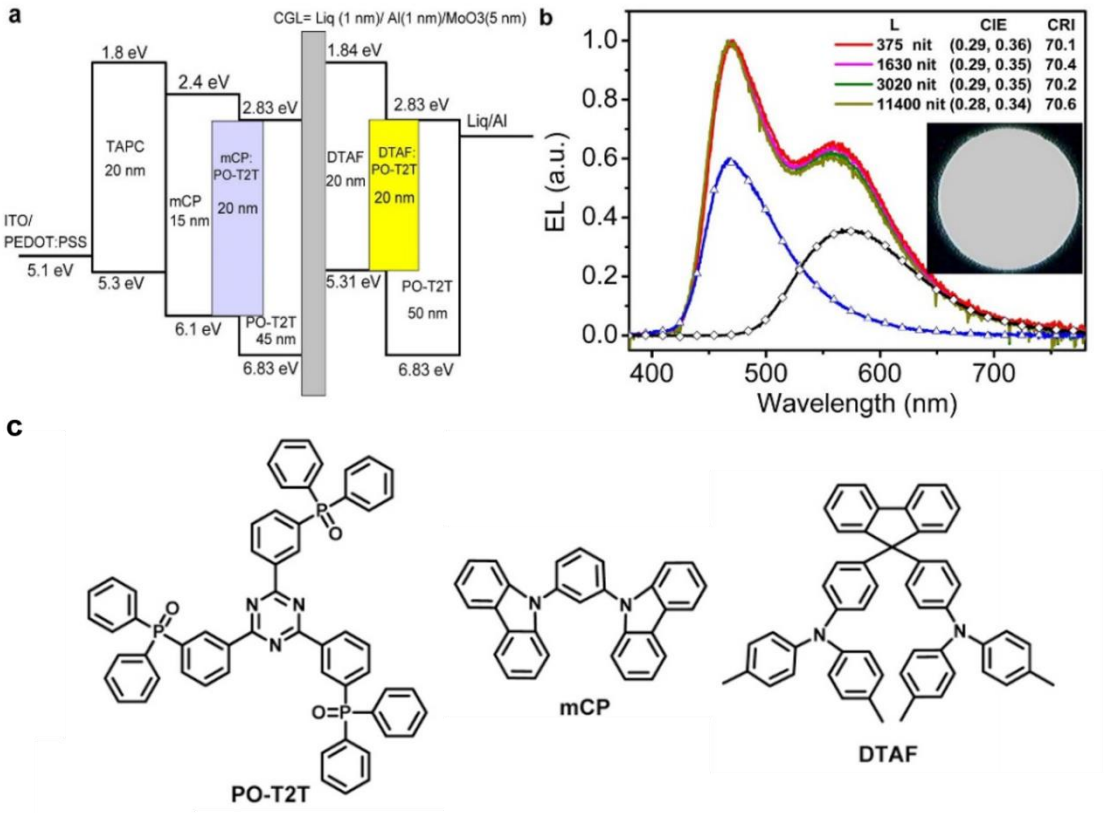

Figure 4-2. The first tandem all-exciplex-based OLEDs. (a) The electronic levels of tandem architecture of white exciplex OLEDs, consist of internal stacking of blue (**mCP**:**PO-T2T**) and yellow (**DTAF**:**PO-T2T**) exciplex devices. (b) EL spectra of white-light emitting devices with different brightness, and the two emission bands corresponding to blue and yellow exciplex emission. (c) Chemical structures of **PO-T2T**, **mCP** and **DTAF** in the white OLED. Readapted with permission from ref 15. Copyright 2014 Springer Nature.

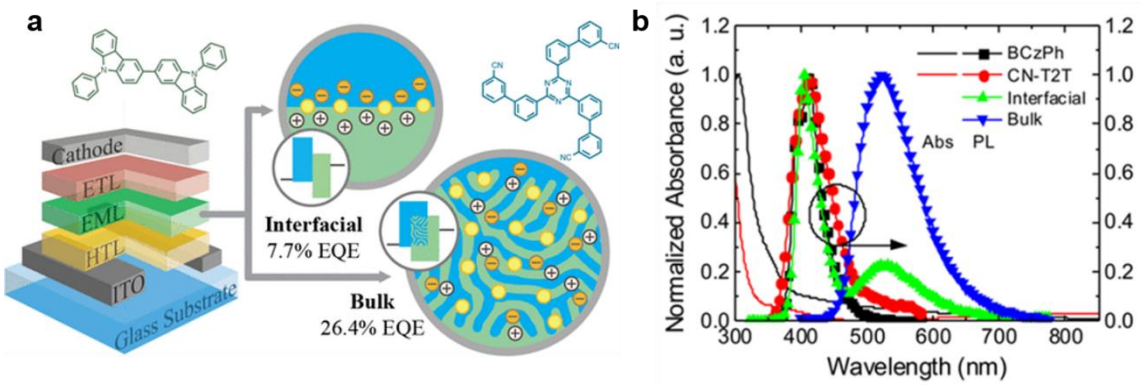

Figure 4-3. Exciplex-type OLEDs using interfacial or bulk heterojunction architectures. (a) Schematic illustration of interfacial or bulk-type green exciplex (**BCzPh**:**CN-T2T**) in the emitting layer of OLEDs. (b) PL spectra of **BCzPh** (black) and **CN-T2T** (red) in neat films and interfacial (green) and bulk (blue) **BCzPh:CN-T2T** blended films. The interfacial blended film shows an intense residual emission from **CN-T2T** and a minor exciplex band, while the bulk blended film only reveals a major exciplex emission band. Reprinted with permission from ref 16. Copyright 2020 American Chemical Society.

4-2 Molecular Design and Synthesis

As mentioned in Chapter 3, numerous strategies can be used to enhance the g_{lum} of luminescent systems, and the use of an emissive exciplex could be an interesting approach. In an exciplex, the angle $cos\theta_{\mu,m}$ between the electric transition dipole moment (μ) and the magnetic transition dipole moment (m) can, in principle, be adjusted to enhance the dissymmetry factor g_{lum} of the luminescence would be influenced during the charge-

transfer process. g_{lum} could be expressed in the equation in **Figure 4-4**.[17-21]

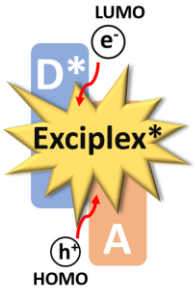

$$g_{lum} = \frac{4|\vec{\mu}_{ij}| \cdot |\vec{m}_{ji}| cos\theta_{\mu,m}}{|\vec{\mu}_{ij}|^2 + |m_{ji}|^2} \quad \text{(Eq 1)}$$

$$= 4\frac{|\vec{m}_{ji}|}{|\vec{\mu}_{ij}|} cos\theta_{\mu,m} \quad \text{(Eq 2)}$$

Figure 4-4. Illustration of circularly polarized exciplex and the equation of g_{lum}.[17-21] The g_{lum} is correlated to electric dipole forbidden/magnetic dipole-allowed transitions. For the transition $i \rightarrow j$ the luminescence dissymmetry factor can be written as Eq 1. μ_{ij} and m_{ji} are the electric and magnetic transition dipole vectors and $\theta_{\mu,m}$ is the angle between them. In the case of an electric dipole-allowed transition, the $|m_{ji}|^2$ term is negligible with respect to $|\mu_{ij}|^2$; thus, the equation could be simplified into Eq 2.

So far, only few groups applied the circular-polarized exciplex strategy to enhance g_{lum} in their work. Meijer's group first reported the exciplex emission from the frustrated Lewis pair (i.e., triphenylborane and tris(pentafluorophenyl)-borane) in chiral 1D supramolecular copolymers (**Figure 4-5**).[22] Upon irradiation, the self-assembled molecular arrangement during copolymerization induced the formation of long-lived charge-transfer states at B-N interfaces, producing delayed circularly polarized emission with a g_{lum} of 10^{-3}. When the D/A mixing solution was drop-cast onto a glass substate, the

PL spectra of bulk blended films showed only exciplex emission without residual emission from homopolymers, suggesting a higher degree of D/A mixing or a efficient exciton migration in solid state. Moreover, Favereau's group demonstrated the use of a luminescent complex composed of chiral bicarbazole donor and achiral acceptor for a novel strategy to design CP-exciplexes (**Figure 4-6**).[23] By mixing the chiral donor materials with diverse acceptors with variable LUMO levels, they were able to tune the exciplex emission color from sky-blue to deep-red. The highly efficient green-yellow chiral exciplex emitted circular polarzied luminescence with PLQY of 10% and g_{lum} of 7×10^{-3} in blended film, which is 10-fold enhancement in comparison with the g_{lum} of chiral donor (7×10^{-4}) in neat film.

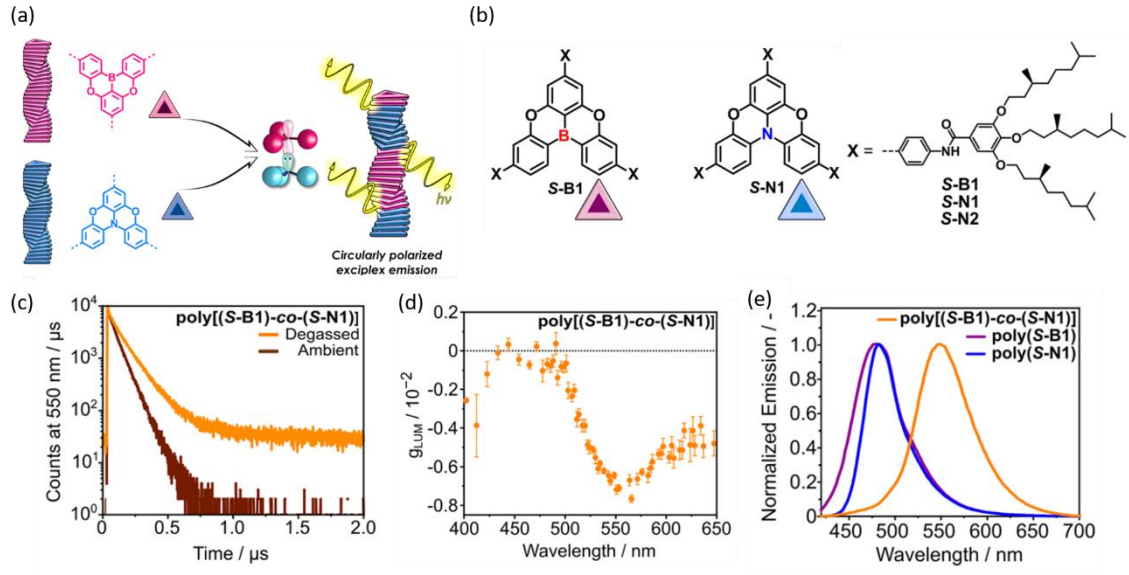

Figure 4-5. The first example of circularly polarized exciplex. (a) Schematic illustration of supramolecular frustrated Lewis pairs (FLP) based copolymers (b) Chemical structure

of chiral triphenylborane and triarylamine monomers. (c) Transient PL decay profiles of FLP copolymers **poly[(*S*-B1)-*co*-(*S*-N1)]** in degassed (orange) or aerated (brown) decalin. Excited at 400 nm, emission at 550 nm, measured at 20°C. (d) CPL spectrum of FLP copolymers **poly[(*S*-B1)-*co*-(*S*-N1)]**. Excited at 365 nm. (e) PL spectra of drop-casted films of **poly(*S*-B1)** (purple), **poly(*S*-N1)** (blue) and **poly[(*S*-B1)-*co*-(*S*-N1)]** (orange). Excited at 400 nm. Readapted with permission from ref 22. Copyright 2020 American Chemical Society.

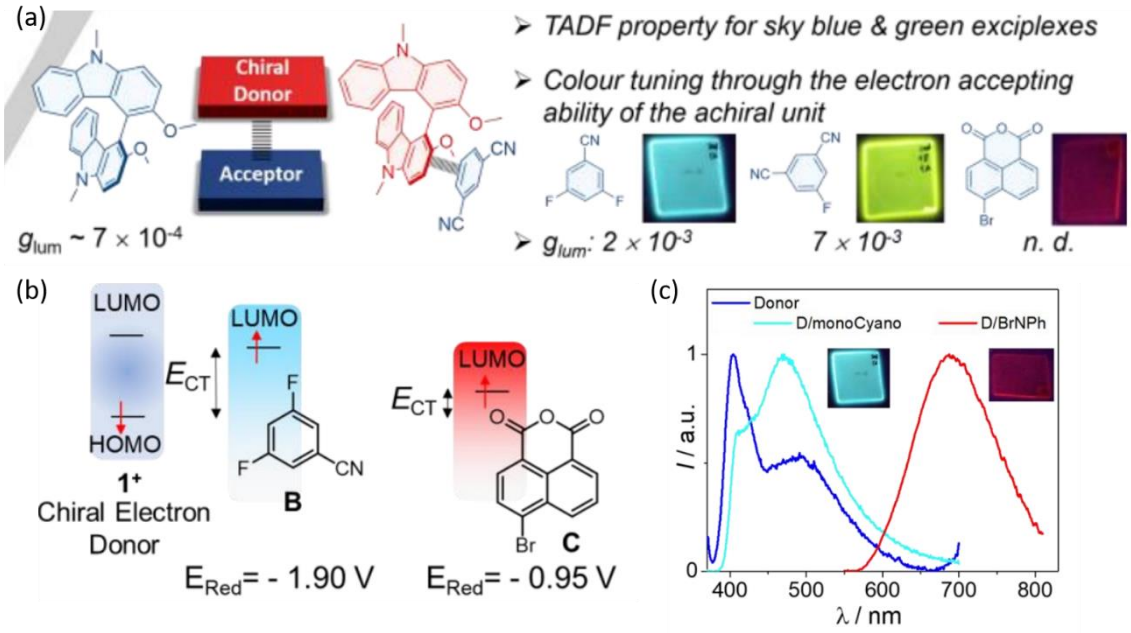

Figure 4-6. (a) Schematic illustration of circular polarized exciplex consist of chiral donor (bicarbazole) and diverse achiral acceptors (3,5-difluorobenzonitrile, 5-fluoroisophthalonitrile and 4- bromonaphthalene monohydride) with different electron-accepting abilities to tune exciplex emission from sky-blue to green-yellow to deep-red. The g_{lum} of CPL are elevated from 10^{-4} to 10^{-3} during the intermolecular charge transfer

process. (b) Energy levels of chiral donors and achiral acceptors. (c) PL spectra of neat film of donor molecules and blended films of donor:difluorobenzonitrile and donor: fluoroisophthalonitrile respectively, with associated pictures. Reused with permission from ref 23. Copyright 2021 Wiley-VCH GmbH.

To explore a strategy to increase g_{lum} based on the formation of a chiral exciplex, we considered five molecules that can constitute chiral electron donor components, illustrated in **Figure 4-7**. First, we choose the CP-TADF emitter **BNCNCz** as the model compound since its triplet energy level is high and it is suitable as an electron donor.[24] Next, we considered binaphthalene-based derivative **7BBNCz** composed of a binaphthalene core with axial chirality and a carbazole with a high triplet energy level to act as the appropriate hole-transporting material. In addition, from Prof. Liao's work on the systematic investigation of high triplet host materials based on phenylcarbazole derivatives,[25] we conceived phenylcarbazole-type derivatives **3CzPh**, **Ph3Cz** and **Ph4Cz** consisting of octahydrobinaphthalene with axial chirality and phenylcarbazole derivatives.

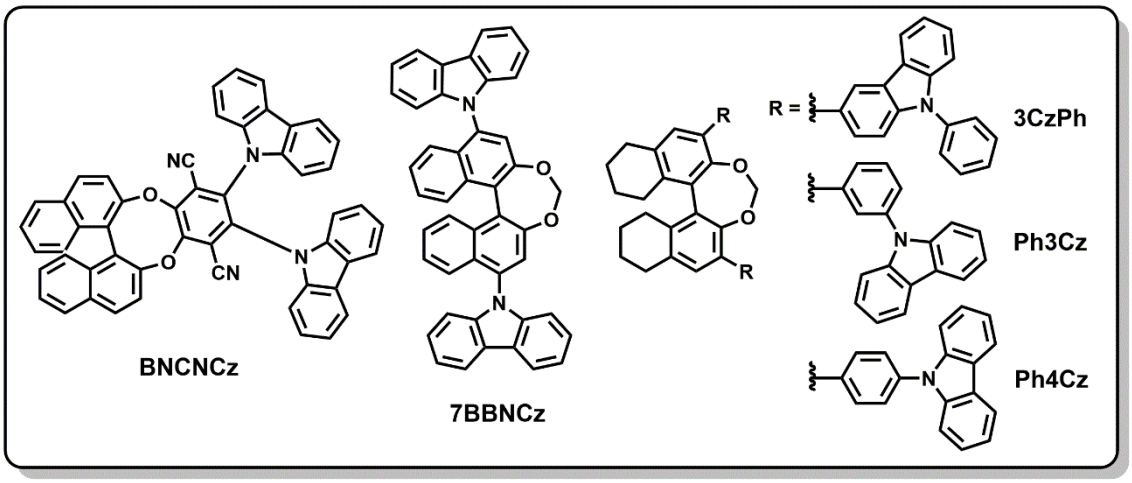

Figure 4-7. Chemical structures of chiral electron donor molecules in exciplex.

BNCNCz was synthesized according to previous literature reports.[24] **7BBNCz** was obtained from Buchwald-Hartwig Coupling between intermediate **7BBNBr2** and carbazole (**Scheme 4-1**). As shown in **Scheme 4-2**, optically-active **BINOL** was treated with Pt(IV)-catalyzed hydrogenation to obtain **H8-BINOL**.[26] After iodination by iodine-morpholine complex, **H8-BINOL** was converted to **H8-BNI2**.[27] Following S_N2 reaction with bromochloromethane to form **H8-7BBNI2**,[28] **Ph4Cz**, **Ph3Cz** and **3CzPh** were obtained after Pd(0)-catalyzed Suzuki-Miyaura coupling with the corresponding phenylcarbazle derivative.

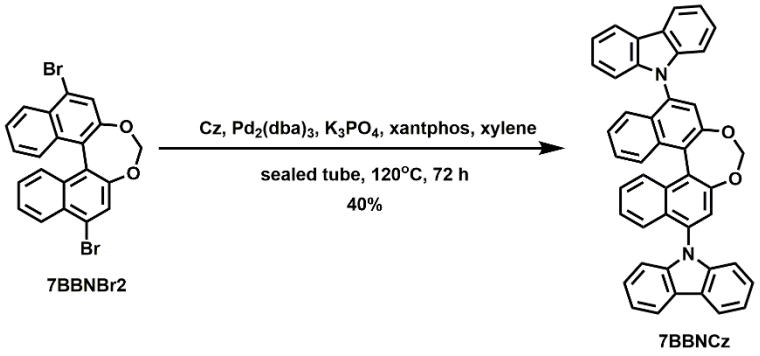

Scheme 4-1. Synthetic route of **7BBNCz**.

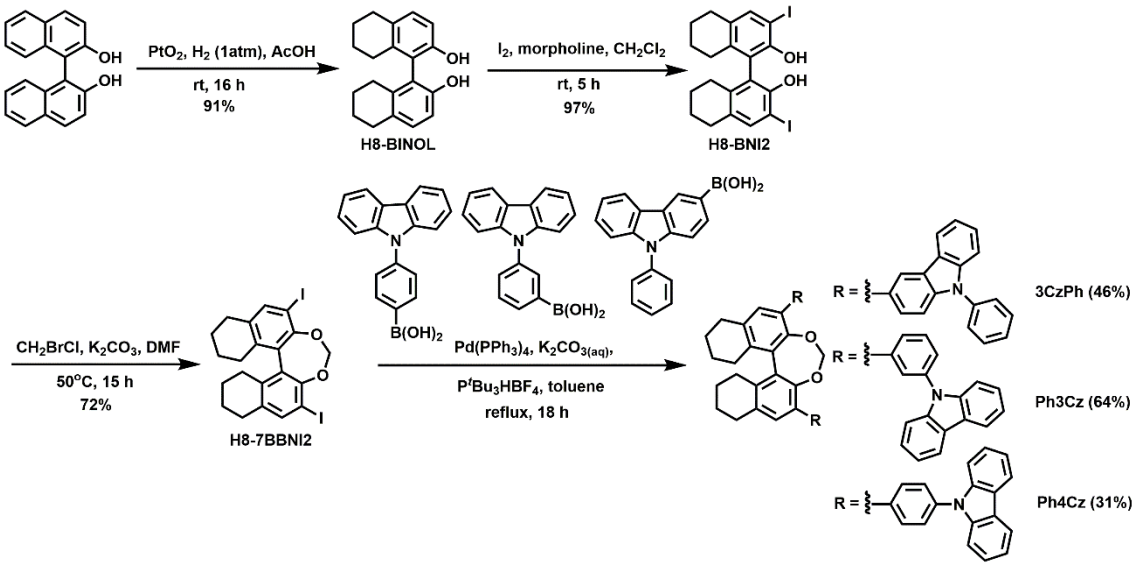

Scheme 4-2. Synthetic routes of phenylcarbazole derivatives.

4-3 Photophysical Properties

The photophysical properties of **7BBNCz** and phenylcarbazole derivatives (**3CzPh**, **Ph3Cz** and **Ph4Cz**) measured in solution (toluene, 10^{-6}M) and in neat films are shown in **Figure 4-8** and summarized in **Table 4-1**. In solution, the intense absorption peak around 300 nm of the four materials are assigned to the π-π* transition localized on the carbazole moiety, whereas the bands between 300 to 400 nm result from the π-π* transition between the carbazole moiety and the neighbor phenyl groups in the molecule.[25, 29-33] The three phenylcarbazole derivatives exhibit strong fluorescence with some vibronic structure, with the emission of **7BBNCz** located bathochromically with respect to the other derivatives due to the longer π-conjugation length. Phosphorescence was observed from

the compounds in toluene solution (10^{-5}M) at 77 K. This allows us to determine the triplet energy level and the E_T values of the four materials are in the sequence of **7BBNCz** (2.48 eV) < **Ph4Cz** (2.98 eV) < **3CzPh** (3.00 eV) < **Ph3Cz** (3.07 eV). They are in the same order as those of reference materials in literature and are high enough to serve as the electron donors for exciplex or host materials.

The compounds behave similarly in neat films as in solution except for a moderate red-shift in the emission owing to molecular aggregation. For the four materials, the deep-blue emission peaks are all above 400 nm and the second band of **7BBNCz** around 550 nm can be attributed to excimer emission (**Figure 4-9**).

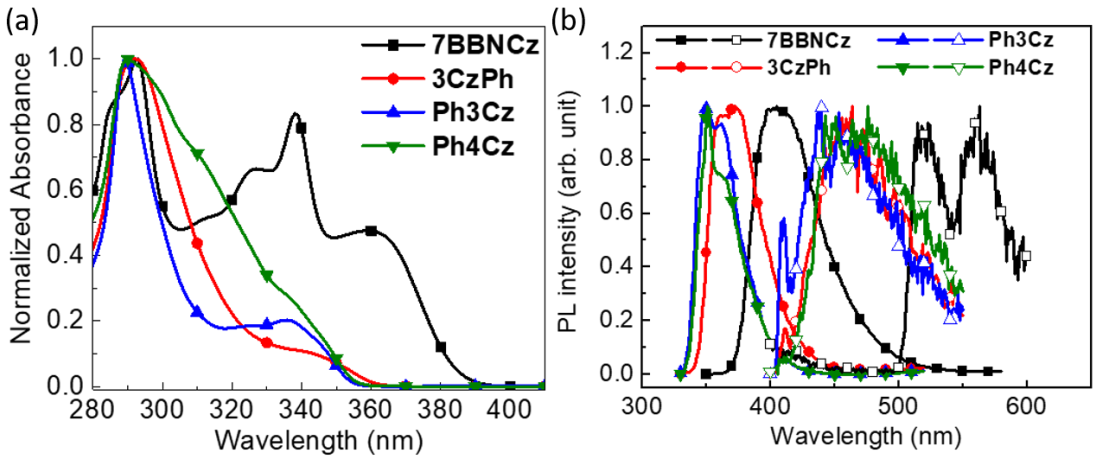

Figure 4-8. (a) Absorption, (b) PL (solid symbols) and phosphorescence (empty symbols) spectra of carbazole-based derivatives in toluene solution (10^{-6}M). PL spectra were excited at 300 nm and measured at 298K. Phosphorescence spectra were excited at 320 nm and measured at 77K.

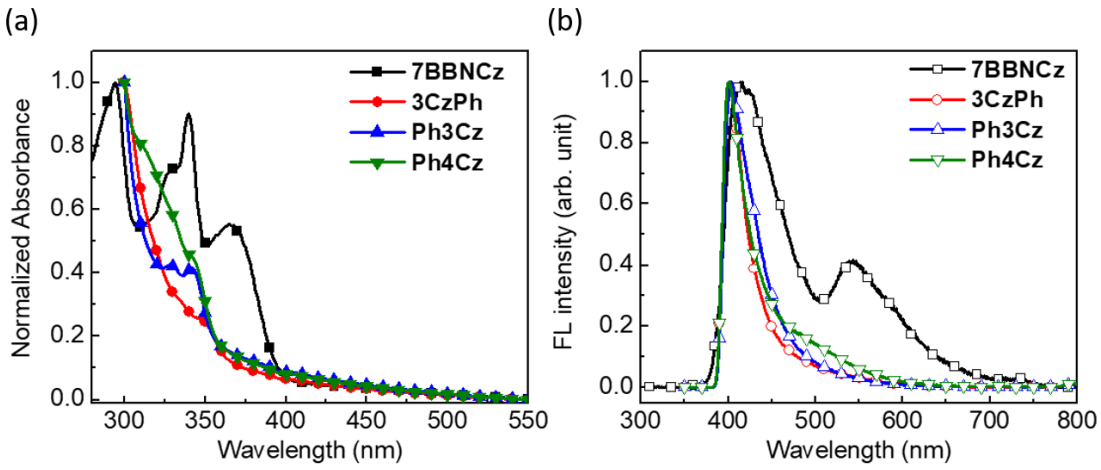

Figure 4-9. (a) Absorption and (b) PL spectra of carbazole-based derivatives in neat films. Excited at 300 nm.

Table 4-1. Summary of photophysical properties of carbazole-based derivatives.

Molecule	$\lambda_{Abs}{}^{a}$ (soln, nm)	λ_{Abs} (films, nm)	$\lambda_{FL}{}^{a}$ (soln, nm)	$\lambda_{FL}{}^{b}$ (films, nm)	$\lambda_{Phos}{}^{c}$ (soln, nm)	$E_T{}^{c}$(eV)
7BBNCz	293, 338, 359	294, 340, 365	405	415	513	2.48
3CzPh	292	349	362, 373	402	442	3.00
Ph3Cz	289, 336	329, 342	349, 362	403	437	3.07
Ph4Cz	290	342	351, 360	401	443	2.98

[a] Measured in dilute (10^{-6}M) toluene solution and excited at 300 nm. [b] Excited at 300 nm. [c] Measured in dilute (10^{-6}M) toluene solution at 77 K and estimated from the onset of phosphorescence spectra. Excited at 320 nm.

The chiroptical properties of carbazole-based derivatives in ground state were investigated by circular dichroism spectroscopy in solutions (CH_2Cl_2, 50 μM) (**Figure 4-**

10). The preferential absorptions of left and right circularly polarized light are identical in magnitude but opposite in sign for all enantiomeric pairs of carbazole-based molecules. The difference in the signs of CD spectra could be attributed to the intrinsic chirality of 1,1'-binaphthalene (R/S-**7BBNCz**) or 5,5',6,6',7,7',8,8'-octahydro-1,1'-binaphthalene (R/S-**3CzPh**, R/S-**Ph3Cz** and R/S-**Ph4Cz**) cores. The R-**7BBNCz** and R-**Ph3Cz** show a positive Cotton effect at 331 nm and at 303 nm, respectively, while R-**3CzPh** and R-**Ph4Cz** possess a negative Cotton effect at 298 nm and 311 nm, respectively, revealing the diverse optical activities in ground states. Compared the CD spectra with the absorption spectra, the strong bisignate Cotton effects for R/S-**3CzPh**, R/S-**Ph3Cz** and R/S-**Ph4Cz** are ascribed to the exciton coupling between neighboring chromophores, which arises from the interaction between the electric transition moments of intramolecular chromophores.[34-36] The $|g_{abs}|$, the quantitative parameters of magnitude of CD signals, for R/S-**3CzPh** (298 nm), R/S-**Ph3Cz** (275 nm) and R/S-**Ph4Cz** (311 nm) are 1.0×10^{-3}, 8.0×10^{-4} and 5.6×10^{-4}, respectively. As for R/S-**7BBNCz**, the $|g_{abs}|$ of 10^{-4}, implying that no enhancement from exciton coupling, originates from the intrinsic chirality of 1,1'-binaphthalene chromophore.

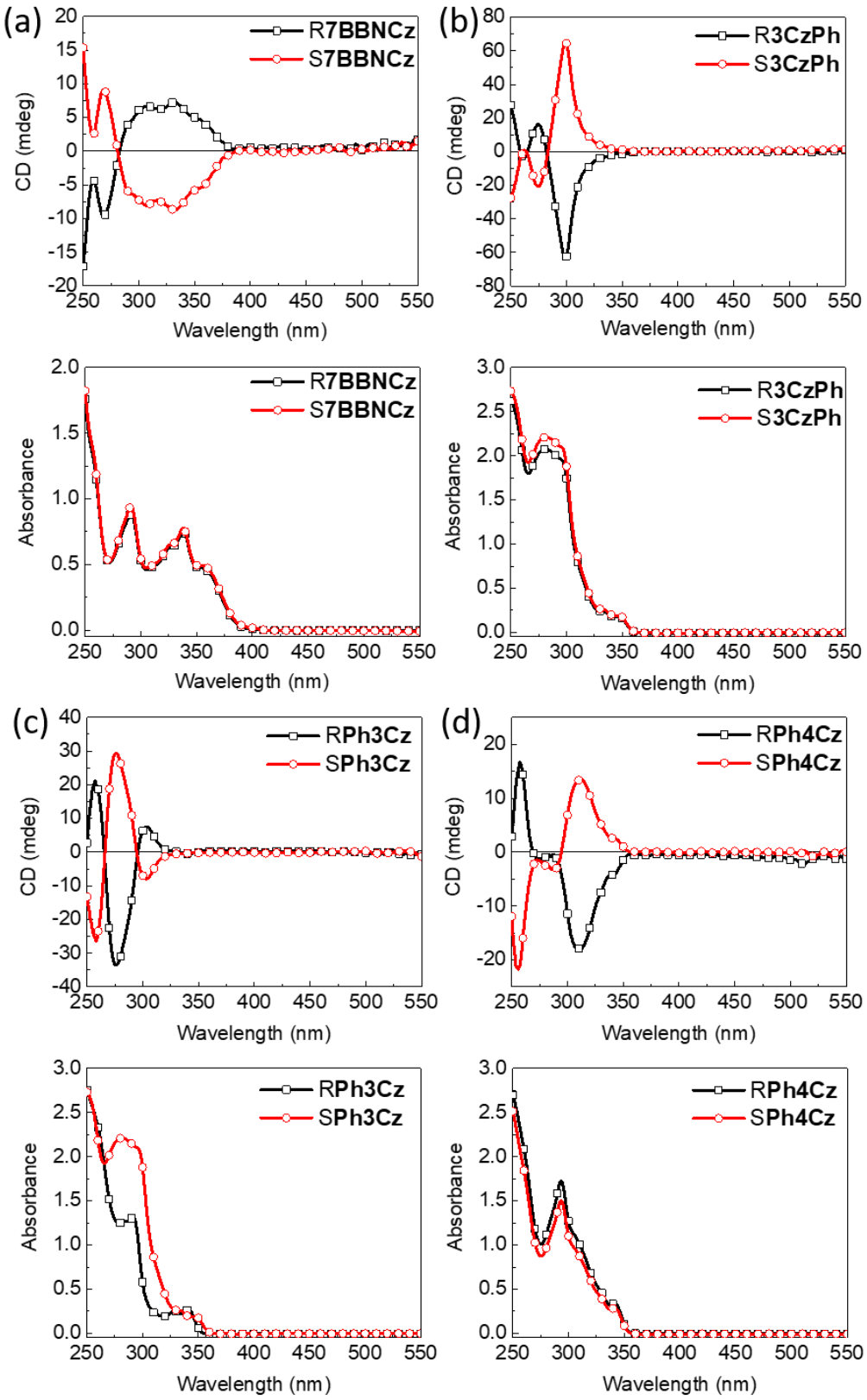

Figure 4-10. CD spectra of (a) R/S-**7BBNCz**, (b) R/S-**3CzPh**, (c) R/S-**Ph3Cz** and (d)

R/S-**Ph4Cz** in CH_2Cl_2 solution (10^{-5}M).

4-4 Thermal and Electrochemical Properties

The thermal stability of the carbazole-based derivatives can be assessed using thermogravimetric analysis (TGA). The four materials exhibit high thermal decomposition temperature (T_d, corresponding to 5% weight loss): 409 ºC for **7BBNCz**, 470 ºC for **3CzPh**, 404 ºC for **Ph3Cz** and 435 ºC for **Ph4Cz**. Nevertheless, the three molecules with aliphatic hydrocarbons (**3CzPh**, **Ph3Cz** and **Ph4Cz**) decomposed upon sublimation, so that these materials should be deposited by solution process for further investigation of photophysical properties in solid state.

The electrochemical properties were probed using cyclic voltammetry (CV) in view of obtaining the HOMO/LUMO levels of the materials. As depicted in **Figure 4-11** and summarized in **Table 4-2**, the redox potentials of **7BBNCz**, **3CzPh**, **Ph3Cz** and **Ph4Cz** were analyzed and calibrated with respect to the ferrocene/ferrocenium (Fc/Fc^+) redox couple. Irreversible oxidation waves were observed at an onset of 0.90, 0.91, 0.86 and 0.92 V for **7BBNCz**, **3CzPh**, **Ph3Cz** and **Ph4Cz**, respectively. It is very likely that the irreversible oxidation behaviors in all compounds can be assigned to the oxidation of the carbazole moiety.[37-41] It is frequently observed that carbazole moieties devoid of protection at the C-3 (or C-6) positions undergo coupling with the second molecule to

generate a dimer upon oxidation.[42-45] The HOMO energies are approximated from the onset of oxidation potentials with reference to the one of ferrocene (4.80 eV below vacuum). The HOMO levels of all the compounds are located at ca. –5.70 eV, which is in line with literature reports for phenylcarbazole analogues.[25] The LUMO levels were calculated from the HOMO values and the optical energy gap and determined to be -2.48, -2.27, -2.14, -2.22 eV for **7BBNCz**, **3CzPh**, **Ph3Cz** and **Ph4Cz**, respectively.

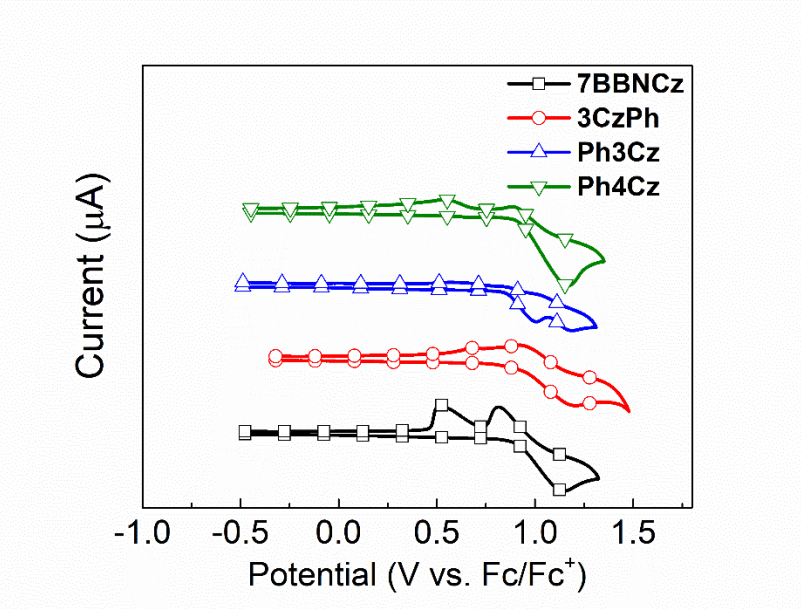

Figure 4-11. Cyclic voltammograms of **7BBNCz**, **3CzPh**, **Ph3Cz** and **Ph4Cz**. Oxidation scan was performed in CH_2Cl_2 solution (10^{-3}M) with 0.1 M of $^nBu_4NPF_6$ as a supporting electrolyte. A glassy carbon electrode was used as the working electrode; Scanning rate 300 mVs^{-1}.

Table 4-2. Electrochemical and thermal properties of carbazole-based derivatives.

Molecule	E_{ox}[a](V)	HOMO[b] (eV)	LUMO[c] (eV)	Optical E_g in solution[d] (eV)	T_d (°C)
7BBNCz	0.90	-5.70	-2.48	3.22	409.43
3CzPh	0.91	-5.71	-2.27	3.44	469.66
Ph3Cz	0.86	-5.66	-2.14	3.52	404.13
Ph4Cz	0.92	-5.72	-2.22	3.50	435.20

[a] Irreversible oxidation, obtained in 10^{-3}M CH_2Cl_2 with 0.1 M of tetrabutylammonium hexafluorophosphate ($^nBu_4NPF_6$) as supporting electrolyte with respect to ferrocene/ferrocene$^+$ (Fc/Fc^+) redox couple (at –4.80 V). [b] The HOMO levels are calculated by HOMO = –4.80 eV – E_{ox}. [c] The LUMO levels are estimated by LUMO = HOMO + E_g. [d] The optical E_g levels are determined by the onset of the absorption spectra.

4-5 Probing Exciplex Formation with T2T, QN Series (AIE Test)

Initially, investigations of exciplex formation in ETM:HTM blended films were lengthy due to the time needed for the fabrication of the films. In 2020, Prof. Chang proposed a fast-screening method (the AIE test) to more rapidly probe potential exciplex formation by acquiring the PL spectra in non-solvent.[46] By mixing the ETM and HTM in an aqueous solution, the formation of a suspension of aggregates mimicked the local conditions of a film, providing a confinement of the electron donor and electron acceptor molecules. The observation of broad, red-shifted emission formation was found to be a good indication of exciplex formation.

Suitable acceptor molecules (**47p-QN**, **47m-QN**, **56p-QN** and **56m-QN**) for chiral

donor molecule **BNCNCz** were selected to form an exciplex on the basis of their energy levels and probed using the AIE test (**Figure 4-12, 4-13** and **Table 4-3**). Based on the emission spectra, **BNCNCz**:**47p-QN** with the largest red-shifted emission band among other systems would be an appropriate candidate for exciplex system.

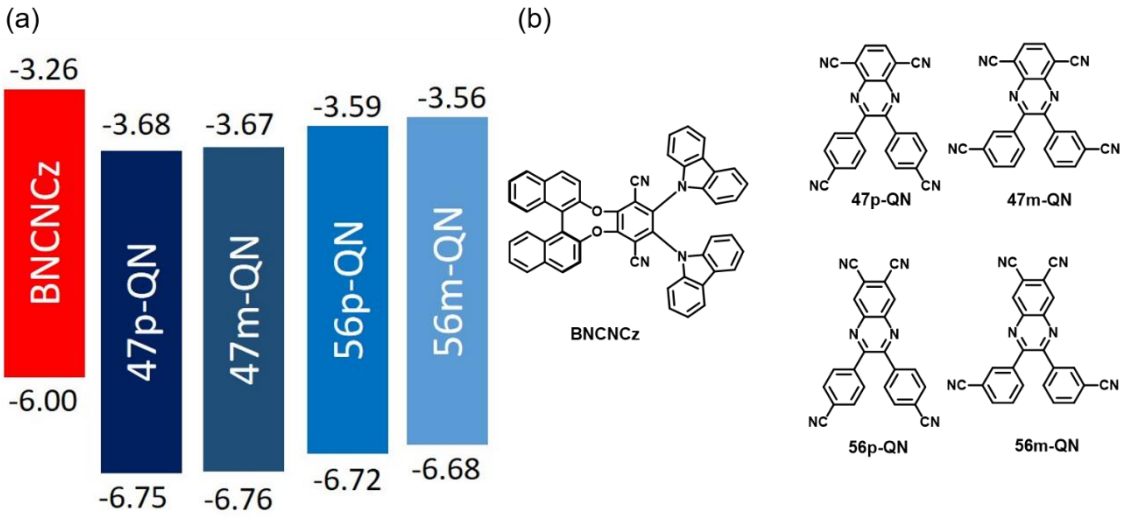

Figure 4-12. (a) Energy levels and (b) chemical structures of **BNCNCz** and QN-series.

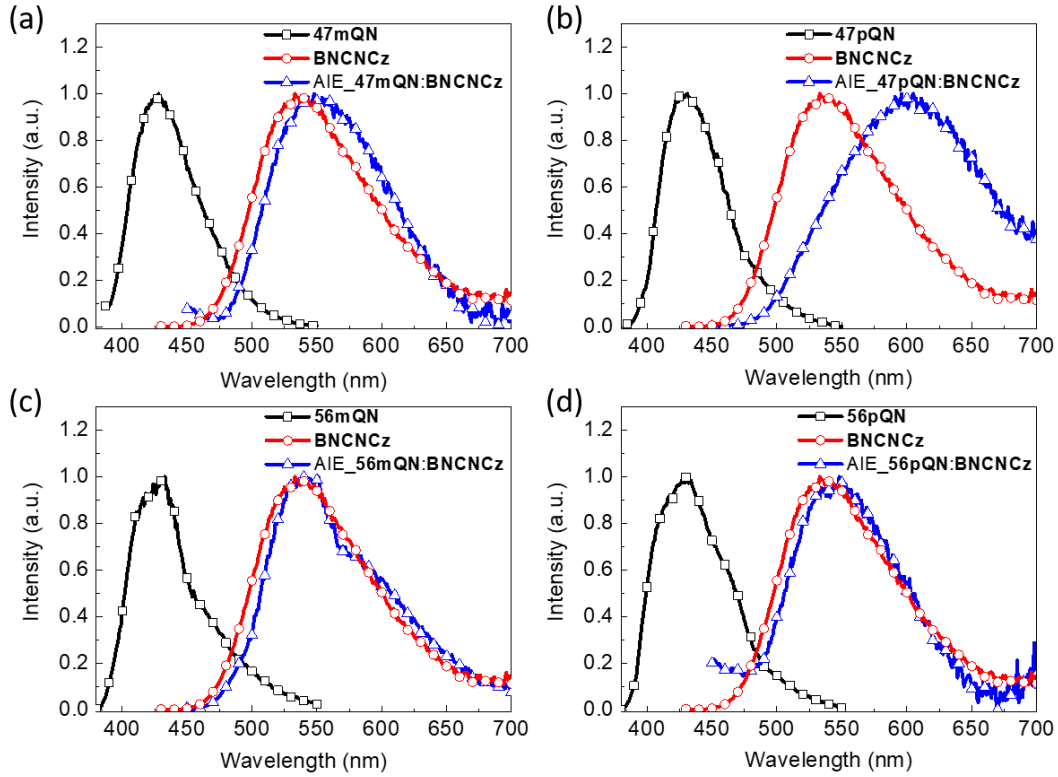

Figure 4-13. PL spectra of mixed (a) **BNCNCz:47m-QN**, (b) **BNCNCz:47p-QN**, (c) **BNCNCz:56m-QN** and (d) **BNCNCz:56p-QN** as suspensions in aqueous solutions. Excited at 350 nm.

With respect to the donor **7BBNCz**, we selected the QN-series as potential acceptor molecules to probe exciplex formation. As depicted in **Figure 4-14**, **4-15** and in **Table 4-3**, broad red-shifted emission, assigned to exciplex emission, is clearly observed from the suspensions of **7BBNCz** and each of the acceptor molecules of the QN-series. The pair **7BBNCz**:**56m-QN** was selected as the optimal exciplex system for further investigation based on its highest photoluminescence quantum yield in suspensions.

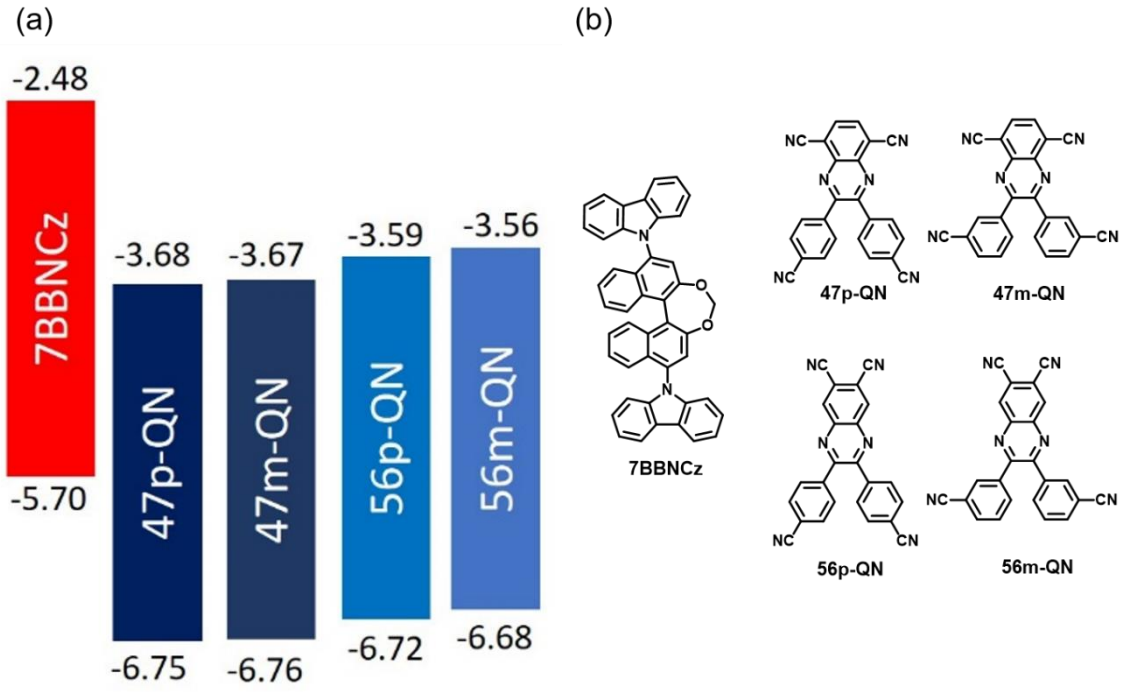

Figure 4-14. (a) Energy levels and (b) chemical structures and of **7BBNCz** and QN-series.

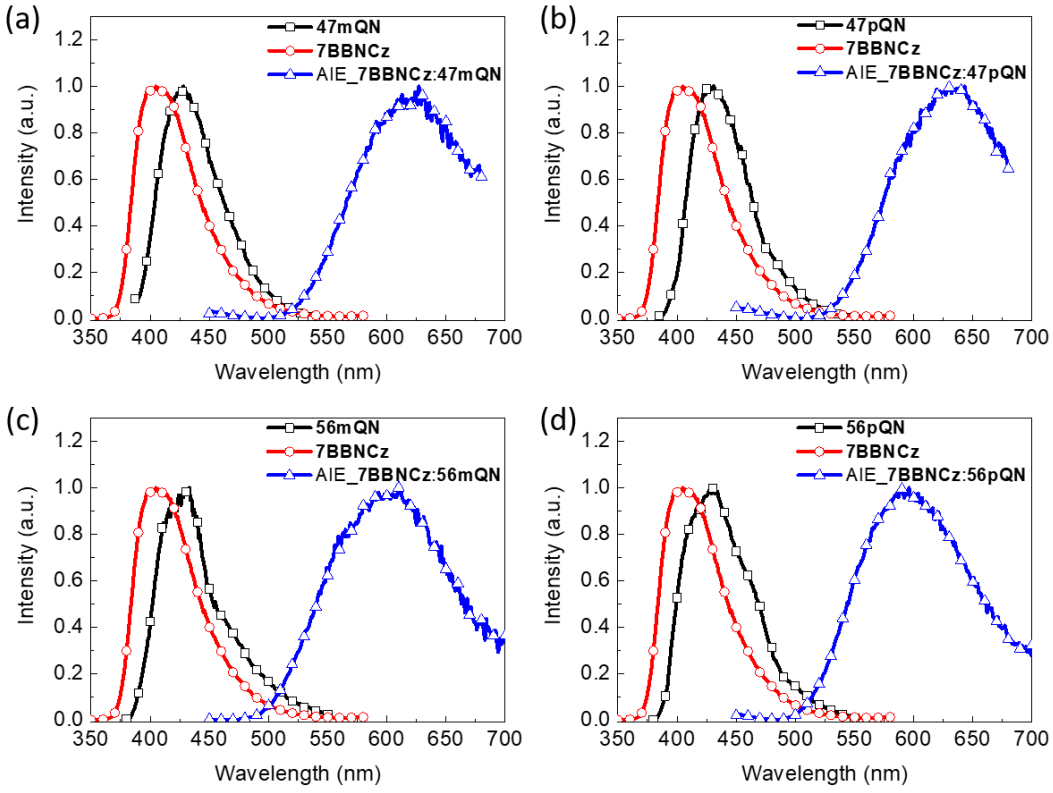

Figure 4-15. PL spectra of mixed (a) **7BBNCz:47mQN**, (b) **7BBNCz:47pQN**, (c)

7BBNCz:56mQN, (d) **7BBNCz:56pQN** in aqueous solutions. Excited at 370 nm.

Table 4-3. Summary of AIE test for **BNCNCz** or **7BBNCz** mixed with the QN series of chiral acceptors in aqueous solutions.

λ_{max}, PLQY	**47m-QN**	**47p-QN**	**56m-QN**	**56p-QN**
BNCNCz	549 nm, 3%	603 nm, 3%	541 nm, 5%	545 nm, 1%
7BBNCz	607 nm, 6%	622 nm, 5%	588 nm, 10%	594 nm, 8%

In order to tune the exciplex emission band towards higher energies, we employed the T2T series of acceptors (**PO-T2T**, **CN-T2T** and **3P-T2T**) that possess higher LUMO levels and high E_T. From the preliminary results of the AIE test (**Figure 4-16**, **4-17** and **Table 4-4**), blue to green exciplex emission could be observed in all the HTM:ETM combinations. From the PL spectra and photoluminescence quantum yields of the suspensions, **PO-T2T** was selected as the optimal acceptor molecule for obtaining sky-blue to green exciplex emission with the phenylcarbazole derivatives.

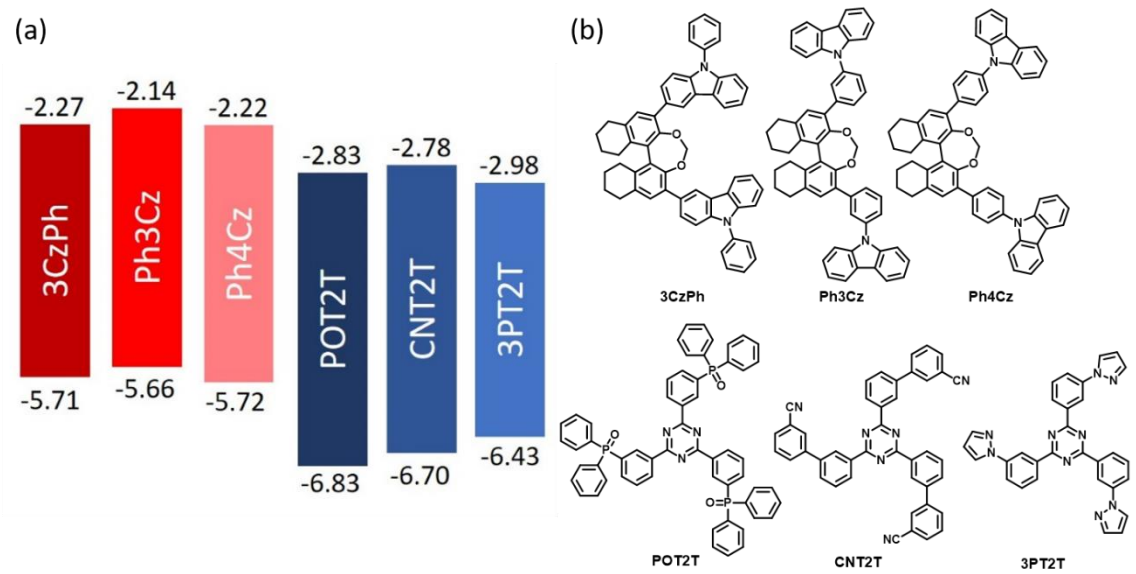

Figure 4-16. (a) Energy levels and (b) chemical structures and of phenylcarbazole derivatives and T2T-series.

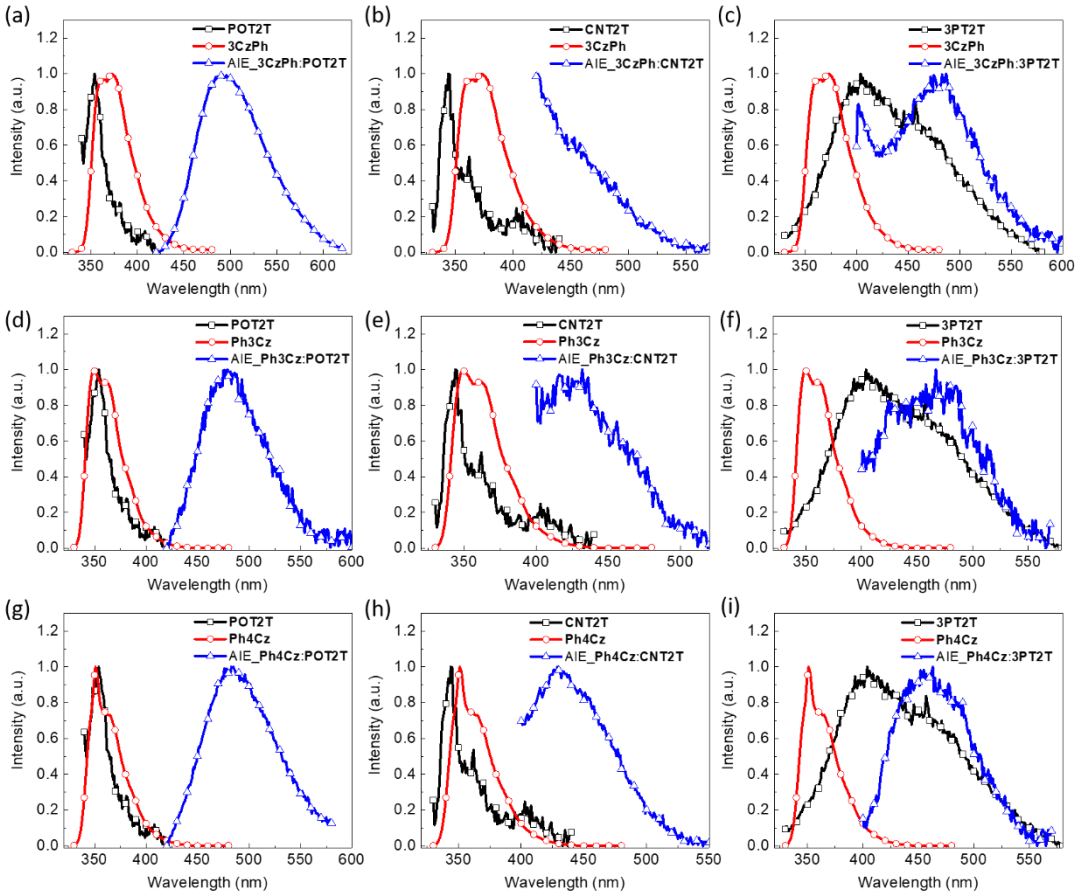

Figure 4-17. PL spectra of mixed (a) **3CzPh:POT2T**, (b) **3CzPh:CNT2T**, (c)

3CzPh:3PT2T, (d) **Ph3Cz:POT2T**, (e) **Ph3Cz:CNT2T**, (f) **Ph3Cz:3PT2T**, (g) **Ph4Cz:POT2T**, (h) **Ph4Cz:CNT2T** and (i) **Ph4Cz:3PT2T** in solutions. Excited at 350 nm.

Table 4-4. Summary of AIE test of phenylcarbazole derivatives mixed with T2T-series in solutions.

λ_{max}, PLQY	**PO-T2T**	**CN-T2T**	**3P-T2T**
3CzPh	491 nm, 15%	421 nm, 4%	487 nm, 5%
Ph3Cz	479 nm, 10%	432 nm, 3%	467 nm, 4%
Ph4Cz	483 nm, 10%	429 nm, 3%	463 nm, 4%

Finally, with the aim of obtaining better green to orange exciplex emission, the CN-(**mCN** and **pCN**) and QN-series (**47p-QN**, **47m-QN**, **56p-QN** and **56m-QN**) were investigated and paired to each of the three carbazole donors shown in **Figure 4-18**. The results of a large number of AIE tests are summarized in **Figure 4-19** and **Table 4-5** and two combinations, **Ph3Cz**:**56m-QN** and **Ph4Cz**:**56m-QN**, with 13% PLQY emerged as potential candidates for green exciplex emission.

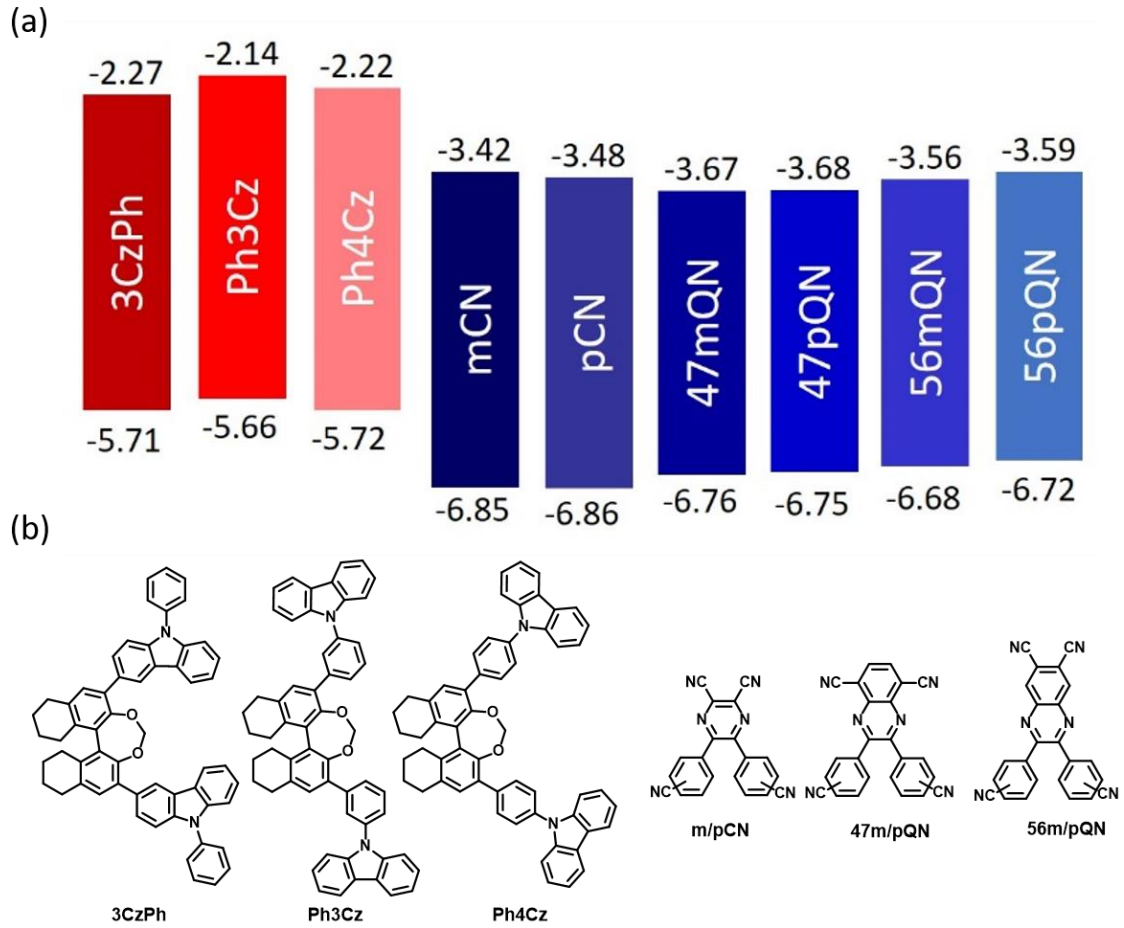

Figure 4-18. (a) Energy levels and (b) chemical structures of phenylcarbazole derivatives and CN- and QN-series.

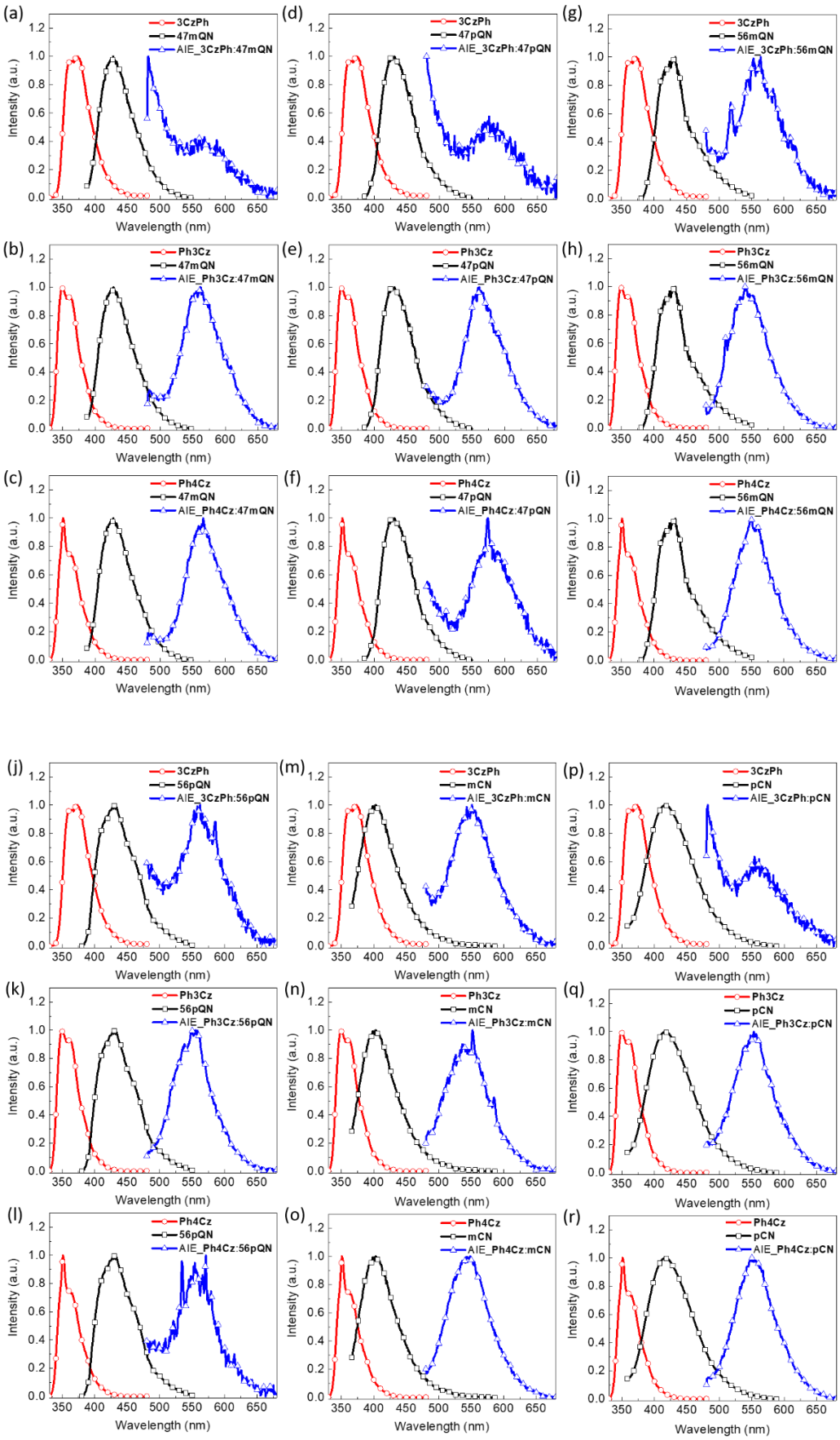
(a)
3CzPh
47mQN
AIE_3CzPh:47mQN
(b)
Ph3Cz
47mQN
AIE_Ph3Cz:47mQN
(c)
Ph4Cz
47mQN
AIE_Ph4Cz:47mQN
(d)
3CzPh
47pQN
AIE_3CzPh:47pQN
(e)
Ph3Cz
47pQN
AIE_Ph3Cz:47pQN
(f)
Ph4Cz
47pQN
AIE_Ph4Cz:47pQN
(g)
3CzPh
56mQN
AIE_3CzPh:56mQN
(h)
Ph3Cz
56mQN
AIE_Ph3Cz:56mQN
(i)
Ph4Cz
56mQN
AIE_Ph4Cz:56mQN
(j)
3CzPh
56pQN
AIE_3CzPh:56pQN
(k)
Ph3Cz
56pQN
AIE_Ph3Cz:56pQN
(l)
Ph4Cz
56pQN
AIE_Ph4Cz:56pQN
(m)
3CzPh
mCN
AIE_3CzPh:mCN
(n)
Ph3Cz
mCN
AIE_Ph3Cz:mCN
(o)
Ph4Cz
mCN
AIE_Ph4Cz:mCN
(p)
3CzPh
pCN
AIE_3CzPh:pCN
(q)
Ph3Cz
pCN
AIE_Ph3Cz:pCN
(r)
Ph4Cz
pCN
AIE_Ph4Cz:pCN
Intensity (a.u.)
Wavelength (nm)

Figure 4-19. PL spectra of mixed (a) **3CzPh:47mQN**, (b) **Ph3Cz:47mQN**, (c) **Ph4Cz:47mQN**, (d) **3CzPh:47pQN**, (e) **Ph3Cz:47pQN**, (f) **Ph4Cz:47pQN**, (g) **3CzPh:56mQN**, (h) **Ph3Cz:56mQN**, (i) **Ph4Cz:56mQN**, (j) **3CzPh:56pQN**, (k) **Ph3Cz:56pQN**, (l) **Ph4Cz:56pQN**, (m) **3CzPh:mCN**, (n) **Ph3Cz:mCN**, (o) **Ph4Cz:mCN**, (p) **3CzPh:pCN**, (q) **Ph3Cz:pCN** and (r) **Ph4Cz:pCN** solutions. Excited at 350 nm.

Table 4-5. Summary of AIE test of phenylcarbazole derivatives mixed with CN- and QN-series in solutions.

λ_{max}, PLQY	**mCN**	**pCN**	**47mQN**	**47pQN**	**56mQN**	**56pQN**
3CzPh	551 nm, 3%	554 nm, 2%	553 nm, 2%	576 nm, 1%	564 nm, 4%	562 nm, 2%
Ph3Cz	552 nm, 5%	553 nm, 7%	561 nm, 7%	561 nm, 5%	540 nm, 13%	555 nm, 7%
Ph4Cz	548 nm, 8%	550 nm, 7%	566 nm, 9%	574 nm, 3%	551 nm, 13%	571 nm, 3%

4-6 Photophysical Properties of Blended Films

From the AIE tests, seven candidates for CP-exciplex systems including **BNCNCz**:**47p-QN**, **7BBNCz**:**56m-QN**, **3CzPh**:**PO-T2T**, **Ph3Cz**:**PO-T2T**, **Ph4Cz**:**PO-T2T**, **Ph3Cz**:**56m-QN** and **Ph4Cz**:**56m-QN** were identified. Blended films of these combinations at the weight ratio of D:A = 1:1 of **BNCNCz**:**47p-QN**, **7BBNCz**:**56m-QN** were prepared by vacuum deposition and the films of other systems were fabricated by

spin-coating procedure from mixing solutions (D: 16 mg + A: 16 mg /mL chlorobenzene) owing to the poor thermal stability of **3CzPh**, **Ph3Cz** and **Ph4Cz**. The photophysical properties of blended films were studied by UV/Vis absorption and PL spectra, and their characteristics of long-lived exciplex emission were evidenced by time-correlated single photon counting. Then, the chiroptical properties of exciplex systems in ground and excited states were investigated by circular dichroism (CD) and circularly polarized photoluminescence (CPL) respectively.

As shown in **Figure 4-20** and summarized in **Table 4-6**, the absorption spectra of R/S-**BNCNCz**:**47p-QN** blended films show intense absorption bands at 283 nm and 375 nm, which are considered as the linear combination of corresponding donor and acceptor materials. The photoluminescence spectra of blended films of R/S-**BNCNCz**:**47p-QN** have bathochromic shift from 550 to 609 nm compared to the emission peak of R/S-**BNCNCz** in neat films, indicating the formation of lower-energy excited state. Based on the fitting curve of transient PL spectra of the blended films, the long-lived excited state species with fluorescence lifetime of hundreds of ns were observed and the ratio of delayed fluorescence in photoluminescence is over 35%, showing exciplex formation, as depicted in **Figure 4-21**.[1]

As depicted in **Figure 4-22**, for the optical activities of R/S-**BNCNCz** in neat films and R/S-**BNCNCz**:**47p-QN** in blended films in ground state, mirror-image relationship

between enantiomers were recorded and the strongest absorption in R/S-**BNCNCz**:**47p-QN** blended films is assigned to the characteristic absorption in the chiral **BNCNCz** moieties. In comparison with the CPL signals in R/S-**BNCNCz** neat films, those of the R/S-**BNCNCz**:**47p-QN** blended films (**Figure 4-23**) reveal more distinct mirror-image relationship for enantiomers and exhibit red-shifted emission. The $|g_{lum}|$ of R/S-**BNCNCz** neat films at 546 nm is 1.6×10^{-4} and that of R/S-**BNCNCz**:**47p-QN** blended films at 603 nm reaches 1.2×10^{-3}. These preliminary results indicate that the chiral induction involved in intermolecular charge transfer process can facilitate the enhancement of CPL intensity but that its effect is limited in this circular polarized exciplex system. Nevertheless, the large overlap of emission spectra of R/S-**BNCNCz** neat films and R/S-**BNCNCz**:**47p-QN** blended films renders it difficult to distinguish exciplex emission from the donor emission, especially for **BNCNCz**.[24] Therefore, one should look for other exciplex systems with less spectral overlap between exciplex emission and donor or acceptor emission. In particular, it can be expected that the rather loose intermolecular exciplex geometry may benefit from better geometrical constraints that fix the relative geometries of the donor and acceptor components.

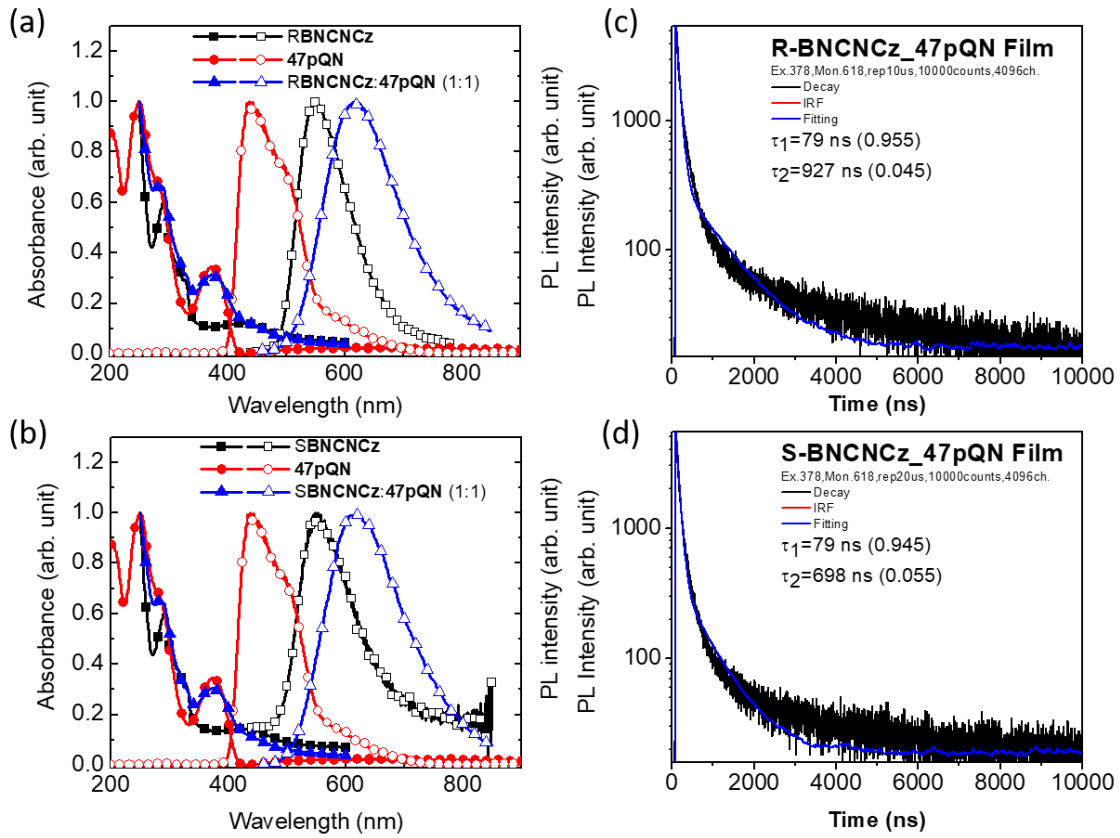

Figure 4-20. UV/Vis absorption and PL spectra of (a) R- and (b) S-**BNCNCz**:**47p-QN** system in neat films and blended films. Excited at 370 nm. Transient PL spectra of (c) R- and (d) S-**BNCNCz:47p-QN** in blended films. Excited at 378 nm.

Table 4-6. Photophysical parameters of R/S-**BNCNCz:47pQN** and R/S-**7BBNCz:56mQN** blended films.

Donor	**Acceptor**	$\lambda_{max,D/A}$[a] (nm)	$\lambda_{max,D}$ (nm)	Φ[b] (%)	Transient PL[c]			
					A_1	τ_1(μs)	A_2	τ_2(ns)
R**BNCNCz**	**47p-QN**	609	550[a]	7	0.045	0.927	0.955	79
SBNCNCz	**47p-QN**	610	552[a]	6	0.055	0.698	0.945	79
R**7BBNCz**	**56m-QN**	601	427[b]	16	0.026	1.5	0.974	145

S7BBNCz	**56m-QN**	598	416[b]	17	0.036	1.02	0.904	133

[a] Excited at 370 nm. [b] Excited at 300 nm. [c] Excited at 378 nm. The decay component was fitted with two exponential decay model as: $I(t) = A_1 \times \exp(-t/\tau_p) + A_2 \times \exp(-t/\tau_d)$.

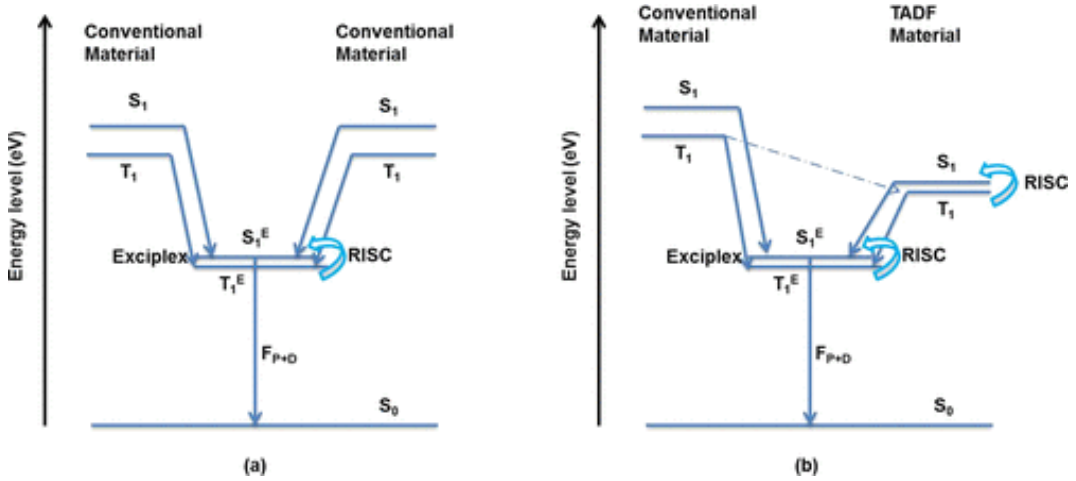

Figure 4-21. Energy diagrams displaying energy transfer in exciplex systems consist of (a) two traditional fluorescent materials and (b) a conventional fluorescent material and a TADF-active emitting material. S_0, S_1 and T_1 represents ground state, singlet excited state and triplet excited state individually (S_1^E and T_1^E are for exciplex). rISC means reverse intersystem crossing from T to S_1. The dashed line denotes intermolecular Dexter energy transfer, and F_{P+D} corresponds to prompt and delayed fluorescence. Reused with permission from ref 1. Copyright 2018, American Chemical Society.

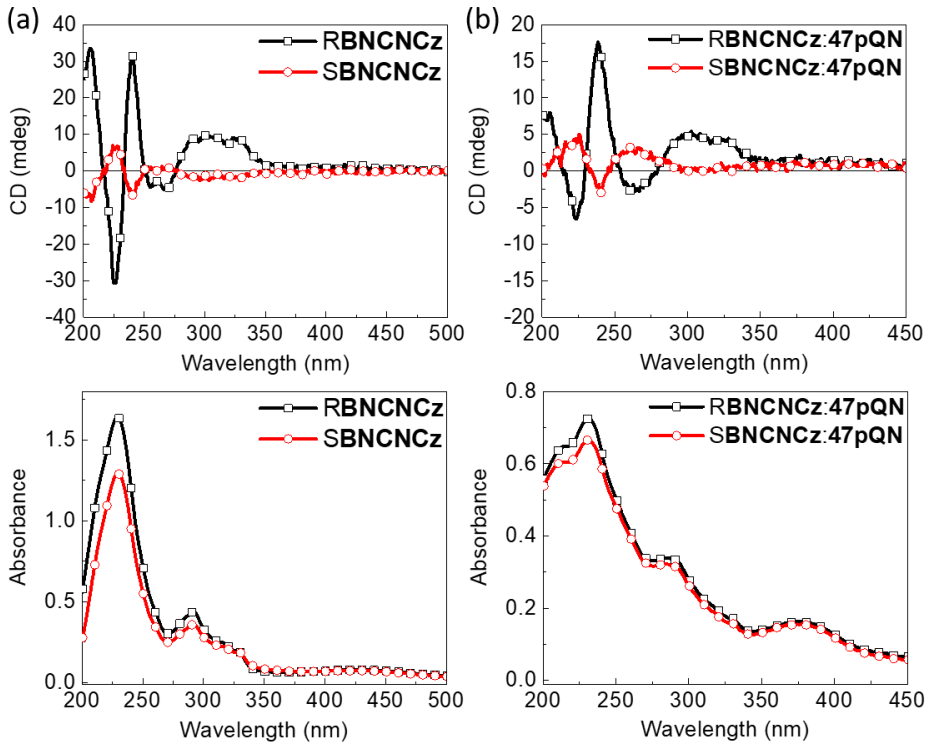

Figure 4-22. CD spectra of (a) R/S-**BNCNCz** in neat films and (b) R/S-**BNCNCz:47pQN** in blended films.

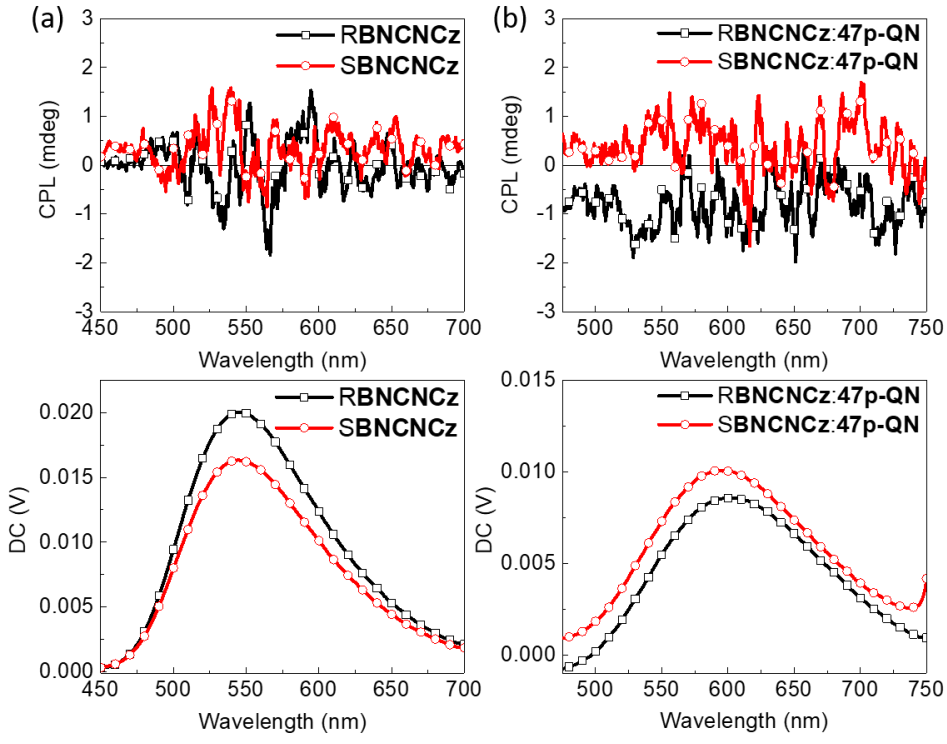

Figure 4-23. CPL spectra of (a) R/S-**BNCNCz** in neat films (excited at 330 nm) and (b) R/S-**BNCNCz**:**47pQN** in blended films (excited at 380 nm).

As depicted in **Figure 4-24** and summarized in **Table 4-6**, the absorption spectra of R/S-**7BBNCz:56m-QN** blended films show characteristic absorption peaks at 292 nm, 340 nm and 362 nm resulting from the contribution of the absorption of donor and acceptor molecules. The photoluminescence spectra of R/S-**7BBNCz:56m-QN** blended films showed a significant bathochromic shift from deep-blue (416 nm) to orange (598 nm), suggesting the formation of low-lying excited state between donor and acceptor. From the transient PL of blended films, the excited species with a lifetime in μs scale were acquired and the contribution of delayed fluorescence is around 20%, revealing the contribution from a long-lived triplet state.

As shown in **Figure 4-25**, the bisiganate Cotton effects in CD spectra of R/S-**7BBNCz:56m-QN** blended films demonstrated the optical activities in ground state and these CD signals could be assigned to the intrinsic chirality of R/S-**7BBNCz**. However, no significant CPL signals were detected in both R/S-**7BBNCz** neat films and R/S-**7BBNCz:56m-QN** blended films (**Figure 4-26**), indicating the chirality induction in this intermolecular charge transfer system is small.

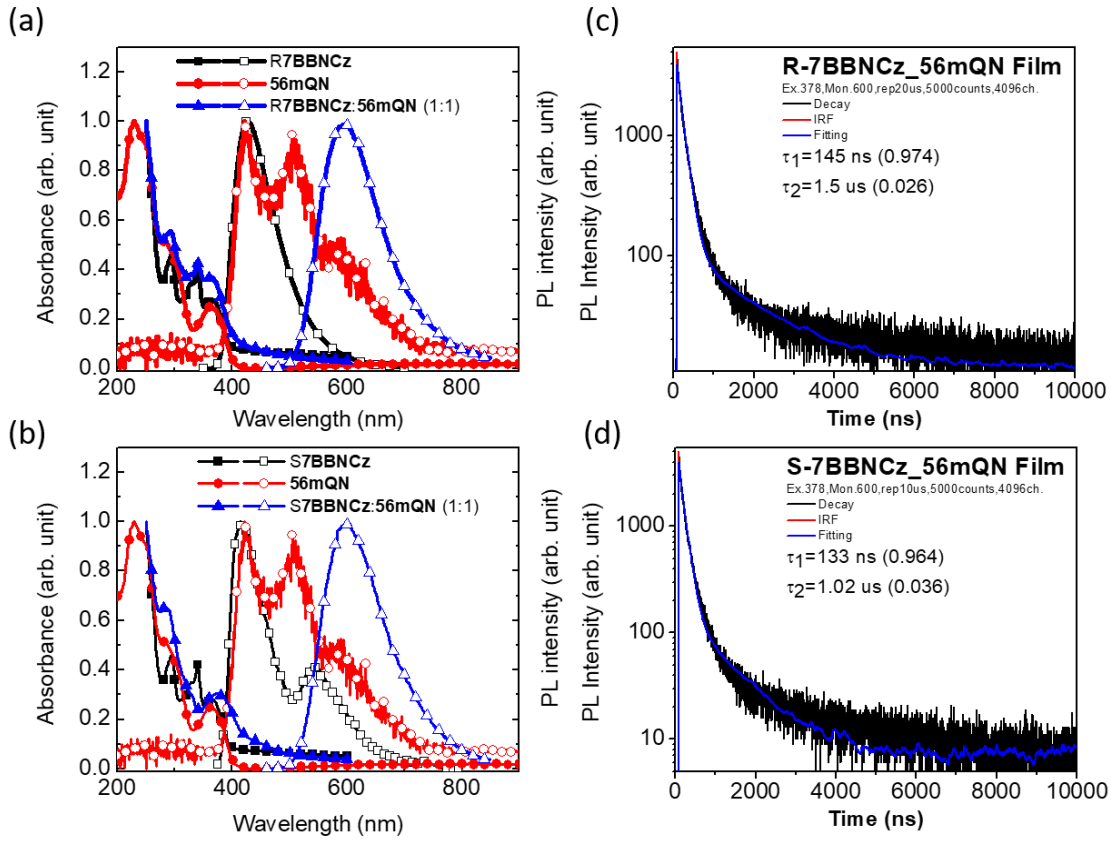

Figure 4-24. UV/Vis absorption and PL spectra of (a) R- and (b) S-**7BBNCz:56mQN** system in neat films (excited at 300 nm) and blended films (excited at 370 nm). Transient PL spectra of (c) R- and (d) S-**7BBNCz:56mQN** in blended films. Excited at 378 nm.

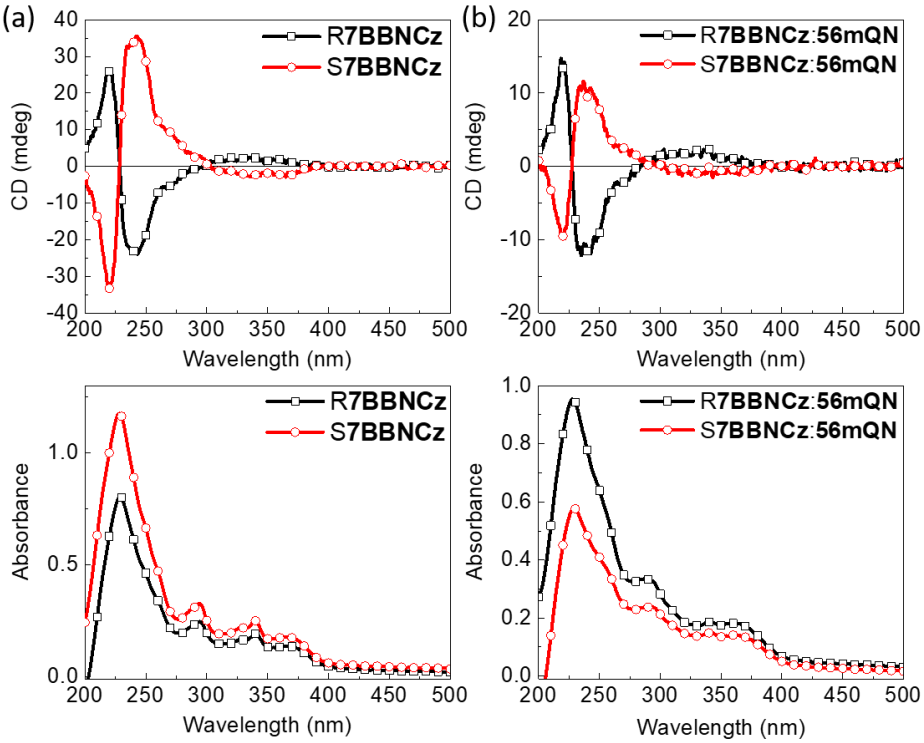

Figure 4-25. CD spectra of (a) R/S-**7BBNCz** in neat films and (b) R/S-**7BBNCz**:**56mQN** in blended films.

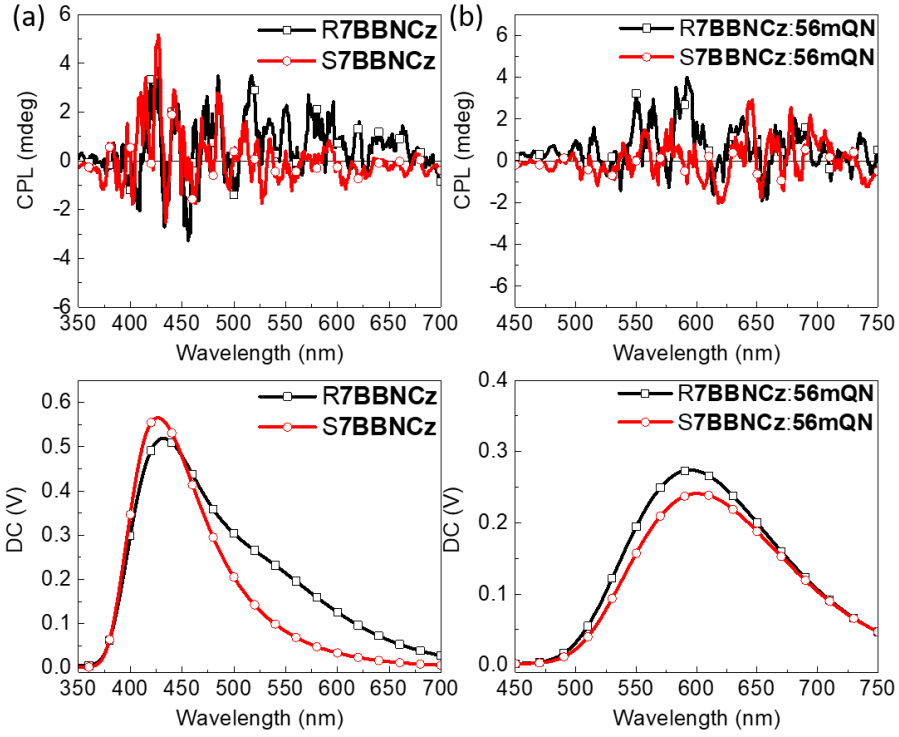

Figure 4-26. CPL spectra of (a) R/S-**7BBNCz** in neat films (excited at 300 nm) and (b) R/S-**7BBNCz**:**56mQN** in blended films. Excited at 375 nm.

As depicted in **Figure 4-27** and summarized in **Table 4-7**, the absorption spectra of chiral carbazole-based donors (R/S-**3CzPh**, R/S-**Ph3Cz** and R/S-**Ph4Cz**) with **PO-T2T** in blended films reveal broad absorption bands below 350 nm, which are the overlap of the absorption spectrum of the chiral donor and **PO-T2T**, indicating no formation of charge-transfer complex in the ground state. All the blended films show sky-blue emission, whose maximal emission wavelengths is 495 nm for R/S-**3CzPh:PO-T2T**, 476 nm for R/S-**Ph3Cz:PO-T2T** and 485 nm for R/S-**Ph4Cz:PO-T2T**, with a moderate photoluminescence quantum yield (Φ) of 35% for R/S-**3CzPh:PO-T2T**, 18% for R/S-**Ph3Cz:PO-T2T** and 19% for R/S-**Ph4Cz:PO-T2T**. Compared to the emission bands of chiral donors in deep-blue regions, the intense emission of red-shifted photoluminescence in blended films is a strong signature of exciplex formation upon photoexcitation. In addition, there is no residual emission from donors or acceptors or from the twisted conformation of **PO-T2T**, in agreement with the absence of phase segregation between donor and acceptor molecules.[15] For the transient PL spectra of these blended films, we are waiting for results from Prof. Pi-Tai Chou's group.

In the CD spectra of R/S-**3CzPh**, R/S-**Ph3Cz** and R/S-**Ph4Cz** in neat films (**Figure**

4-28), the three enantiomeric pairs show perfect mirror-image relationship between the enantiomers and R/S-**Ph3Cz** and R/S-**Ph4Cz** still retain the intense bisignate bands, ascribed to the strong exciton coupling between chromophores in neat films.[34-36] As for the blended films of R/S-**3CzPh:PO-T2T**, R/S-**Ph3Cz:PO-T2T** and R/S-**Ph4Cz:PO-T2T** (**Figure 4-29**), these not only preserve the identical but opposite sign relationship between optical isomers but also exhibit the characteristic CD bands of R/S-**3CzPh**, R/S-**Ph3Cz** and R/S-**Ph4Cz** separately. However, there is no CPL activity from either R/S-**3CzPh**, R/S-**Ph3Cz** and R/S-**Ph4Cz** neat films and R/S-**3CzPh:PO-T2T**, R/S-**Ph3Cz:PO-T2T** and R/S-**Ph4Cz:PO-T2T** blended films (**Figure 4-30** and **4-31**), inferring that chirality induction does not occur in the charge transfer excited states or that the angle $cos\theta_{\mu,m}$ between electric transition dipole moment (μ) and magnetic transition dipole moment (m) in the excite state (**Figure 4-4**) is increased during the charge transfer process in these exciplex systems. In addition, the emission bands in long wavelength region in fluorescence spectra of R/S-**3CzPh**, R/S-**Ph3Cz** and R/S-**Ph4Cz** in **Figure 4-30** are attributed to the background noise signals instead of excimer emission, since the emission intensities of these neat films are very weak.

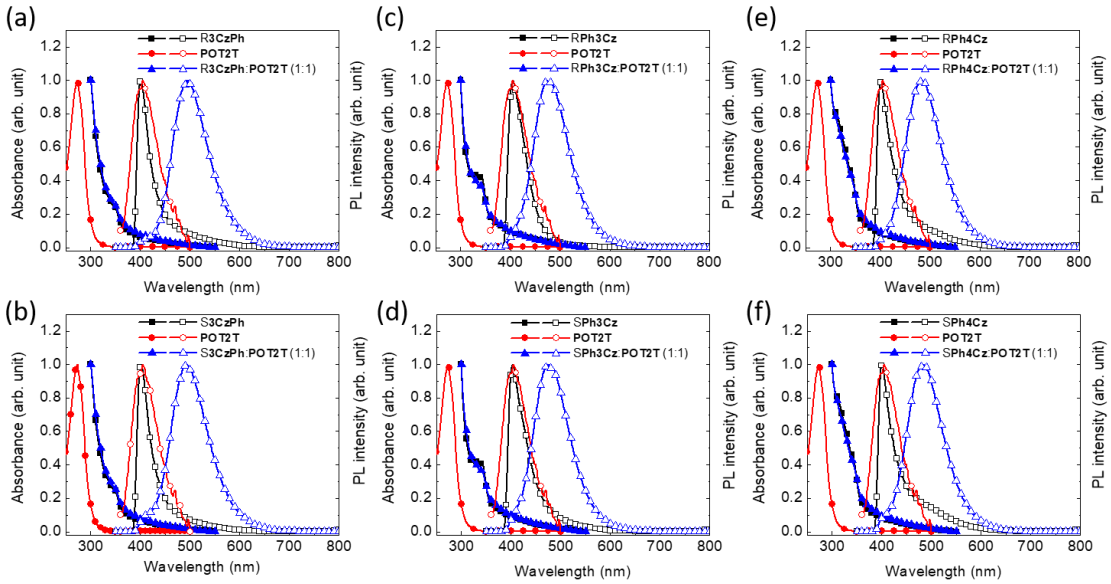

Figure 4-27. UV/Vis absorption and PL spectra of (a) R- and (b) S-**3CzPh**:**PO-T2T**, (c) R- and (d) S-**Ph3Cz**:**PO-T2T**, (e) R- and (f) S-**Ph4Cz**:**PO-T2T** systems in neat films and blended films. Excited at 300 nm.

Table 4-7. Photophysical parameters of carbazole derivative:**PO-T2T** blended films.

Donor	Acceptor	$\lambda_{max,D/A}{}^{a}$ (nm)	$\lambda_{max,D}{}^{a}$ (nm)	Φ^{b}(%)
R**3CzPh**	**PO-T2T**	495	401	22
S**3CzPh**	**PO-T2T**	493	402	35
R**Ph3Cz**	**PO-T2T**	476	405	18
S**Ph3Cz**	**PO-T2T**	476	403	16
R**Ph4Cz**	**PO-T2T**	485	401	19
S**Ph4Cz**	**PO-T2T**	486	401	16

[a] Excited at 350 nm. [b] Excited at 330 nm.

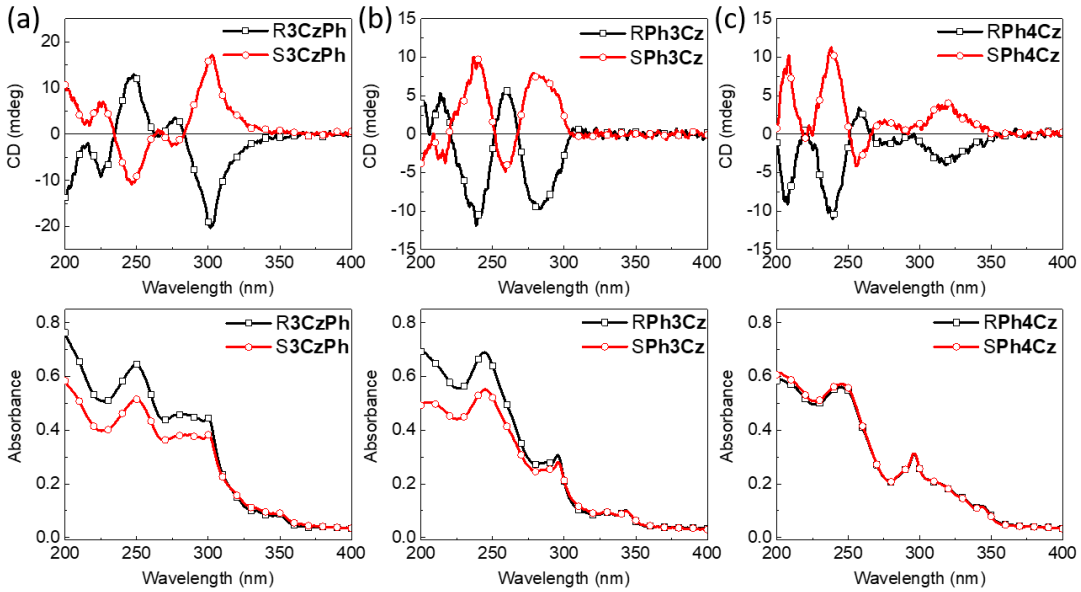

Figure 4-28. CD spectra of (a) R/S-**3CzPh**, (b) R/S-**Ph3Cz** and (c) R/S- **Ph4Cz** in neat films.

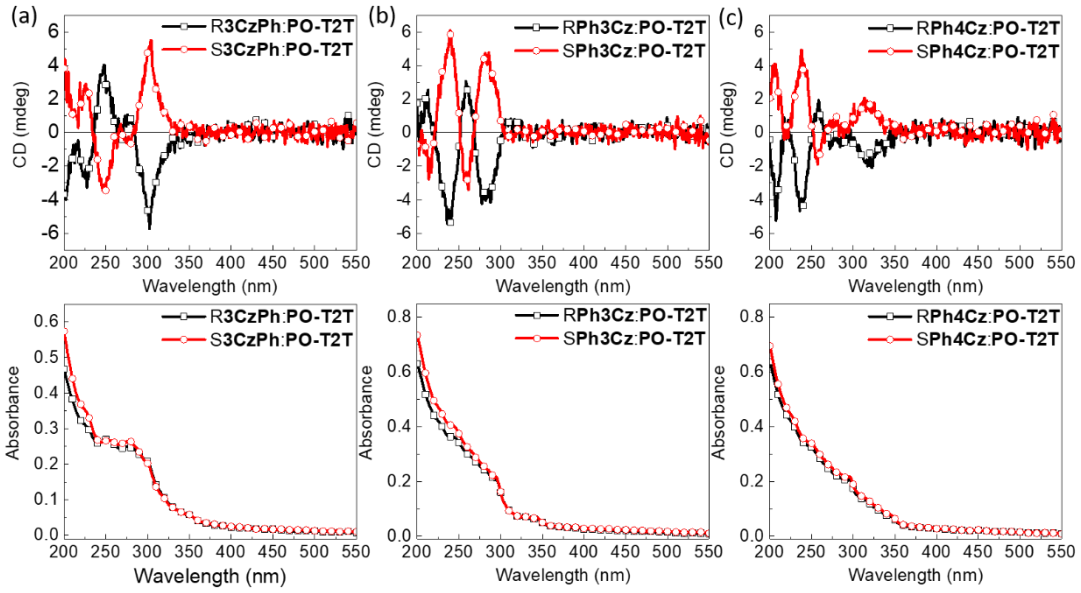

Figure 4-29. CD spectra of (a) R/S-**3CzPh**:**PO-T2T**, (b) R/S-**Ph3Cz**:**PO-T2T** and (c) R/S-**Ph4Cz**:**PO-T2T** in blended films.

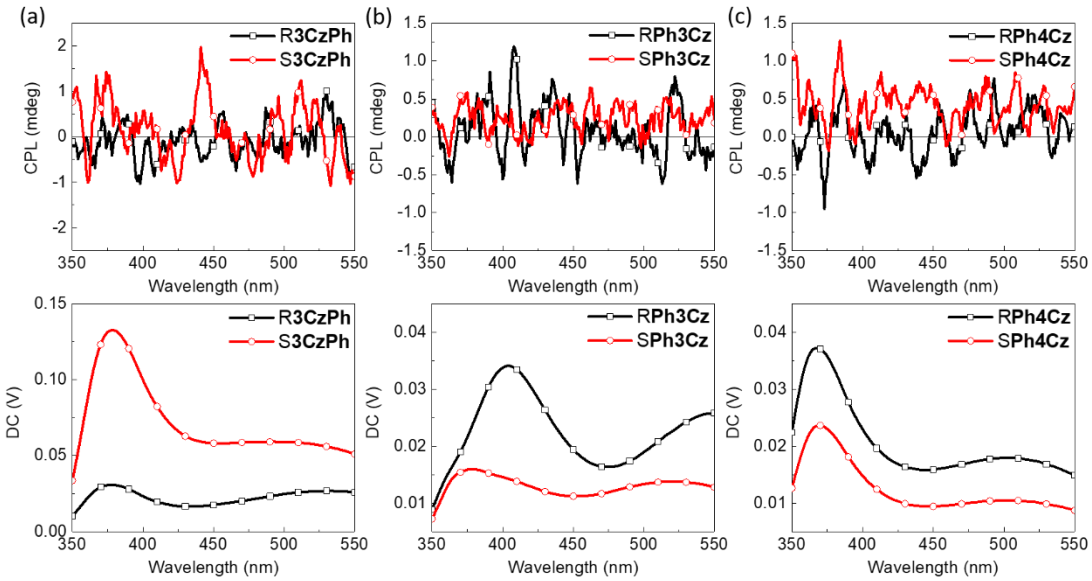

Figure 4-30. CPL spectra of (a) R/S-**3CzPh**, (b) R/S-**Ph3Cz** and (c) R/S-**Ph4Cz** in neat films. Excited at 300 nm.

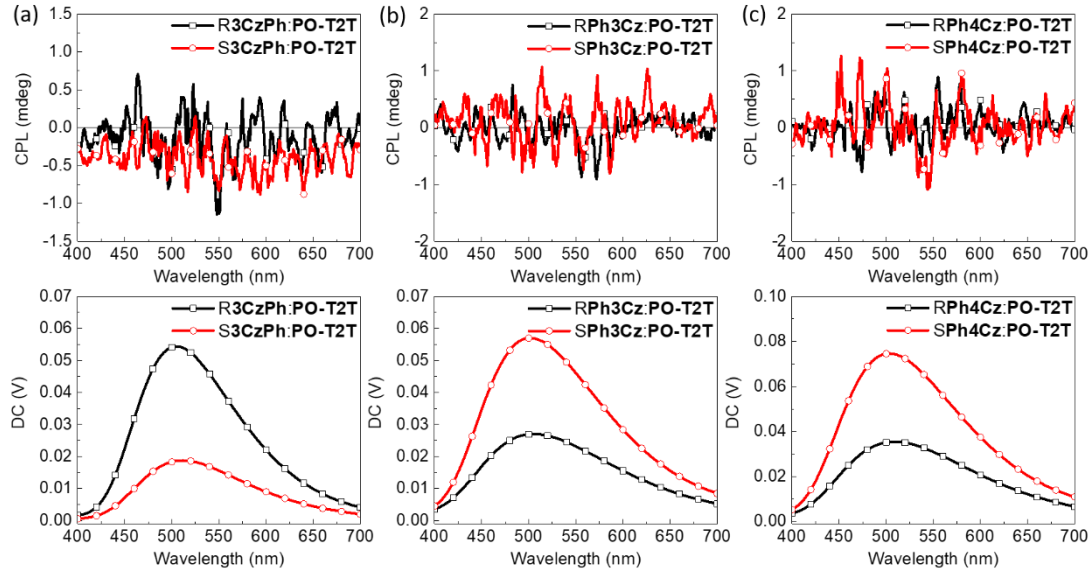

Figure 4-31. CPL spectra of (a) R/S-**3CzPh**:**PO-T2T**, (b) R/S-**Ph3Cz**:**PO-T2T** and (c) R/S-**Ph4Cz**:**PO-T2T** in blended films. Excited at 300 nm.

The absorption and emission spectra of R/S-**Ph3Cz:56m-QN** and R/S-**Ph4Cz:56m-**

QN blended films are shown in shown in **Figure 4-32** and summarized in **Table 4-8**. The blended films exhibit the absorption peaks at 242 nm, 295 nm and 343 nm for R/S-**Ph3Cz:56m-QN** and 245 nm, 296 nm and 369 nm for **R/S-Ph4Cz:56m-QN**, which are the spectral overlap between the absorption spectrum of donor and acceptor molecules. No significant new absorption bands are found in the blended films, implying the lack of ground state interactions between donors and acceptors. In contrast, the blended films R/S-**Ph3Cz:56m-QN** and R/S-**Ph4Cz:56m-QN** both have distinct emission bands that are different from those of the components. In comparison with the individual emission spectra of donor or acceptor, the bathochromic-shifted emission of blended films, 602 nm for R/S-**Ph3Cz:56m-QN** and 616 nm for R/S-**Ph4Cz:56m-QN**, suggests the formation of exciplex upon photoexcitation at 325 nm. For the transient PL spectra of these blended films, we are waiting for results from Prof. Pi-Tai Chou's group.

The CD spectra of R/S-**Ph3Cz:56m-QN** and R/S-**Ph4Cz:56m-QN** blended films (**Figure 4-33**) all exhibit a mirror-image relationship for the enantiomers. The CD spectra of R-**Ph3Cz** and R-**Ph4Cz** in neat films show negative Cotton effects in the long wavelength region (**Figure 4-28**); however, the blended films R-**Ph3Cz:56m-QN** have clear positive Cotton effects in 300-380 nm, which matches well with the absorption band of **56m-QN**, and implies induced chiral character in ground state.[47-50] In contrast, there is no new peaks in the CD spectra of the blended films R-**Ph4Cz:56m-QN**. As shown in

Figure 4-34, the CPL spectra of R/S-**Ph3Cz:56m-QN** display a perfect mirror-image relationship between the enantiomers and their $|g_{lum}|$ are 3.3×10^{-4} at the maximal wavelength of CPL spectra. As a comparison, without chiral induction in the ground state, R/S-**Ph4Cz:56m-QN** blended films have no optical activity in the excited states.

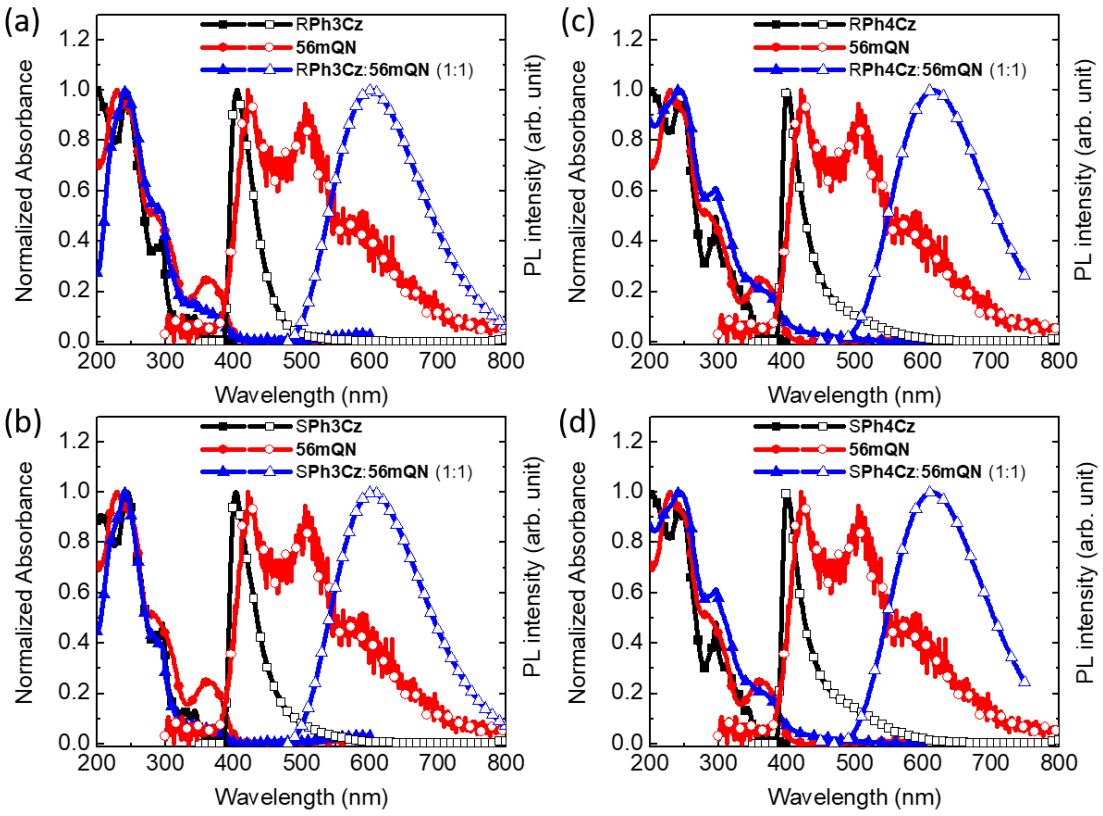

Figure 4-32. UV/Vis absorption and PL spectra of (a) R- and (b) S-**Ph3Cz**:**56m-QN**, (c) R- and (d) S-**Ph4Cz**:**56m-QN** systems in neat films and blended films. Excited at 300 nm.

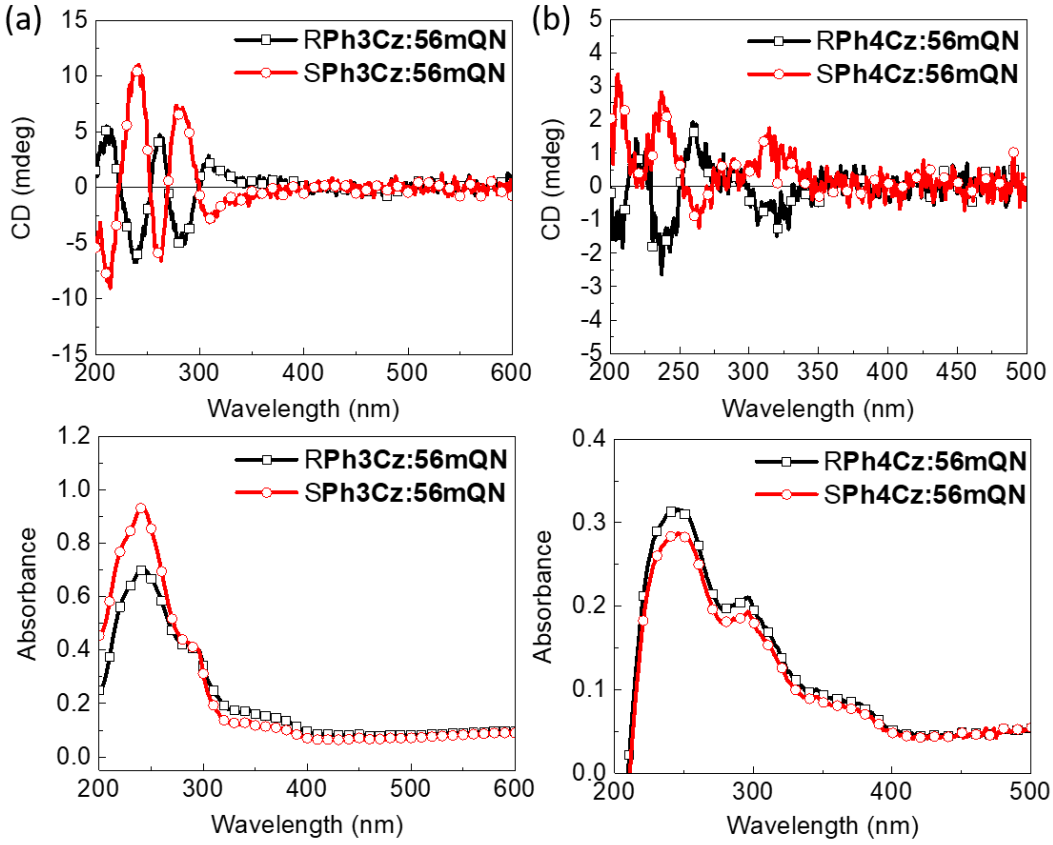

Figure 4-33. CD spectra of (a) R/S-**Ph3Cz**:**56m-QN** and (b) R/S-**Ph4Cz**:**56m-QN** in blended films.

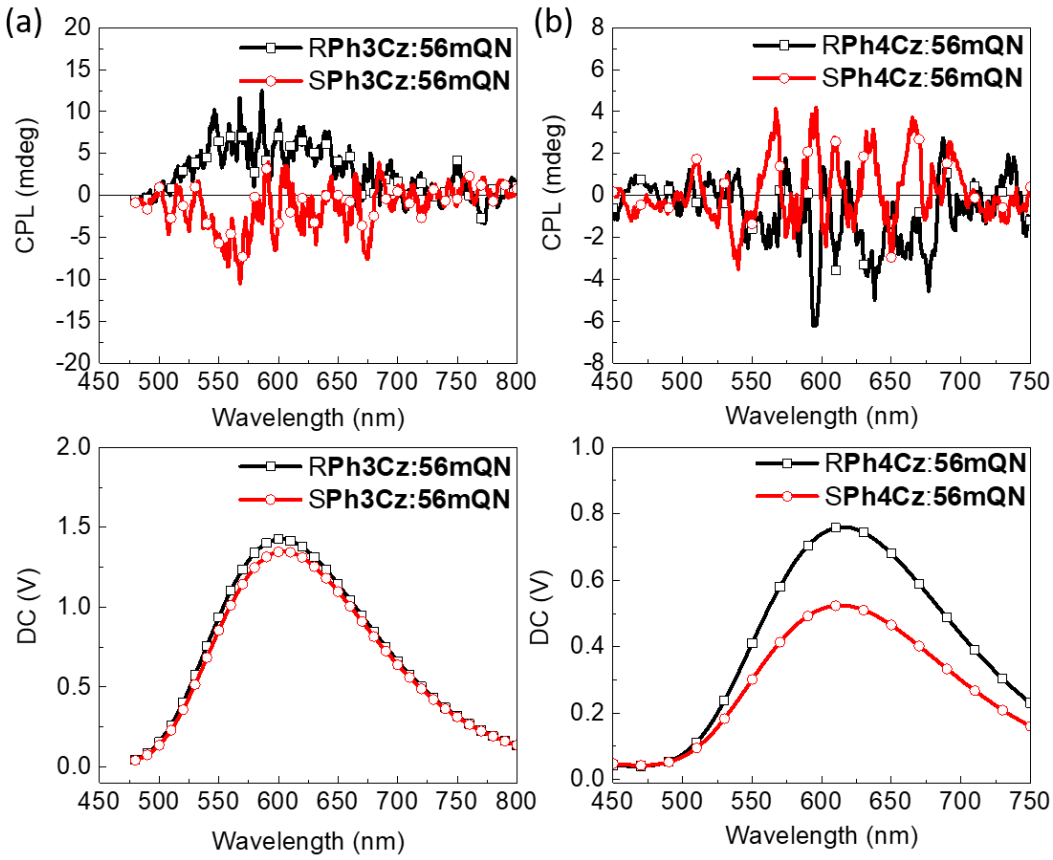

Figure 4-34. CPL spectra of (a) R/S-**Ph3Cz**:**56m-QN** and (b) R/S-**Ph4Cz**:**56m-QN** in blended films. Excited at 325 nm.

Table 4-8. Photophysical parameters of R/S-**Ph3Cz**:**56m-QN** and R/S- **Ph4Cz**:**56m-QN** blended films.

Donor	**Acceptor**	$\lambda_{max,D/A}{}^{a}$ (nm)	$\lambda_{max,D}{}^{b}$ (nm)	Φ^{a} (%)
R**Ph3Cz**	**56m-QN**	602	405	15
SPh3Cz	**56m-QN**	604	403	14
R**Ph4Cz**	**56m-QN**	616	401	11
S**Ph4Cz**	**56m-QN**	615	401	11

[a] Excited at 330 nm. [b] Excited at 300 nm.

4-7 Summary

In this section, we pursed a novel approach to conceive exciplexes emitting circularly polarized luminescence by pairing a chiral carbazole donor to various acceptors. According to the energy levels of CP-TADF material R/S-**BNCNCz**, we utilized AIE test to probe for potential exciplex formation. Blended films of R/S-**BNCNCz**:**47p-QN** show a 50-nm bathochromic shift in the steady-state PL and a τ_{DF} of 0.927 μs or 0.698 μs for R- or S-**BNCNCz**:**47p-QN** respectively. Nevertheless, the exciplex emission in CPL spectra is small and with $|g_{lum}|$ of 10^{-4}.

To improve the CP-exciplex intensity and readily identify exciplex emission from that of the donor or acceptor, we conceived a series of axially-chiral carbazole-based electron donors, **7BBNCz**, **3CzPh**, **Ph3Cz** and **Ph4Cz**. **7BBNCz** that is composed of chiral binaphthalene core and is an analogue of 4,4'-bis(*N*-carbazolyl)-2,2'-biphenyl (CBP) with a lower triplet energy of 2.48 eV. The phenylcarbazole derivatives of **3CzPh**, **Ph3Cz** and **Ph4Cz** consist of a chiral octahydrobinaphthalene and *N*-phenylcarbazole isomers with high triplet energies at ca. 3.00 eV. These could serve as suitable hole-transporting materials in exciplex or as host materials for energy transfer process in host-guest system.

All the compounds show intense deep-blue emission centered at 350 nm, except for **7BBNCz**, which shows red-shifted emission at around 405 nm owing to the longer π-conjugation length. Taking advantage of HOMO/LUMO energies and AIE tests, we identified several candidate exciplex systems: **7BBNCz**:**56mQN**, **3CzPh**:**POT2T**, **Ph3Cz**:**POT2T**, **Ph4Cz**:**POT2T**, **Ph3Cz**:**56mQN** and **Ph4Cz**:**56mQN** with moderate Φ_{lum} in aqueous solutions.

Blended films evidence the formation of long-lived exciplex systems resulting in bathochromically-shifted emission and characterized by transient PL decay profiles. These chiral exciplex candidates revealed optical activities in ground state and exhibit mirror-image relationship between the enantiomers in CD spectra. Although most of the systems are chiroptically inactive in excited state, we identified one CPL-active system, R/S-**Ph3Cz**:**56m-QN**, with clear chiral induction between chiral donors and achiral acceptors, which supports our approach as feasible. In the future, we will fabricate the electroluminescence devices, consist of the exciplex system R/S-**Ph3Cz:56m-QN**, and deeply investigate the properties of circularly polarized electroluminescence.

4-8 References

1 Sarma, M.; Wong, K.-T. *ACS Appl. Mater. Interfaces* **2018**, *10*, 19279.

2 Lin, T. C.; Sarma, M.; Chen, Y. T.; Liu, S. H.; Lin, K. T.; Chiang, P. Y.; Chuang, W. T.; Liu, Y. C.; Hsu, H. F.; Hung, W. Y.; Tang, W. C.; Wong, K. T.; Chou, P. T. *Nat. Commun.* **2018**, *9*, 1.

3 Gu, J.; Tang, Z.; Guo, H.; Chen, Y.; Xiao, J.; Chen, Z.; Xiao, L. *J. Mater. Chem. C* **2022**, *10*, 4521.

4 Osaheni, J. A.; Jenekhe, S. A. *Macromolecules* **1994**, *27*, 739.

5 Wang, J. F.; Kawabe, Y.; Shaheen, S. E.; Morrell, M. M.; Jabbour, G. E.; Lee, P. A.; Anderson, J.; Armstrong, N. R.; Kippelen, B.; Mash, E. A.; Peyghambarian, N. *Adv. Mater.* **1998**, *10*, 230.

6 Palilis, L. C.; Mäkinen, A. J.; Uchida, M.; Kafafi, Z. H. *Appl. Phys. Lett.* **2003**, *82*, 2209.

7 Goushi, K.; Yoshida, K.; Sato, K.; Adachi, C. *Nat. Photonics* **2012**, *6*, 253.

8 Graves, D.; Jankus, V.; Dias, F. B.; Monkman, A. *Adv. Funct. Mater.* **2013**, *24*, 2343.

9 Park, Y. S.; Lee, S.; Kim, K. H.; Kim, S. Y.; Lee, J. H.; Kim, J. J. *Adv. Funct. Mater.* **2013**, *23*, 4914.

10 Hung, W. Y.; Fang, G. C.; Chang, Y. C.; Kuo, T. Y.; Chou, P. T.; Lin, S. W.; Wong, K. T. *ACS Appl. Mater. Interfaces* **2013**, *5*, 6826.

11 Li, J.; Nomura, H.; Miyazaki, H.; Adachi, C. *Chem. Commun.* **2014**, *50*, 6174.

12 Liu, X. K.; Chen, Z.; Zheng, C. J.; Liu, C. L.; Lee, C. S.; Li, F.; Ou, X. M.; Zhang, X. H. *Adv. Mater.* **2015**, *27*, 2378.

13 Liu, W.; Chen, J. X.; Zheng, C. J.; Wang, K.; Chen, D. Y.; Li, F.; Dong, Y. P.; Lee, C. S.; Ou, X. M.; Zhang, X. H. *Adv. Funct. Mater.* **2016**, *26*, 2002.

14 Goushi, K.; Adachi, C. *Appl. Phys. Lett.* **2012**, *101*, 023306.

15 Hung, W.-Y.; Fang, G.-C.; Lin, S.-W.; Cheng, S.-H.; Wong, K.-T.; Kuo, T.-Y.; Chou, P.-T. *Sci. Rep.* **2014**, *4*, 5161.

16 Amin, N. R. A.; Kesavan, K. K.; Biring, S.; Lee, C.-C.; Yeh, T.-H.; Ko, T.-Y.; Liu, S.-W.; Wong, K.-T. *ACS Appl. Eletron. Mater.* **2020**, *2*, 1011.

17 Richardson, F. S.; Riehl, J. P. *Chem. Rev.* **1977**, *77*, 773.

18 Riehl, J. P.; Richardson, F. S. *Chem. Rev.* **1986**, *86*, 1.

19 Zinna, F.; Di Bari, L. *Chirality* **2015**, *27*, 1.

20 Sánchez-Carnerero, E. M.; Agarrabeitia, A. R.; Moreno, F.; Maroto, B. L.; Muller, G.; Ortiz, M. J.; de la Moya, S. *Chem. Eur. J.* **2015**, *21*, 13488.

21 Tanaka, H.; Inoue, Y.; Mori, T. *ChemPhotoChem* **2018**, *2*, 386.

22 Adelizzi, B.; Chidchob, P.; Tanaka, N.; Lamers, B. A. G.; Meskers, S. C. J.; Ogi, S.; Palmans, A. R. A.; Yamaguchi, S.; Meijer, E. W. *J. Am. Chem. Soc.* **2020**, *142*, *39*, 16681.

23 Sumsalee, P.; Abella, L.; Kasemthaveechok, S.; Vanthuyne, N.; Cordier, M.; Pieters, G.; Autschbach, J.; Crassous, J.; Favereau, L. *Chem. Eur. J.* **2021**, *27*, 1.

24 Feuillastre, S.; Pauton, M.; Gao, L.; Desmarchelier, A.; Riives, A. J.; Prim, D.; Tondelier, D.; Geffroy, B.; Muller, G.; Clavier, G.; Pieters, G. *J. Am. Chem. Soc.* **2016**, *138*, 3990.

25 Cui, L-S.; Dong, S.-C.; Liu, Y.; Li, Q.; Jiang, Z.-Q.; Liao, L.-S. *J. Mater. Chem. C* **2013**, *1*, 3967.

26 Li, L.; Liu, Y.; Peng, Y.; Yu, L.; Wu, X.; Yan, H. *Angew. Chem. Int. Ed.* **2016**, *55*, 33.

27 Brenet, S.; Minozzi, C.; Clarens, B.; Amiri, L.; Berthiol, F. *Synthesis* **2015**, *47*, *24*, 3859.

28 Takaishi, K.; Hinoide, S.; Matsumoto, T.; Ema, T. *J. Am. Chem. Soc.* **2019**, *141*, *30*, 11852.

29 Diduch, K.; Wübbenhorst, M.; Kucharski, S. *Synth. Met.* **2003**, *139*, 515.

30 Loiseau, F.; Campagna, S.; Hameurlaine, A.; Dehaen, W. *J. Am. Chem. Soc.* **2005**, *127*, 11352.

31 Kortekaas, L.; Lancia, F.; Steen, J. D.; Browne, W. R. *J. Phys. Chem. C* **2017**, *121*, 14688.

32 Bhattacharya, S.; Biswas, C.; Raavi, S. S. K.; Venkata Suman Krishna, J.; Vamsi Krishna, N.; Giribabu, L.; Soma, V. R. *J. Phys. Chem. C* **2019**, *123*, 11118.

33 Serevičius, T.; Dodonova, J.; Skaisgiris, R.; Banevičius, D.; Kazlauskas, K.; Juršėnas, S.; Tumkevičius, S. *J. Mater. Chem. C* **2020**, *8*, 11192.

34 Harada, N.; Nakanishi, K. *Acc. Chem. Res.* **1972**, *5*, 257.

35 Nakanishi, K.; Berova, N.; Woody, R. W. *Circular dichroism: Principles and Applications.* (Wiley, New York, **2000**), 361.

36 Berova, N.; Di Bari, L.; Pescitelli, G. *Chem. Soc. Rev.* **2007**, *36*, 914.

37 Ambrose, J. F.; Nelson, R. F. *J. Electrochem. Soc.* **1968**, *115*, 1159.

38 Taoudi, H.; Bernede, J. C.; Del Valle, M. A.; Bonnet, A.; Morsli, M. *J. Mater. Sci.* **2001**, *36*, 631.

39 Zotti, G.; Schiavon, G.; Zecchin, S.; Morin, J. F.; Leclerc, M. *Macromolecules* **2002**, *35*, 2122.

40 Venkateswararao, A.; Thomas, K. J.; Lee, C. P.; Li, C. T.; Ho, K. C. *ACS Appl. Mater. Interfaces* **2014**, *6*, 2528.

41 Karon, K.; Lapkowski, M. *J. Solid State Electrochem.* **2015**, *19*, 2601.

42 Omer, K. M.; Ku, S. Y.; Chen, Y. C.; Wong, K. T.; Bard, A. J. *J. Am. Chem. Soc.* **2010**, *132*, 10944.

43 Chiu, S. K.; Chung, Y. C.; Liou, G. S.; Su, Y. O. *J. Chin. Chem. Soc.* **2012**, *59*, 331.

44 Linton, K. E.; Fisher, A. L.; Pearson, C.; Fox, M. A.; Pålsson, L.-O.; Bryce, M. R.; Petty, M. C. *J. Mater. Chem.* **2012**, *22*, 11816.

45 Chen, L. M.; Lin, I. H.; You, Y. C.; Wei, W. C.; Tsai, M. J.; Hung, W. Y.; Wong, K. T. *Mater. Chem. Front.* **2021**, *5*, 5044.

46 Luo, D.; Liao, C.-W.; Chang, C.-H.; Tsai, C.-C.; Lu, C.-W.; Chuang, T. C.; Chang, H.-H. *J. Phys. Chem. C* **2020**, *124*, 10175.

47 Luo, X.; Chang, J.; Deng, J.; Yang, W. *React. Funct. Polym.* **2010**, *70*, 116.

48 Huang, H.; Hong, S.; Liang, J.; Shi, Y.; Deng, J. *Polym. Chem.* **2017**, *8*, 5726.

49 Zhao, B.; Pan, K.; Deng, J. *Macromolecules* **2019**, *52*, 376.

50 Lu, N.; Gao, X.; Pan, M.; Zhao, B.; Deng, J. *Macromolecules* **2020**, *53*, 8041.

GENERAL CONCLUSION

Supramolecular self-assembly is a feasible approach to manipulate desired nanostructures driven by specific intermolecular interactions and proper molecular design, and provide an opportunity to investigate the relationship between the properties and the self-assembled nanostructures. In spite of their Lewis acid and base character, H-bonding donor – acceptor sites do not interfere with charge transport in organic materials and allow structuration of the active layer in the pursuit of specific properties.

The system, consists of D-π-A type TADF chromophores and hydrogen-bonding assisted biuret motifs, demonstrated the capability of tuning the emission spectrum by tailoring the energy gap between ground state and excited state by using various electron-accepting moieties, while remaining the spontaneous formation of TADF spherical vesicles in the size of 250 nm to 500 nm, evident from SEM, TEM and DLS analysis. The PL spectra of different temperature and fluorescence decay profiles indicated that the TADF properties result in improved luminescence efficiency. By introducing DMSO into TADF vesicles in solutions, the dissolution of well-defined aggregates led to the disappearance of TADF behavior, suggesting a supramolecular gating of TADF process due to energy hopping. The EL devices, whose emitting layer is composed of TADF materials doped in a host CBP matrix, exhibit improved performance with external quantum efficiency of 1.5%, which was 5 to 10 times greater than the system without

TADF materials. The CFM images of the active layer deposited by ink-jet printing process show that the spherical aggregates remained intact with a notable increase in PL and EL intensity. Combining the above results, the approach of TADF-active self-assembled aggregates could be used to strike the balance between high-resolution and improve performance in EL devices, demonstrating a proof-of-concept for fabrication of future generation micro-OLED displays. This, in turn, confirms the compatibility of organic electronic devices and TADF with H-bonding interactions.

Using the guiding principles of self-assembly, diverse chiral chromophores endowed with biuret motifs were designed and the relationship between chiroptical properties and the nanostructures in ground state and excited state was investigated. The series of axially chiral binaphthalene exhibits the capability of forming well-defined nanospheres in specific environments and tunable emission from deep-blue to yellow through the introduction of benzothiadiazole moieties into the π-conjugated backbone. All the fluorophores reveal intense Cotton effects with mirror-image relationship for the enantiomers in their CD spectra. Remarkably, the g_{abs} value of R**7BBNPB** (1.7×10^{-3}) in the cisoid conformation is 3-fold higher than that of R**BNPB** (6.0×10^{-4}) in the open form, indicating that the cisoid conformation promotes the amplification of chirality in ground state. Besides, the cisoid conformation results in a remarkable CPL intensity with g_{lum} up to 0.12 as well – but this should be confirmed for both enantiomers. Upon the addition of

DMSO to solutions of vesicles, the vanished CPL signals suggest that the aggregation exerts a positive influence in enhancing the g_{lum} through self-organization.

By modifying the chiral dopants **THBTTF**, a chiral oxy-analogue **ADOT** could be obtained from simplified synthetic routes and the resulting **ADOT** compounds retain deep-blue emission spectra and similar Φ_{lum}. Limited by the weak optical activities in ground state (g_{abs} of 10^{-4}), the **ADOT** series show poor CPL signals, comparable to **THBTTF**. With the introduction of biuret motifs, the generation of self-assembled vesicles of the **ADOTPB** series were evidenced by SEM. However, the ordered arrangement between chromophores does not facilitate the optical activities in ground state and excited state, implying that inductive effect of alkyl chains in chiral core brings about the little enhancement of the chiroptical properties of these compounds in solution or in aggregated state.

The chiral cyclohexyl derivatives substituted with pyrene moieties display exciplex formation through excited-state symmetry-breaking. By bridging with biuret motifs, homogeneous spherical vesicles are produced in organic solvents. From the Lippert-Mataga plots, the chromophore **DACHPyPB** also exhibits a high dipole moment of 11.2 D in the excited state, assigned to a pyrene exciplex formation. In CD spectra, **DACHPyPB** show a bisignate Cotton effect at 418 nm owing to exciton coupling between pyrene chromophores. Contrary to our expectations, the self-assembled vesicles

give rise to a relatively weak CPL activity compared to that of **DiPy** without biuret. This could be attributed to structural constraints are unsuited for formation of an emissive exciplex or the cancelling of the polarization due to the summation from different positions in highly ordered aggregates.

The approach to design exciplexes emitting circularly polarized luminescence by pairing a chiral carbazole donor with an acceptor was explored. Based on the energy levels of CP-TADF materials R/S-**BNCNCz** and the results of AIE test to probe the suitable acceptor, the blended films of R/S-**BNCNCz**:**47p-QN** exhibit a 50-nm bathochromic shift in the steady-state PL and long-lived excited state with lifetime of 0.927 μs or 0.698 μs for R- or S-**BNCNCz**:**47p-QN** respectively. However, the exciplex emission in CPL spectra is small and with $|g_{lum}|$ of 10^{-4}. To improve the CP-exciplex intensity and readily identify exciplex emission from that of the donor or acceptor, we conceived a series of axially-chiral carbazole-based electron donors, **7BBNCz**, **3CzPh**, **Ph3Cz** and **Ph4Cz**. **7BBNCz** is composed of a chiral binaphthalene core and possesses a lower triplet energy of 2.48 eV owing to longer π-conjugation length, while the chiral octahydrobinaphthalene derivatives of **3CzPh**, **Ph3Cz** and **Ph4Cz** have higher triplet energies at ca. 3.00 eV. These could serve as suitable hole-transporting materials in exciplex or as host materials for energy transfer process in host-guest system. Taking advantage of HOMO/LUMO energies and AIE tests, we identified several candidate

exciplex systems: **7BBNCz**:**56mQN**, **3CzPh**:**POT2T**, **Ph3Cz**:**POT2T**, **Ph4Cz**:**POT2T**, **Ph3Cz**:**56mQN** and **Ph4Cz**:**56mQN** with moderate Φ_{lum} in aqueous solutions. Blended films of all the long-lived exciplex systems are evidenced by bathochromic-shifted emission in PL spectra and characterized by transient PL decay profiles. These chiral exciplex candidates revealed optical activities in ground states and exhibit mirror-image relationship between the enantiomers in CD spectra. Although most of the systems are chiroptically inactive in excited state, we identified one CPL-active system, R/S-**Ph3Cz**:**56m-QN**, with clear chiral induction between chiral donors and achiral acceptors, which supports our approach as feasible.

Perhaps the most remarkable observation throughout this work is the propensity for all of the bis-biuret derivatives to spontaneously form hollow spheres in solution. The spontaneous formation of vesicles is rare, and restricted to some phospholipids and polymersomes. In contrast, all of the compounds investigated herein adopt vesicle-like morphologies even in the absence of aqueous environments. Clearly, the bis-biuret motif is a robust supramolecular programming code for such assemblies.

Chapter 5. Experimental Section

5-1 General Methods

All the starting materials and solvents were purchased from commercial sources and used without further purification unless stated otherwise. ^{1}H and ^{13}C NMR spectra of compounds were collected on a Varian 400 Unity plus (400 MHz) spectrometer in deuterated solvents as internal reference at room temperature. Mass spectra were recorded using a Bruker micrOTOF-QII mass spectrometer and Bruker Daltonics autoflex speed with electrospray ionization (ESI) and matrix-assisted laser desorption/ionization (MALDI) as ionization method. The mass spectrum recorded with JEOL JMS-700 with electron ionization (EI). We thank the support from Mass Core Facility at National Taiwan University. UV-visible absorption spectra were recorded on a spectrophotometer (HITACHI U2800A) or Perkin-Elmer spectrophotometer. PL spectra were measured with a fluorescence spectrophotometer (HITACHI F9500) or a Horiba Fluoromax instrument. Photoluminescence quantum yields (PLQYs) for solution and thin-film samples were determined with a calibrated integrating sphere system (HAMAMATSU C9920). The circular dichroism (CD) spectra were measured on a JASCO J-810 circular dichroism spectrometer with 'Standard' sensitivity. The scan speed was set as 200 nm/min with a 0.1 nm resolution and a response time of 2.0 s. The circularly polarized photoluminescence (CP-PL) spectra were measured on a JASCO CPL-300 spectrophotometer with 'Standard' sensitivity at 100 nm/min scan speed and a response time of 4.0 s employing "slit" mode. Thanks for Prof. Yu-Chiang Chao and the technical assistance of Department of Physics, National Taiwan Normal University with CPL spectrophotometer.

5-2 Preparation of Nanospheres

Solutions of compounds were prepared by adding the appropriate volume of THF (dried over Na/ benzophenone and distilled prior to use), acetone (ACS reagent, 99.5+%, for analysis), or methanol (ACS reagent, 99.5+%, for analysis) to a glass vial containing a solid sample of the compound to produce a 0.1 mM solution. Dissolution was achieved by gentle shaking of the vial for 30 min. The solutions were drop-casted onto the substrates using a syringe to deposit approximately 50 μL of solution, and the solvent was allowed to evaporate in air.

5-3 Techniques for Characterization

Scanning Electron Microscopy

Samples were prepared by drop-casting a THF or acetone or methanol solution of self-assembled compounds (0.1 mM) onto a flat SiO_2/Si substrate as described above. The samples were imaged using a FEI Nova NanoSEM 200 in low-vacuum mode with no conductive overcoat. The chamber pressure was maintained at 0.45 Torr water using a differential pumping system. An immersion lens was employed and the secondary electrons amplified by gas vapor and collected by an electrode mounted on the pole piece. Thanks for Prof. Jing-Jong Shyue and the technical assistance of Research Center for Applied Sciences, Academia Sinica with SEM.

Transmission Electron Microscopy

Samples were drop-casted onto a 200 mesh copper grid coated with formvar film stabilized with vacuum-evaporated carbon and dried under air. The samples were

examined in electron microscopes operating at 75 kV (Hitachi H-7650). We thanks to the technical assistance of Technology Commons, College of Life Science, NTU with TEM.

Confocal Fluorescence Microscopy

Measurements were performed on a Picoquant Microtime 200 inverted confocal microscope, using a PicoHarp 300 multichannel single photon counter and two MPD SPADs. The excitation originates from a frequency doubled Ti-Sa laser (Coherent) tuned at 385 nm with picosecond pulses (6 ps) at 4.76 MHz repetition rate. Average powers of typically 0.24 Wcm^{-2} (peak power of ca. 16 $kWcm^{-2}$), and up to 24Wcm^{-2}, have been used for image and spectra acquisition. The laser beam is injected by 908 reflection on a 80%T/20%R spectrally flat beam splitter into the microscope objective (100 ×UPLSAPO, N.A. 1.4). The emission is collected by transmission through the same beam splitter and a suitable interferential filter before being focused on a 50 μm pinhole. After the pinhole, light can be diverted into an Andor SR300i spectrometer equipped with a Newton EM-CCD for spectroscopy measurements. All spectra are QE corrected. All decays obtained using the confocal setup were tail-fitted as the emission is accumulated on a broad spectral range and the instrument response function (IRF) is wavelength dependent. The fit is done according to $I(t) = \sum A_i e(-t/\tau_i)$ and the average decay times are defined as $\sum A_i \tau_i^2 / A_i \tau_i$.

Variable-Temperature PL spectra and Time-Correlated Single Photon Counting

Decay parameters were extracted from reconvolution of the time-resolved emission decay profiles collected using a home-built TC-SPC instrument equipped with a Picoquant 310 nm or 350 nm pulsed excitation source and a Hamamatsu R6427 photomultiplier and Timeharp 260 collection electronics. A monochromator or 420 long-pass filter was used to isolate the emission from the sample. Variable-temperature spectra

and lifetimes were obtained using an Oxford DN optistat connected to an ITC controller (precision = ± 0.1K).

Thermogravimetric Analysis

Decomposed temperature (T_d, 5% weight loss) were measured with a Dynamic Q500 Thermo-Gravimetric Analyzer under a nitrogen atmosphere with heating and cooling rates of 10 °C min^{-1}. Thanks for the TGA data from Thermal Analysis System of Instrumentation Center, National Taiwan University.

Electrochemical Characterization

The electrochemical properties of molecules were investigated by cyclic voltammetry (CV). The measurement of oxidation potentials was carried out in anhydrous CH_2Cl_2 solution (1.0 mM) containing 0.1 M tetrabutylammonium hexafluorophosphate ($TBAPF_6$) as a supporting electrolyte, while the measurements of the reduction potentials were conducted in anhydrous THF solution (1.0 mM) containing 0.1 M tetrabutylammonium perchlorate (TBAP) as a supporting electrolyte, purged with argon prior to conduct the measurements. A glassy carbon electrode and a platinum wire was used as the working electrode and counter electrode, respectively. All potentials were recorded versus Ag/AgCl (saturated) as a reference electrode and calibrated with ferrocene/ferrocenium (Fc/Fc^+) redox couple.

EL Device Fabrication and Characterization

The EL devices were placed flat on the sample tray and the set-up was used to collect the EL by transmission through the dichroic optics before being focused on a 50 μm pinhole. After the pinhole, light can be diverted into an Andor SR300i spectrometer

equipped with a Newton EM-CCD for spectroscopy measurements or to time-resolved avalanche photodiodes (MPD). External quantum efficiency measurements: A 3D-printed device's compartment coupled, via optical fiber, to a UV-VIS spectrophotometer (Ocean Optics HR2000) was employed for the quantitative device's EQE analysis. The system was calibrated using a commercially available white light-emitting diode (Thorlabs, model LEDSW30), whose *optical power vs forward current and angular intensity distribution* data are provided by the supplier, aligned to the optical fiber entrance. A constant current of 0.1 mA was applied with a Power-Source-Unit (Keithley 2400) and the corresponding EL spectrum was registered during the integration time (50 ms); according to the *optical power/current dependence*, 0.1 mA yields an optical power of 0.072 mW, and therefore, the area below the EL spectrum was normalized to this value with the aim of converting from counts to optical power units. Upon calibration, the optical power spectra of our devices at different voltages were measured during the same integration time, while the electrical current was monitored. Considering the different spectral distribution of the target devices compared to the reference LED, a conversion from power units to number of photons was carried out; subsequent integration was performed to obtain the absolute number of photons, and then divided by the electric charge that flowed during the integration time, to finally obtain the corresponding EQE values. The different angular distributions and active areas of both kind of samples were contemplated for a more accurate EQE estimation. The active areas of both kind of devices, reference and target, were always placed at the exactly same position/distance from the optical fiber entrance to ensure reliability.

5-4 Synthesis

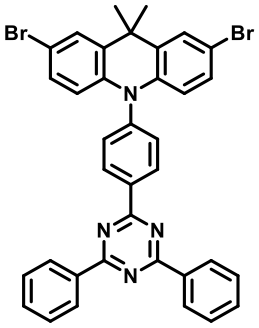

DTBr2

Synthesis of DTBr2. A mixture of **DMAC-TRZ** (500 mg, 0.97 mmol), NBS (758 mg, 4.26 mmol) was dissolved in THF and stirred at 0ºC for 1 h and warmed to room temperature for 2 h. The reaction was quenched by adding saturated K_2CO_3 aqueous solution and extracted with CH_2Cl_2. The combined organic phase was washed with brine and dried over $MgSO_4$. The crude product was purified by column chromatography on silica gel (CH_2Cl_2/hexanes = 1/4) to afford pure **DTBr2** (76%, 496 mg) as a yellow solid. ^{1}H NMR ($CDCl_3$, 400 MHz) δ 9.03 (d, *J* = 3.40 Hz, 2H), 8.81 (d, *J* = 4.00 Hz, 4H), 7.67-7.59 (m, 6H), 7.56 (d, *J* = 1.20 Hz, 2H), 7.51 (d, *J* = 4.20 Hz, 2H), 7.11 (d, *J* = 1.00 Hz, 2H), 7.09 (d, *J* = 1.00 Hz, 2H), 6.26 (d, *J* = 4.40 Hz, 2H), 1.70 (s, 6H); ^{13}C NMR ($CDCl_3$, 100 MHz) δ 171.9, 170.9, 144.3, 139.4, 136.7, 136.0, 132.7, 131.8, 131.7, 129.4, 129.0, 128.7, 128.2, 115.9, 113.6, 36.3, 31.0; HRMS (m/z, MALDI) Calcd for $C_{36}H_{26}{}^{79}Br_2N_4$ 673.0597; found 673.0540; Calcd for $C_{36}H_{26}{}^{79}Br^{81}BrN_4$ 675.0580; found 675.0680; Calcd for $C_{36}H_{26}{}^{81}Br_2N_4$ 677.0568; found 677.0840.

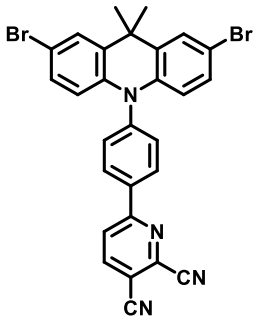

Py56Br2

Synthesis of Py56Br2. A mixture of **Py56** (800 mg, 1.94 mmol), NBS (686 mg, 3.88 mmol) was dissolved in THF and stirred at 0ºC for 1 h and warmed to room temperature for 2 h. The reaction was quenched by adding saturated K_2CO_3 aqueous solution and extracted with CH_2Cl_2. The combined organic phase was washed with brine and dried over $MgSO_4$. The crude product was purified by column chromatography on silica gel (CHCl3/hexanes = 1/3) to afford pure **Py56Br2** (87%, 970 mg) as an orange solid. ^{1}H NMR (d_6-DMSO, 400 MHz) δ 8.75 (d, J = 8.5 H, 1H), 8.66 (d, J = 8.5 Hz, 1H), 8.51 (d, J = 8.5 Hz, 2H), 7.63 (dd, J = 11.8, 5.4 Hz, 4H), 7.19 (dd, J = 2.3 Hz, 2H), 6.15 (d, J = 8.8 Hz, 2H), 1.64 (s, 6H); ^{13}C NMR (d_6-DMSO, 100 MHz) δ 158.67, 142.48, 138.74, 135.47, 135.45, 131.64, 131.37, 130.50, 129.29, 127.99, 123.89, 115.68, 114.89, 114.63, 112.68, 112.24, 35.85, 30.86; HRMS (m/z, MALDI) Calcd for $C_{28}H_{18}{}^{79}Br_2N_4$ 568.9970; found 568.9912; Calcd for $C_{28}H_{18}{}^{79}Br^{81}BrN_4$ 570.9952; found 570.9906; Calcd for $C_{28}H_{18}{}^{81}Br_2N_4$ 572.9938; found 572.9912.

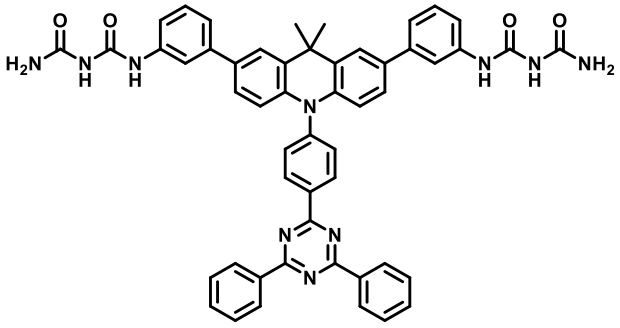

DTMB

Synthesis of DTMB. A mixture of $Pd(PPh_3)_4$ (85 mg, 0.073 mmol), K_2CO_3 (615 mg, 4.45 mmol), **DTBr2** (500 mg, 0.74 mmol), 3-pinacolatoboronic ester-benzenebiuret (475 mg, 1.55 mmol) in degassed THF (7.5 mL) and water (2.2 mL) was refluxed for two days. The reaction was quenched by adding water and extracted with THF. The combined organic solution was washed with brine and dried over $MgSO_4$. The crude product was purified by column chromatography on silica gel (THF/CH_2Cl_2 = 1/1) to afford **DTMB** (22%, 141 mg) as a yellow solid. ^{1}H NMR (d_6-DMSO, 400 MHz) δ 10.02 (s, 2H), 9.06 (d, *J* = 4.20 Hz, 2H), 8.86 (s, 2H), 8.79 (d, *J* = 3.80 Hz, 4H), 7.80 (s, 2H), 7.74-7.64 (m, 12H), 7.43 (d, *J* = 3.60 Hz, 2H), 7.36-7.30 (m, 6H), 6.90 (bs, 4H), 6.36 (d, *J* = 4.00 Hz, 2H), 1.82 (s, 6H); ^{13}C NMR (d_6-DMSO, 100 MHz) δ 171.2, 170.5, 155.4, 152.1, 144.8, 140.9, 139.3, 138.6, 135.5, 135.3, 133.1, 132.7, 131.7, 131.5, 130.2, 129.4, 129.0, 128.7, 125.1, 124.2, 121.0, 117.5, 116.8, 114.4, 36.0, 32.0; HRMS (m/z, MALDI) Calcd for $C_{52}H_{42}N_{10}O_4$ 870.3390; found 870.3322.

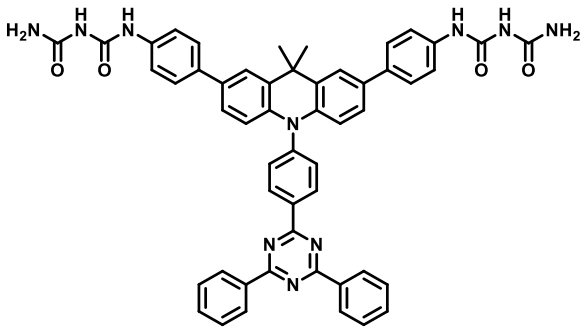

DTPB

Synthesis of DTPB. A mixture of $Pd(PPh_3)_4$ (68 mg, 0.059 mmol), K_2CO_3 (492 mg, 3.56 mmol), **DTBr2** (400 mg, 0.59 mmol), 4-pinacolatoboronic ester-benzenebiuret (380 mg, 1.24 mmol) in degassed THF (6 mL) and water (1.8 mL) was refluxed for two days. The reaction was quenched by adding water and extracted with THF. The combined organic solution was washed with brine and dried over $MgSO_4$. The crude product was purified by column chromatography on silica gel (THF/CH_2Cl_2 = 1/1) to afford **DTPB** (17%, 90 mg) as a yellow solid. ^{1}H NMR (d_6-DMSO, 400 MHz) δ 10.01 (s, 2H), 9.05 (d, *J* = 4.00 Hz, 2H), 8.86 (s, 2H), 8.79 (d, *J* = 3.60 Hz, 4H), 7.80 (s, 2H), 7.74-7.67 (m, 8H), 7.60 (d, *J* = 4.20 Hz, 4H), 7.50 (d, *J* = 4.20 Hz, 4H), 7.31 (d, *J* = 4.20 Hz, 2H), 6.90 (bs, 4H), 6.34 (d, *J* = 4.40 Hz, 2H), 1.82 (s, 6H); ^{13}C NMR (d_6-DMSO, 100 MHz) δ 171.2, 170.5, 155.4, 151.9, 144.9, 138.9, 136.9, 135.4, 135.3, 134.8, 133.1, 132.3, 131.6, 131.4, 131.3, 130.2, 129.0, 128.7, 128.6, 126.5, 124.6, 123.7, 119.4, 114.4, 36.0, 32.0; HRMS (m/z, MALDI) Calcd for $C_{52}H_{42}N_{10}O_4$ 870.3390; found 870.3472.

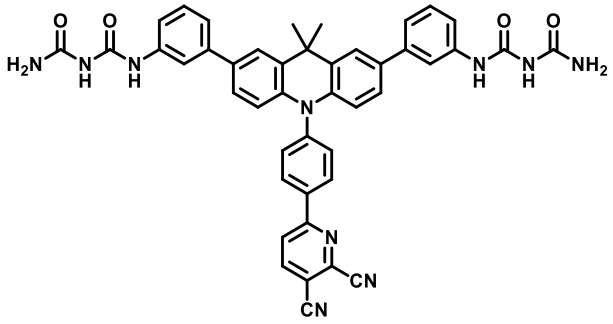

Py56MB

Synthesis of Py56MB. A mixture of $Pd(PPh_3)_4$ (40 mg, 0.035 mmol), K_3PO_4 (447 mg, 2.10 mmol), **Py56Br2** (200 mg, 0.35 mmol), 3-pinacolatoboronic ester-benzenebiuret (225 mg, 0.74 mmol) in degassed THF (7.5 mL) and water (1.0 mL) was refluxed for two days. The reaction was quenched by adding water and extracted with THF. The combined organic solution was washed with brine and dried over $MgSO_4$. The crude product was purified by column chromatography on silica gel (THF/CH_2Cl_2 = 1/1) to afford **Py56MB** (12%, 33 mg) as an orange solid. ^{1}H NMR (d_6-DMSO, 400 MHz) δ 10.02 (s, 2H), 8.87 (s, 2H), 8.74 (d, *J* = 4.20 Hz, 1H), 8.66 (d, *J* = 4.20 Hz, 1H), 8.53 (d, *J* = 4.00 Hz, 2H), 7.78 (s, 2H), 7.67 (d, *J* = 4.20 Hz, 2H), 7.63 (s, 2H), 7.43 (d, *J* = 4.00 Hz, 2H), 7.38-7.28 (m, 6H), 6.90 (bs, 4H), 6.31 (d, *J* = 4.20 Hz, 2H), 1.80 (s, 6H); ^{13}C NMR (d_6-DMSO, 100 MHz) δ 159.0, 155.4, 152.1, 143.4, 142.6, 141.0, 138.6, 135.6, 135.4, 132.7, 131.7, 130.5, 130.2, 129.3, 125.1, 124.1, 124.0, 121.0, 117.5, 116.8, 115.1, 114.8, 114.4, 112.3, 36.0, 31.8; HRMS (m/z, MALDI) Calcd for $C_{44}H_{34}N_{10}O_4$ 766.2764; found 766.2783.

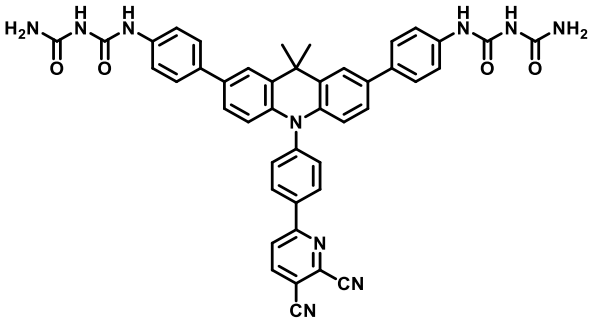

Py56PB

Synthesis of Py56PB. A mixture of $Pd(PPh_3)_4$ (40 mg, 0.035 mmol), K_3PO_4 (447 mg, 2.10 mmol), **Py56Br2** (200 mg, 0.35 mmol), 4-pinacolatoboronic ester-benzenebiuret (225 mg, 0.74 mmol) in degassed THF (7.5 mL) and water (1.0 mL) was refluxed for two days. The reaction was quenched by adding water and extracted with THF. The combined organic solution was washed with brine and dried over $MgSO_4$. The crude product was purified by column chromatography on silica gel (THF/CH_2Cl_2 = 1/1) to afford **Py56PB** (15%, 41 mg) as an orange solid. ^{1}H NMR (d_6-DMSO, 400 MHz) δ 10.01 (s, 2H), 8.86 (s, 2H), 8.74 (d, *J* = 4.20 Hz, 1H), 8.66 (d, *J* = 4.20 Hz, 1H), 8.52 (d, *J* = 4.20 Hz, 2H), 7.78 (s, 2H), 7.65 (d, *J* = 4.40 Hz, 2H), 7.59 (d, *J* = 4.40 Hz, 4H), 7.50 (d, *J* = 4.20 Hz, 4H), 7.29 (d, *J* = 3.40 Hz, 2H), 6.90 (bs, 4H), 6.28 (d, *J* = 4.20 Hz, 2H), 1.80 (s, 6H); ^{13}C NMR (d_6-DMSO, 100 MHz) δ 159.0, 155.4, 151.9, 143.5, 142.6, 138.9, 136.9, 135.6, 135.3, 134.8, 132.3, 131.7, 130.5, 130.3, 126.5, 124.6, 124.0, 123.7, 119.4, 115.1, 114.8, 114.4, 112.3, 36.0, 31.8; HRMS (m/z, MALDI) Calcd for $C_{44}H_{34}N_{10}O_4$ 766.2764; found 766.2777.

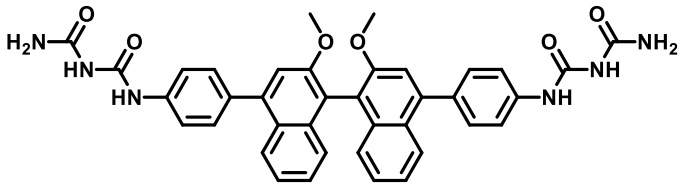

BNPB

Synthesis of **BNPB**. A mixture of $Pd(PPh_3)_4$ (49 mg, 0.042 mmol), K_2CO_3 (351 mg, 2.54 mmol), **BNOMe** (200 mg, 0.42 mmol), 4-pinacolatoboronic ester-benzenebiuret (271 mg, 0.89 mmol) in degassed THF (4.5 mL) and water (1.3 mL) was refluxed for two days. The reaction was quenched by adding water and extracted with THF. The combined organic solution was washed with brine and dried over $MgSO_4$. The crude product was purified by column chromatography on silica gel (THF/CH_2Cl_2 = 1/1) to afford **BNPB** (55%, 155 mg) as a white solid. ^{1}H NMR (d_6-DMSO, 400 MHz) δ 10.14 (s, 2H), 8.95 (s, 2H), 7.85 (d, *J* = 3.8 Hz, 2H), 7.66 (d, *J* = 4.0 Hz, 2H), 7.59 (d, *J* = 4.0 Hz, 2H), 7.47 (s, 2H), 7.27 (quint, *J* = 6.8 Hz, 4H), 7.04 (d, *J* = 4.0 Hz, 2H), 6.95 (bs, 4H), 3.76 (s, 6H); ^{13}C NMR (d_6-DMSO, 100 MHz) δ 155.5, 154.1, 152.1, 140.7, 137.7, 134.6, 133.9, 130.6, 126.6, 126.4, 125.7, 125.1, 123.6, 119.1, 117.9, 115.0, 56.2; HRMS (m/z, MALDI) Calcd for $C_{38}H_{32}N_6O_6$ 668.2383; found 668.2398.

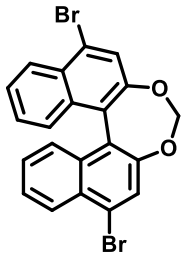

7BBNBr2

Synthesis of **7BBNBr2**. A mixture of **BNOH** (820 mg, 1.84 mmol), K_2CO_3 (2.55 g, 18.5

mmol) in dried DMF (61.5 mL) were stirred in argon atmosphere at 50°C for 15 min, followed by addition of bromochloromethane (3.72 mL, 55.2 mmol) dropwise and stirred in argon atmosphere at 50°C for 15 h. The reaction was quenched by adding water and brine and extracted by ethyl acetate. The combined organic phase was dried over $MgSO_4$. The crude product was purified by column chromatography on silica gel (hexanes /CH_2Cl_2 = 4/1) to afford **7BBNBr2** (86%, 725 mg) as a white solid. ^{1}H NMR ($CDCl_3$, 400 MHz) δ 8.36 (d, *J* = 4.4 Hz, 2H), 7.82 (s, 2H), 7.58-7.54 (m, 2H), 7.45 (d, *J* = 4.0 Hz), 7.36-7.32 (m, 2H), 5.68 (s, 2H); ^{13}C NMR ($CDCl_3$, 100 MHz) δ 132.6, 130.3, 127.6, 127.1, 127.0, 126.5, 125.5, 125.2, 124.9, 124.0, 121.5, 103.3; HRMS (m/z, MALDI) Calcd for $C_{21}H_{12}{}^{79}Br_2O_2$ 453.9198; found 453.9177; Calcd for $C_{21}H_{12}{}^{79}Br^{81}BrO_2$ 455.9179; found 455.9190; Calcd for $C_{21}H_{12}{}^{81}Br_2O_2$ 457.9162; found 457.9209;

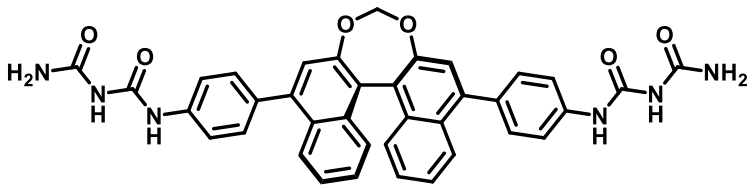

7BBNPB

Synthesis of **7BBNPB**. A mixture of $Pd(PPh_3)_4$ (30 mg, 0.026 mmol), K_2CO_3 (447 mg, 2.99 mmol), **7BBNBr2** (228 mg, 0.50 mmol), 4-pinacolatoboronic ester-benzenebiuret (335 mg, 1.10 mmol) in degassed THF (25 mL) and water (1.5 mL) was refluxed for two days. The reaction was quenched by adding water and extracted with THF. The combined organic solution was washed with brine and dried over $MgSO_4$. The crude product was

purified by column chromatography on silica gel (THF/CH_2Cl_2 = 1/1) to afford **7BBNPB** (63%, 205 mg) as a white solid. ^{1}H NMR (d_6-DMSO, 400 MHz) δ 10.02 (s, 2H), 8.97 (s, 2H), 7.99 (d, *J* = 4.4 Hz, 2H), 7.68 (d, *J* = 4.0 Hz, 2H), 7.59 (d, *J* = 4.0 Hz, 2H), 7.50-7.48 (m, 6H), 7.43 (d, *J* = 3.6 Hz, 2H), 6.95 (bs, 4H), 5.78 (s, 2H); ^{13}C NMR (d_6-DMSO, 100 MHz) δ 155.5, 152.1, 150.6, 141.8, 138.0, 133.8, 132.0, 130.5, 129.3, 126.5, 126.4, 125.5, 124.5, 121.9, 119.1, 103.0; HRMS (m/z, MALDI) Calcd for $C_{37}H_{28}N_6O_6$ 652.2070; found 652.2033.

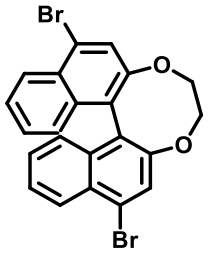

8BBNBr2

Synthesis of **8BBNBr2**. A mixture of **BNOH** (444 mg, 1.00 mmol), K_2CO_3 (1.03 g, 7.49 mmol) and ethylene glycol ditosylate (462 mg, 1.25 mmol) in dried DMF (13 mL) were stirred in argon atmosphere at 80°C for 18 h. The reaction was quenched by adding water and brine and extracted by ethyl acetate. The combined organic phase was dried over $MgSO_4$. The crude product was purified by column chromatography on silica gel (hexanes/CH_2Cl_2 = 4/1 to 2/1) to afford **8BBNBr2** (50%, 235 mg) as a white solid. ^{1}H NMR (CD_2Cl_2, 400 MHz) δ 8.31 (d, *J* = 4.6 Hz, 2H), 7.82 (s, 2H), 7.53 (t, *J* = 6.4 Hz, 2H), 7.28 (t, *J* = 7.2 Hz, 2H), 7.20 (d, *J* = 4.2 Hz, 2H), 4.41 (q, *J* = 9.2 Hz, 2H), 4.16 (q,

J = 8.8 Hz, 2H); ^{13}C NMR (CD_2Cl_2, 100 MHz) δ 156.7, 134.0, 130.1, 127.8, 127.8, 127.7, 127.4, 126.9, 124.7, 124.3, 73.8; HRMS (m/z, MALDI) Calcd for $C_{22}H_{14}{}^{79}Br_2O_2$ 467.9355; found 467.9375; Calcd for $C_{22}H_{14}{}^{79}Br^{81}BrO_2$ 469.9335; found 469.9378; Calcd for $C_{22}H_{14}{}^{81}Br_2O_2$ 471.9319; found 471.9376.

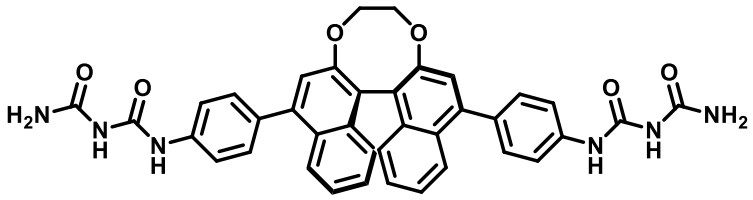

8BBNPB

Synthesis of **8BBNPB**. A mixture of $Pd(PPh_3)_4$ (6.5 mg, 0.0056 mmol), K_2CO_3 (93 mg, 0.67 mmol), **8BBNBr2** (53 mg, 0.11 mmol), 4-pinacolatoboronic ester-benzenebiuret (76 mg, 0.25 mmol) in degassed THF (5.0 mL) and water (0.3 mL) was refluxed for two days. The reaction was quenched by adding water and extracted with THF. The combined organic solution was washed with brine and dried over $MgSO_4$. The crude product was purified by column chromatography on silica gel (THF/CH_2Cl_2 = 1/1) to afford **8BBNPB** (28%, 21 mg) as a white solid. ^{1}H NMR (d_6-DMSO, 400 MHz) δ 10.15 (s, 2H), 8.95 (s, 2H), 7.92 (d, J = 4.4 Hz, 2H), 7.65 (d, J = 4.2 Hz, 2H), 7.58 (d, J = 4.4 Hz, 2H), 7.43 (s, 2H), 7.40 (d, J = 4.2 Hz, 2H), 7.32 (t, J = 7.2 Hz, 2H), 7.23 (d, J = 4.4 Hz, 2H), 6.95 (bs, 4H), 4.41 (d, J = 4.4 Hz, 2H), 4.15 (d, J = 4.4 Hz, 2H); ^{13}C NMR (d_6-DMSO, 100 MHz) δ 155.9, 155.5, 152.1, 142.1, 137.9, 134.0, 132.9, 130.5, 128.5, 126.8, 126.5, 125.9, 125.1, 123.5, 122.9, 119.1, 72.9; HRMS (m/z, MALDI) Calcd for $C_{38}H_{30}N_6O_6$ 667.2299; found

667.2268 (M+1).

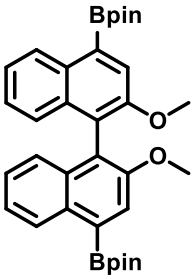

BNBpin2

Synthesis of **BNBpin2**. A mixture of **BNOMe** (100 mg, 0.21 mmol), bis(pinacolato)diborane (162 mg, 0.63 mmol), KOAc (125 mg, 1.26 mmol) and [Pd(dppf)Cl_2] (14 mg, 0.02 mmol) in dried THF (5 mL) were stirred in argon atmosphere at 80℃ for 18 h. The reaction was cooled and concentrated in vacuo to get crude. The crude product was purified by column chromatography on silica gel (hexanes/THF = 4/1) to afford **BNBpin2** (82%, 97 mg) as white crystals. ^{1}H NMR (d_6-DMSO, 400 MHz) δ 8.70 (d, *J* = 4.4 Hz, 2H), 7.93 (s, 2H), 7.38 (t, *J* = 8.0 Hz, 2H), 7.21 (t, *J* = 8.0 Hz, 2H), 6.91 (d, *J* = 4.0 Hz, 2H), 3.72 (s, 6H), 1.43 (s, 24H); ^{13}C NMR (d_6-DMSO, 100 MHz) δ 153.5, 133.3, 132.1, 128.6, 128.1, 126.2, 124.8, 124.0, 122.5, 122.3, 83.9, 56.2, 24.7; HRMS (m/z, MALDI) Calcd for $C_{34}H_{40}B_2O_6$ 566.3011; found 566.3035.

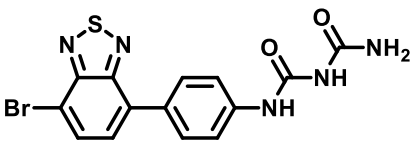

BTBiuret

Synthesis of **BTBiuret**. A mixture of $Pd(PPh_3)_4$ (37.8 mg, 0.033 mmol), K_2CO_3 (271 mg, 1.96 mmol), **BTBr2** (385 mg, 1.31 mmol), 4-pinacolatoboronic ester-benzenebiuret (200

mg, 0.65 mmol) in degassed THF (26 mL) and water (1.0 mL) was refluxed for two days. The reaction was quenched by adding water and extracted with THF and saturated $NH_4Cl_{(aq)}$. The combined organic solution was washed with brine and dried over $MgSO_4$. The crude product was purified by column chromatography on silica gel (THF/ hexanes = 1/1 to 3/1) to afford **BTBiuret** (56%, 290 mg) as a yellow solid. ^{1}H NMR (d_6-DMSO, 400 MHz) δ 10.18 (s, 2H), 8.95 (s, 2H), 8.10 (d, J = 3.8 Hz, 2H), 7.95 (d, J = 4.4 Hz, 4H), 7.76 (d, J = 3.8 Hz, 2H), 7.63 (d, J = 4.2 Hz, 4H), 6.90 (bs, 4H); ^{13}C NMR (d_6-DMSO, 100 MHz) δ 165.1, 162.8, 162.1, 161.6, 148.3, 142.2, 142.0, 140.3, 139.4, 137.6, 128.6, 121.3.

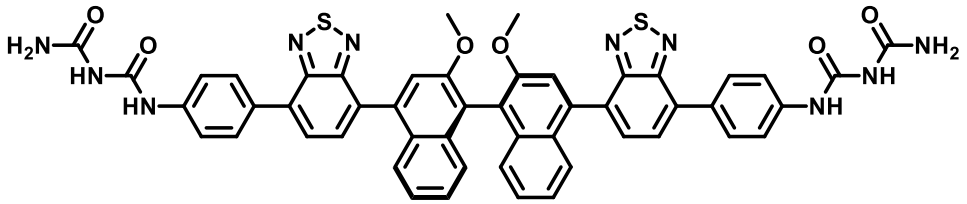

BNBTPB

Synthesis of **BNBTPB**. A mixture of $Pd(PPh_3)_4$ (20 mg, 0.010 mmol), K_2CO_3 (146 mg, 1.05 mmol), **BTBiuret** (148 mg, 0.37 mmol), **BNBpin2** (100 mg, 0.18 mmol) in degassed THF (7.0 mL) and water (0.5 mL) was refluxed for two days. The reaction was quenched by adding water and extracted with THF. The combined organic solution was washed with brine and dried over $MgSO_4$. The crude product was purified by column chromatography on silica gel (THF/CH_2Cl_2 = 1/1) to afford **BNBTPB** (45%, 74 mg) as a yellow solid. ^{1}H NMR (d_6-DMSO, 400 MHz) δ 10.20 (s, 2H), 8.97 (s, 2H), 8.09 (d, J = 4.2 Hz, 4H), 8.03

(q, J = 7.2 Hz, 4H), 7.77 (s, 2H), 7.68 (d, J = 4.4 Hz, 4H), 7.56 (d, J = 4.2 Hz, 2H), 7.30 (t, J = 7.2 Hz, 2H), 7.18 (t, J = 6.0 Hz, 2H), 7.13 (d, J = 6.0 Hz, 2H), 6.90 (bs, 4H), 3.79 (s, 6H); ^{13}C NMR (d_6-DMSO, 100 MHz) δ 155.5, 154.8, 154.1, 152.9, 152.1, 138.5, 137.1, 133.7, 132.4, 131.8, 131.5, 131.0, 129.8, 128.9, 128.2, 127.4, 127.2, 126.5, 123.7, 119.1, 118.9, 116.2, 56.3; HRMS (m/z, MALDI) Calcd for $C_{50}H_{36}N_{10}O_6S_2$ 936.2261; found 936.2278.

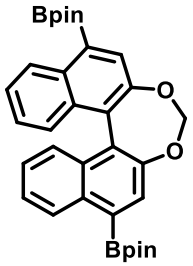

7BBNBpin2

Synthesis of **7BBNBpin2**. A mixture of **7BBNBr2** (228 mg, 0.50 mmol), bis(pinacolato)diborane (381 mg, 1.50 mmol), KOAc (294 mg, 3.00 mmol) and [Pd(dppf)Cl_2] (70 mg, 0.10 mmol) in dried THF (10 mL) were stirred in argon atmosphere at 80℃ for 18 h. The reaction was cooled and concentrated in vacuo to get crude. The crude product was purified by column chromatography on silica gel (hexanes/THF = 3/1) to afford **7BBNBpin2** (84%, 230 mg) as white crystals. ^{1}H NMR (d_6-DMSO, 400 MHz) δ 8.78 (d, J = 4.4 Hz, 2H), 7.93 (s, 2H), 7.55 (t, J = 8.0 Hz, 2H), 7.34 (quin, J = 8.0 Hz, 4H), 5.72 (s, 2H), 1.22 (s, 24H); ^{13}C NMR (d_6-DMSO, 100 MHz) δ 150.2, 134.5, 131.5, 129.8, 128.7, 128.5, 126.3, 126.2, 125.7, 103.0, 84.1, 82.8, 81.4, 24.8; HRMS (m/z,

MALDI) Calcd for $C_{33}H_{36}B_2O_6$ 550.2698; found 550.2722.

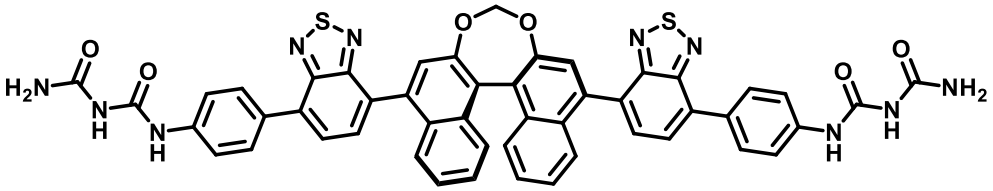

7BBNBTPB

Synthesis of **7BBNBTPB**. A mixture of $Pd(PPh_3)_4$ (19 mg, 0.016 mmol), K_2CO_3 (136 mg, 0.98 mmol), **BTBiuret** (137 mg, 0.34 mmol), **7BBNBpin2** (90 mg, 0.16 mmol) in degassed THF (7.0 mL) and water (0.5 mL) was refluxed for two days. The reaction was quenched by adding water and extracted with THF. The combined organic solution was washed with brine and dried over $MgSO_4$. The crude product was purified by column chromatography on silica gel (THF/CH_2Cl_2 = 1/1) to afford **7BBNBTPB** (35%, 53 mg) as an orange solid. ^{1}H NMR (d_6-DMSO, 400 MHz) δ 10.22 (s, 2H), 8.99 (s, 2H), 8.12 (d, J = 3.8 Hz, 4H), 8.08-8.01 (m, 4H), 7.76 (s, 2H), 7.70 (d, J = 4.2 Hz, 4H), 7.60 (d, J = 4.0 Hz, 2H), 7.46-7.41 (m, 4H), 7.00 (bs, 4H), 5.83 (s, 2H); ^{13}C NMR (d_6-DMSO, 100 MHz) δ 155.5, 154.7, 152.9, 152.1, 150.6, 138.6, 138.3, 132.6, 131.8, 131.3, 131.0, 130.9, 129.9, 129.4, 127.4, 126.9, 126.6, 126.4, 125.7, 125.5, 125.3, 123.1, 119.0, 103.2; HRMS (m/z, MALDI) Calcd for $C_{49}H_{32}N_{10}O_6S_2$ 920.1948; found 921.2061 (M+1).

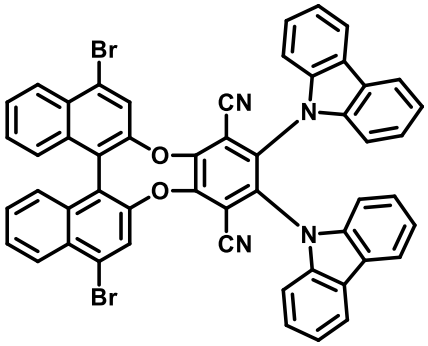

BNCNCzBr2

Synthesis of **BNCNCzBr2**. A mixture of **BNOH** (222 mg, 0.50 mmol), K_2CO_3 (138 mg, 1.00 mmol) and tetrafluoroterephthalonitrile (100 mg, 0.50 mmol) in dried DMF (2.5 mL) were stirred in argon atmosphere at room temperature for 12 h, followed by addition of K_2CO_3 (346 mg, 2.50 mmol) and carbazole (184 mg, 1.10 mmol) at room temperature for another 12 h. The solution was turned to in dark-green color with precipitates and quenched by adding water and extracted by CH_2Cl_2. The combined organic phase was dried over $MgSO_4$. The crude product was purified by column chromatography on silica gel (hexanes/ethyl acetate = 9/1) to afford **BNCNCzBr2** (40%, 180 mg) as a yellow solid. ^{1}H NMR (d_6-acetone, 400 MHz) δ 8.46 (d, *J* = 4.2 Hz, 2H), 8.14 (s, 2H), 7.85-7.80 (m, 4H), 7.77 (d, *J* = 4.2 Hz, 2H), 7.63 (d, *J* = 2.4 Hz, 4H), 7.46 (d, *J* = 4.0 Hz, 2H), 7.27 (d, *J* = 3.6 Hz, 2H), 7.20 (t, *J* = 7.6 Hz, 2H), 7.11 (t, *J* = 7.2 Hz, 2H), 6.98 (quint, *J* = 7.6 Hz, 4H); ^{13}C NMR (d_6-acetone, 100 MHz) δ 206.0, 152.2, 149.6, 140.6, 140.2, 137.2, 133.3, 131.9, 129.8, 129.4, 128.5, 128.1, 126.6, 125.8, 125.7, 124.7, 124.6, 121.9, 121.8, 121.0, 120.8, 116.1, 112.7, 111.5, 111.4, ; HRMS (m/z, MALDI) Calcd for $C_{52}H_{26}{}^{79}Br_2N_4O_2$

896.0422; found 896.0312; Calcd for $C_{52}H_{26}{}^{79}Br^{81}BrN_4O_2$ 898.0403; found 898.0380; Calcd for $C_{52}H_{26}{}^{81}Br_2N_4O_2$ 900.0398; found 900.0386;

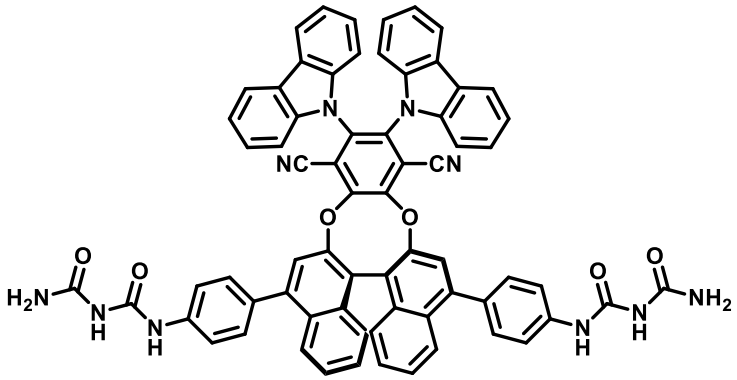

BNCNCzPB

Synthesis of **BNCNCzPB**. A mixture of $Pd(PPh_3)_4$ (10 mg, 0.0086 mmol), K_2CO_3 (83 mg, 0.60 mmol), **BNCNCzBr2** (90 mg, 0.10 mmol), 4-pinacolatoboronic ester-benzenebiuret (70 mg, 0.23 mmol) in degassed THF (3.0 mL) and water (0.3 mL) was refluxed for two days. The reaction was quenched by adding water and extracted with THF. The combined organic solution was washed with brine and dried over $MgSO_4$. The crude product was purified by column chromatography on silica gel (THF/CH_2Cl_2 = 1/2 to 1/1) to afford **BNCNCzPB** (67%, 74 mg) as a yellow solid. ^{1}H NMR (d_6-DMSO, 400 MHz) δ 10.22 (s, 2H), 8.99 (s, 2H), 8.14 (d, *J* = 4.4 Hz, 2H), 7.86 (t, *J* = 8.0 Hz, 4H), 7.74 (d, *J* = 2.2 Hz, 4H), 7.69 (m, 6H), 7.63 (s, 2H), 7.60 (d, *J* = 2.6 Hz, 4H), 7.54 (d, *J* = 4.0 Hz, 2H), 7.42 (d, *J* = 3.4 Hz, 2H), 7.15 (d, *J* = 4.0 Hz, 2H), 7.10-7.04 (m, 6H), 6.95 (bs, 4H); ^{13}C NMR (d_6-DMSO, 100 MHz) δ 155.4, 152.1, 151.3, 148.3, 143.2, 139.3, 139.2, 138.4, 135.6, 133.0, 132.0, 130.6, 130.3, 130.1, 127.9, 125.5, 123.3, 122.8, 121.4, 120.8, 120.1, 120.0,

119.6, 114.4, 112.1, 110.8, 110.7; HRMS (m/z, MALDI) Calcd for $C_{68}H_{42}N_{10}O_6$ 1094.3289; found 1095.3400 (M+1).

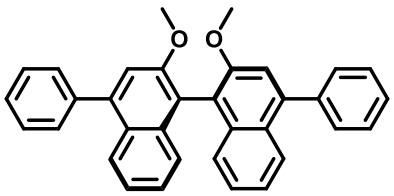

BNPh

Synthesis of **BNPh**. A mixture of $Pd(PPh_3)_4$ (18 mg, 0.015 mmol), K_2CO_3 (268 mg, 1.94 mmol), **BNOMe** (153 mg, 0.32 mmol), phenylboronic acid (83 mg, 0.68 mmol) and tri-tert-butylphosphonium tetrafluoroborate (9 mg, 0.031 mmol) in dried toluene (10 mL) and degassed water (1.0 mL) was refluxed overnight. The reaction was quenched by adding water and extracted with ethyl acetate twice. The combined organic solution was washed with brine and dried over $MgSO_4$. The crude product was purified by column chromatography on silica gel (hexanes/chloroform = 2/1) to afford **BNPh** (56%, 85 mg) as a white solid. ^{1}H NMR (d_6-acetone, 400 MHz) δ 7.90 (dd, *J* = 6.8, 1.6 Hz, 2H), 7.67 (d, *J* = 8.4 Hz, 4H), 7.60 (t, *J* = 7.2 Hz, 4H), 7.54 (m, 4H), 7.28 (qd, *J* = 9.2, 1.2 Hz, 4H), 7.20 (dd, *J* = 6.8, 1.6 Hz, 2H), 3.84 (s, 6H); ^{13}C NMR (d_6-acetone, 100 MHz) δ 155.6, 142.7, 141.7, 135.6, 131.1, 129.4, 128.5, 128.3, 127.1, 126.9, 126.4, 124.5, 119.8, 116.0, 58.9.

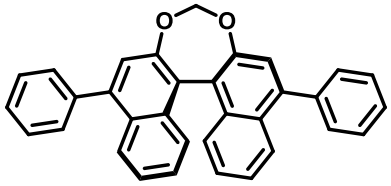

7BBNPh

Synthesis of **7BBNPh**. A mixture of $Pd(PPh_3)_4$ (17 mg, 0.015 mmol), K_2CO_3 (250 mg, 1.81 mmol), **7BBNBr2** (138 mg, 0.30 mmol), phenylboronic acid (77 mg, 0.63 mmol) and tri-tert-butylphosphonium tetrafluoroborate (8 mg, 0.027 mmol) in dried toluene (10 mL) and degassed water (1.0 mL) was refluxed overnight. The reaction was quenched by adding water and extracted with ethyl acetate twice. The combined organic solution was washed with brine and dried over $MgSO_4$. The crude product was purified by column chromatography on silica gel (hexanes/chloroform = 2/1) to afford **7BBNPh** (54%, 73 mg) as a white solid. ^{1}H NMR (d_6-acetone, 400 MHz) δ 7.97 (d, J = 8.0 Hz, 2H), 7.63-7.55 (m, 10H), 7.52 (dt, J = 6.0, 1.6 Hz, 2H), 7.49-7.46 (m, 2H), 7.45 (dd, 6.8, 1.6 Hz, 2H), 7.37 (td, 6.8, 1.2 Hz, 2H), 5.77 (s, 2H); ^{13}C NMR (d_6-acetone, 100 MHz) δ 152.0, 143.8, 140.9, 133.6, 130.9, 130.9, 129.5, 128.8, 127.9, 127.4, 127.1, 126.2, 126.2, 122.9, 104.2.

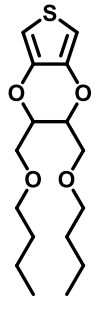

ADOT

Synthesis of **ADOT**. A mixture of 1,4-dibutoxybutane-2,3-diol (4.5 g, 19.4 mmol), 3,4-dimethoxythiophene (1.4 g, 9.71 mmol) and *p*-toluenesulfonic acid (169 mg, 0.98 mmol) in dried toluene (2.5 mL) in Dean-Stark apparatus were stirred in argon atmosphere at 130℃ for 3 d. The reaction was tracked by TLC (hexanes/chloroform = 3/1) and cooled to room temperature. The solvent was removed by evaporation and the crude product was purified by column chromatography on silica gel (hexanes/chloroform = 3/1) to afford **ADOT** (28%, 870 mg) as a colorless liquid. ^{1}H NMR ($CDCl_3$, 400 MHz) δ 6.29 (s, 2H), 4.21 (s, 2H), 3.70 (s, 4H), 3.52-3.42 (m, 4H), 1.56-1.52 (m, 4H), 1.37-1.31 (m, 4H), 0.89 (t, J = 7.2 Hz, 6H); ^{13}C NMR ($CDCl_3$, 100 MHz) δ 141.5, 99.5, 74.0, 71.7, 69.4, 31.7, 19.3, 13.9; HRMS (m/z, MALDI) Calcd for $C_{16}H_{26}O_4S_1$ 314.1552; found 314.1605.

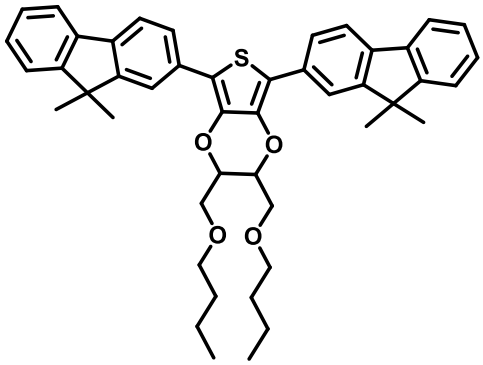

ADOTMF

Synthesis of **ADOTMF**. A mixture of **ADOT** (46 mg, 0.15 mmol), 2-bromo-9,9-dimethylfluorene (88 mg, 0.32 mmol), $Pd(OAc)_2$ (3.3 mg, 0.015 mmol), potassium acetate (34 mg, 0.35 mmol), and tetrabutylammonium bromide (47 mg, 0.15 mmol) in dried DMF (3 mL) in Schlenk flask were stirred in argon atmosphere at 90℃ for 2 h. The

reaction was tracked by TLC (hexanes/chloroform = 3/1) and cooled to room temperature. The reaction was quenched by adding water and extracted by ethyl acetate. The combined organic phase was washed by water and brine and dried over $MgSO_4$. The crude product was purified by column chromatography on silica gel (hexanes/chloroform = 3/1 to 1/1) to afford **ADOTMF** (79%, 81 mg) as a light-yellow solid. ^{1}H NMR ($CDCl_3$, 400 MHz) δ 7.86 (s, 2H), 7.82 (d, J = 4.0 Hz, 2H), 7.72 (d, J = 4.0 Hz, 4H), 7.45 (d, J = 3.2 Hz, 2H), 7.33 (m, 4H), 4.46 (s, 2H), 3.88 (s, 4H), 3.63-3.56 (m, 4H), 1.62-1.57 (m, 4H), 1.54 (s, 12H), 1.43-1.37 (m, 4H), 0.93 (t, J = 7.6 Hz, 6H); ^{13}C NMR ($CDCl_3$, 100 MHz) δ 153.9, 153.8, 139.0, 138.2, 137.6, 132.2, 127.0, 127.0, 125.1, 122.6, 120.1, 120.1, 119.9, 115.6, 74.0, 71.9, 69.5, 46.9, 31.8, 27.2, 19.3, 13.9; HRMS (m/z, MALDI) Calcd for $C_{46}H_{50}O_4S_1$ 698.3430; found 698.3399.

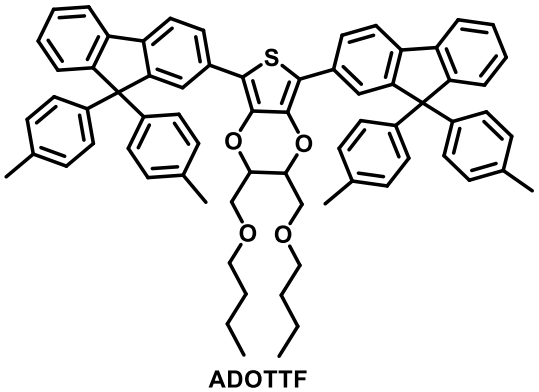

ADOTTF

Synthesis of **ADOTTF**. A mixture of **ADOT** (100 mg, 0.32 mmol), 2-bromo-9,9-bis(4-methylphenyl)-9H-fluorene (297 mg, 0.67 mmol), $Pd(OAc)_2$ (7.1 mg, 0.032 mmol), potassium acetate (75 mg, 0.76 mmol), and tetrabutylammonium bromide (102 mg, 0.32

mmol) in dried DMF (3 mL) in Schlenk flask were stirred in argon atmosphere at 90°C for 2 h. The reaction was tracked by TLC (hexanes/chloroform = 3/1) and cooled to room temperature. The reaction was quenched by adding water and extracted by ethyl acetate. The combined organic phase was washed by water and brine and dried over $MgSO_4$. The crude product was purified by column chromatography on silica gel (hexanes/chloroform = 3/1 to 1/1) to afford **ADOTTF** (60%, 191 mg) as a light-yellow solid. ^{1}H NMR (CD_2Cl_2, 400 MHz) δ 7.86 (s, 2H), 7.78-7.72 (m, 6H), 7.37 (t, *J* = 8.0 Hz, 4H), 7.27 (td, *J* = 6.8, 0.4 Hz, 2H), 7.14-7.04 (m, 16H), 4.31 (s, 2H), 3.78 (q, *J* = 8.4 Hz, 4H), 3.54-3.40 (m, 4H), 2.31 (s, 6H), 2.30 (s, 6H), 1.53-1.46 (m, 4H), 1.33 (sext, *J* = 7.2 Hz, 4H), 0.90 (t, *J* = 7.2 Hz, 6H); ^{13}C NMR (CD_2Cl_2, 100 MHz) δ 152.5, 152.3, 143.5, 143.4, 140.4, 139.3, 139.0, 137.0, 133.1, 129.5, 128.5, 128.0, 126.6, 125.8, 124.1, 120.9, 120.7, 115.6, 75.0, 72.3, 70.0, 65.5, 32.3, 21.2, 19.9, 14.2; HRMS (m/z, MALDI) Calcd for $C_{70}H_{66}O_4S_1$ 1002.4681; found 1002.4648.

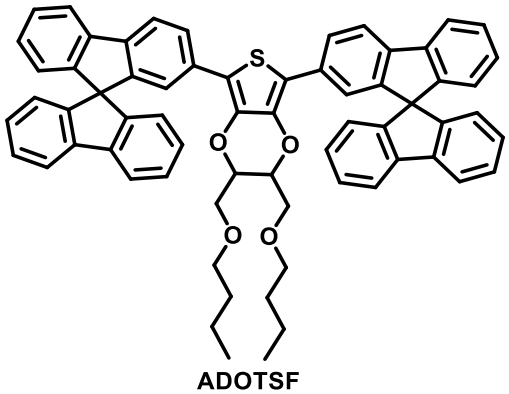

ADOTSF

Synthesis of **ADOTSF**. A mixture of **ADOT** (46 mg, 0.15 mmol), 2-bromo-9,9'-spiro-bi-

(9H-fluorene) (127 mg, 0.32 mmol), $Pd(OAc)_2$ (3.3 mg, 0.015 mmol), potassium acetate (34 mg, 0.35 mmol), and tetrabutylammonium bromide (47 mg, 0.15 mmol) in dried DMF (3 mL) in Schlenk flask were stirred in argon atmosphere at 90℃ for 2 h. The reaction was tracked by TLC (hexanes/chloroform = 3/1) and cooled to room temperature. The reaction was quenched by adding water and extracted by ethyl acetate. The combined organic phase was washed by water and brine and dried over $MgSO_4$. The crude product was purified by column chromatography on silica gel (hexanes/chloroform = 3/1 to 1/1) to afford **ADOTSF** (66%, 90 mg) as a light-yellow solid. ^{1}H NMR ($CDCl_3$, 400 MHz) δ 7.85-7.80 (m, 4H), 7.79 (d, *J* = 8.0 Hz, 4H), 7.72 (d, *J* = 4.0 Hz, 2H), 7.39-7.32 (m, 6H), 7.13-7.04 (m, 8H), 6.75 (t, *J* = 8.0 Hz, 4H), 6.69 (d, *J* = 8.0 Hz, 2H), 4.09 (s, 2H), 3.67 (d, *J* = 5.8 Hz, 2H), 3.44 (d, *J* = 5.8 Hz, 2H), 3.36-3.23 (m, 4H), 1.47-1.40 (m, 4H), 1.34-1.26 (m, 4H), 0.88 (t, *J* = 7.2 Hz, 6H); ^{13}C NMR ($CDCl_3$, 100 MHz) δ 149.1, 149.0, 148.7, 148.7, 141.7, 141.6, 141.4, 140.0, 138.5, 132.7, 127.8, 127.7, 127.6, 127.5, 125.6, 124.2, 124.1, 123.9, 121.4, 120.0, 119.8, 119.8, 119.8, 114.9, 74.3, 71.8, 69.3, 65.9, 31.7, 19.3, 13.9; HRMS (m/z, MALDI) Calcd for $C_{66}H_{54}O_4S_1$ 942.3743; found 942.3775.

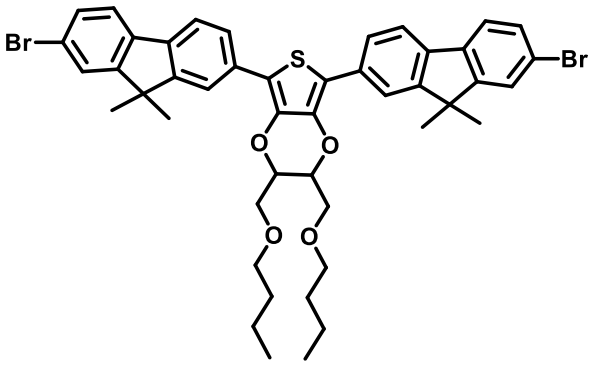

ADOTMFBr2

Synthesis of **ADOTMFBr2**. A mixture of **ADOTMF** (50 mg, 0.072 mmol), anhydrous $FeCl_3$ (0.23 mg, 0.0014 mmol), bromine (0.008 mL, 0.16 mmol) in dried CH_2Cl_2 (8 mL) in the dark were stirred and refluxed for 12 h. The reaction was quenched by adding $K_2CO_{3(aq)}$ and extracted by CH_2Cl_2. The combined organic phase was washed by water and brine and dried over $MgSO_4$. The crude product was purified by column chromatography on silica gel (hexanes/chloroform = 2/1) to afford **ADOTMFBr2** (42%, 26 mg) as a light-yellow solid. ^{1}H NMR ($CDCl_3$, 400 MHz) δ 7.97 (s, 2H), 7.61 (s, 2H), 7.55 (d, J = 3.8 Hz, 4H), 7.48 (d, J = 8.0 Hz, 2H), 4.42 (s, 2H), 3.82-3.76 (m, 4H), 3.55-3.44 (m, 4H), 1.58-1.52 (m, 4H), 1.49 (s, 12H), 1.37-1.31 (m, 4H), 0.89 (t, J = 8.0 Hz, 6H); ^{13}C NMR ($CDCl_3$, 100 MHz) δ 156.0, 152.1, 139.6, 137.7, 136.6, 131.7, 130.4, 126.9, 126.3, 124.8, 122.8, 122.0, 121.7, 115.2, 73.5, 71.7, 69.2, 47.1, 31.7, 26.8, 19.3, 13.9; HRMS (m/z, MALDI) Calcd for $C_{46}H_{48}{}^{79}Br_2O_4S_1$ 854.1634; found 854.1641; Calcd for $C_{46}H_{48}{}^{79}Br^{81}BrO_4S_1$ 856.1619; found 856.1659; Calcd for $C_{46}H_{48}{}^{81}Br_2O_4S_1$ 858.1610; found 858.1667.

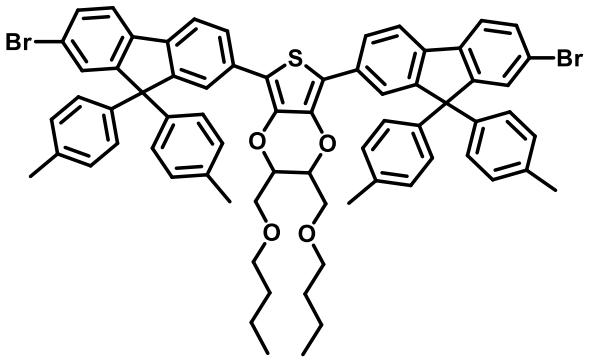

ADOTTFBr2

Synthesis of **ADOTTFBr2**. A mixture of **ADOTTF** (27 mg, 0.027 mmol), anhydrous $FeCl_3$ (0.10 mg, 0.0005 mmol), bromine (0.003 mL, 0.060 mmol) in dried CH_2Cl_2 (5 mL) in the dark were stirred and refluxed for 12 h. The reaction was quenched by adding $K_2CO_{3(aq)}$ and extracted by CH_2Cl_2. The combined organic phase was washed by water and brine and dried over $MgSO_4$. The crude product was purified by column chromatography on silica gel (hexanes/chloroform = 3/1 to 2/1) to afford **ADOTTFBr2** (80%, 25 mg) as a light-yellow solid. ^{1}H NMR ($CDCl_3$, 400 MHz) δ 7.99 (s, 2H), 7.58 (d, *J* = 8.8 Hz, 6H), 7.53-7.48 (m, 4H), 7.13-7.06 (m, 16H), 4.30 (s, 2H), 3.70 (q, *J* = 9.2 Hz, 4H), 3.42-3.31 (m, 4H), 2.32 (s, 12H), 1.47 (quin, *J* = 6.8 Hz, 4H), 1.31 (sex, *J* = 7.6 Hz, 4H), 0.89 (t, *J* = 7.2 Hz, 6H); ^{13}C NMR ($CDCl_3$, 100 MHz) δ 154.0, 150.2, 141.6, 141.6, 140.0, 138.1, 137.4, 136.6, 136.3, 132.0, 130.8, 130.1, 129.5, 129.1, 129.0, 128.0, 127.9, 125.0, 122.9, 122.2, 121.7, 115.0, 73.6, 71.6, 69.2, 64.8, 31.6, 20.9, 19.2, 13.9; HRMS (m/z, MALDI) Calcd for $C_{70}H_{64}{}^{79}Br_2O_4S_1$ 1158.2886; found 1158.2908; Calcd for $C_{70}H_{64}{}^{79}Br^{81}BrO_4S_1$ 1160.2877; found 1160.2912; Calcd for $C_{70}H_{64}{}^{81}Br_2O_4S_1$ 1162.2878;

found 1162.2976.

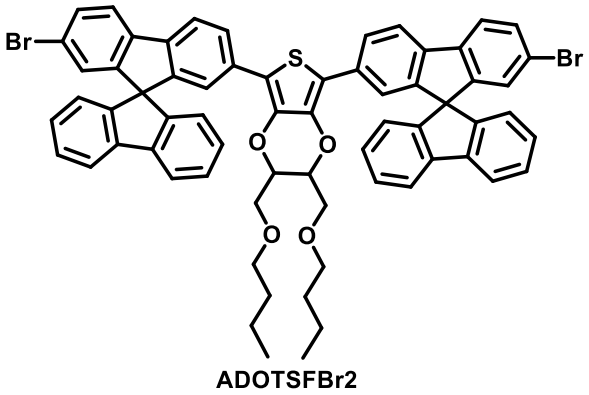

ADOTSFBr2

Synthesis of **ADOTSFBr2**. A mixture of **ADOTSF** (200 mg, 0.21 mmol), anhydrous $FeCl_3$ (0.68 mg, 0.0042 mmol), bromine (0.024 mL, 0.48 mmol) in dried CH_2Cl_2 (23 mL) in the dark were stirred and refluxed for 12 h. The reaction was quenched by adding $K_2CO_{3(aq)}$ and extracted by CH_2Cl_2. The combined organic phase was washed by water and brine and dried over $MgSO_4$. The crude product was purified by column chromatography on silica gel (hexanes/chloroform = 3/1 to 2/1) to afford **ADOTSFBr2** (85%, 199 mg) as a light-yellow solid. ^{1}H NMR (CD_2Cl_2, 400 MHz) δ 8.10 (s, 2H), 7.84 (d, J = 3.4 Hz, 4H), 7.69 (d, J = 4.0 Hz, 2H), 7.50 (dd, J = 8.0, 1.6 Hz, 2H), 7.40-7.36 (m, 4H), 7.13 (tt, J = 7.2, 1.2 Hz, 4H), 6.86 (d, J = 4.0 Hz, 2H), 6.81 (s, 2H), 6.78-6.72 (m, 4H), 4.09 (s, 2H), 3.54 (d, J = 8.0 Hz, 2H), 3.44 (d, J = 8.0 Hz, 2H), 3.45-3.23 (m, 4H), 1.43 (quin, J = 3.6 Hz, 4H), 1.29 (sex, J = 5.2 Hz, 4H), 0.89 (t, J = 5.6 Hz, 6H); ^{13}C NMR (CD_2Cl_2, 100 MHz) δ 152.0, 148.4, 148.3, 148.2, 147.6, 142.6, 142.3, 142.3, 139.6, 138.5, 132.7, 131.7, 128.8, 128.6, 128.6, 128.5, 128.2, 127.7, 125.6, 124.4, 124.0, 122.8, 122.5,

120.9, 120.8, 120.7, 114.9, 74.3, 72.0, 69.6, 66.0, 32.2, 19.8, 14.2; HRMS (m/z, MALDI) Calcd for $C_{66}H_{52}{}^{79}Br_2O_4S_1$ 1098.1948; found 1098.1911; Calcd for $C_{66}H_{52}{}^{79}Br^{81}BrO_4S_1$ 1100.1937; found 1100.2000; Calcd for $C_{66}H_{52}{}^{81}Br_2O_4S_1$ 1102.1936; found 1102.2105.

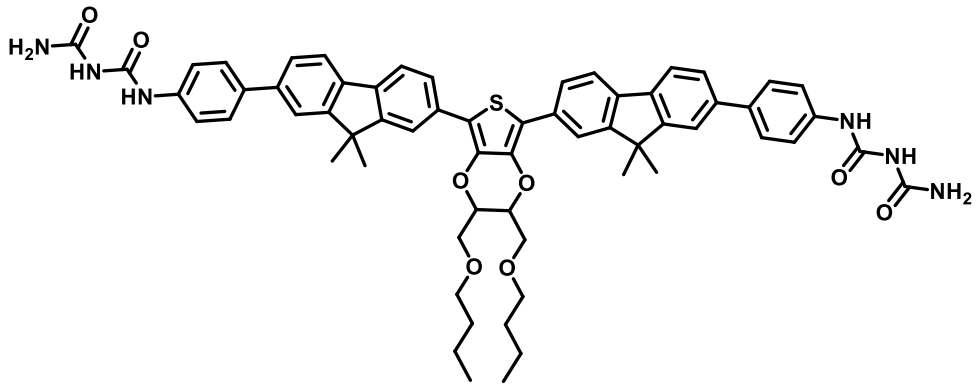

ADOTMFPB

Synthesis of **ADOTMFPB**. A mixture of $Pd(PPh_3)_4$ (3.5 mg, 0.0030 mmol), K_2CO_3 (25.0 mg, 0.18 mmol), **ADOTMFBr2** (26 mg, 0.030 mmol), 4-pinacolatoboronic ester-benzenebiuret (20 mg, 0.066 mmol) in degassed THF (5 mL) and water (0.1 mL) was refluxed for two days. The reaction was quenched by adding water and extracted with THF. The combined organic solution was washed with brine and dried over $MgSO_4$. The crude product was purified by column chromatography on silica gel (THF/CH_2Cl_2 = 1/2 to 1/1) to afford **ADOTMFPB** (33%, 10 mg) as a light-yellow solid. ^{1}H NMR (d_6-DMSO, 400 MHz) δ 10.08 (s, 2H), 8.90 (s, 2H), 8.23 (s, 2H), 7.94 (d, *J* = 6.8 Hz, 2H), 7.84 (d, *J* = 4.2 Hz, 4H), 7.74-7.69 (m, 4H), 7.64-7.58 (m, 2H), 7.54 (d, *J* = 4.0 Hz, 4H), 7.20 (m, 2H), 6.95 (bs, 4H), 4.39 (d, *J* = 14.4 Hz, 2H), 3.77-3.67 (m, 4H), 3.25 (m, 4H), 1.49 (s, 12H), 1.37-1.22 (m, 8H), 0.81-0.77 (m, 6H); ^{13}C NMR (d_6-DMSO, 100 MHz) δ 155.6,

154.8, 154.4, 154.2, 153.0, 152.1, 140.4, 140.0, 138.4, 137.8, 137.7, 135.8, 135.1, 134.9, 130.4, 127.4, 127.3, 126.8, 122.1, 119.5, 114.6, 114.5, 70.8, 70.7, 46.8, 31.3, 27.0, 26.6, 18.9, 13.8; HRMS (m/z, MALDI) Calcd for $C_{62}H_{64}N_6O_8S_1$ 1052.4506; found 1052.4557.

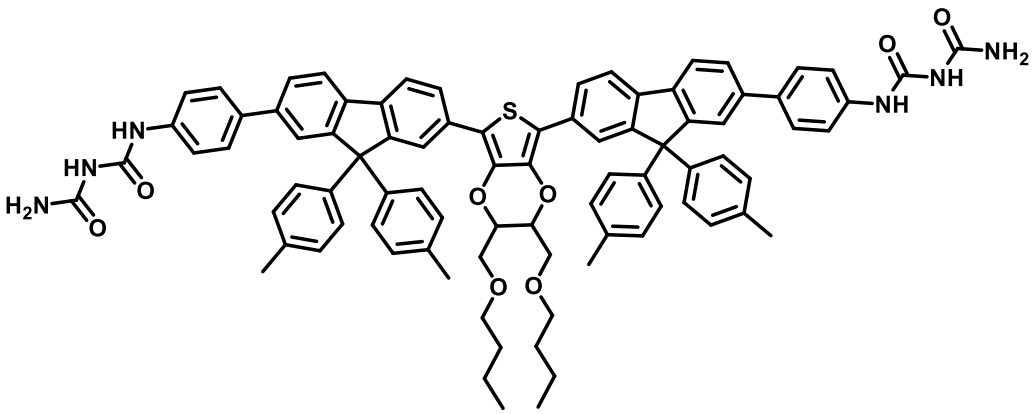

ADOTTFPB

Synthesis of **ADOTTFPB**. A mixture of $Pd(PPh_3)_4$ (3.5 mg, 0.0045 mmol), K_2CO_3 (37 mg, 0.27 mmol), **ADOTTFBr2** (52 mg, 0.045 mmol), 4-pinacolatoboronic ester-benzenebiuret (30 mg, 0.098 mmol) in degassed THF (5 mL) and water (0.1 mL) was refluxed for two days. The reaction was quenched by adding water and extracted with THF. The combined organic solution was washed with brine and dried over $MgSO_4$. The crude product was purified by column chromatography on silica gel (THF/CH_2Cl_2 = 1/2 to 1/1) to afford **ADOTTFPB** (26%, 16 mg) as a light-yellow solid. ^{1}H NMR (d_6-DMSO, 400 MHz) δ 10.03 (s, 2H), 8.86 (s, 2H), 7.80 (dt, *J* = 9.6, 7.6 Hz, 6H), 7.67-7.54 (m, 8H), 7.49 (d, *J* = 4.4 Hz, 6H), 7.06 (d, *J* = 3.6 Hz, 16H), 4.29 (s, 2H), 3.69 (m, 4H), 3.29 (m, 4H), 2.21 (s, 6H), 2.20 (s, 2H), 1.35-1.31 (m, 4H), 1.22-1.14 (m, 4H), 0.78 (t, *J* = 7.6 Hz, 6H); ^{13}C NMR (d_6-DMSO, 100 MHz) δ 155.5, 152.1, 152.0, 142.6, 139.2, 138.9, 137.9,

136.0, 135.9, 131.7, 129.0, 128.9, 127.7, 127.3, 127.2, 121.1, 119.5, 114.1, 88.2, 81.0, 70.9, 53.1, 31.1, 28.3, 24.3, 20.5, 19.8, 13.7; HRMS (m/z, MALDI) Calcd for $C_{86}H_{80}N_6O_8S_1$ 1356.5758; found 1356.5788.

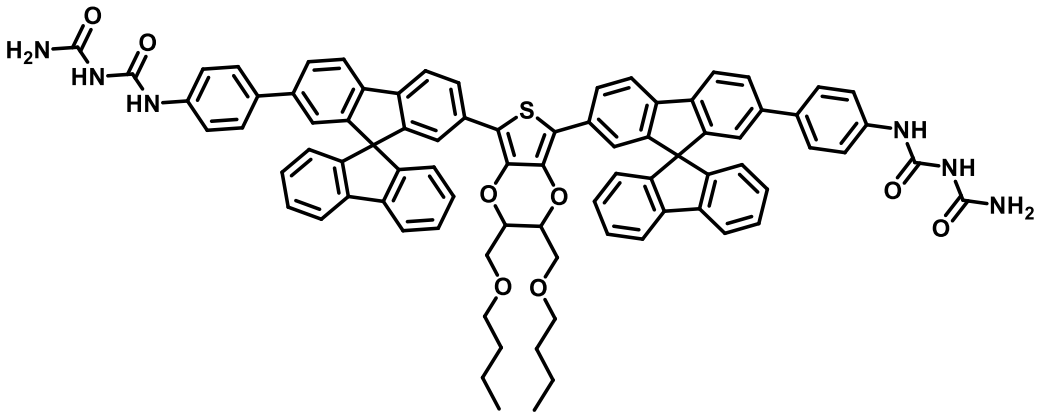

ADOTSFPB

Synthesis of **ADOTSFPB**. A mixture of $Pd(PPh_3)_4$ (7.5 mg, 0.0065 mmol), K_2CO_3 (54 mg, 0.39 mmol), **ADOTSFBr2** (72 mg, 0.065 mmol), 4-pinacolatoboronic ester-benzenebiuret (44 mg, 0.14 mmol) in degassed THF (6 mL) and water (0.2 mL) was refluxed for two days. The reaction was quenched by adding water and extracted with THF. The combined organic solution was washed with brine and dried over $MgSO_4$. The crude product was purified by column chromatography on silica gel (THF/CH_2Cl_2 = 1/2 to 1/1) to afford **ADOTSFPB** (29%, 25 mg) as a light-yellow solid. ^{1}H NMR (d_6-DMSO, 400 MHz) δ 9.99 (s, 2H), 8.83 (s, 2H), 8.05-7.98 (m, 6H), 7.71 (t, *J* = 8.0 Hz, 2H), 7.62 (d, *J* = 3.8 Hz, 2H), 7.40 (m, 12 H), 7.15-7.10 (m, 4H), 7.00 (s, 2H), 6.80-6.66 (m, 8H), 4.01 (s, 2H), 3.50 (m, 4H), 3.26-3.13 (m, 4H), 1.34-1.14 (m, 8H), 0.84-0.75 (m, 6H) ; ^{13}C NMR (d_6-DMSO, 100 MHz) δ 155.4, 151.8, 149.7, 148.0, 147.8, 142.7, 141.3, 140.4,

140.0, 139.4, 138.7, 138.5, 137.8, 137.6, 134.1, 133.9, 131.8, 130.6, 128.9, 128.2, 127.1, 126.6, 126.4, 125.4, 125.3, 125.2, 123.6, 122.6, 122.1, 121.2, 120.9, 120.6, 120.3, 119.3, 113.5, 74.3, 70.8, 68.6, 65.5, 31.1, 18.7, 13.7; HRMS (m/z, MALDI) Calcd for $C_{82}H_{68}N_6O_8S_1$ 1296.4819; found 1296.4889.

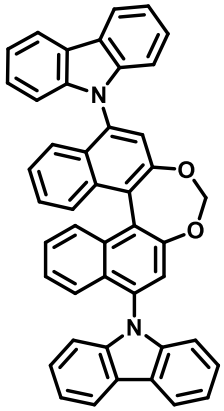

7BBNCz

Synthesis of **7BBNCz**. A mixture of $Pd_2(dba)_3$ (90 mg, 0.098 mmol), carbazole (275 mg, 1.64 mmol), **7BBNBr2** (300 mg, 0.66 mmol), (9,9-Dimethyl-9H-xanthene-4,5-diyl)bis(diphenylphosphane) (114 mg, 0.20 mmol) and K_3PO_4 (698 mg, 3.29 mmol) in dried xylene (5 mL) was conducted at 120℃ for 72 h. The reaction was cooled and filtered by Celite pad. The collected filtrate was concentrated in reduced pressure to remove xylene and extracted by CH_2Cl_2 and dried over $MgSO_4$. The crude product was purified by column chromatography on silica gel (hexanes /CH_2Cl_2 = 4/1) to afford **7BBNCz** (41%, 168 mg) as a white solid. ^{1}H NMR (CD_2Cl_2, 400 MHz) δ 8.28 (d, *J* = 3.8 Hz, 4H), 7.84 (d, *J* = 4.4 Hz, 2H), 7.77 (s, 2H), 7.48-7.40 (m, 8H), 7.39-7.33 (m, 6H), 7.24 (d, *J* = 1.8 Hz, 2H), 7.22 (d, *J* = 1.8 Hz, 2H), 5.85 (s, 2H); ^{13}C NMR (CD_2Cl_2, 100 MHz) δ 152.0,

142.8, 142.7, 136.8, 133.9, 129.9, 128.0, 127.7, 127.5, 126.7, 124.6, 124.0, 123.9, 122.5, 120.9, 120.7, 110.9, 110.8, 104.4; HRMS (m/z, MALDI) Calcd for $C_{45}H_{28}N_2O_2$ 628.2151; found 628.2171.

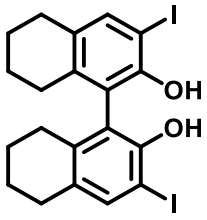

H8BNI2

Synthesis of **H8BNI2**. A mixture of 5,5',6,6',7,7',8,8'-cctahydro-1,1'-bi-2-naphthol (3.00 g, 10.19 mmol), iodine (5.17 g, 20.38 mmol) and morpholine (5.40 mL, 61.14 mmol) in dried CH_2Cl_2 (90 mL) were stirred at room temperature for 5 h. The color of the solution was turned to progressively red. The reaction was quenched by adding 12 N $HCl_{(aq)}$ and extracted by CH_2Cl_2. The combined organic phase was washed by $NaHSO_{3(aq)}$ for three times and brine and dried over $MgSO_4$. The filtrate was concentrated by evaporation in reduced pressure to afford **H8BNI2** (97%, 5.43 g) as a white solid. ^1H NMR ($CDCl_3$, 400 MHz) δ 7.51 (s, 2H), 4.99 (s, 2H), 2.76-2.71 (m, 4H), 2.30-2.23 (m, 2H), 2.13-2.04 (m, 2H), 1.74-1.56 (m, 8H); ^{13}C NMR ($CDCl_3$, 100 MHz) δ 149.8, 139.3, 137.7, 132.4, 120.6, 81.0, 28.8, 26.9, 22.7, 22.6; HRMS (m/z, MALDI) Calcd for $C_{20}H_{20}I_2O_2$ 545.9553; found 545.9525.

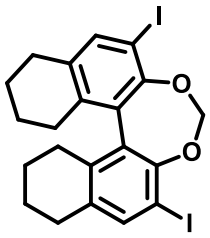

H87BBNI2

Synthesis of **H87BBNI2**. A mixture of **H8BNI2** (144 mg, 0.26 mmol), K_2CO_3 (364 mg, 2.63 mmol) in dried DMF (5 mL) were stirred in argon atmosphere at 50℃ for 15 min, followed by addition of bromochloromethane (0.53 mL, 7.89 mmol) dropwise and stirred in argon atmosphere at 50ºC for 15 h. The reaction was quenched by adding water and brine and extracted by CH_2Cl_2. The combined organic phase was dried over $MgSO_4$. The crude product was purified by column chromatography on silica gel (hexanes/CH_2Cl_2 = 4/1) to afford **H87BBNI2** (72%, 106 mg) as a white solid. ^{1}H NMR ($CDCl_3$, 400 MHz) δ 7.55 (s, 2H), 5.33 (s, 2H), 2.79-2.78 (m, 4H), 2.65-2.58 (m, 2H), 2.30-2.23 (m, 2H), 1.82-1.75 (m, 8H); ^{13}C NMR (CD_2Cl_2, 100 MHz) δ 150.0, 139.0, 138.9, 138.0, 131.9, 100.3, 86.5, 29.2, 28.1, 22.8, 22.6; HRMS (m/z, MALDI) Calcd for $C_{21}H_{20}I_2O_2$ 557.9553; found 557.9602.

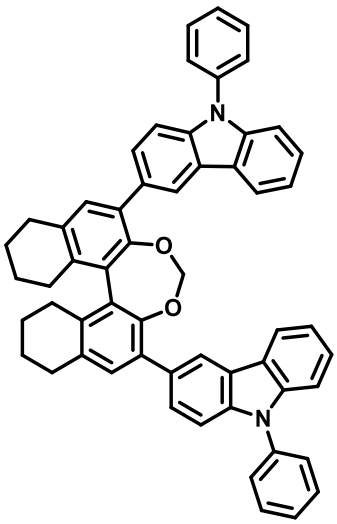

3CzPh

Synthesis of **3CzPh**. A mixture of $Pd(PPh_3)_4$ (10 mg, 0.0086 mmol), **H87BBNI2** (100 mg, 0.18 mmol), (9-phenyl-9H-carbazol-3-yl)boronic acid (113 mg, 0.39 mmol), K_2CO_3 (148 mg, 1.07 mmol) and tri-tert-butylphosphonium tetrafluoroborate (5.2 mg, 0.018 mmol) in dried toluene (7.5 mL) and water (0.6 mL) was refluxed overnight. The reaction was quenched by adding water and extracted with ethyl acetate. The combined organic solution was washed with brine and dried over $MgSO_4$. The crude product was purified by column chromatography on silica gel (hexanes/CH_2Cl_2 = 3/1) to afford **3CzPh** (46%, 66 mg) as a white solid. ^{1}H NMR (CD_2Cl_2, 400 MHz) δ 8.34 (s, 2H), 8.13 (d, *J* = 3.8 Hz, 2H), 7.64-7.57 (m, 10H), 7.48 (tt, *J* = 6.8, 2.0 Hz, 2H), 7.43-7.39 (m, 6H), 7.38 (s, 2H), 7.27 (td, *J* = 8.0, 2.8 Hz, 2H), 4.93 (s, 2H), 3.00-2.96 (m, 4H), 2.91-2.83 (m, 2H), 2.54-2.46 (m, 2H), 1.95-1.93 (m, 8H); ^{13}C NMR (CD_2Cl_2, 100 MHz) δ 147.6, 141.8, 140.6, 138.2, 137.0, 135.5, 132.7, 132.5, 131.2, 130.4, 130.3, 128.3, 128.0, 127.5, 126.5, 124.0, 123.8, 121.7, 120.8, 120.5, 110.4, 109.8, 100.7, 29.8, 28.3, 23.5, 23.3; HRMS (m/z,

MALDI) Calcd for $C_{57}H_{44}N_2O_2$ 788.3403; found 788.3437.

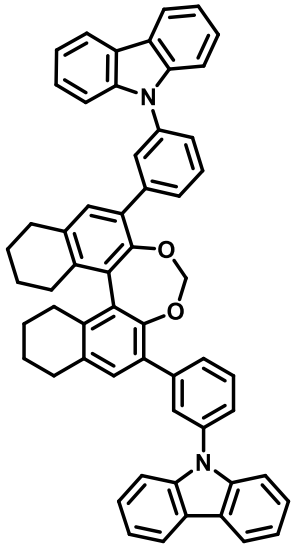

Ph3Cz

Synthesis of **Ph3Cz**. A mixture of $Pd(PPh_3)_4$ (10 mg, 0.0086 mmol), **H87BBNI2** (100 mg, 0.18 mmol), 3-(9H-carbazol-9-yl)phenylboronic acid (113 mg, 0.39 mmol), K_2CO_3 (148 mg, 1.07 mmol) and tri-tert-butylphosphonium tetrafluoroborate (5.2 mg, 0.018 mmol) in dried toluene (7.5 mL) and water (0.6 mL) was refluxed overnight. The reaction was quenched by adding water and extracted with ethyl acetate. The combined organic solution was washed with brine and dried over $MgSO_4$. The crude product was purified by column chromatography on silica gel (hexanes/CH_2Cl_2 = 3/1) to afford **Ph3Cz** (64%, 90 mg) as a white solid. ^{1}H NMR (CD_2Cl_2, 400 MHz) δ 8.15 (d, J = 4.0 Hz, 4H), 7.81 (s, 2H), 7.70-7.64 (m, 4H), 7.56 (dt, J = 3.4, 2.0 Hz, 2H), 7.48 (d, J = 4.0 Hz, 4H), 7.39 (td, J = 7.2, 0.6 Hz, 4H), 7.31 (d, J = 4.8 Hz, 2H), 7.27 (d, J = 3.8 Hz, 4H), 5.12 (s, 2H), 2.93-2.86 (m, 4H), 2.83-2.76 (m, 2H), 2.44-2.38 (m, 2H), 1.90-1.83 (m, 8H); ^{13}C NMR

(CD_2Cl_2, 100 MHz) δ 147.4, 141.4, 140.1, 138.3, 137.9, 135.9, 132.5, 130.8, 130.2, 128.9, 128.6, 126.5, 125.9, 123.9, 123.9, 120.8, 120.5, 110.4, 101.0, 29.7, 28.3, 23.2, 23.0; HRMS (m/z, MALDI) Calcd for $C_{57}H_{44}N_2O_2$ 788.3403; found 788.3423.

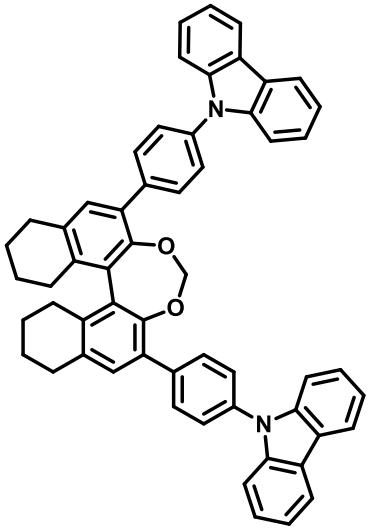

Ph4Cz

Synthesis of **Ph4Cz**. A mixture of $Pd(PPh_3)_4$ (10 mg, 0.0086 mmol), **H87BBNI2** (100 mg, 0.18 mmol), 4-(9H-carbazol-9-yl)phenylboronic acid (113 mg, 0.39 mmol), K_2CO_3 (148 mg, 1.07 mmol) and tri-tert-butylphosphonium tetrafluoroborate (5.2 mg, 0.018 mmol) in dried toluene (7.5 mL) and water (0.6 mL) was refluxed overnight. The reaction was quenched by adding water and extracted with ethyl acetate. The combined organic solution was washed with brine and dried over $MgSO_4$. The crude product was purified by column chromatography on silica gel (hexanes/CH_2Cl_2 = 3/1) to afford **Ph4Cz** (31%, 44 mg) as a white solid. ^{1}H NMR (CD_2Cl_2, 400 MHz) δ 8.16 (d, J = 3.8 Hz, 4H), 7.83 (d, J = 7.4 Hz, 4H), 7.62 (d, J = 5.2 Hz, 4H), 7.50 (d, J = 4.2 Hz, 4H), 7.42 (td, J = 7.2, 0.8

Hz, 4H), 7.36 (s, 2H), 7.30 (td, J = 5.2, 2.0 Hz, 4H), 5.11 (s, 2H), 2.99-2.90 (m, 4H), 2.89-2.83 (m, 2H), 2.52-2.45 (m, 2H), 1.96-1.89 (m, 8H); ^{13}C NMR (CD_2Cl_2, 100 MHz) δ 147.6, 141.4, 138.1, 137.5, 137.1, 135.8, 132.6, 131.5, 131.0, 130.9, 127.0, 126.5, 123.9, 120.8, 120.5, 110.4, 101.1, 29.8, 28.4, 23.4, 23.1; HRMS (m/z, MALDI) Calcd for $C_{57}H_{44}N_2O_2$ 788.3403; found 788.3414.

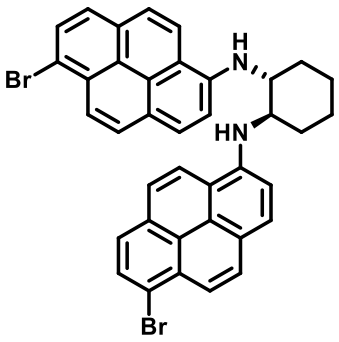

DACHPyBr2

Synthesis of **DACHPyBr2**. A mixture of $Pd(OAc)_2$ (1.6 mg, 0.007 mmol), sodium tert-butoxide (144 mg, 1.5 mmol), and 2,2'-Bis(diphenylphosphino)-1,1'-binaphthyl (94 mg, 0.065 mmol) in dried toluene (12 mL) were stirred in argon atmosphere at room temperature for 20 min. Followed by addition of 1,2-diaminocyclohexanes (57 mg, 0.50 mmol) and 1,6-dibromopyrene (378 mg, 1.05 mmol), the reaction was conducted at 100℃ for 16 h. The reaction was cooled and diluted by hexanes and filtered by silica pad. The collected filtrate was concentrated in reduced pressure and purified by column chromatography on silica gel (hexanes/Et_2O = 7/3) to afford **DACHPyBr2** (49%, 167 mg) as a white solid. ^{1}H NMR (d_6-DMSO, 400 MHz) δ 8.07-8.01 (m, 4H), 7.99 (d, J = 4.0 Hz,

2H), 7.92 (d, J = 4.8 Hz, 2H), 7.73-7.68 (m, 6H), 7.58 (d, J = 4.6 Hz, 2H), 6.44 (s, 2H), 4.11 (s, 2H), 2.25 (d, J = 6.0 Hz, 2H), 1.87 (s, 2H), 1.71 (s, 2H), 1.53 (s, 2H); ^{13}C NMR (d_6-DMSO, 100 MHz) δ 144.2, 130.9, 129.8, 129.5, 127.4, 126.0, 124.7, 123.5, 122.8, 121.5, 120.7, 119.4, 116.2, 115.4, 110.4, 57.5, 32.4, 25.0; HRMS (m/z, MALDI) Calcd for $C_{38}H_{28}{}^{79}Br_2N_2$ 670.0614; found 670.0587; Calcd for $C_{38}H_{28}{}^{79}Br^{81}BrN_2$ 672.0597; found 672.0664; Calcd for $C_{38}H_{28}{}^{81}Br_2N_2$ 674.0586; found 674.0778.

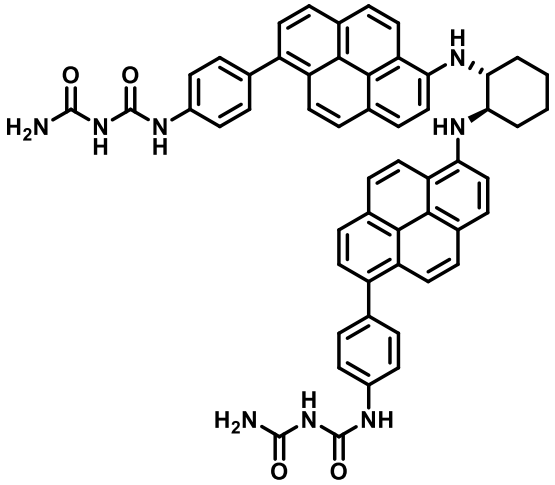

DACHPyPB

Synthesis of **DACHPyPB**. A mixture of $Pd(PPh_3)_4$ (29 mg, 0.025 mmol), K_2CO_3 (208 mg, 1.50 mmol), **DACHPyBr2** (169 mg, 0.25 mmol), 4-pinacolatoboronic ester-benzenebiuret (167 mg, 0.55 mmol) in degassed THF (23 mL) and water (1.2 mL) was refluxed for two days. The reaction was quenched by adding water and extracted with THF. The combined organic solution was washed with brine and dried over $MgSO_4$. The crude product was purified by column chromatography on silica gel (THF/CH_2Cl_2 = 3/4 to 1/1) to afford **DACHPyPB** (13%, 28 mg) as a yellow solid. ^{1}H NMR (d_6-DMSO, 400

MHz) δ 10.09 (s, 2H), 8.93 (s, 2H), 8.18 (d, *J* = 5.2 Hz, 2H), 8.04 (d, *J* = 4.2 Hz, 2H), 7.91 (d, *J* = 4.0 Hz, 2H), 7.81 (d, *J* = 4.0 Hz, 2H), 7.75 (d, *J* = 4.6 Hz, 2H), 7.70 (d, *J* = 3.8 Hz, 4H), 7.63-7.60 (m, 6H), 7.45 (d, *J* = 4.2 Hz, 2H), 6.95 (bs, 4H), 6.44 (s, 2H), 4.13 (s, 2H), 2.31 (d, *J* = 5.4 Hz, 2H), 1.87 (s, 2H), 1.66 (s, 2H), 1.55 (s,2H); ^{13}C NMR (d_6-DMSO, 400 MHz) δ 155.5, 152.1, 143.7, 137.3, 137.2, 135.7, 134.2, 130.8, 130.6, 129.1, 127.9, 127.4, 126.5, 125.9, 125.4, 124.0, 122.1, 121.3, 120.8, 119.1, 118.9, 115.7, 109.6, 56.8, 32.4, 25.0; HRMS (m/z, MALDI) Calcd for $C_{54}H_{44}N_8O_4$ 868.3485; found 868.3483.

Appendix

^{1}H and ^{13}C NMR Spectra

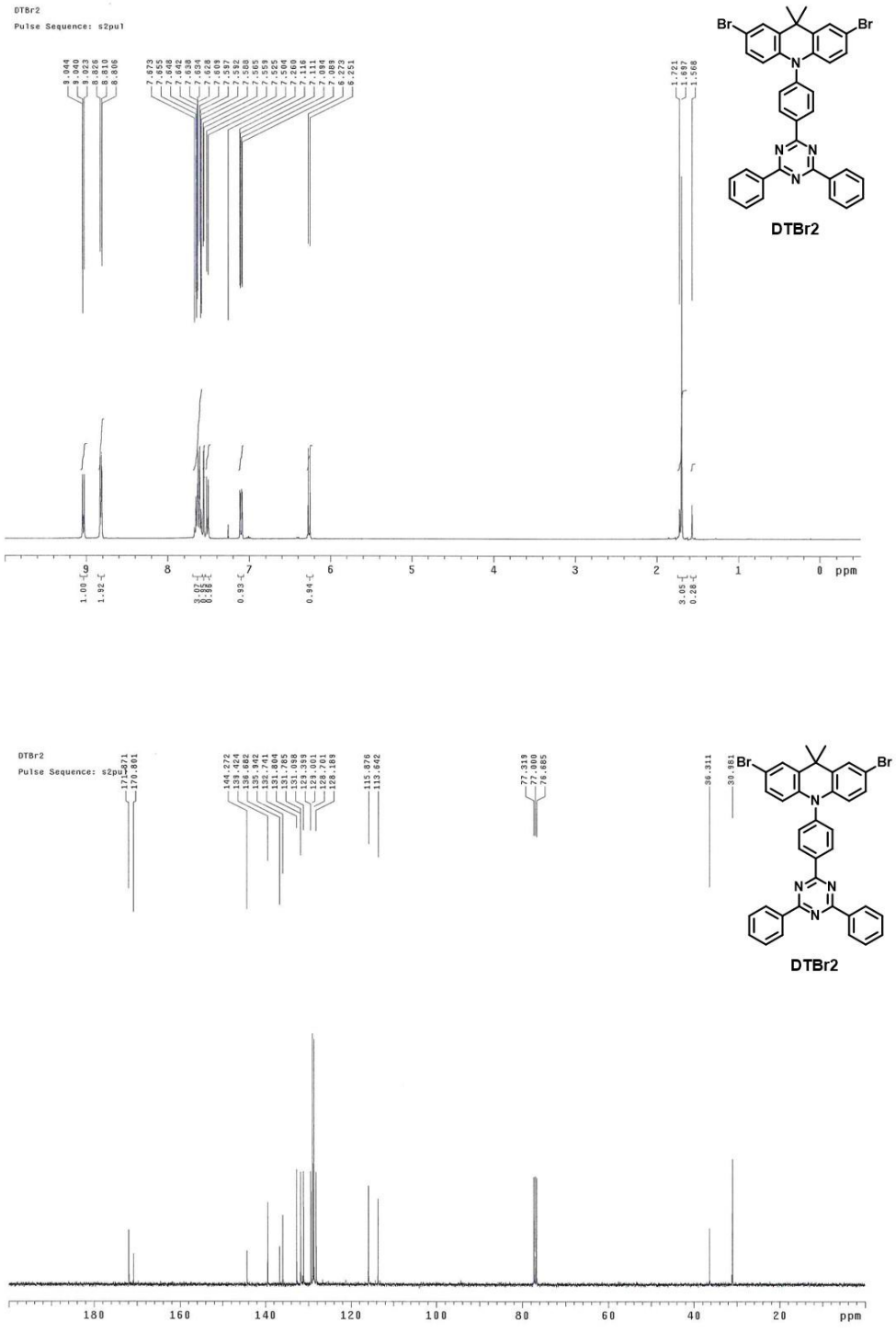

^{1}H and ^{13}C spectra of compound **DTBr2**.

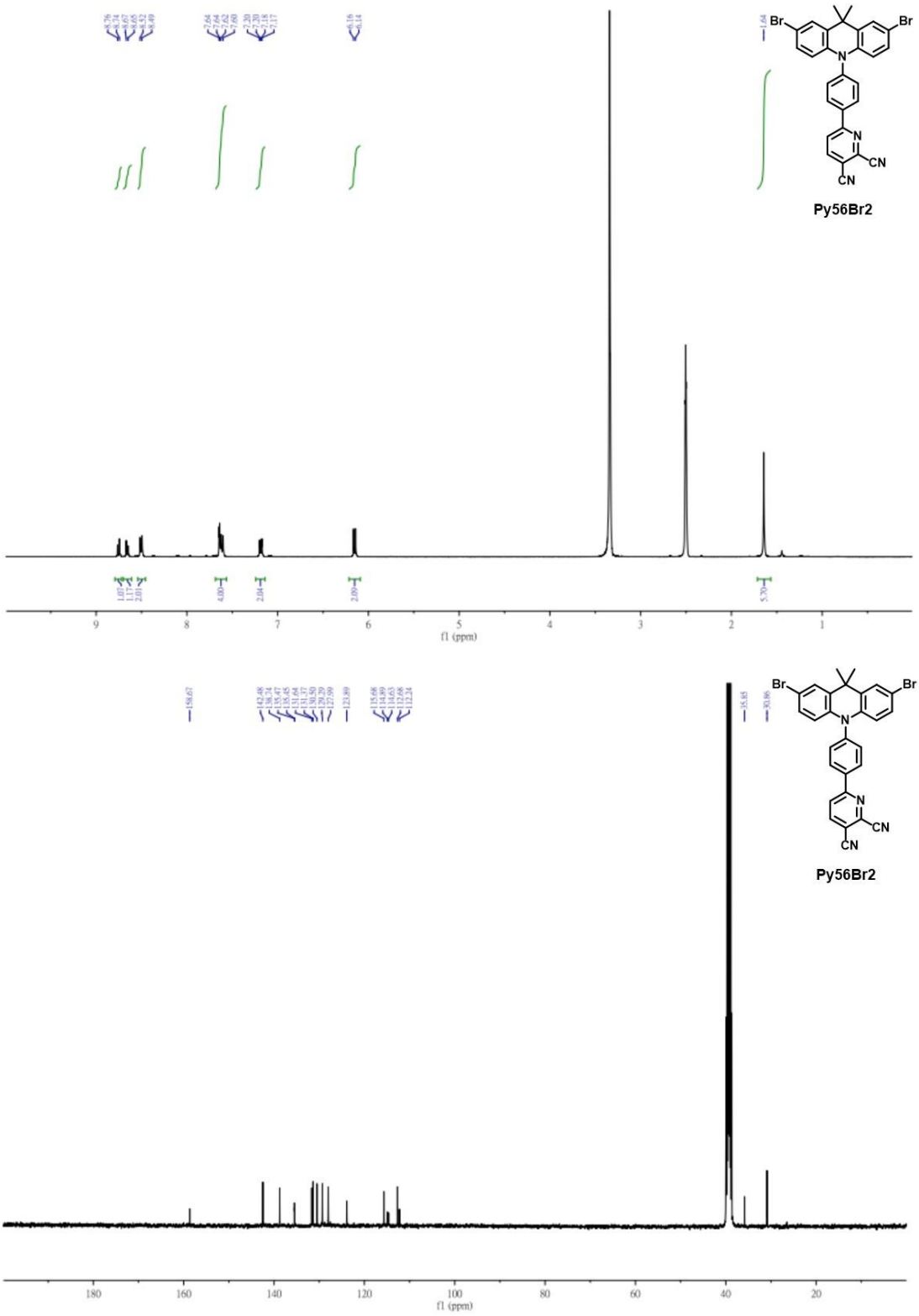

^{1}H and ^{13}C spectra of compound **Py56Br2**.

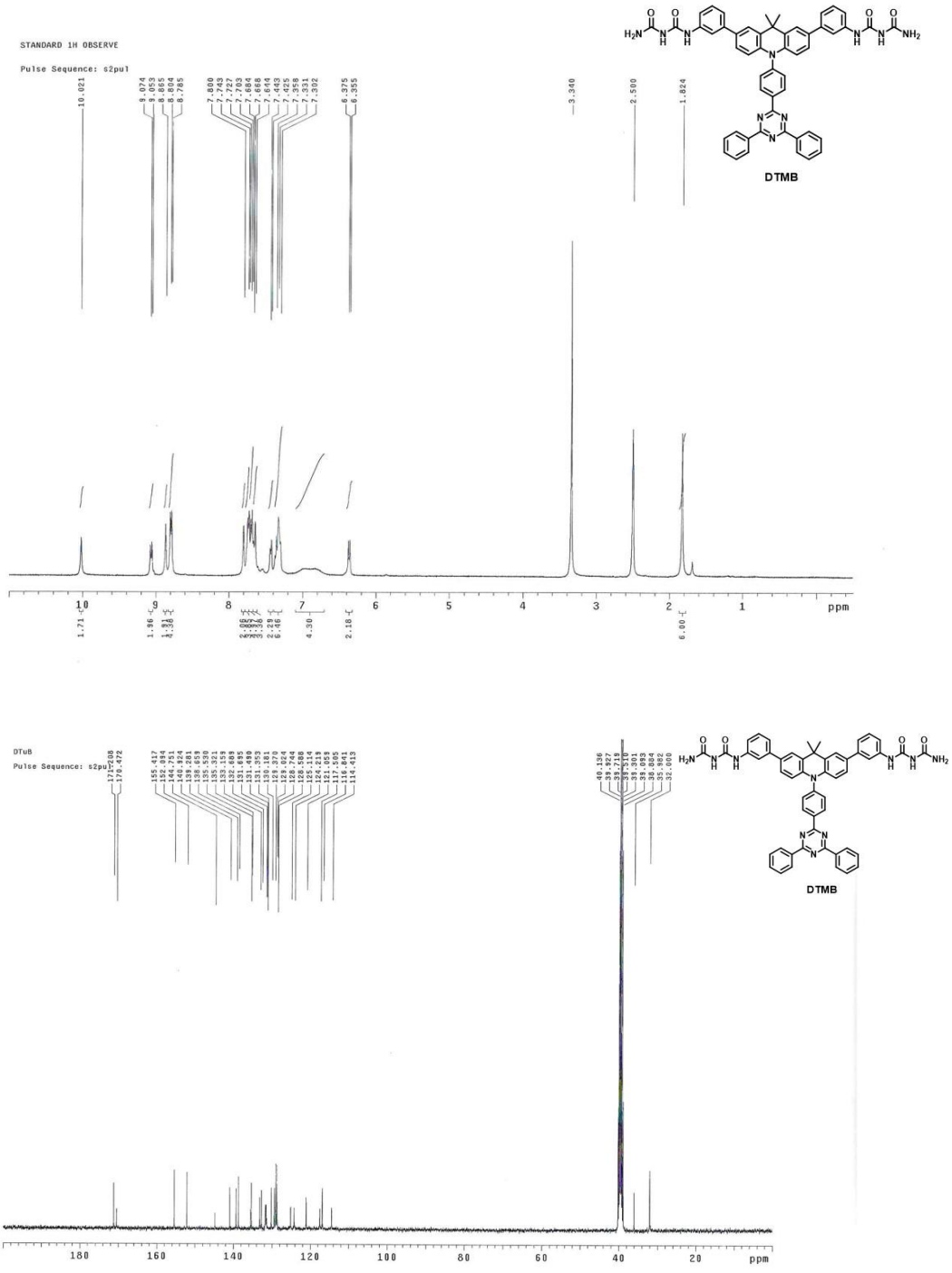

^{1}H and ^{13}C spectra of compound **DTMB**.

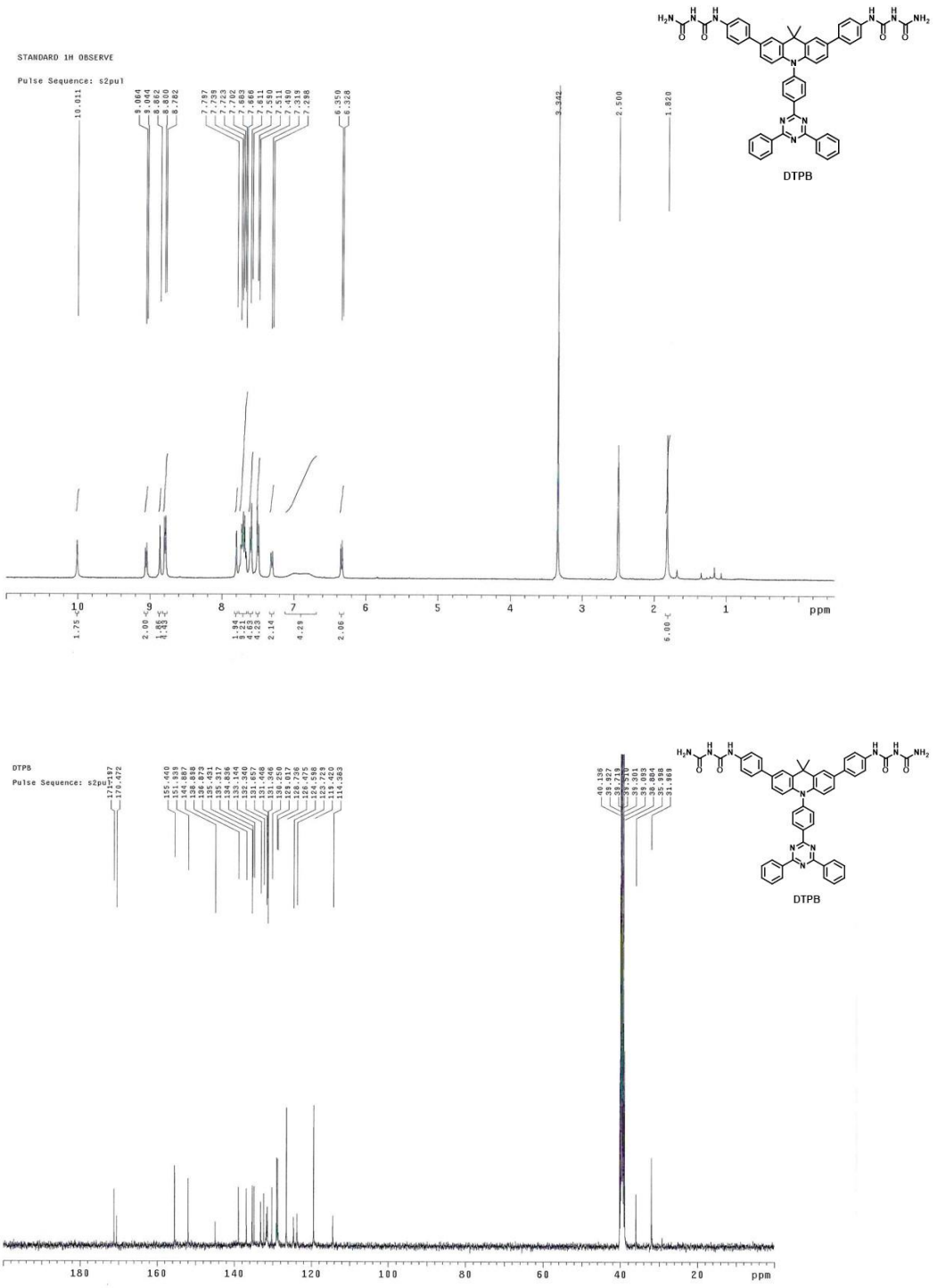

^{1}H and ^{13}C spectra of compound **DTPB**.

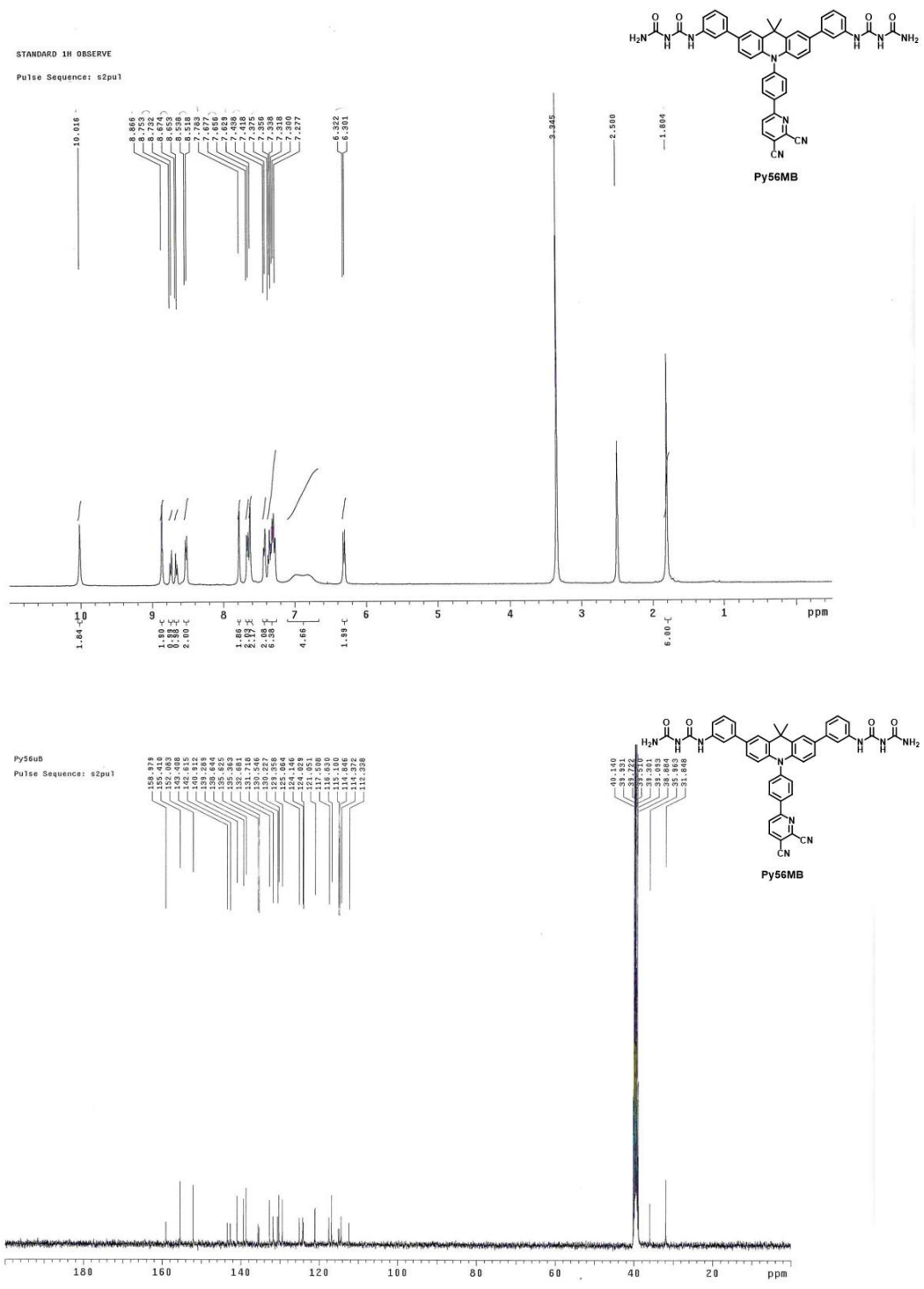

^{1}H and ^{13}C spectra of compound **Py56MB**.

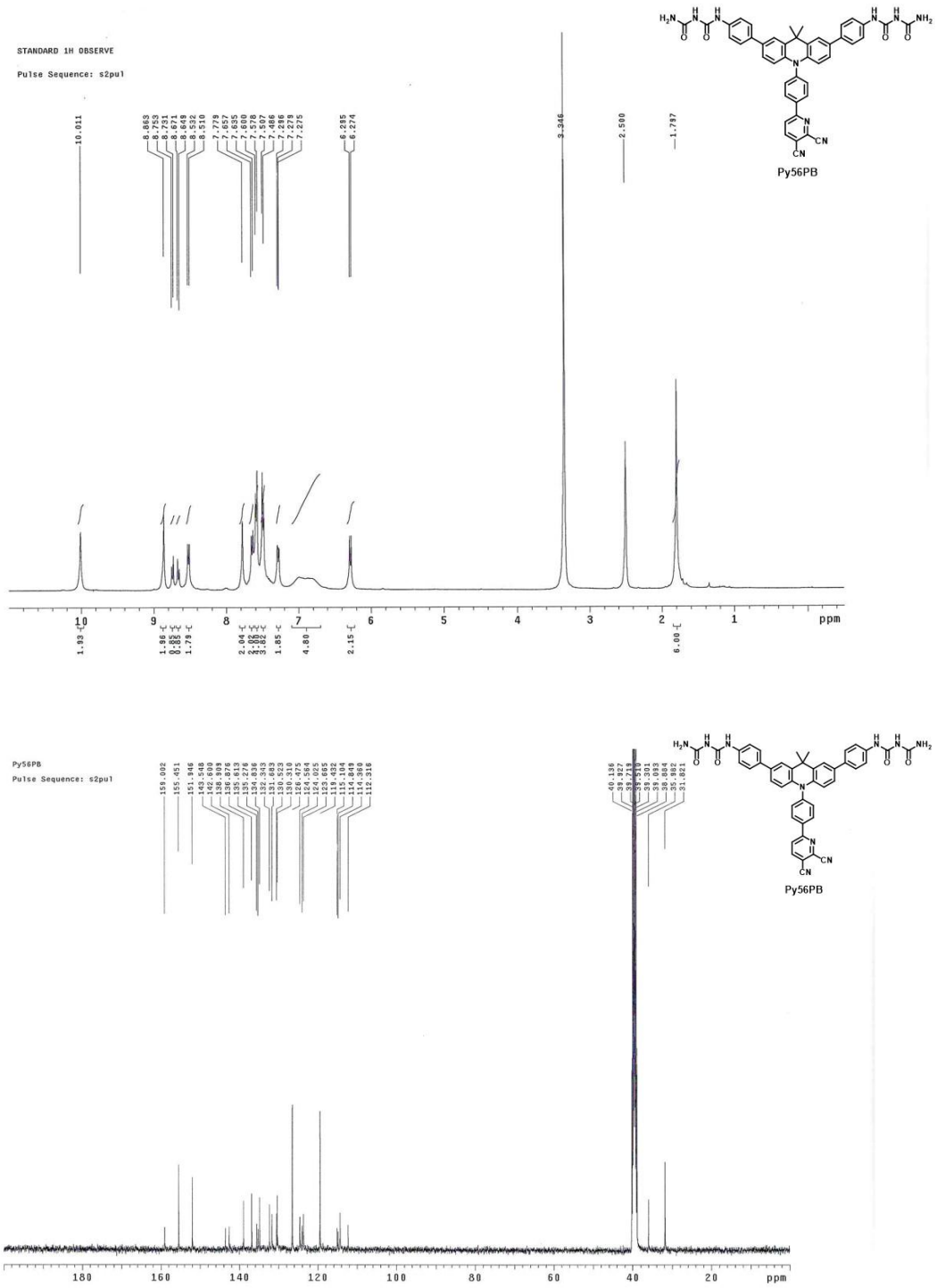

^{1}H and ^{13}C spectra of compound **Py56PB**.

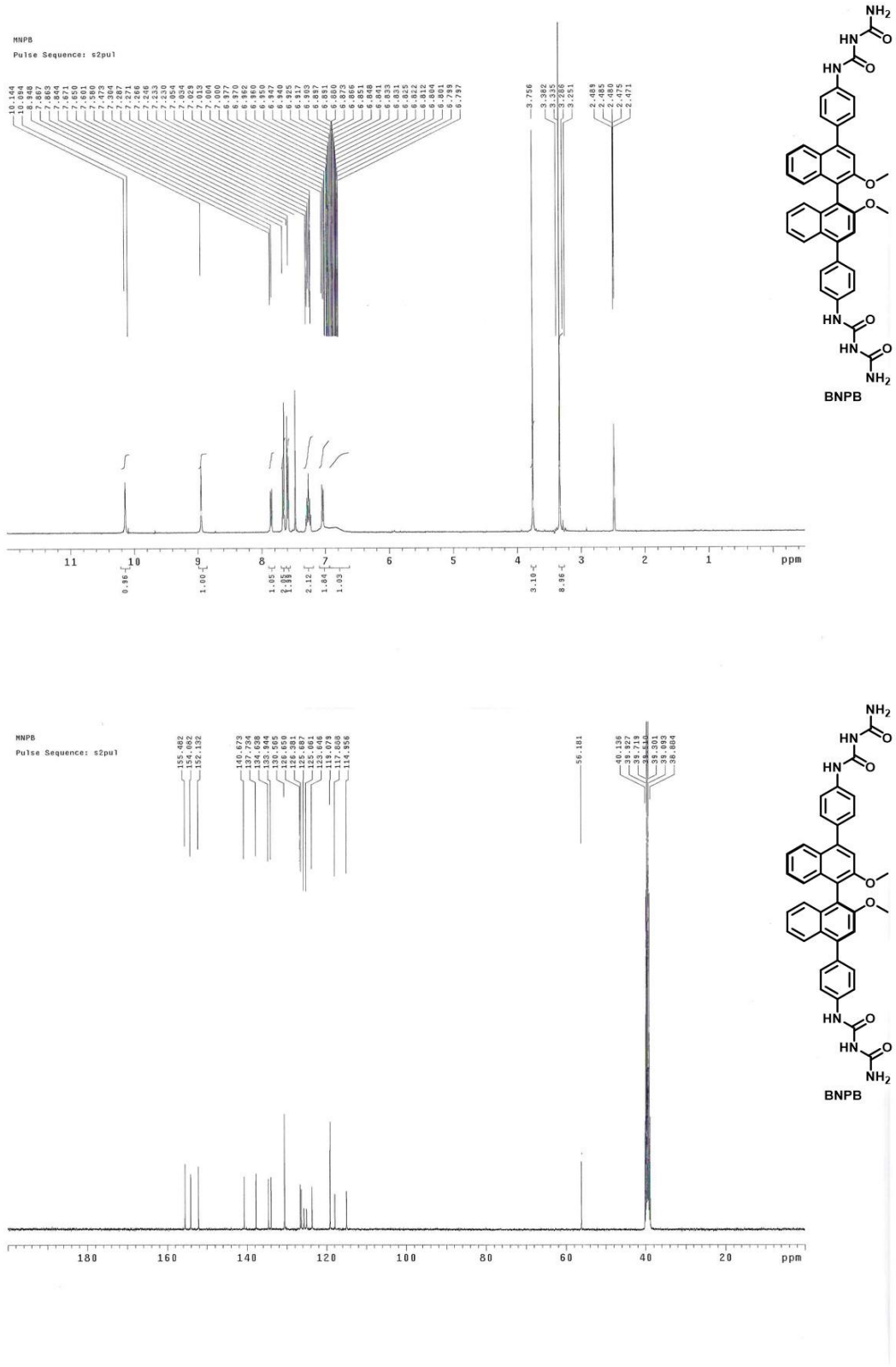

^{1}H and ^{13}C spectra of compound **BNPB**.

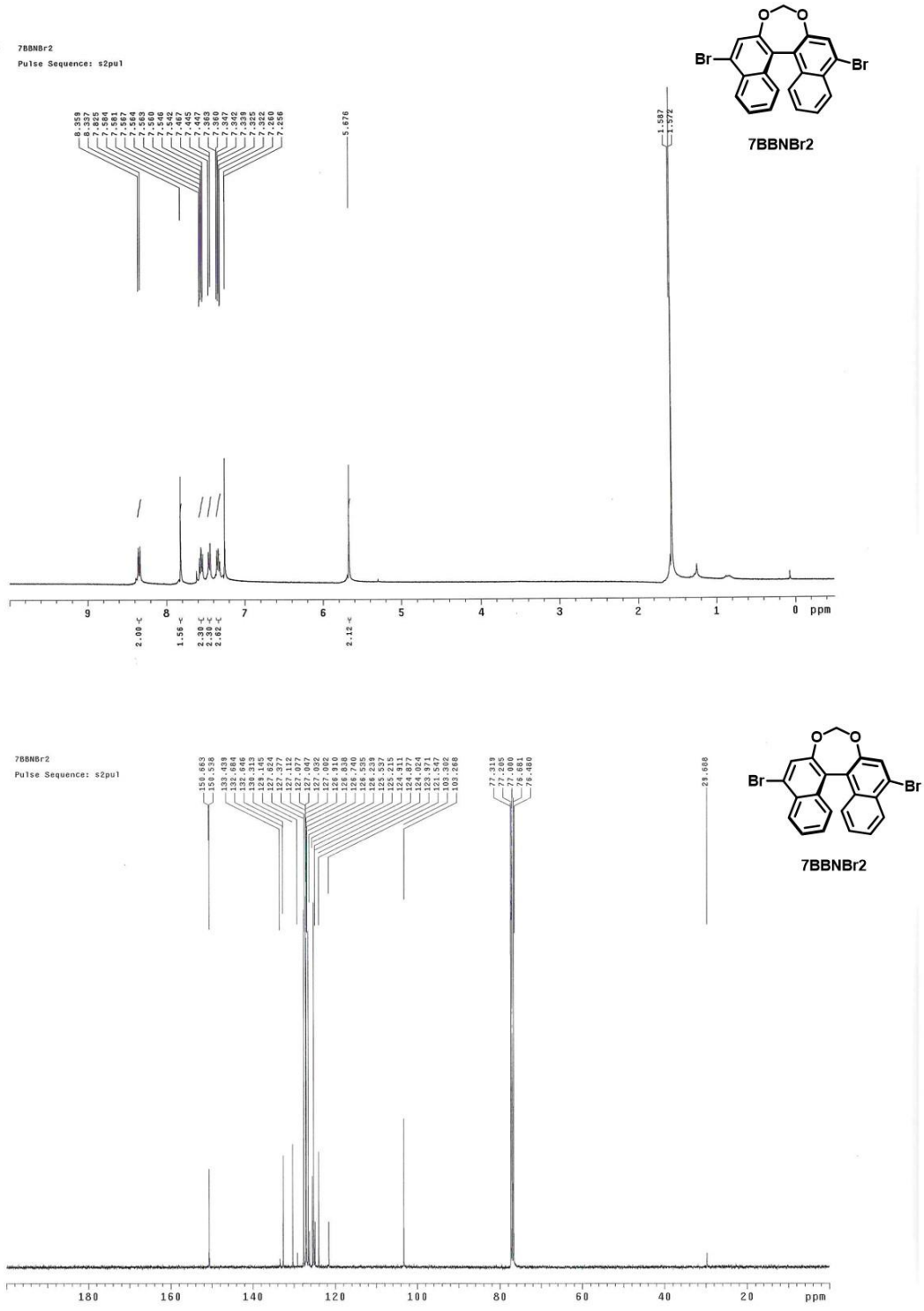

^{1}H and ^{13}C spectra of compound **7BBNBr2**.

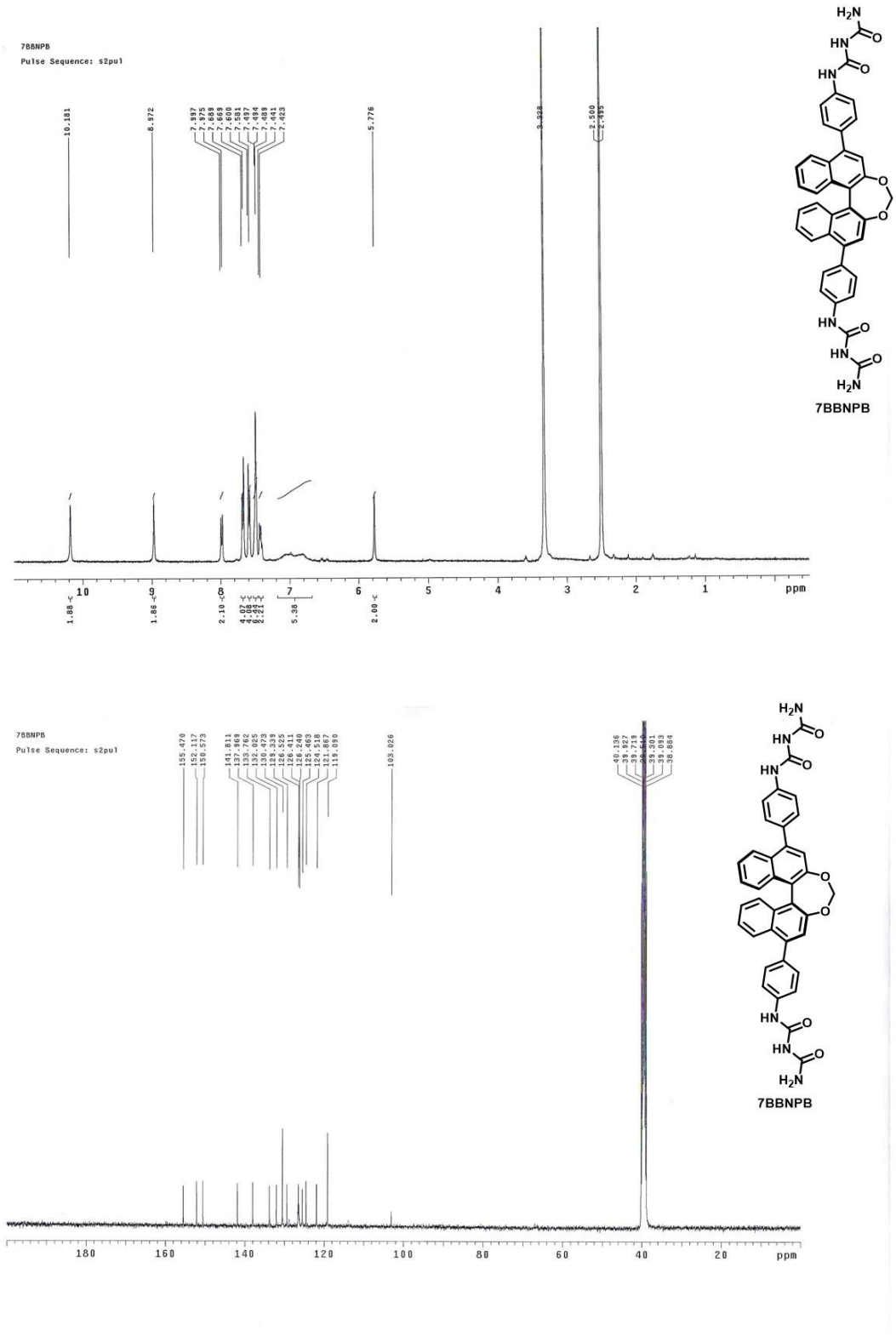

^{1}H and ^{13}C spectra of compound **7BBNPB**.

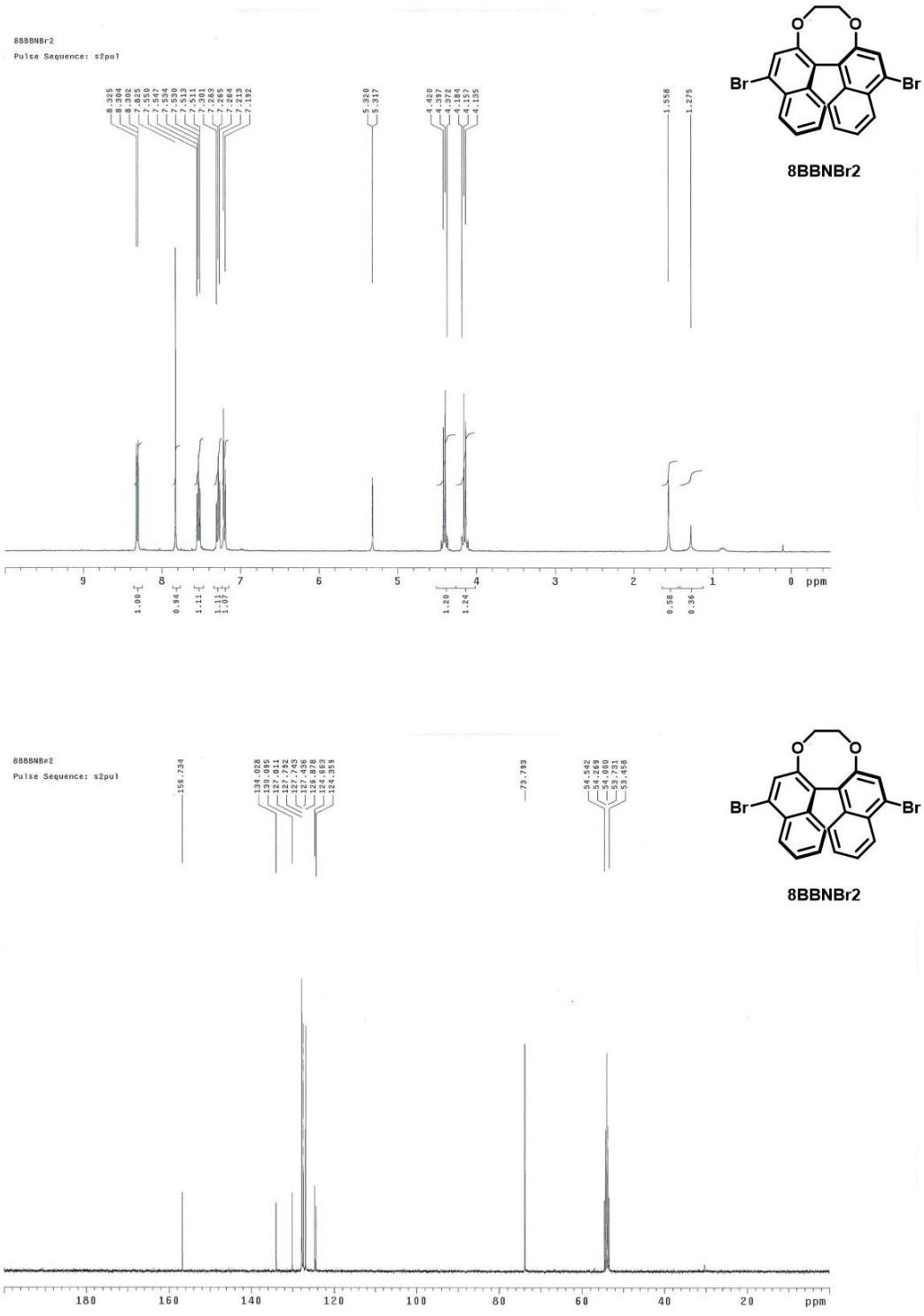

^{1}H and ^{13}C spectra of compound **8BBNBr2**.

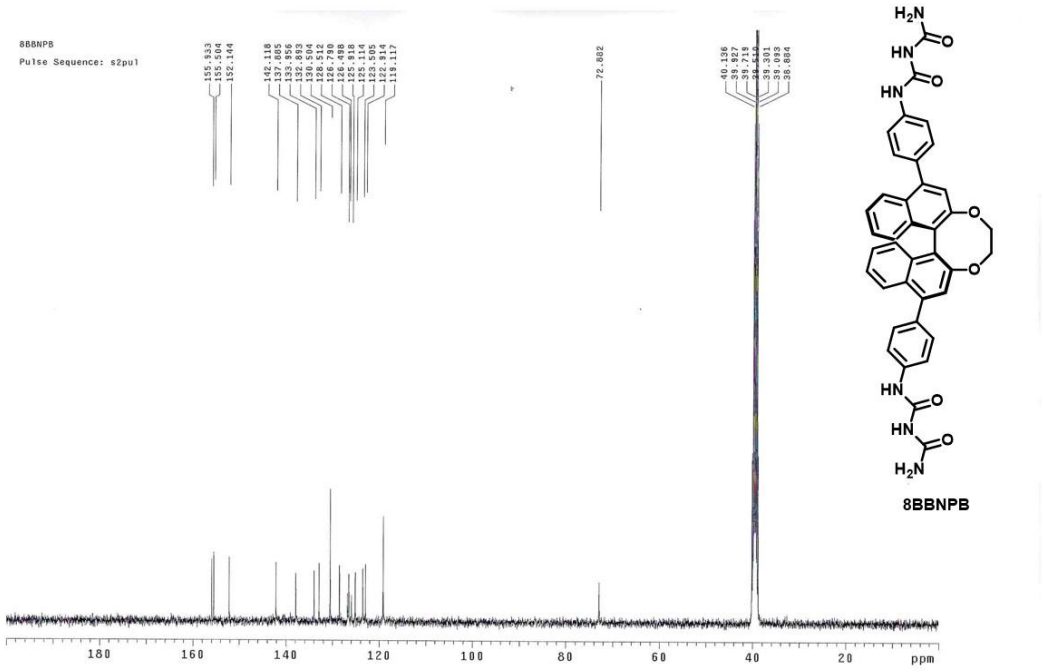

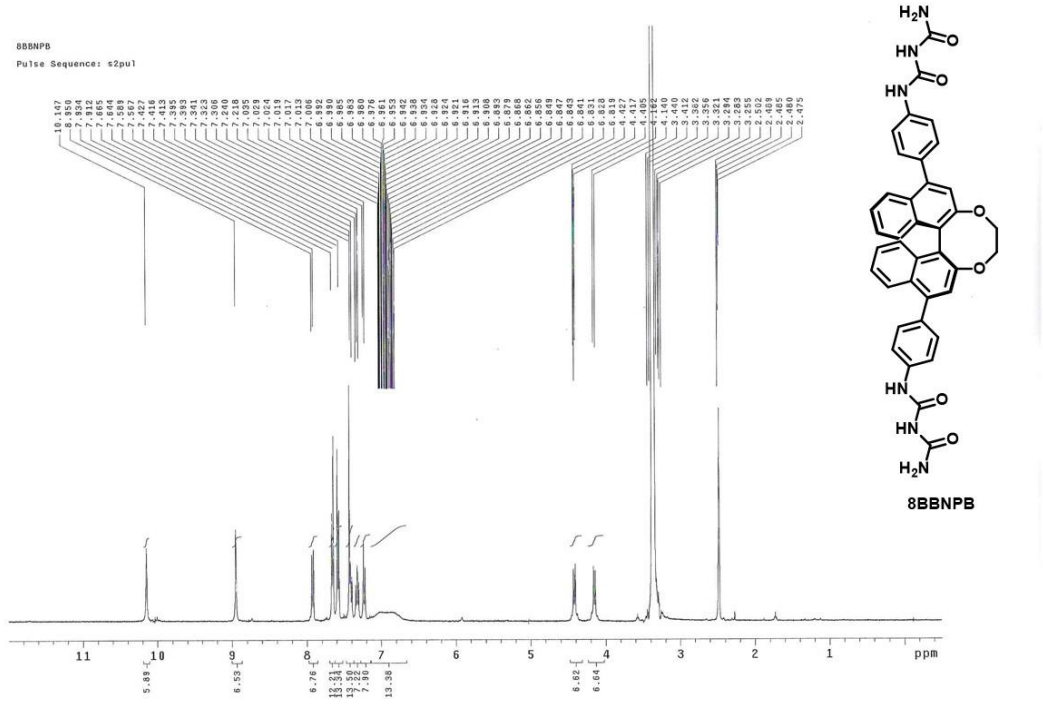

^{1}H and ^{13}C spectra of compound **8BBNPB**.

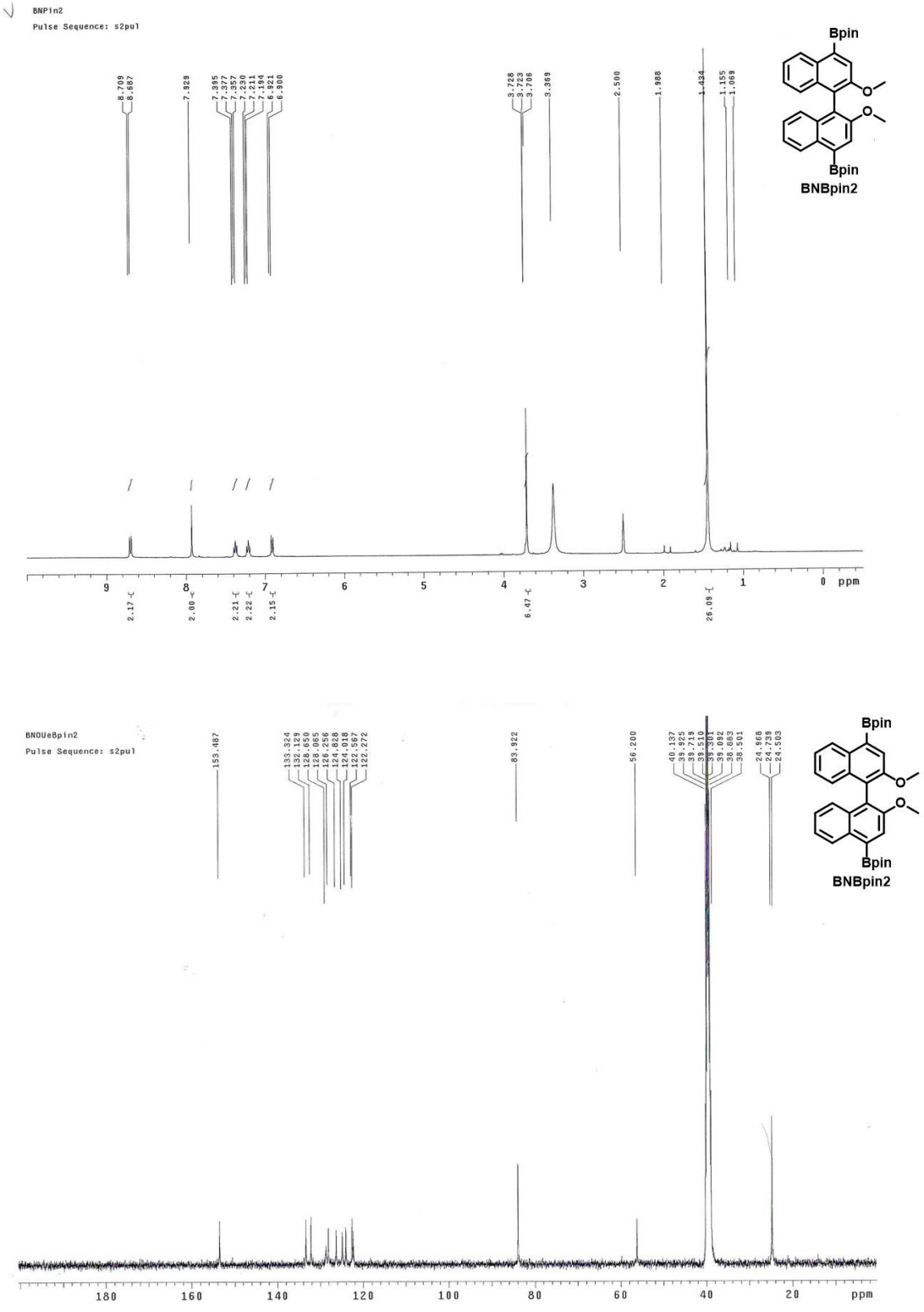

^{1}H and ^{13}C spectra of compound **BNBpin2**.

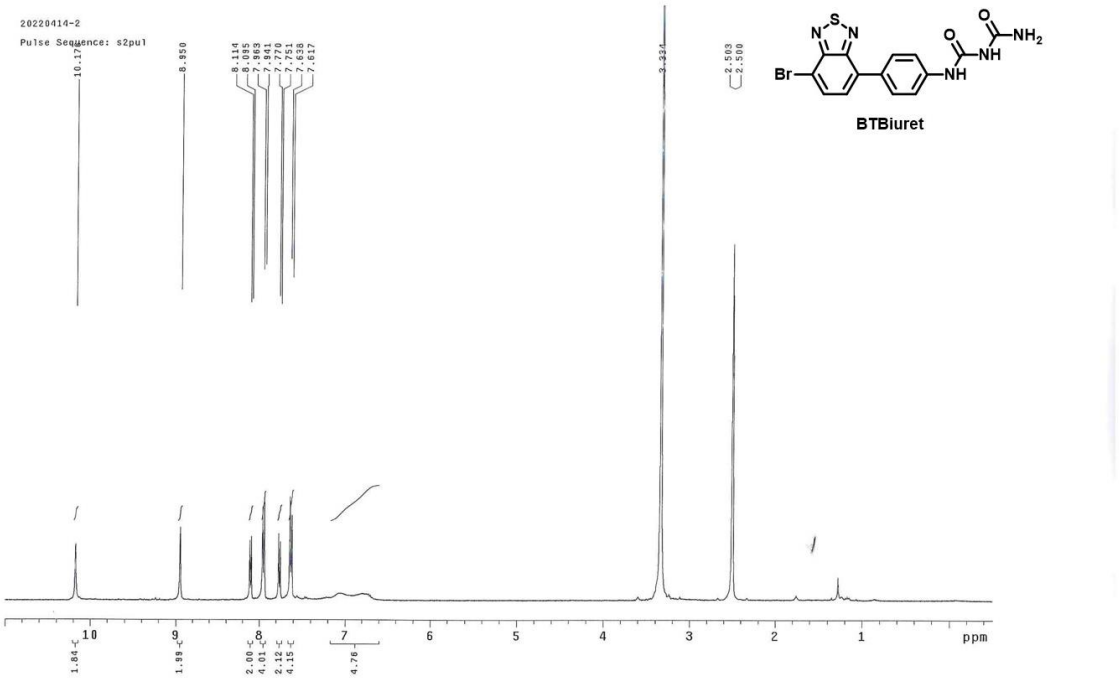

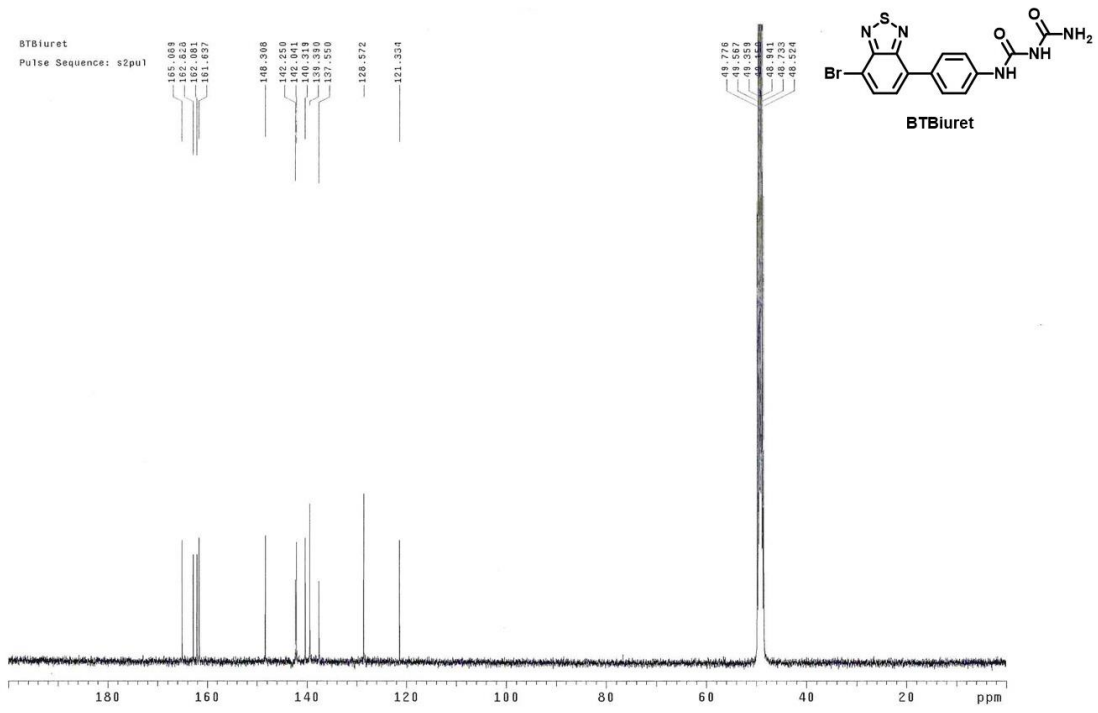

^{1}H and ^{13}C spectra of compound **BTBiuret**.

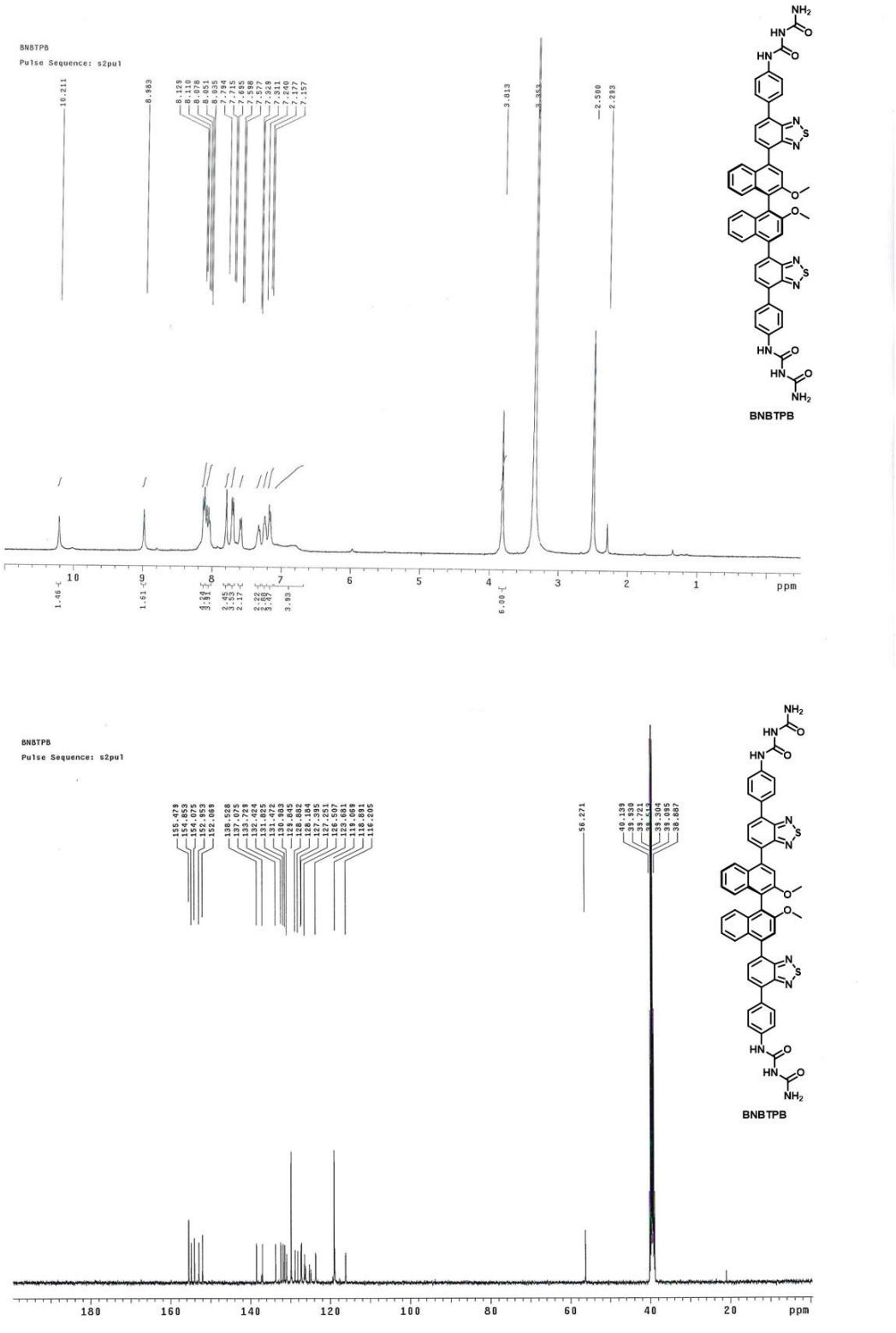

^{1}H and ^{13}C spectra of compound **BNBTPB**.

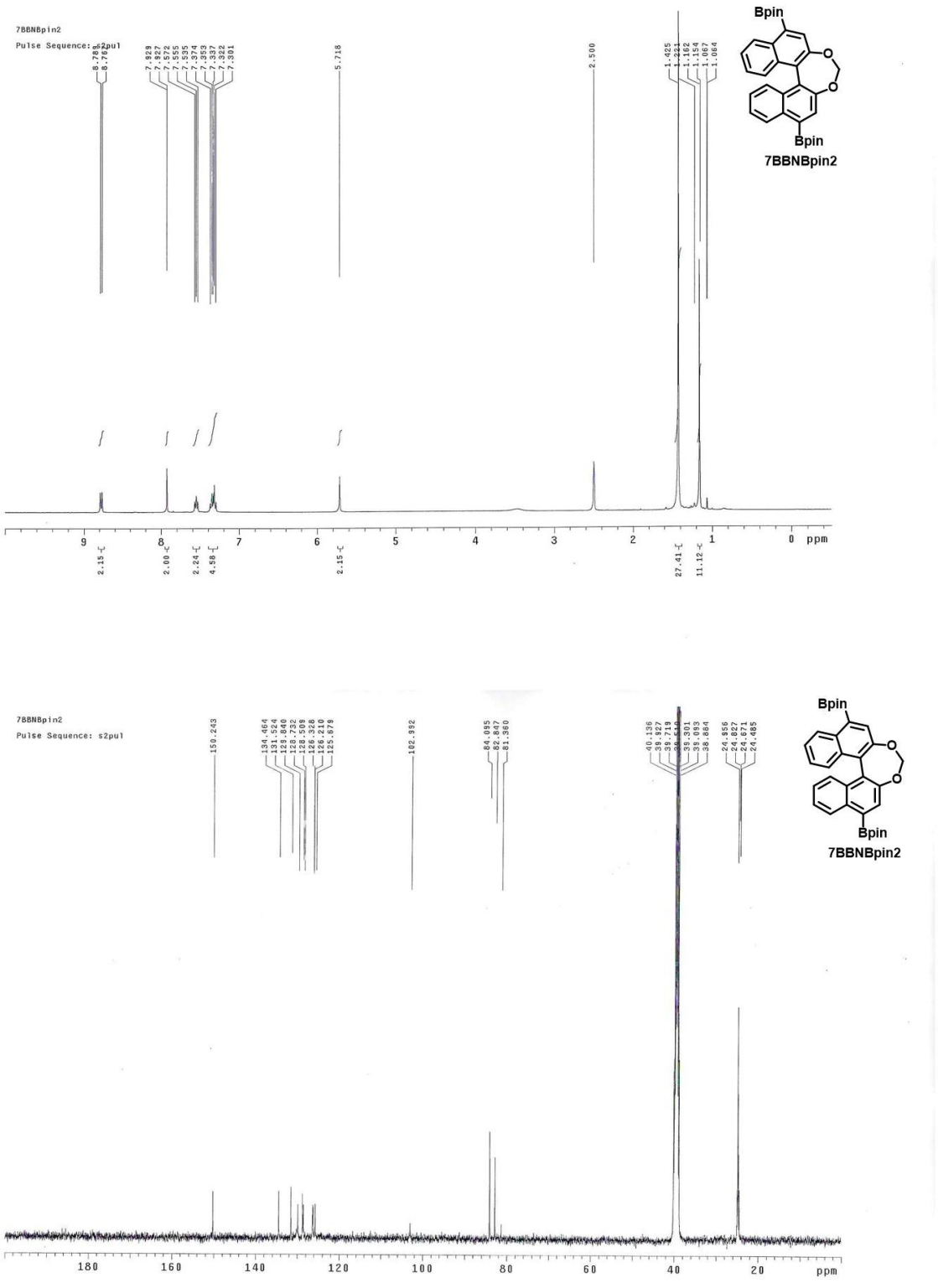

^{1}H and ^{13}C spectra of compound **7BBNBpin2**.

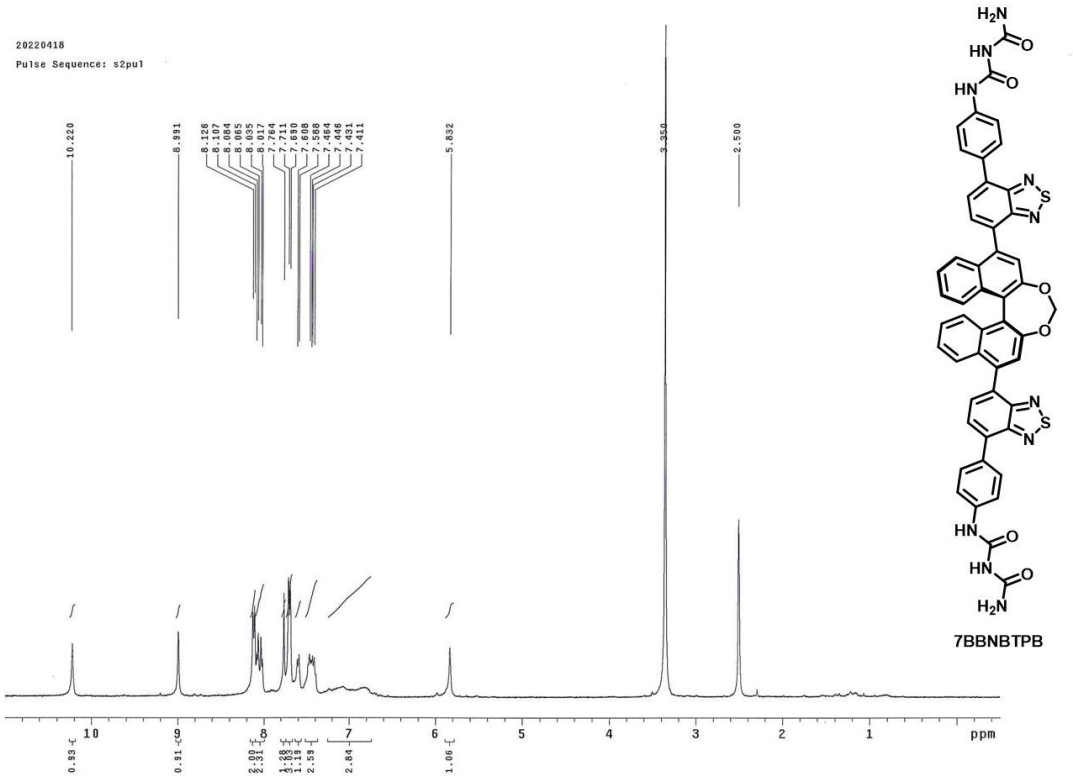

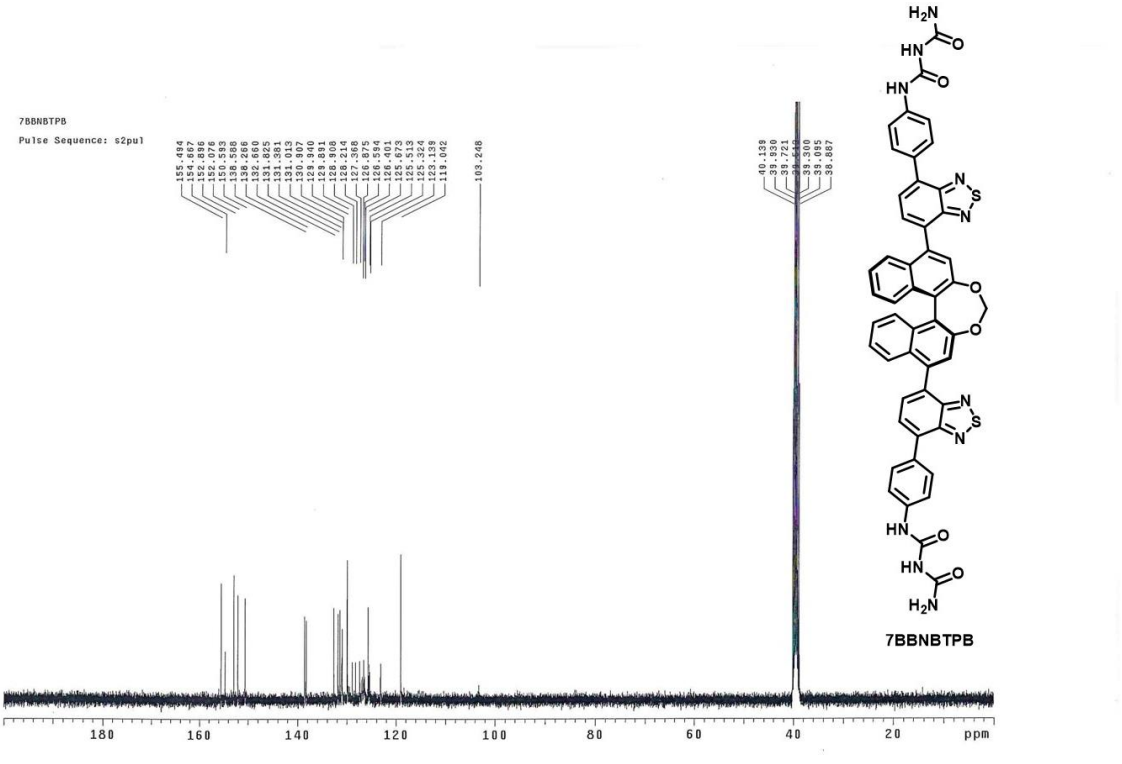

^{1}H and ^{13}C spectra of compound **7BBNBTPB**.

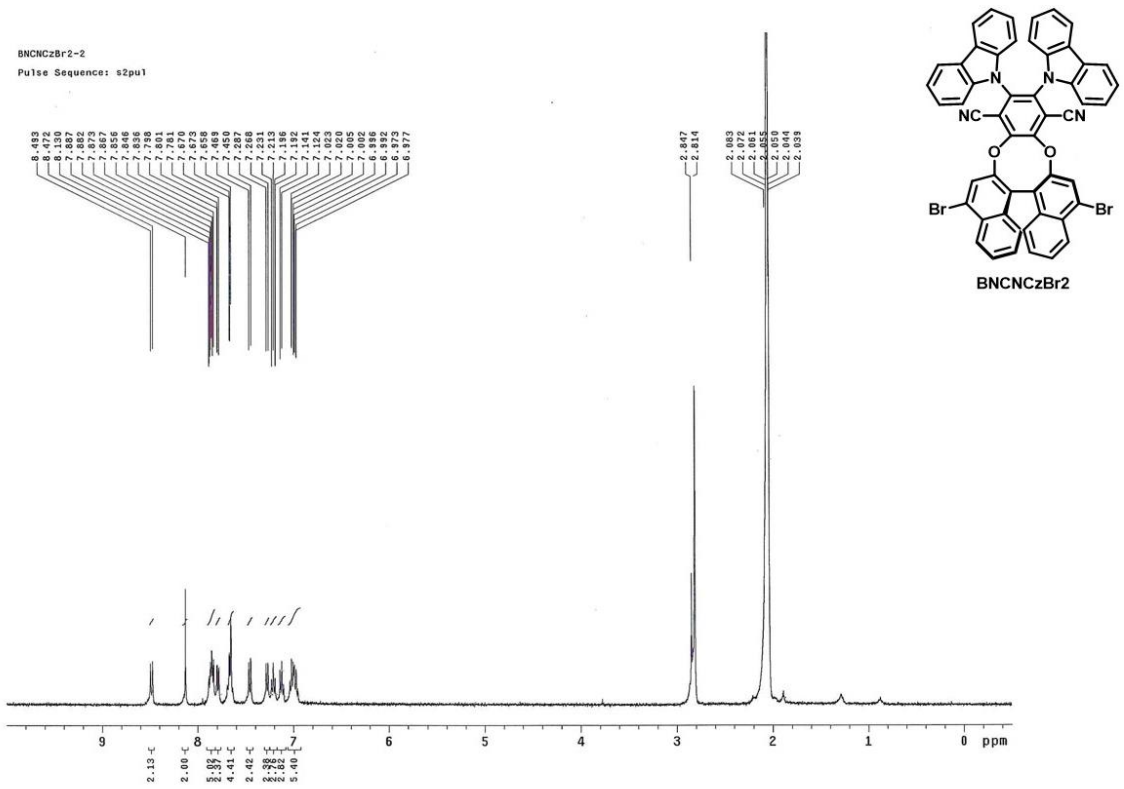

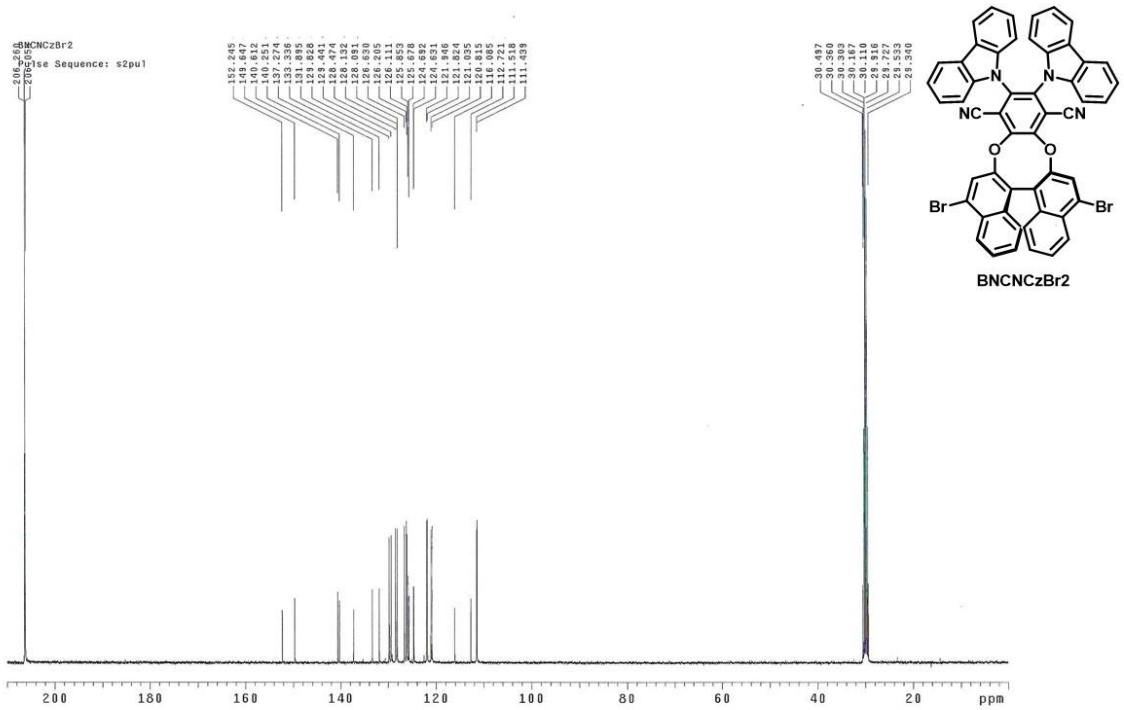

^{1}H and ^{13}C spectra of compound **BNCNCzBr2**.

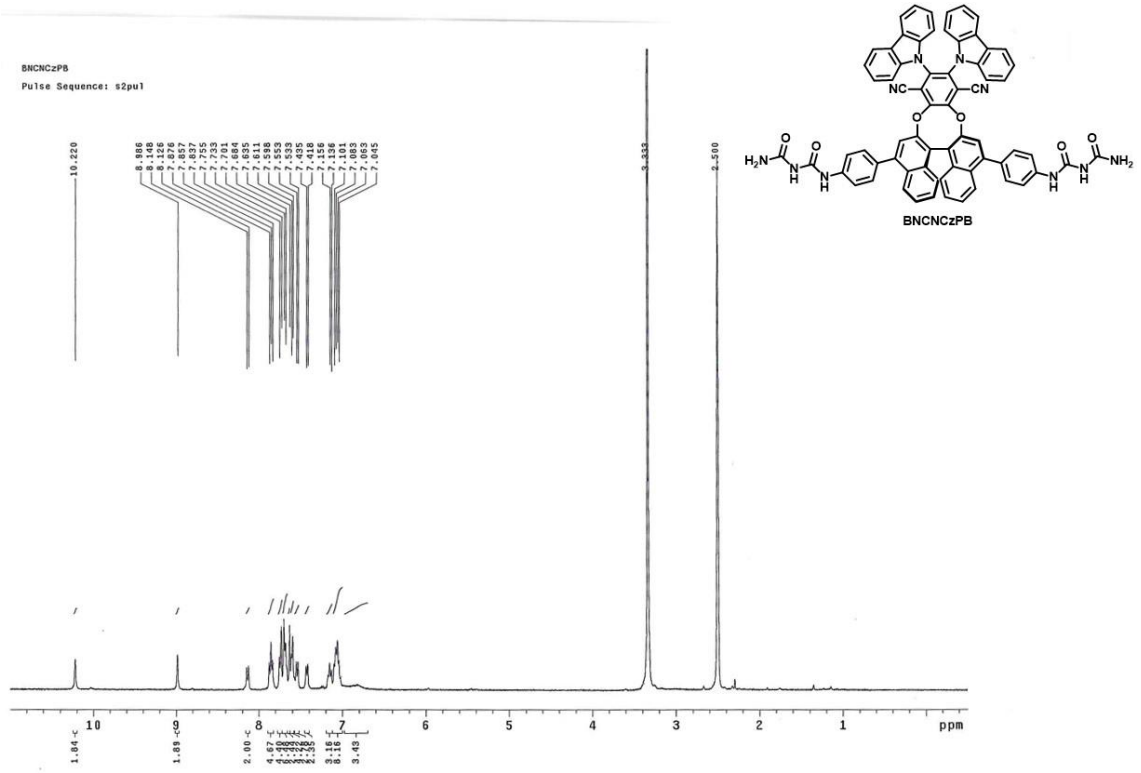

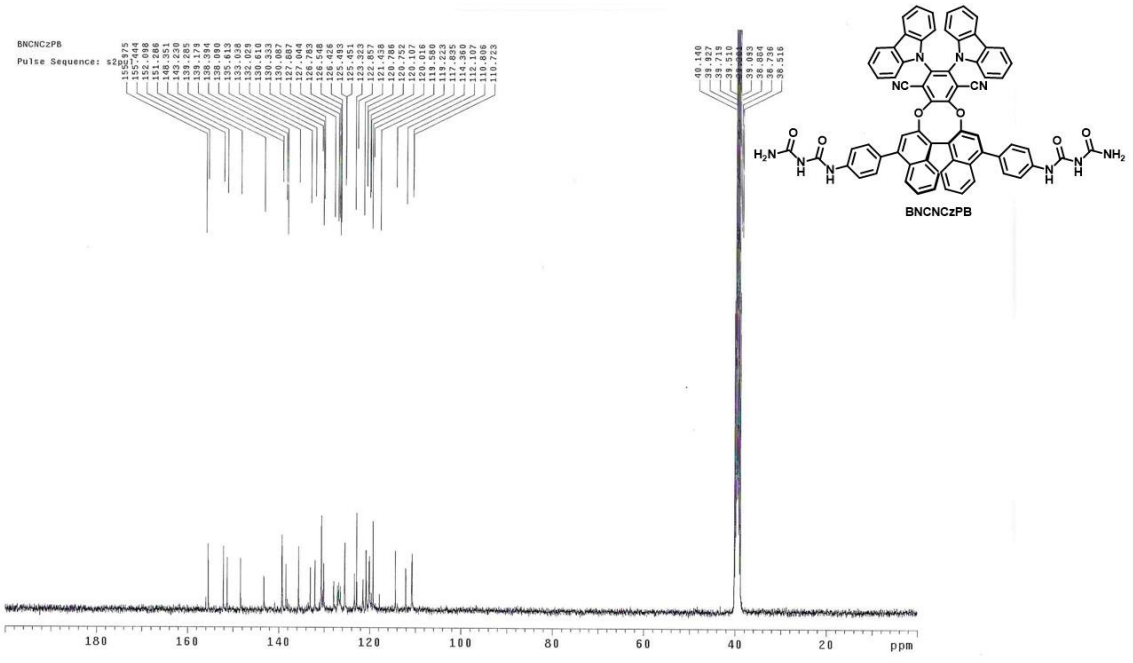

^{1}H and ^{13}C spectra of compound **BNCNCzPB**.

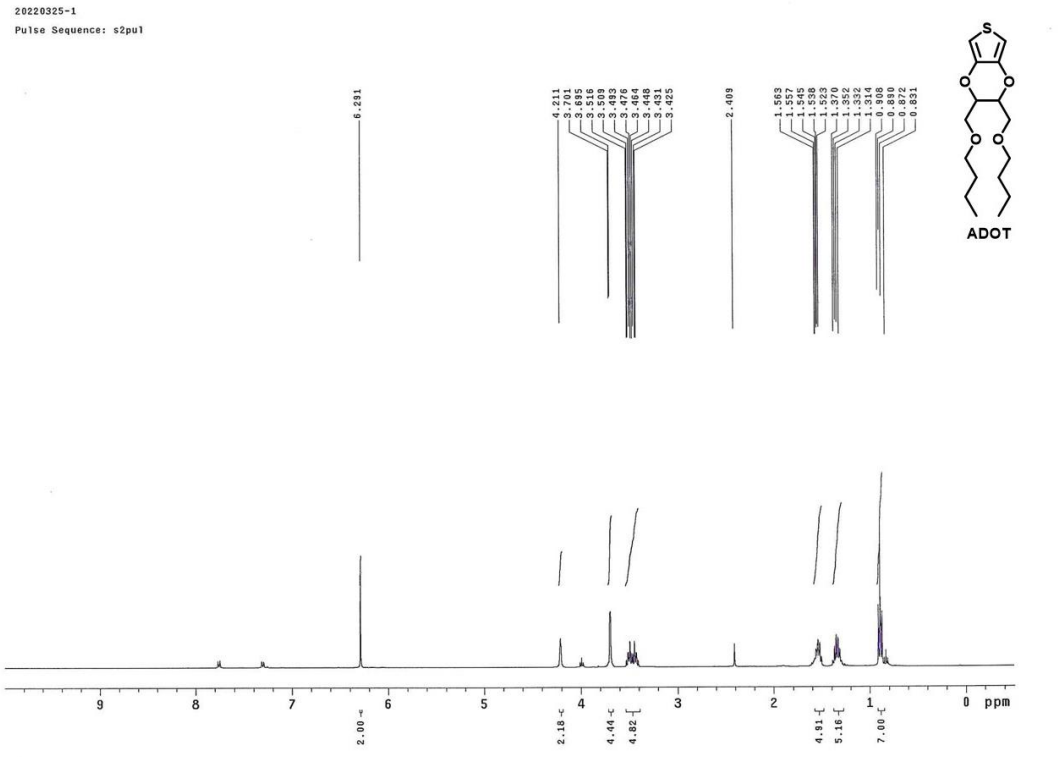

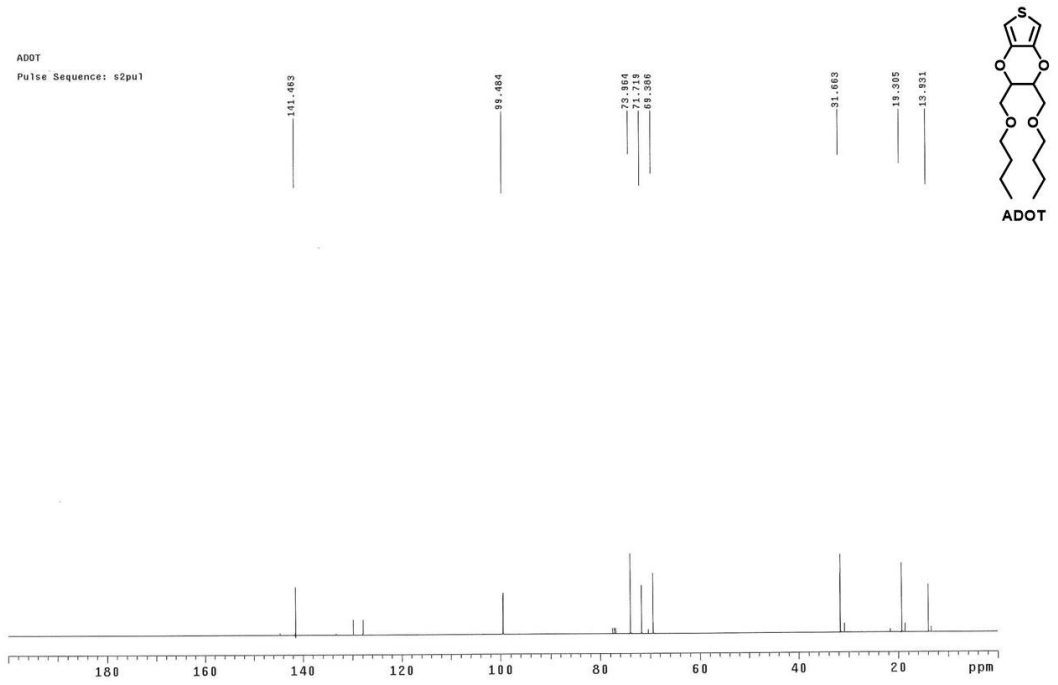

^{1}H and ^{13}C spectra of compound **ADOT**.

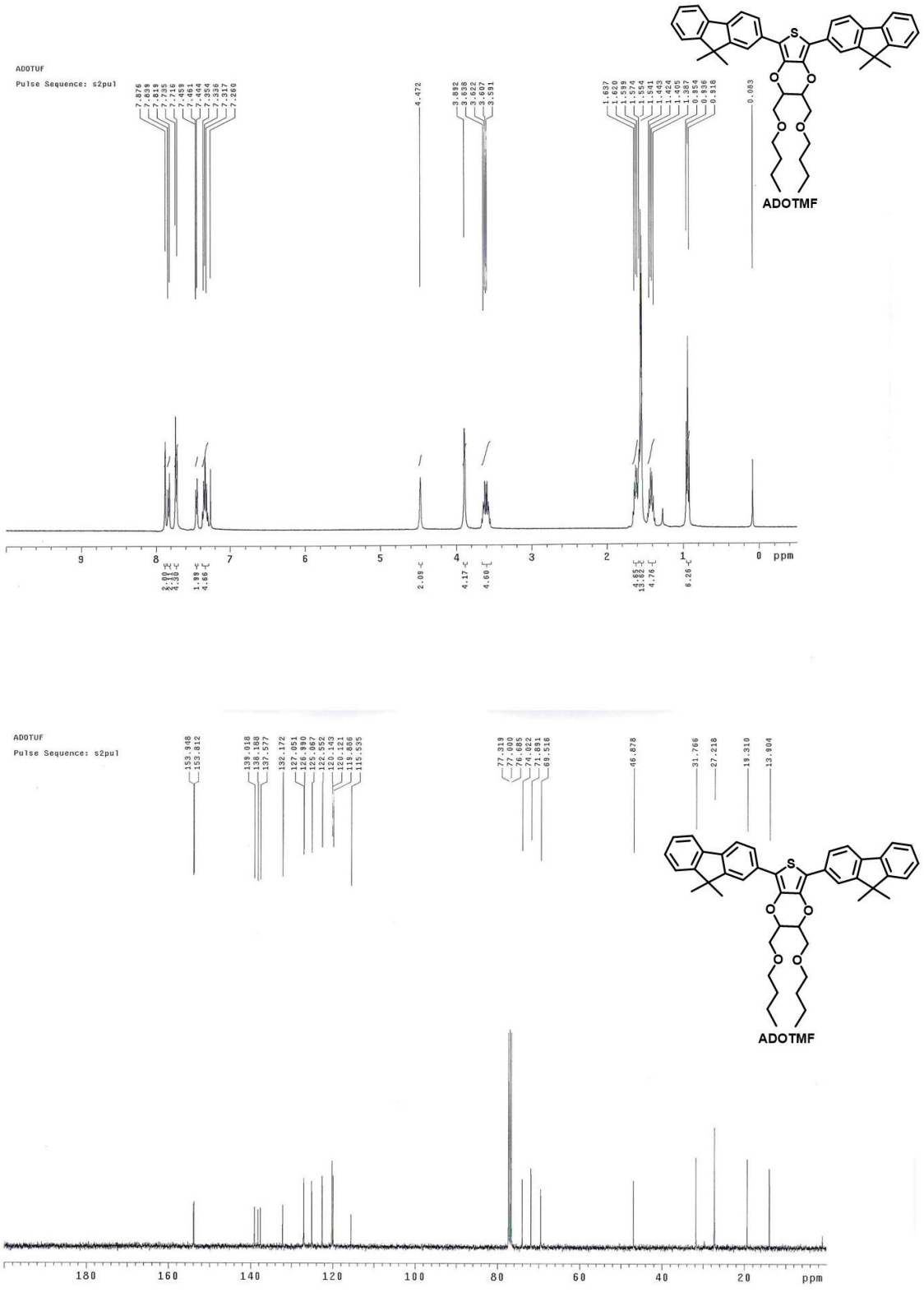

^{1}H and ^{13}C spectra of compound **ADOTMF**.

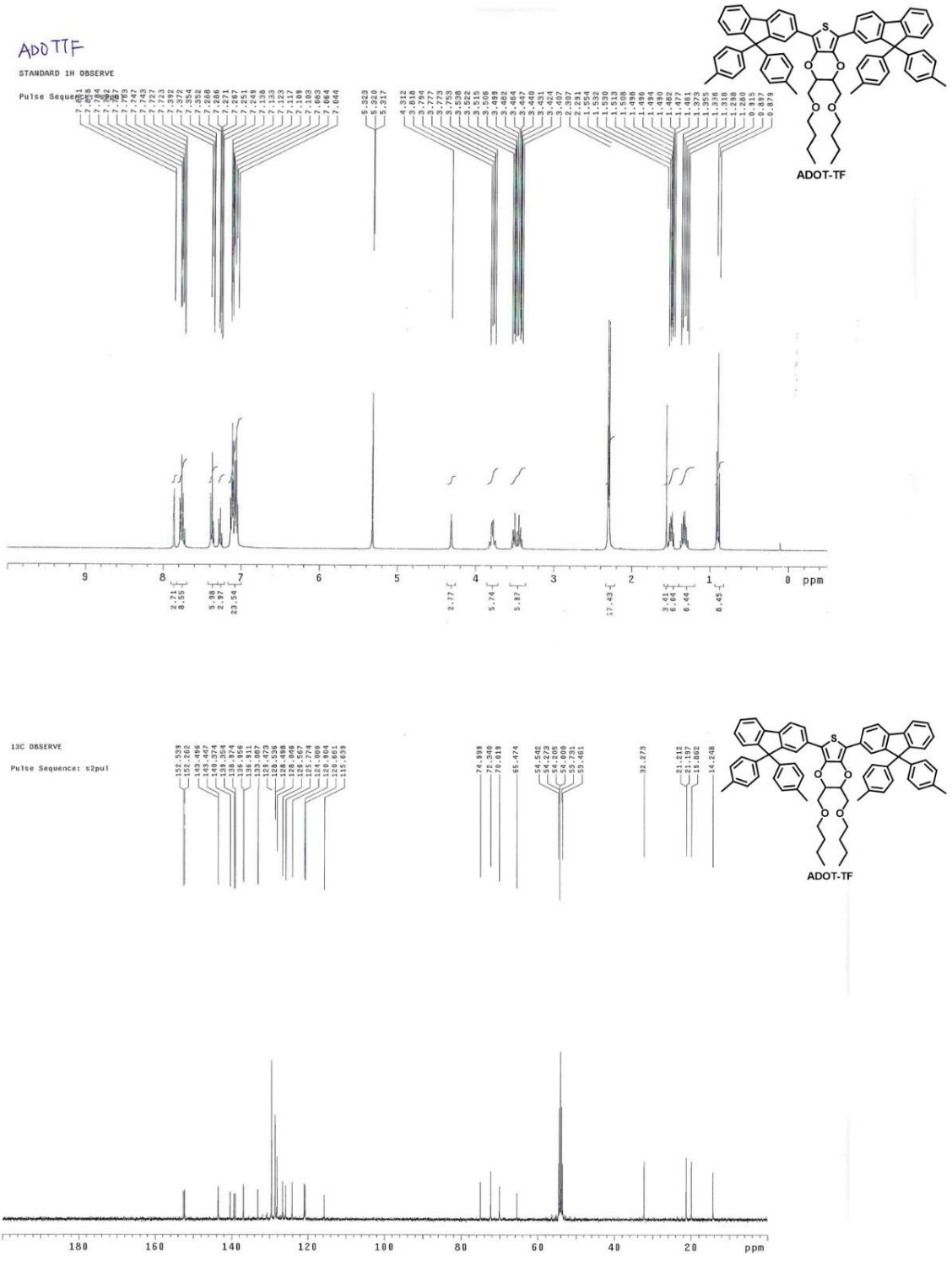

^{1}H and ^{13}C spectra of compound **ADOTTF**.

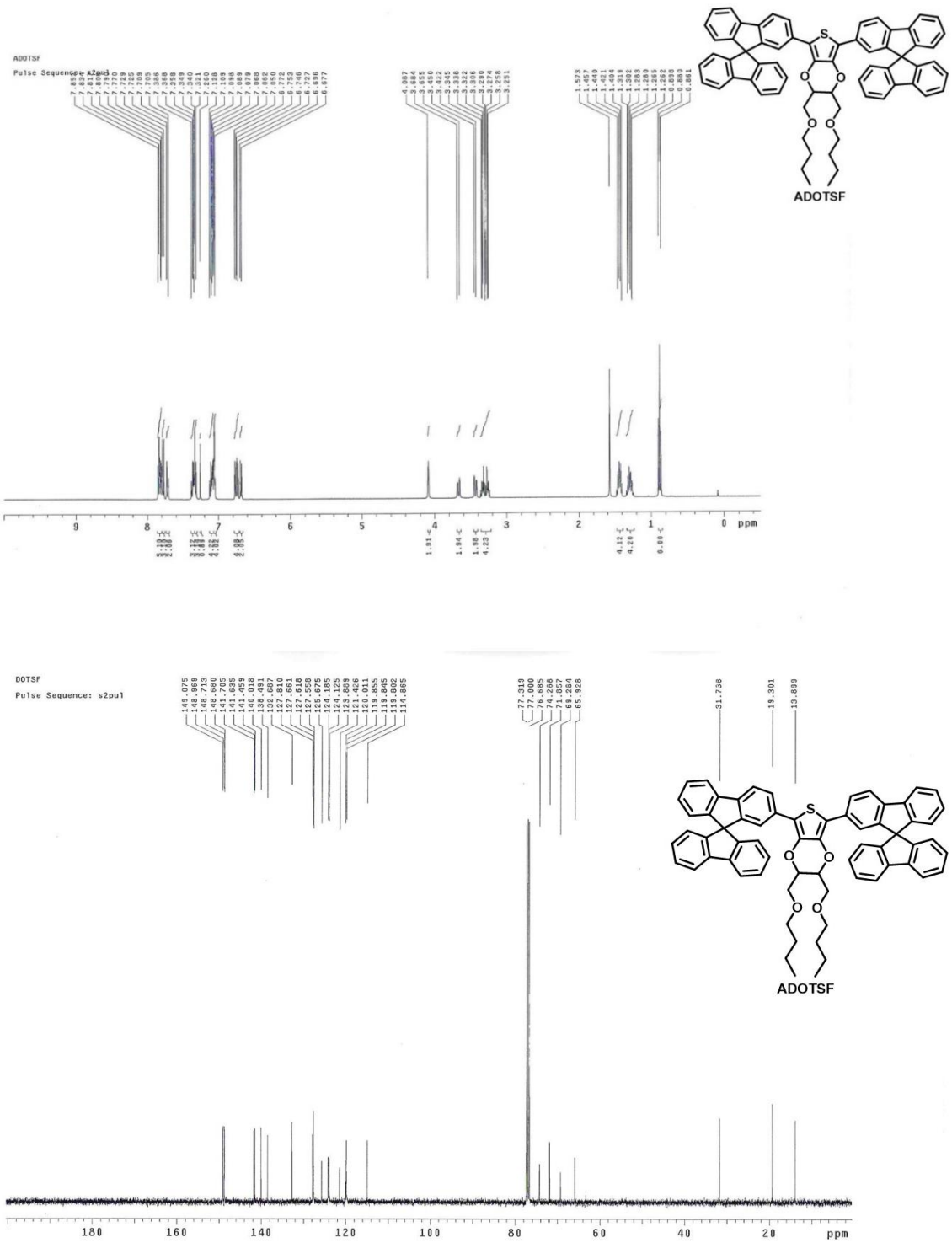

^{1}H and ^{13}C spectra of compound **ADOTSF**.

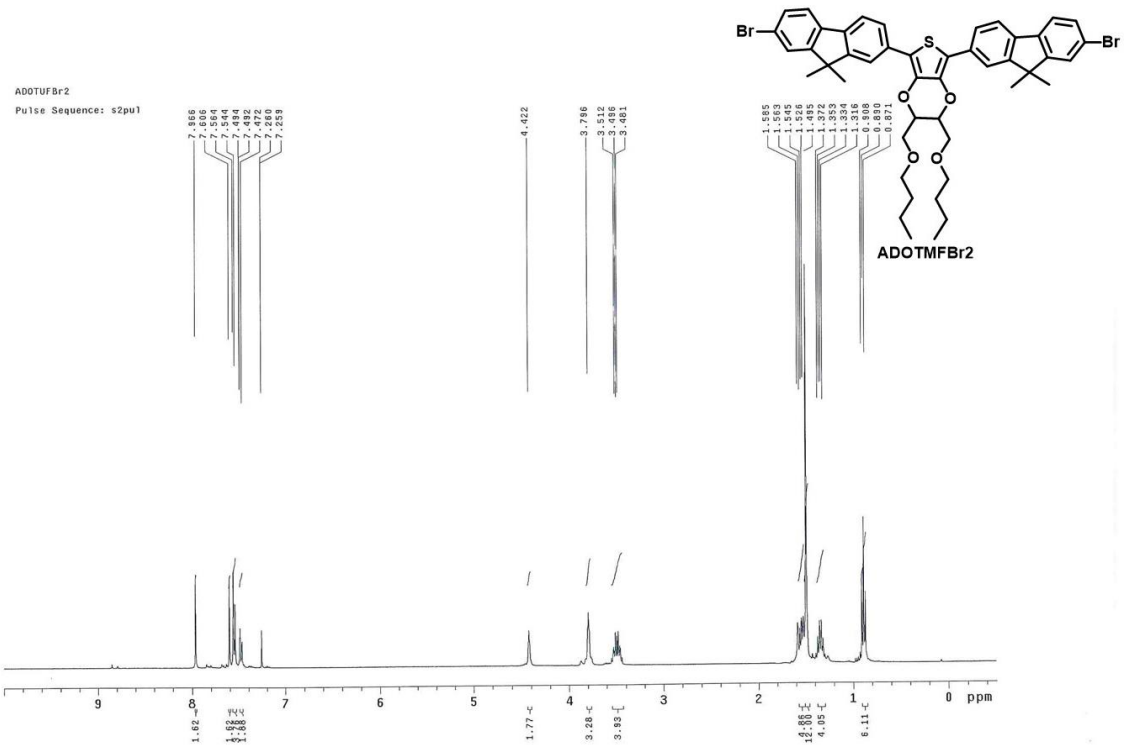

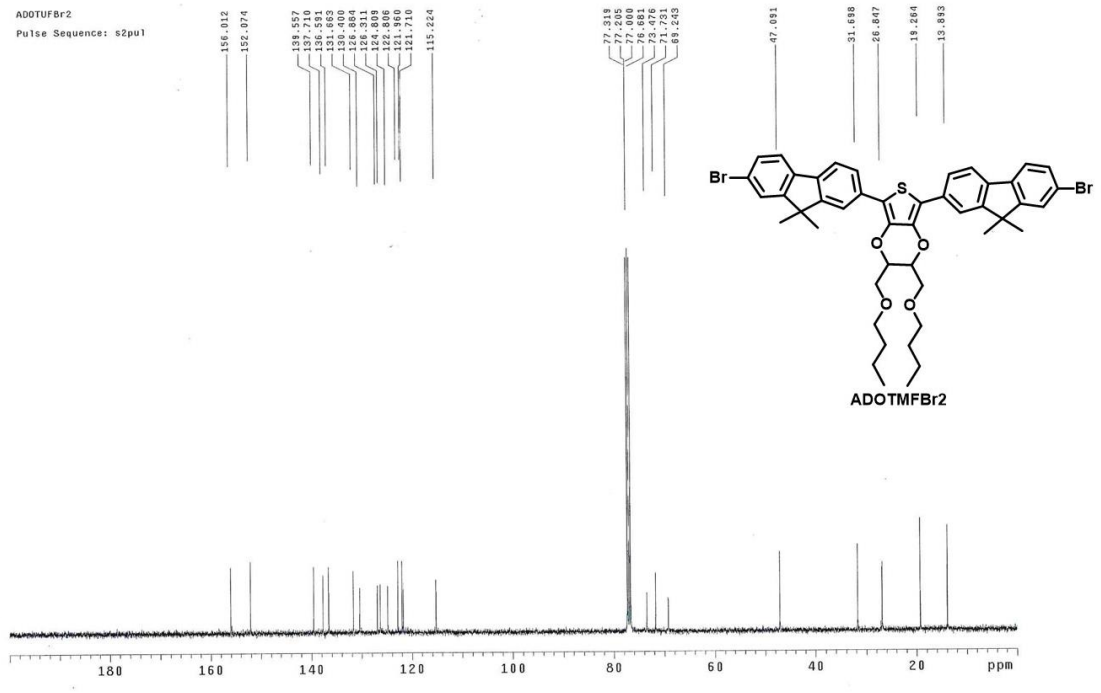

^{1}H and ^{13}C spectra of compound **ADOTMFBr2**.

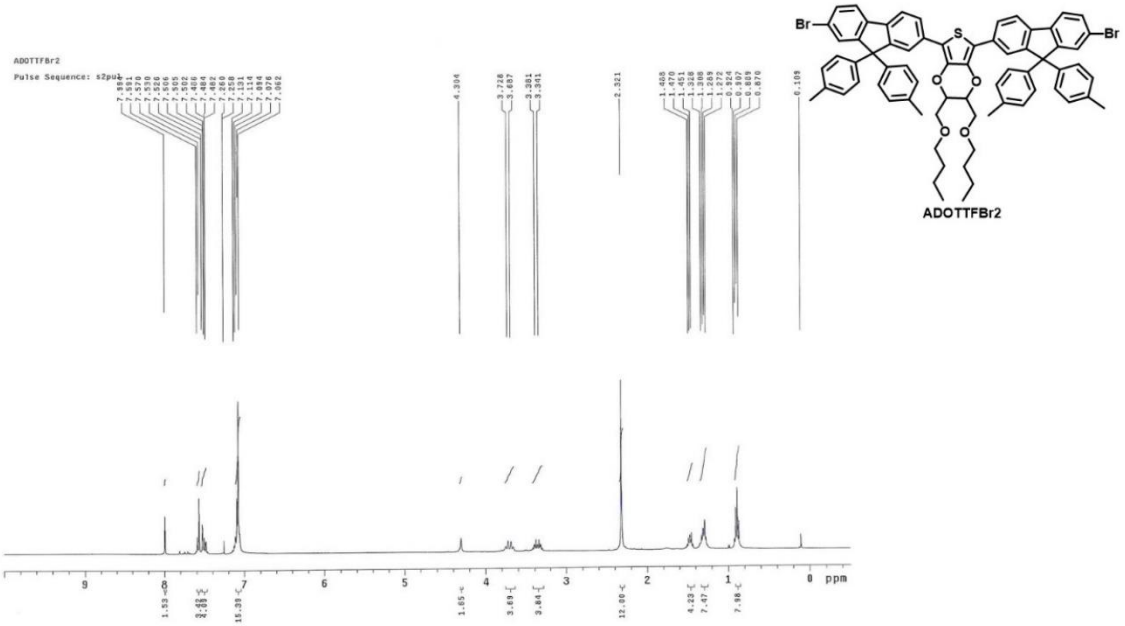

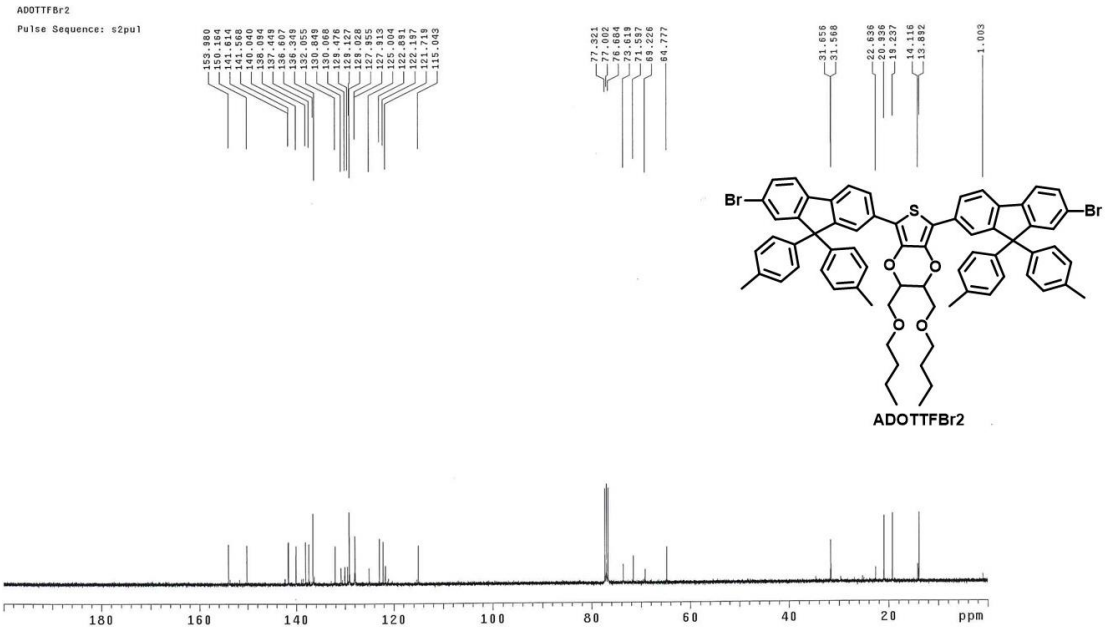

^{1}H and ^{13}C spectra of compound **ADOTTFBr2**.

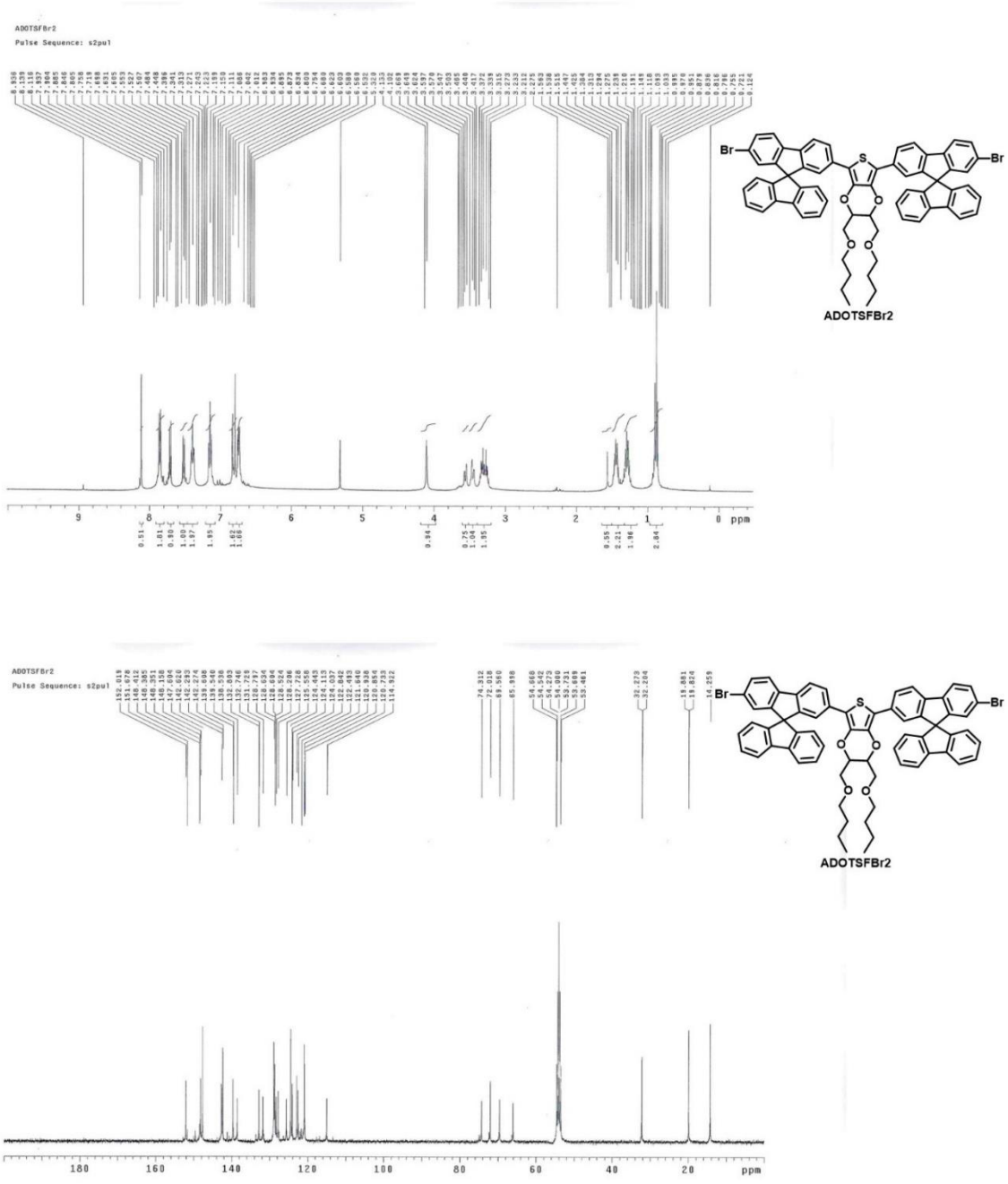

^{1}H and ^{13}C spectra of compound **ADOTSFBr2**.

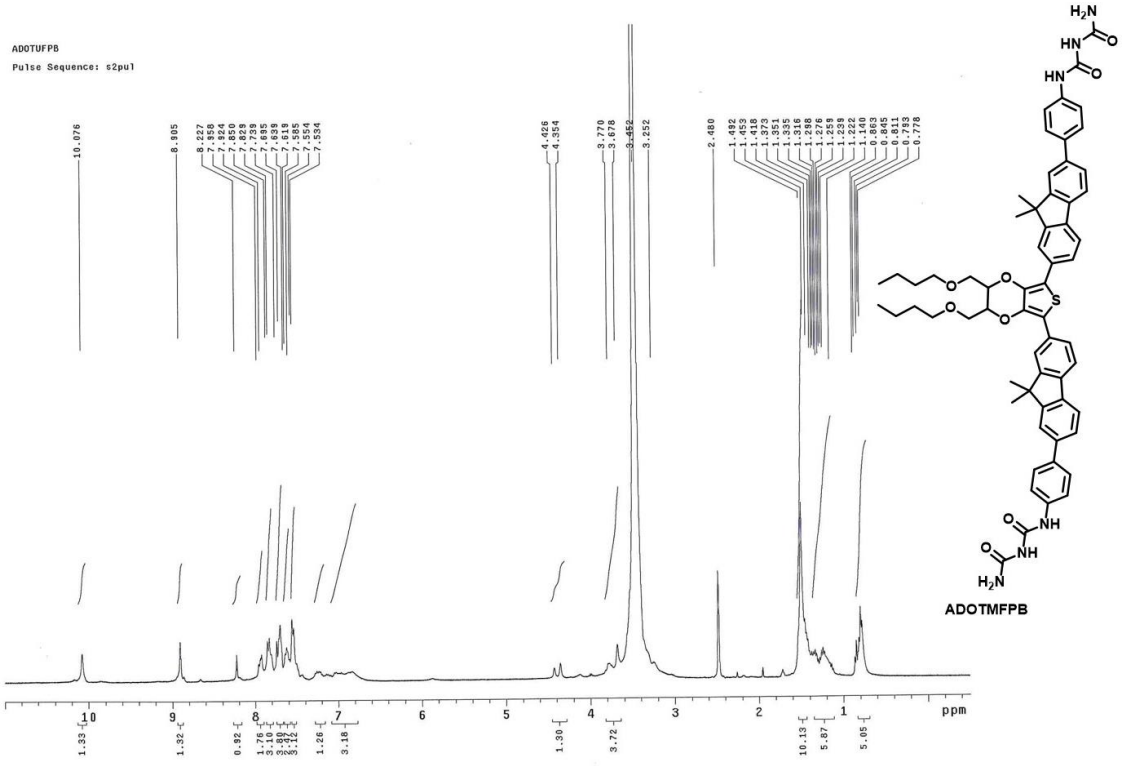

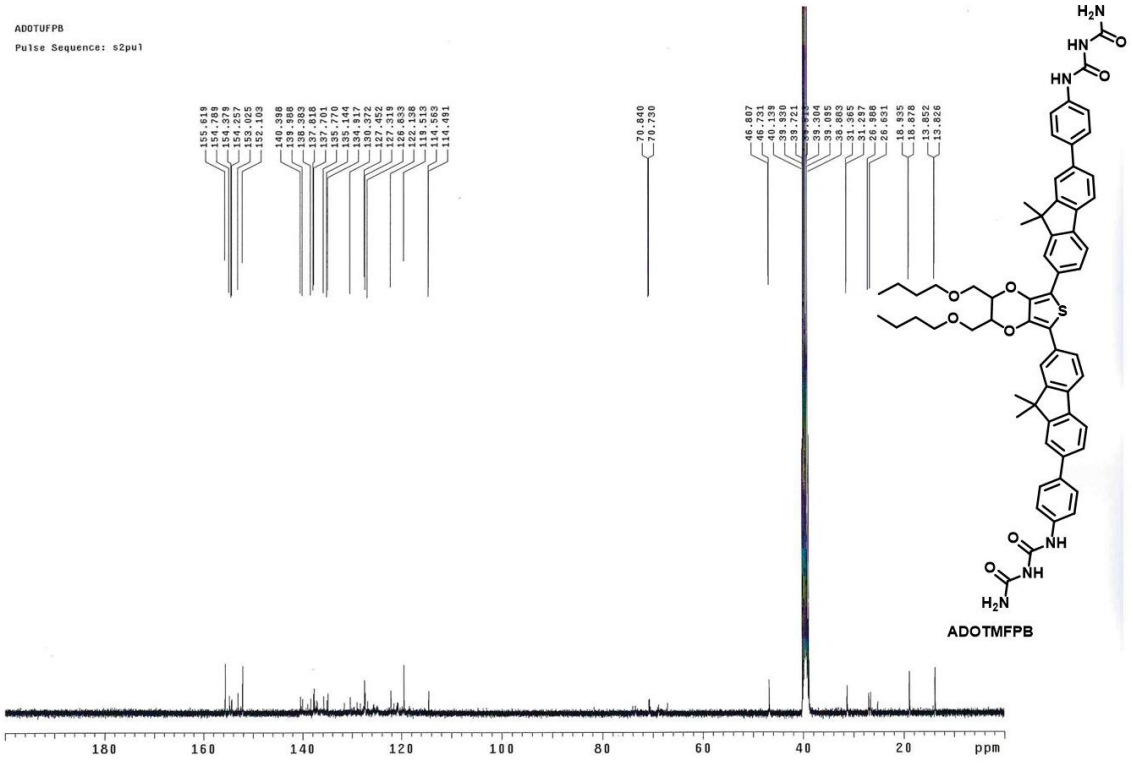

^{1}H and ^{13}C spectra of compound **ADOTMFPB**.

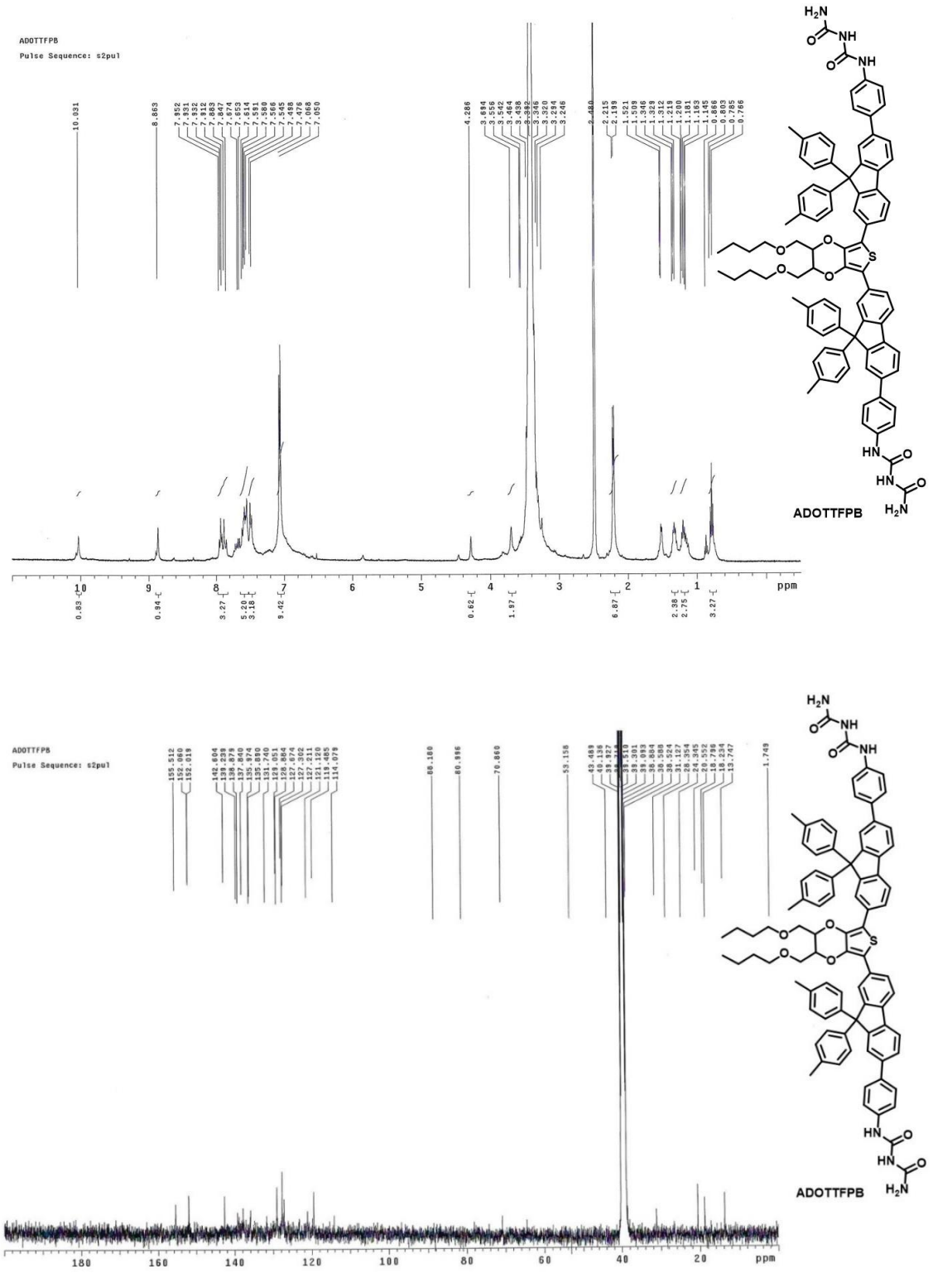

^{1}H and ^{13}C spectra of compound **ADOTTFPB**.

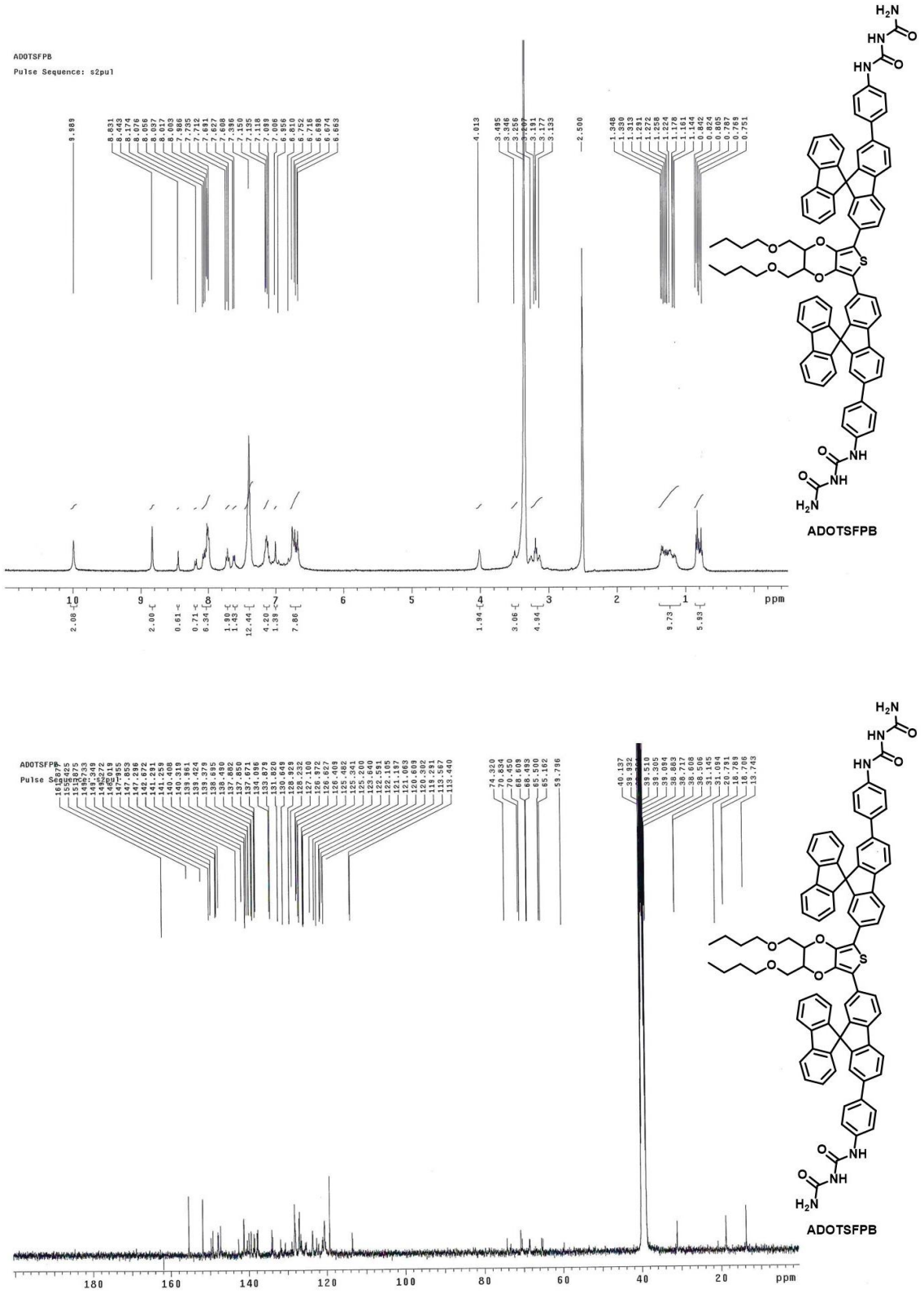

^{1}H and ^{13}C spectra of compound **ADOTSFPB**.

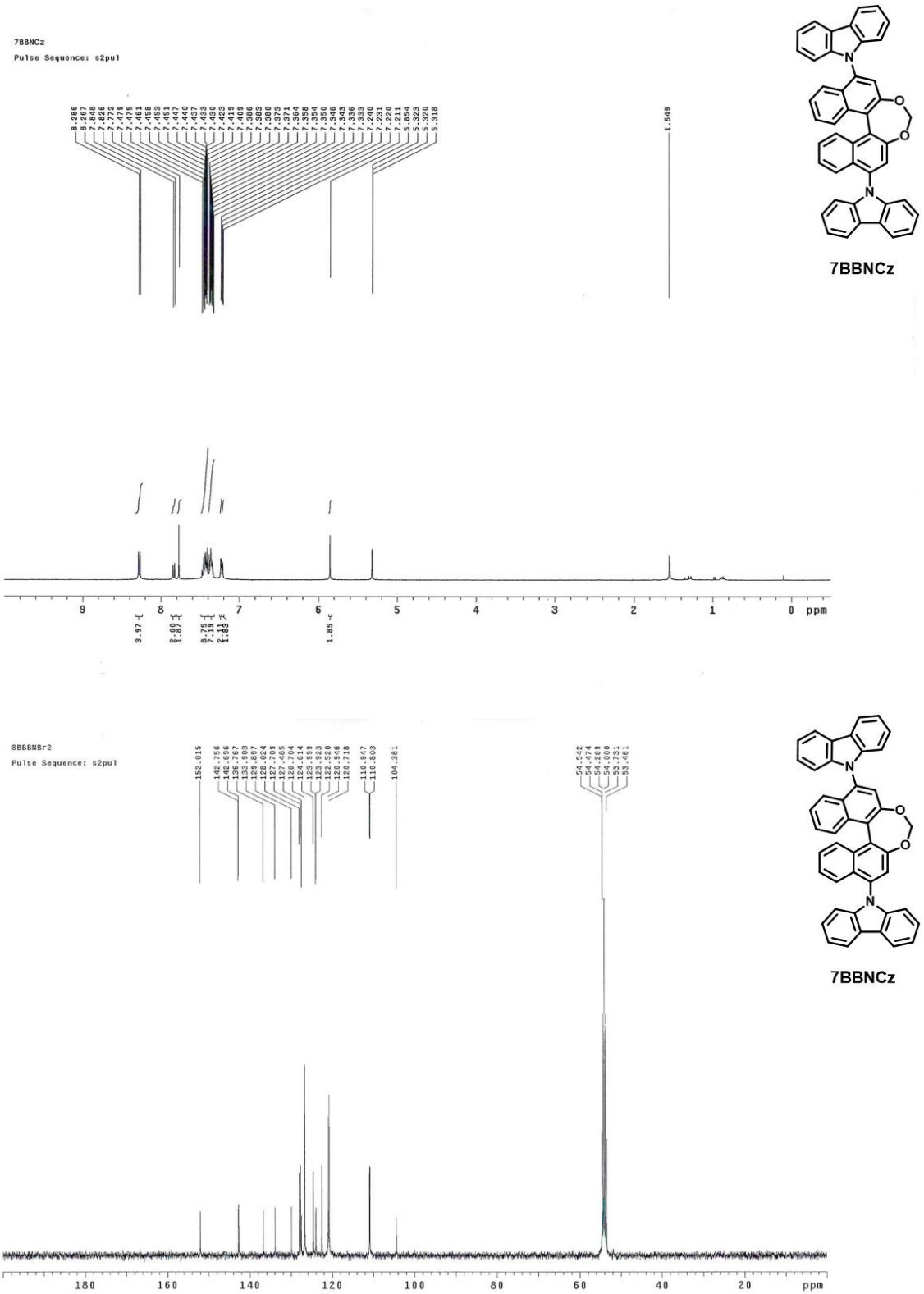

^{1}H and ^{13}C spectra of compound **7BBNCz**.

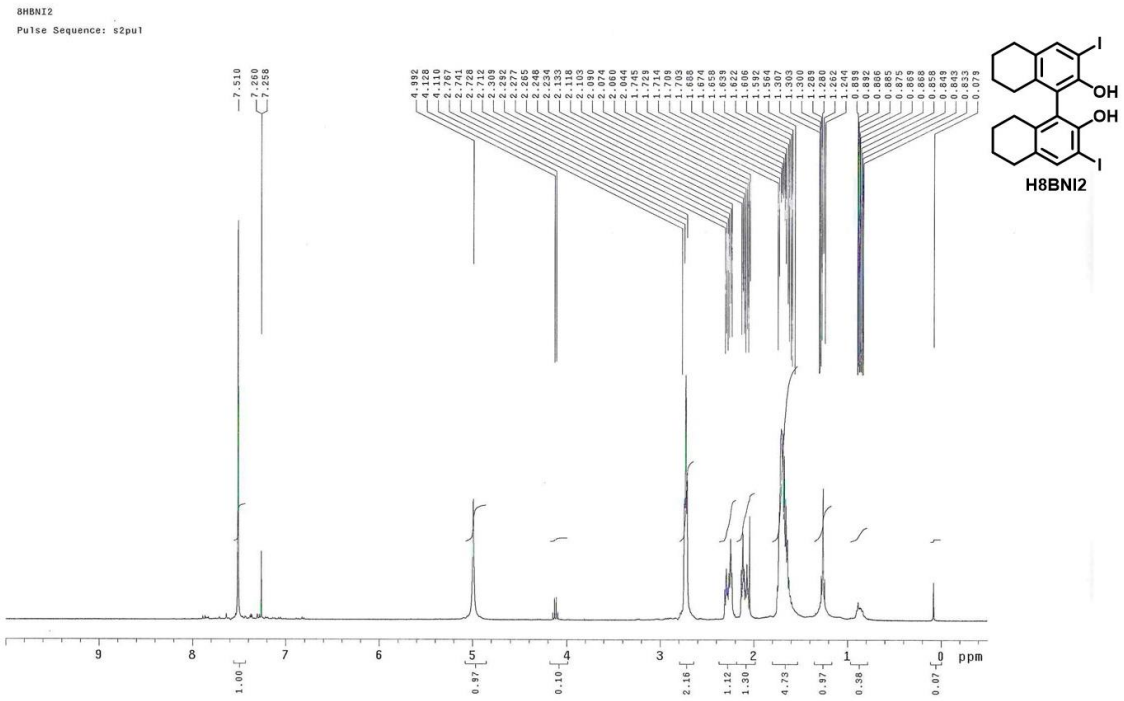

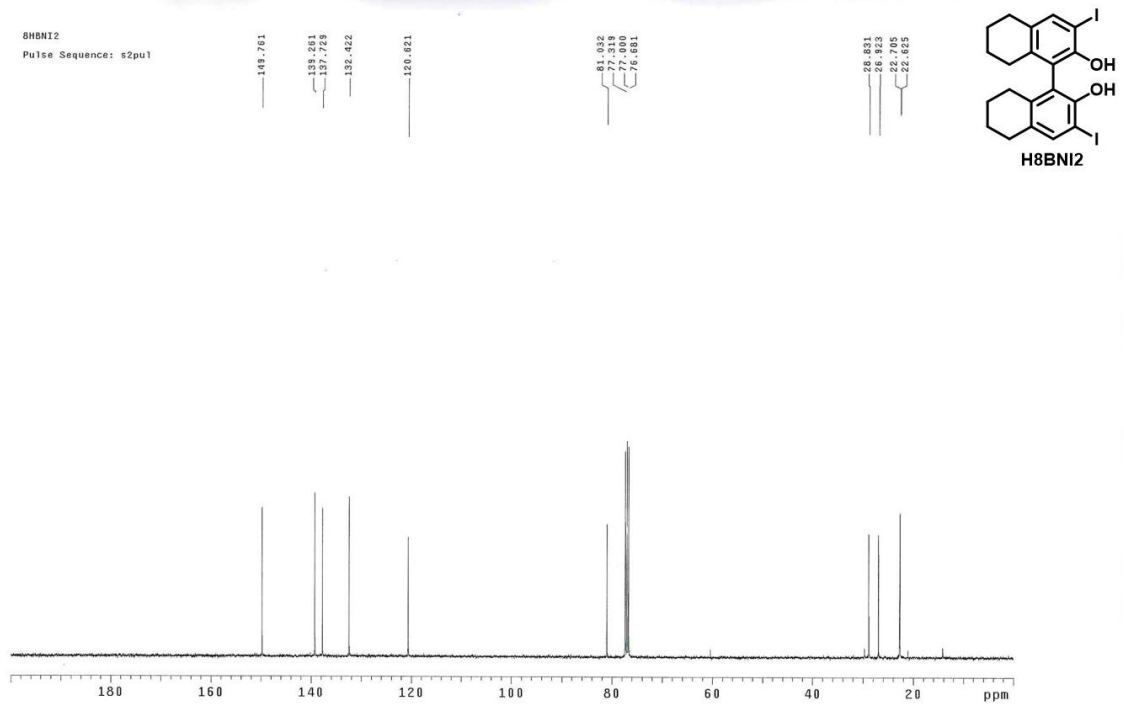

^{1}H and ^{13}C spectra of compound **H8BNI2**.

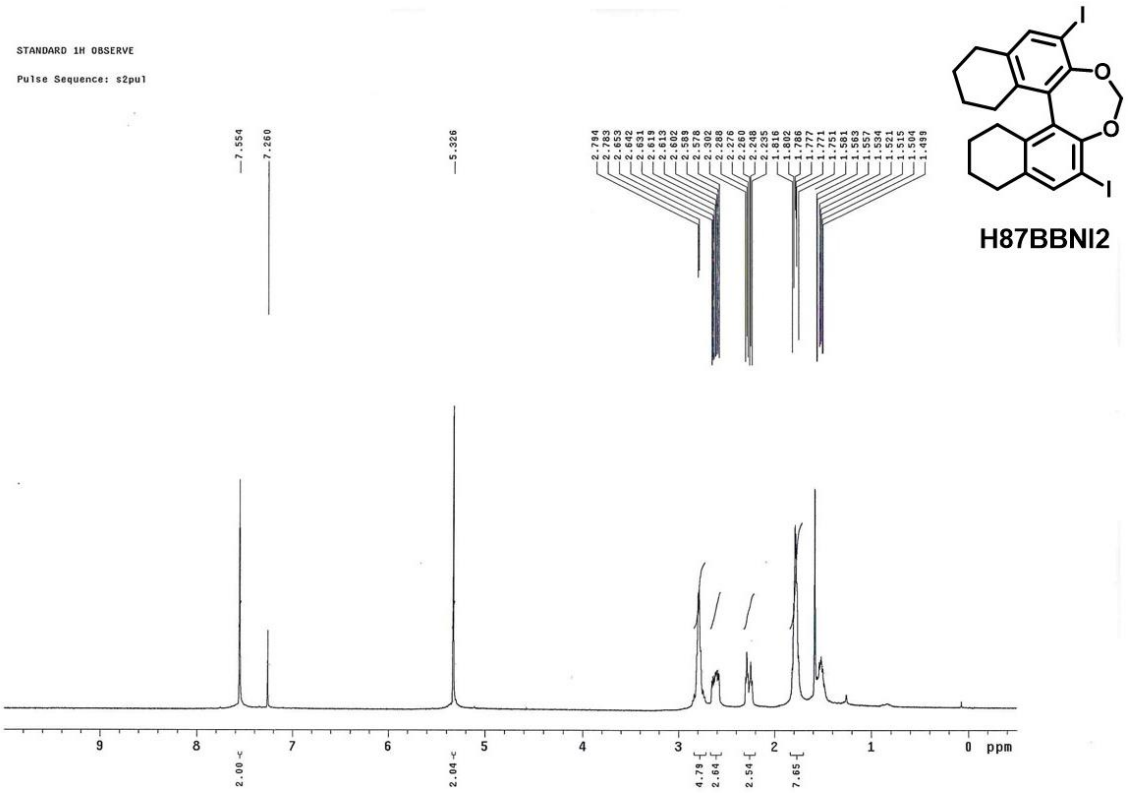

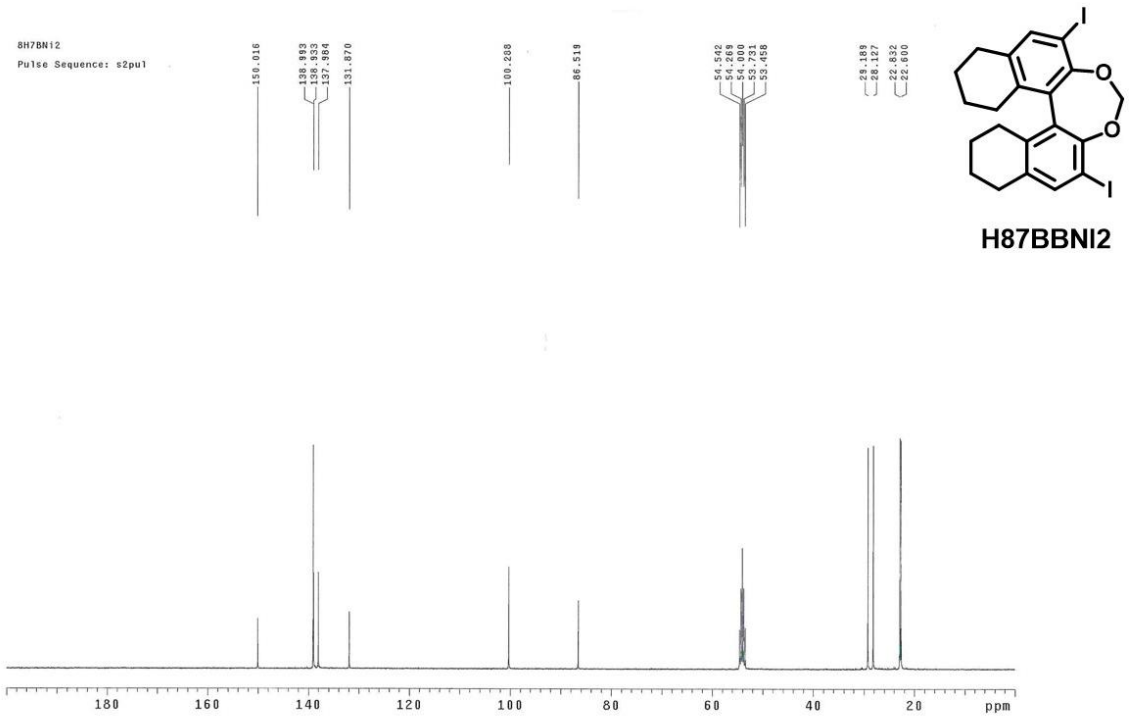

^{1}H and ^{13}C spectra of compound **H87BBNI2**.

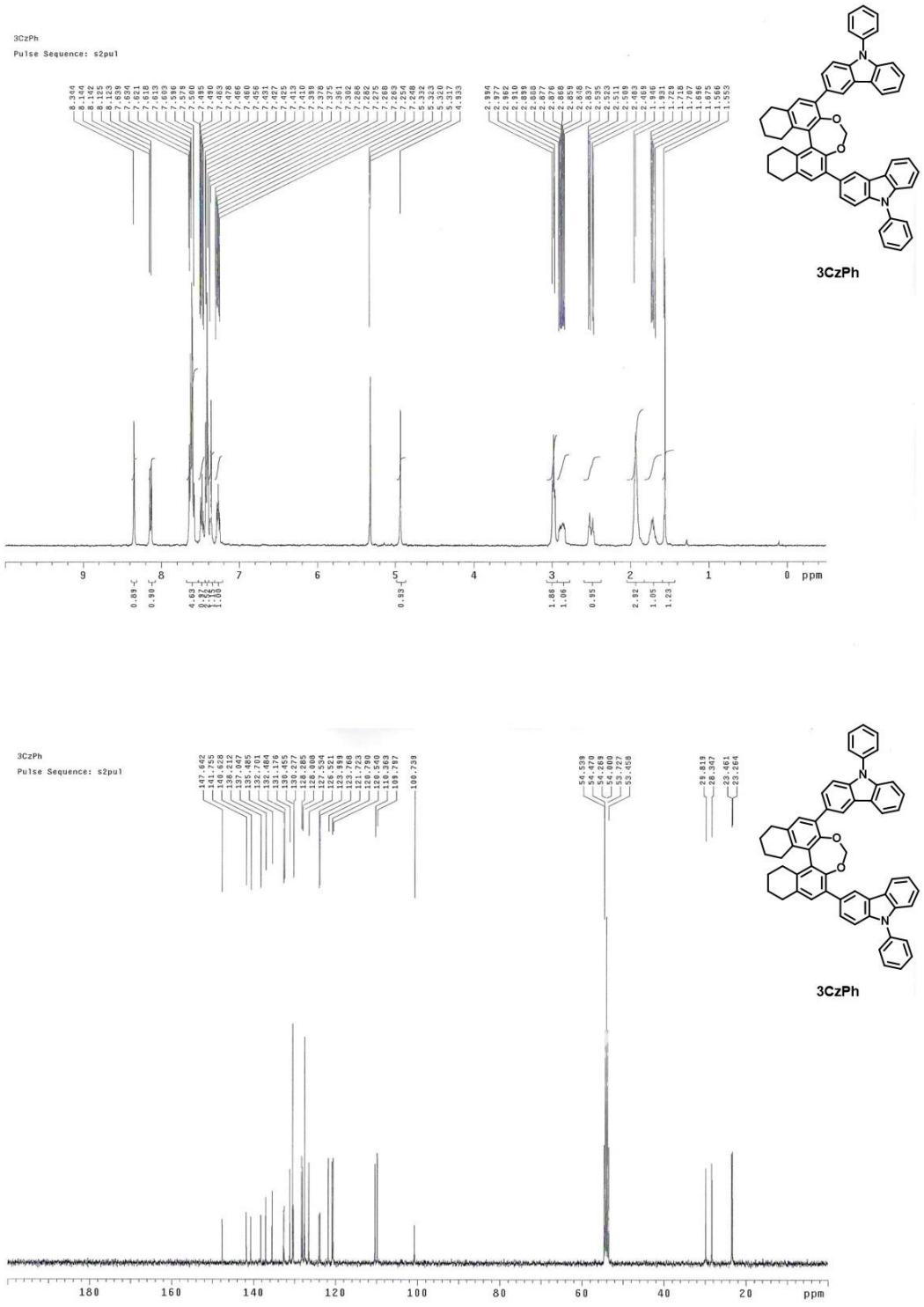

^{1}H and ^{13}C spectra of compound **3CzPh**.

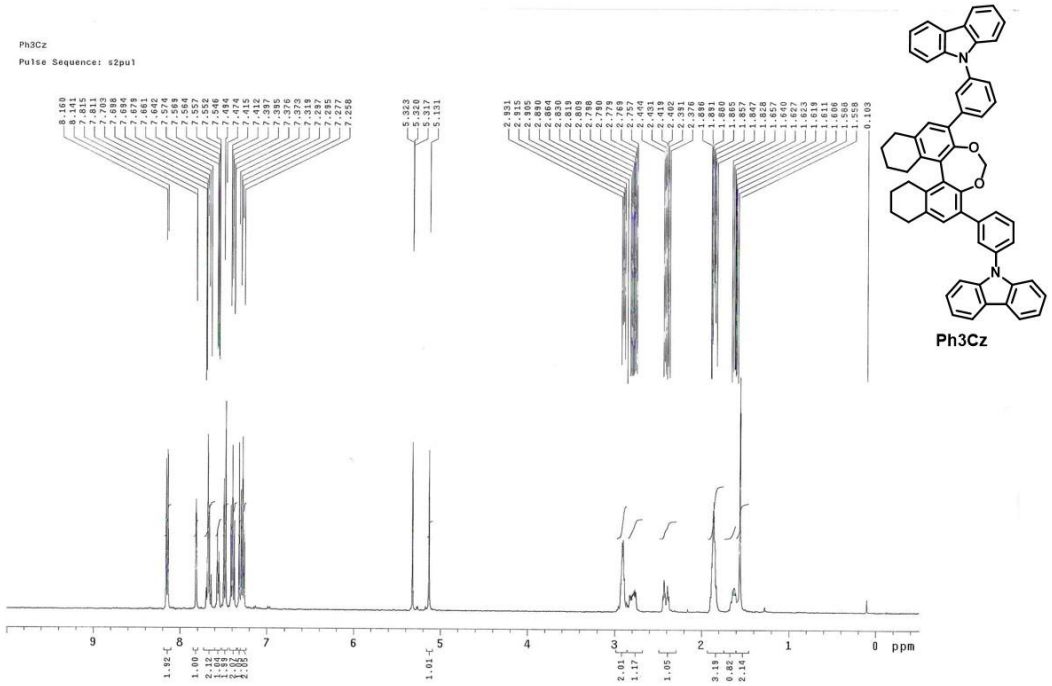

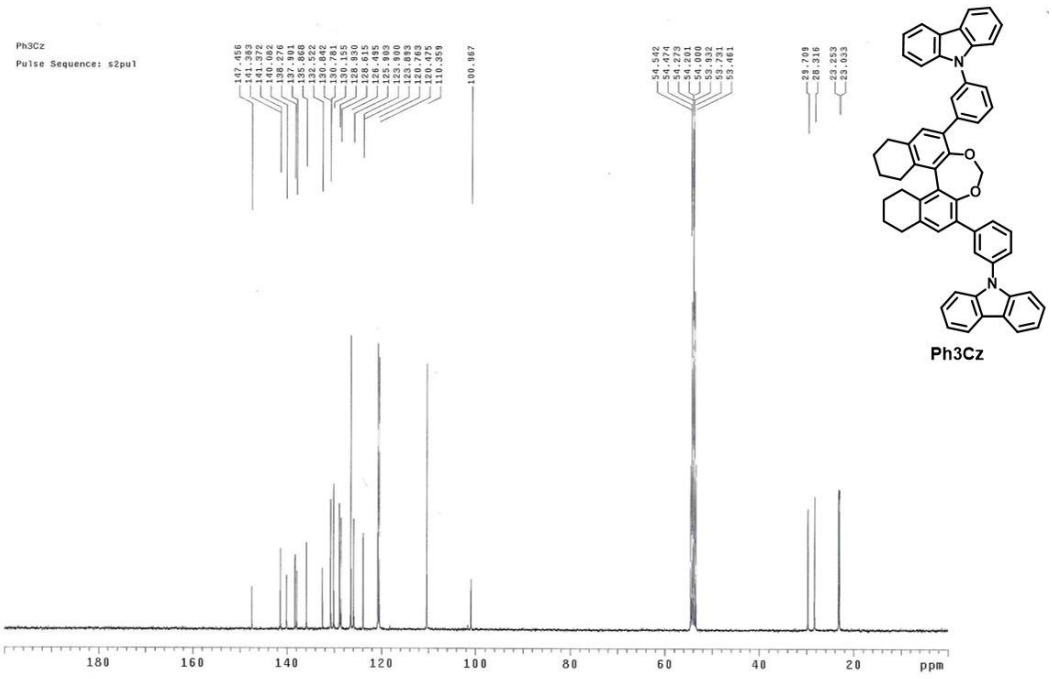

^{1}H and ^{13}C spectra of compound **Ph3Cz**.

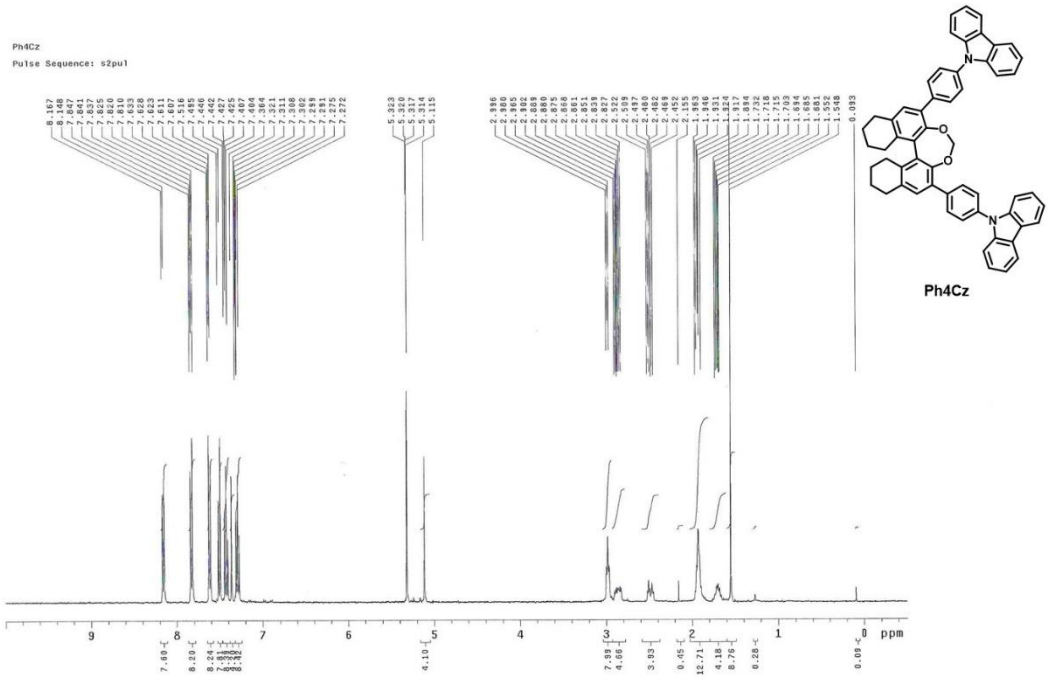

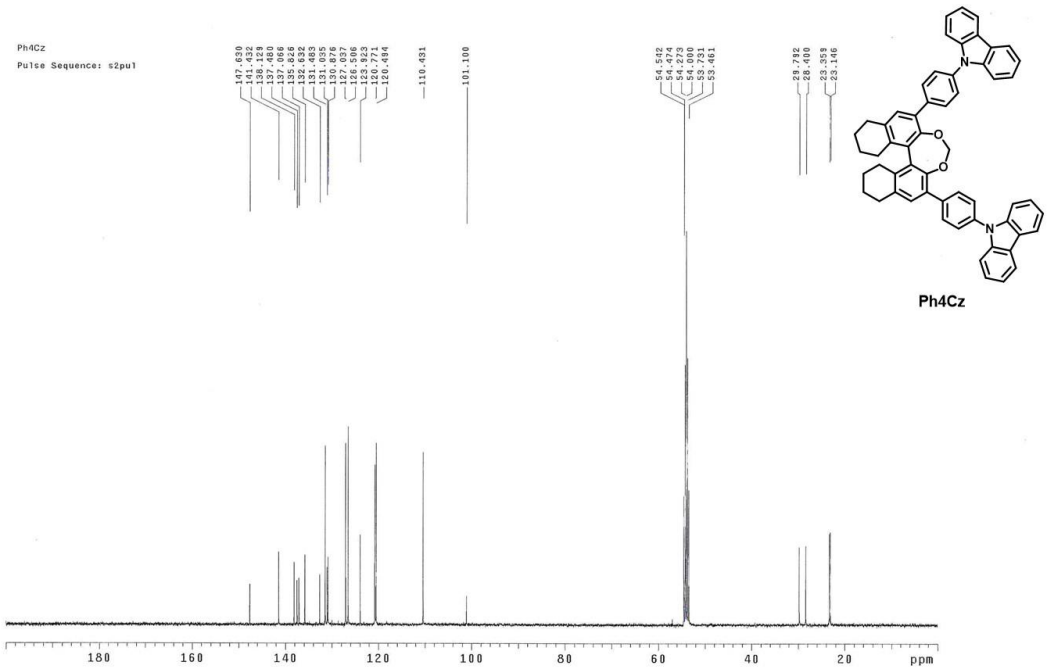

^{1}H and ^{13}C spectra of compound **Ph4Cz**.

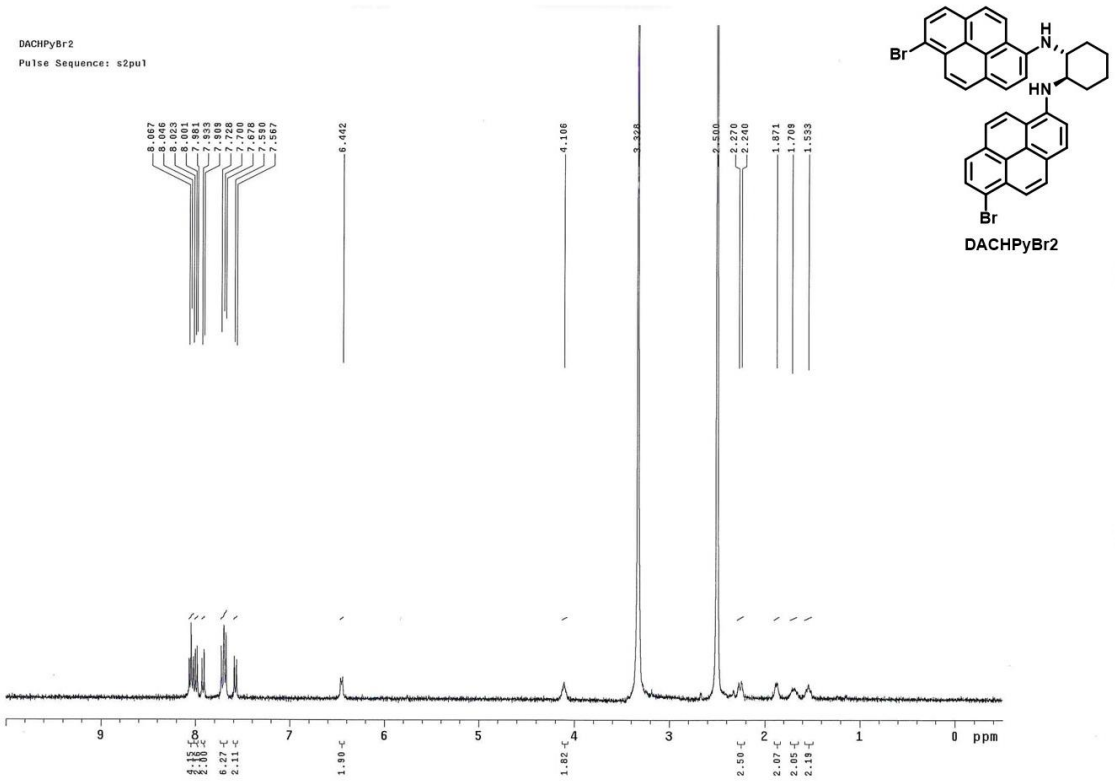

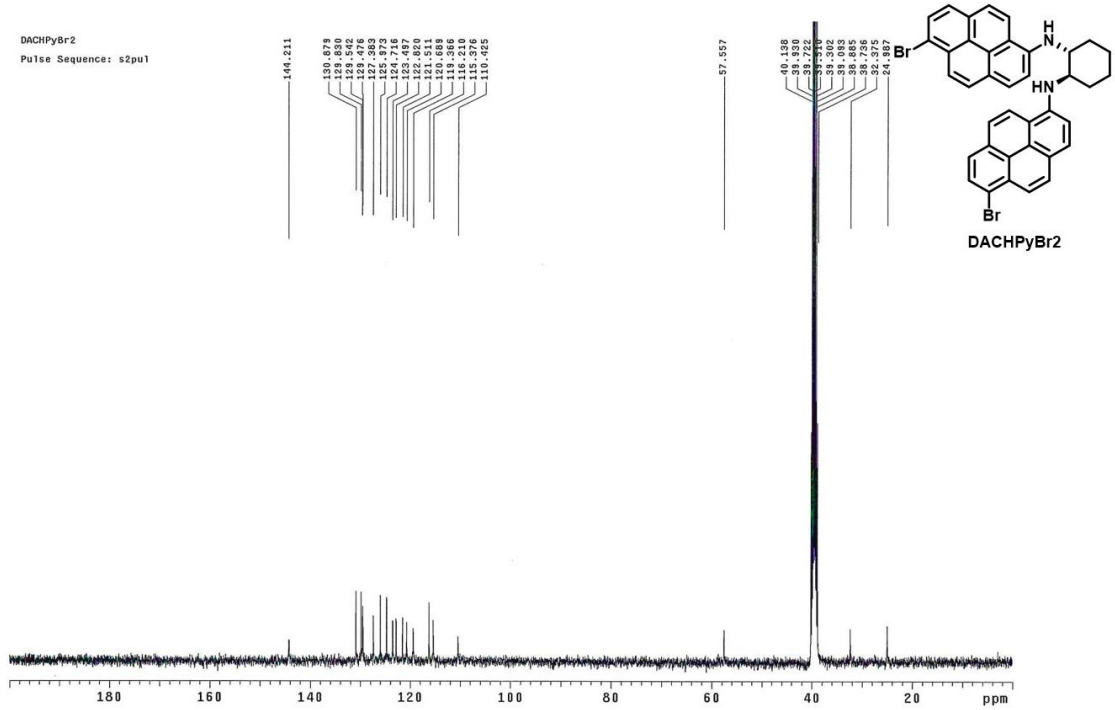

^{1}H and ^{13}C spectra of compound **DACHPyBr2**.

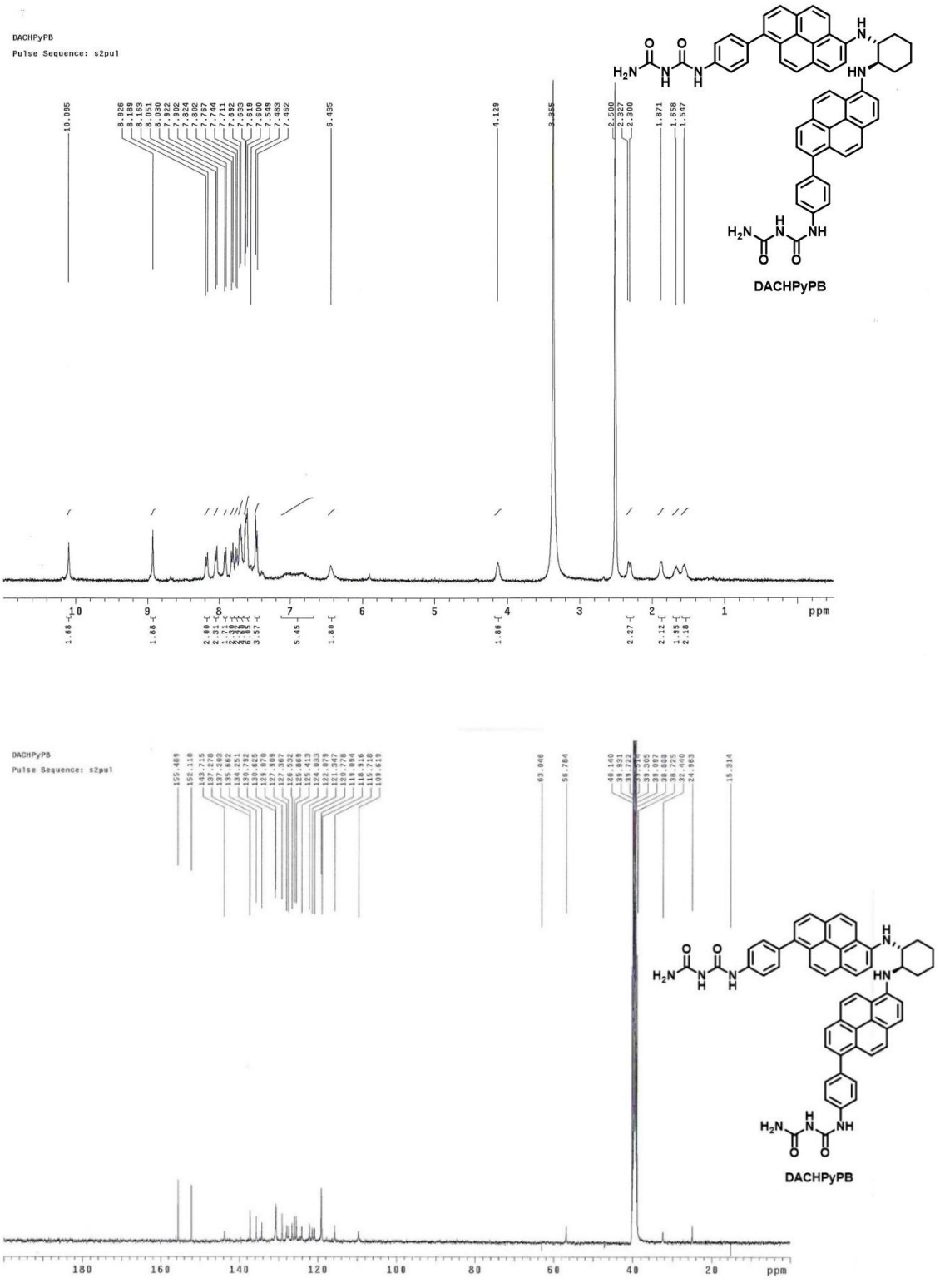

^{1}H and ^{13}C spectra of compound **DACHPyPB**.

Titre: Synthèse et caractérisation de nanostructure auto-assemblées pour la fabrication de dispositifs OLED fonctionnels

Résumé: L'auto-assemblage est une approche prometteuse pour organiser les nanomatériaux organiques fonctionnels en partant de la structure moléculaire. Dans le chapitre 1, nous introduisons le concept d'auto-assemblage et les développements de matériaux fonctionnels organiques supramoléculaires. Dans le chapitre 2, nous concevons des systèmes constitués de chromophores TADF de type D-π-A combinant des motifs de reconnaissance moléculaire de type bis-urée permettant la formation spontanée d'agrégats sphériques bien définis. Les dispositifs électroluminescents utilisant ces matériaux TADF sont capables de récolter des excitons triplets et présentent des efficacités quantiques externes 5 à 10 fois supérieures à celles des systèmes analogues sans comportement TADF, tout en conservant la formation de domaines émissifs de taille inférieure au micron. Dans le chapitre 3, nous combinons des motifs biuret avec divers chromophores chiraux, tels que des 1,1'-binaphtalènes axialement chiraux, des 3,4-alkylènedioxythiophènes chiraux et des dérivés *E*-cyclohexyle chiraux, pour s'auto-assembler en agrégats ordonnés afin d'amplifier les propriétés chiroptiques dans l'état fondamental et excité. Dans le chapitre 4, nous synthétisons une série de dérivés à base de carbazole avec une chiralité axiale capable de former des exciplexes chiraux afin d'améliorer l'intensité de la luminescence polarisée circulairement par un processus de transfert de charge et sondons plusieurs systèmes d'exciplex candidats pour étudier leurs propriétés photophysiques et chiroptiques dans des films.

Mots-clés: chimie supramoléculaire, émission circulairement polarisée, OLED, TADF, aggregats

Abstract: Self-assembly is a promising approach to organize functional organic nanomaterials from the molecular level using molecular design. In Chapter 1, we introduce the concept of self-assembly and the developments of supramolecular organic functional materials. In Chapter 2, we design systems consisting of D-π-A type TADF chromophores and biuret molecular recognition motifs that combine tunable emission wavelength with the spontaneous formation of well-defined spherical aggregates. Electroluminescent devices using these TADF materials capable of harvesting triplet excitons exhibit 5- to 10-times greater external quantum efficiencies compared to analogous systems without TADF behavior while retaining the formation of sub-micron sized emissive domains. In Chapter 3, we combine biuret motifs with various chiral chromophores, such as axially chiral 1,1'-binaphthalenes, chiral 3,4-alkylenedioxythiophenes and chiral *E*-cyclohexyl derivatives, to self-assemble into ordered aggregates to amplify the chiroptical properties in the ground and excited state. In Chapter 4, we synthesize a series of carbazole-based derivatives with axially chirality in application of circularly polarized exciplex to enhance the intensity of circularly polarized luminescence through charge transfer process and probe several candidate exciplex systems to investigate their photophysical and chiroptical properties in films.

Keywords: supramolecular chemistry, OLED, circularly polarized emission, TADF, aggregates